Gate-defined superconducting nanostructures in bilayer graphene weak links

Zur Erlangung des akademischen Grades eines
Doktors der Naturwissenschaften (Dr. rer. nat.)

von der KIT-Fakultät für Physik des
Karlsruher Instituts für Technologie (KIT)
genehmigte

DISSERTATION

von

M. Sc. Rainer Kraft

Tag der mündlichen Prüfung:	22. November 2019
Referent:	Prof. Dr. Wolfgang Wernsdorfer
Korreferent:	Prof. Dr. Ralph Krupke

Acknowledgements

At this point, I would like to express my gratitude to everyone who had his or her part in accomplishing my PhD project:

First of all, I would like to thank Prof. Dr. Wolfgang Wernsdorfer for willing to examine my thesis and giving me the opportunity to conduct this PhD project.

I would like to acknowledge Prof. Dr. Ralph Krupke as my second referee, as well as for allowing me to work in his research unit. He offered helpful advice and food for thought.

Special thanks goes to Dr. Romain Danneau for taking me into his research group, his guidance during my PhD work, and for introducing me to the fascinating world of graphene. It was great to delve into this diverse and manifold topic of 2D materials and van der Waals heterostructures.

My former colleagues and/or predecessor group members Jens Mohrmann, Renjun Du and Stefan Kolenda were instrumental in introducing me to the lab work. For this, and for welcoming me in the group, I am very grateful.
I would further like to thank Simone Dehm for technical support in the lab and Dr. Detlef Beckmann as contact person for questions regarding the electrical measurements as well as for providing his well-maintained molecular beam epitaxy system where we could fabricate our metal contacts and gate structures.
Also, I appreciate all the contributions and support from any member of staff of the Institute of Nanotechnology who made it possible that I could accomplish this work.

During essentially my entire PhD work I shared the office with my colleague Preeti Pandey. I would like to thank her for the friendly atmosphere, her good team spirit and for helping each other out.
In this sense, I would also like to give thanks to all my colleagues and the group members for cooperative team work and having a good time.

For my projects, we had many fruitful collaborations with theory colleagues without which the interpretation of our results would not have been possible. Firstly, I would like to acknowledge Dr. Igor Gornyi for being our in-house go-to guy for many theoretical questions. Together with his students Umut Nefta Kanilmaz and Vanessa

Gall, as well as his colleagues from Ioffe Institute in St. Petersburg Dr. Igor Krainov and Dr. Alexander Dmitriev, he provided valuable input to our results.
I also appreciate our collaboration with Prof. Dr. Anton Akhmerov and Muhammad Irfan from TU Delft. Further on, I would like to thank Dr. Angelika Knothe from the University of Manchester for insightful discussions.
I would like to give special thanks to Dr. Ming-Hao Liu, now Professor at the Cheng-Kung University in Taiwan, for great scientific cooperation but in particular for becoming a friend. I am very thankful to him for inviting me to Taiwan or hosting me as a guest while being guest himself in his former group of Prof. Dr. Klaus Richter at the Uni Regensburg which were great experiences for me.

Finally, I want to thank my parents as well as my brother and sister for always being there for me and for their support at any stage of my life.
And last but not least, I thank my girlfriend Elaine. She is the one special person in my life whom I can trust and rely on and who would still take care of me no matter how stressful or demanding my needs when work was a heavy load. I honestly don't know how I would have done this without her.

Abstract

State-of-the-art edge-connected graphene/hexagonal boron nitride van der Waals heterostructures provide low contact resistivity, high charge carrier mobilities as well as a large mean free path. In combination with their high device geometry flexibility they appear thus to be predestined for realizing high-quality tunable weak links in Josephson junctions, which can be readily implemented into superconducting circuits for quantum technological applications. However, designing gate-controlled nanostructures in monolayer graphene remains a serious challenge due to its lack of a band gap which hinders the confinement of charge carriers. The present thesis aims to address this shortcoming by establishing bilayer graphene as a suitable alternative. Unlike the single-layer relative, bilayer graphene offers the opportunity to open an electronic band gap by breaking the layer symmetry which is possible with the ease of exposing electric displacement fields across the two layers. In this regard, employing the combination of locally defined back and top gate architectures allows to design electrostatically induced nanostructures based on spatial band structure engineering.

In this thesis, at first the realization of a gate-tunable charge carrier confinement is presented. The formation of the constriction is demonstrated by means of superconducting magneto-interferometry measurements. Building on the successfully induced electrostatic confinement and in combination with a more sophisticated double top gate structure, a fully operable quantum point contact is implemented within the bilayer graphene weak link. When the junction is measured in the normal state, quantized conductance is observed due to the formation of one-dimensional subbands. Though, unlike in other material systems we here explore the complexity of the degeneracy of spin, valley and unusual mini-valley quantum degrees of freedom. In final measurements, the quantum point contact is probed in the superconducting state. The measured critical current through the junction displays a discrete variation directly correlated to the quantized steps in the normal state conductance. These results pave the way towards the study of individual Andreev bound levels through this superconducting quantum point contact.

In conclusion, the presented work demonstrates the implementation of electrostatically tunable superconducting nanostructures in bilayer graphene weak links which serves as a platform for the design of more complex electronic circuits.

Kurzzusammenfassung

Modernste Graphen/hexagonales Bornitrid van der Waals Heterostrukturen mit Randkontakten scheinen prädestiniert zu sein, um qualitativ hochwertige und abstimmbare schwach-gekoppelte Verknüpfungen in einem Josephson-Kontakt zu realisieren, da sie geringe Kontaktwiderstände, hohe Ladungsträger-Mobilitäten und eine lange mittlere freie Weglänge sowie eine große Flexibilität im Design der Probengeometrie aufweisen. Diese können in supraleitende Schaltkreise für Anwendungen in der Quantentechnologie integriert werden. Die Entwicklung von elektrostatisch induzierten Nanostrukturen in einlagigem Graphen bleibt jedoch eine Herausforderung, da aufgrund einer fehlenden Bandlücke die Möglichkeit zur räumlichen Einschränkung von Ladungsträgern verhindert wird. Die vorliegende Arbeit hat die Zielsetzung eine potentielle Lösungsstrategie für diese Problematik zu entwickeln, indem zweilagiges Graphen als geeignete Alternative vorgestellt wird. Im Gegensatz zu einlagigem Graphen lässt sich hier eine elektronische Bandlücke öffnen. Dies ist durch brechen der Symmetrie der beiden Schichten in zweilagigem Graphen möglich, was mittels einer angelegten senkrechten elektrischen Flussdichte umgesetzt werden kann. Entsprechend lassen sich mittels einer Kombination aus räumlich lokal definierten Gate-Strukturen auf der Unter- und Oberseite gezielt elektrostatisch kontrollierte Nanostrukturen herstellen.

In dieser Arbeit wird zunächst eine elektrostatisch kontrollierte Ladungsträgereinschränkung realisiert, welche mithilfe von supraleitenden magnetischen Interferenzmessungen nachgewiesen wird. Darauf aufbauend sowie mittels einer erweiterten doppelschichtigen oberen Gate-Struktur wird die Implementierung eines funktionsfähigen Quantenpunktkontakts demonstriert. Bei Messungen im normalleitenden Zustand ist der Leitwert aufgrund der Ausbildung eindimensionaler Subbänder quantisiert. Anders als in anderen Materialsystemen erforschen wir hier jedoch eine komplexe Entartung der Subbänder in Spin-, Valley- und Minivalley-Quantenfreiheitsgraden. In abschließenden Messungen wird der Quantenpunktkontakt im supraleitenden Zustand untersucht. Hier weist der gemessene kritische Strom diskrete Änderungsschritte in direkter Korrelation mit den quantisierten Stufen des Leitwerts im normalleitenden Zustand auf. Die Ergebnisse sind Voraussetzung zur Untersuchung einzelner Andreev-gebundener Zustände durch den supraleitenden Quantenpunktkontakt in zukünftigen Experimenten.

Kurzzusammenfassung

Zusammenfassend lässt sich sagen, dass in der vorliegenden Arbeit elektrostatisch kontrollierbare Nanostrukturen in zweilagigem Graphen hergestellt wurden, welche in einer supraleitenden schwach-gekoppelten Verknüpfung in einem Josephson-Kontakt integriert sind. Die Ergebnisse sind Grundlage für die Entwicklung komplexerer (supraleitender) Schaltkreise.

Contents

List of Abbreviations

1D	one-dimensional
2D	two-dimensional
2DEG	two-dimensional electron gas
3D	three-dimensional
AFM	atomic force microscopy
ALD	atomic layer deposition
BG	back gate
BLG	bilayer graphene
hBN	hexagonal boron nitride
JJ	Josephson junction
MAR	multiple Andreev reflection
NS	normal metal–superconductor
QD	quantum dot
QPC	quantum point contact
PDMS	polydimethylsiloxane
PMMA	polymethyl methacrylate
PPC	polypropylene carbonate
SG	split gate
SIS	superconductor–insulator–superconductor
SNS	superconductor–normal metal–superconductor
SQPC	superconducting quantum point contact
SQUID	superconducting quantum interference device
TG	top gate
vdW	van der Waals

1 Introduction

Ever since its successful isolation, the first truly two-dimensional (2D) material named graphene has attracted great interest and sparked enormous worldwide research activities [GN07]. As the single-layer of graphite, graphene is a monoatomic layer consisting of sp^2 hybridized carbon atoms arranged in a honeycomb lattice. Although 2D layers of graphite were theoretically described much earlier and have been known as the integral part of bulk structures, strictly 2D crystals were presumed to be thermodynamically unstable under ambient conditions and therefore could not exist free standing on their own [GN07]. It was only in 2004, that Konstantin Novoselov and Andre Geim announced the successful isolation and identification of atomically thin layers of graphite [Nov+04]. Their revolutionary but simple idea was to look for the leftover thin crystal flakes on a piece of adhesive tape after peeling off layers from bulk graphite. Indeed, even monoatomic layers of graphene can be obtained owing to the strong in-plane bonds but weak van der Waals (vdW) interactions between different layers. For the subsequently performed experiments on this first of its kind 2D material both received the Nobel Prize in Physics in 2010.

What makes graphene particularly special is its unique electronic band structure arising from the inversion symmetry of two non-equivalent atomic sites in the honeycomb lattice. It is a gapless semimetal where conduction and valence bands touch at the six corner points of the hexagonal first Brillouin zone. In the vicinity of these so-called Dirac points the electronic energy spectrum can be described in terms of a Dirac-like Hamiltonian in the basis of the "pseudo-spin" spinor wave function of the two sublattices [Cas+09]. The resulting energy band structure is linear and the charge carriers in graphene behave like massless quasiparticles. Their relativistic nature gives rise to unusual phenomena such as the half-integer quantum Hall effect [Nov+05a; Zha+05] and Klein tunneling observed as an anisotropic perfect transmission through p–n barriers [KNG06].

Apart from the intriguing possibility to mimic quantum relativistic physics in a condensed matter analogue [GN07], graphene has been envisioned early on to revolutionize in many facets technological applications owing to its superior physical properties with many outstanding material parameters in terms of mechanical strength and elasticity, thermal and electrical conductivities, impermeability to gases as well as many

more [Nov+12]. Probably the most intensely driven field of research on graphene is about its electronic properties with one possible direction of employing graphene for the development of new electronic circuits in quantum technological applications. For instance graphene quantum dots (QDs) are proposed to be used for designing spin qubits [Tra+07] with improved coherence times due to suppressed decoherence mechanisms in carbon-based devices. Moreover, exploiting the additional valley quantum degree of freedom in graphene is anticipated as a platform for developing devices in the new field of valleytronics [RTB07].

However, there is one major obstacle in designing electronic circuits and nanostructures based on graphene, which is its gapless band structure that hardly allows to completely close a conducting channel and confine charge carriers. One amongst other pursued strategies to overcome this problem involved the etching and patterning of graphene into nanoribbons with the eventual opening of a band gap [SCL06], but these devices suffered from scattering from the rough edges [Bis+16]. The good news is that there exists one suitable alternative, which is bilayer graphene (BLG). Being constituted of two coupled monolayers of graphene, BLG provides many similar properties as its single-layer relative, but features also significant differences as it hosts massive Dirac fermions due to a parabolic energy band structure [MK13]. Most importantly though, it is possible to open up an electronic band gap by breaking the inversion symmetry of the two layers [McC06].

The feasibility of engineering spatially defined electronic band gaps by means of electrostatic gating makes BLG an appealing candidate for designing tunable nanostructures. While already in earliest transport experiments on dual-gated BLG devices [Oos+08] the induced opening of a gap has been observed by a largely increasing resistance, a full pinch-off in gate-defined nanostructures appeared to be hampered by leakage arising from hopping transport due to the inhomogeneous developed band gap of initial BLG devices on Si/SiO_2 substrates [Miy+10]. In fact, the Si/SiO_2 substrate was understood as the main limiting factor for earliest graphene devices causing impaired device performance with reduced charge carrier mobilities [HAD07].

The full electronic potential of substrate supported graphene devices was only brought forward by combining it with another 2D material, namely hexagonal boron nitride (hBN), which has been identified as the most ideal substrate material for graphene and gave the field a new boost [Dea+10]. In fact, there exists by now a large zoo of all kinds of 2D materials including metals, semiconductors, insulators, ferromagnets etc., which can be readily assembled into so-called vdW heterostructures [GG13]. While interlayer effects in stacked 2D materials give rise to new intriguing phenomena [Yan+19], the assembly of vdW heterostructures has developed into a new research field by its own [Nov+16]. However for this work, it is most important

to note that hBN can be employed as the perfect atomically flat featureless dielectric substrate retaining graphene's intrinsic properties.

Thanks to further sample fabrication improvements [Wan+13], where graphene is fully encapsulated between a top and bottom hBN flake and connected from the edge of the mesa, extremely clean devices with high contact transparencies can be realized. With this new generation of graphene devices ballistic transport has been demonstrated over micron distance scales. Nevertheless, despite the improved quality of devices with significantly reduced disorder, further attempts of creating electrostatically induced nanostructures in BLG still did not show the aimed success [Goo+12; Drö+12].

The present work is designed to deal with the outlined issues and establish BLG as a versatile platform for realizing tunable nanostructures based on spatially defined band gap engineering by means of electrostatic gating. In our approach we employ state-of-the-art encapsulated devices, but placed onto a pre-patterned back gate (BG) covered by a layer of Al_2O_3 deposited by atomic layer deposition (ALD), thereby fully avoiding effects of inhomogeneities on Si/SiO_2 substrates. Another addressed aspect in this work will be to employ BLG as highly tunable weak link material in a Josephson junction (JJ). Such a device consists of weakly coupled superconductors and makes it possible to measure a supercurrent across an otherwise non-superconducting material. Originally predicted and observed in superconductor–insulator–superconductor (SIS) tunnel junctions [Jos62; AR63], it is actually possible to implemented any kind of conductive system as a so-called weak link [Lik79]. Here we draw on the high-quality and purity of graphene/hBN vdW heterostructures with high contact transparencies that allows to pass a supercurrent over large distance between the superconducting electrodes. This way, we study the tunability of the supercurrent in the BLG weak link coupled to superconducting Ti/Al metal contacts and demonstrate its full monitoring both spatially and in amplitude by means of gate-induced confinement geometries based on locally defined top gate structures. The measurements are performed at mK temperatures in a $^3He/^4He$ dilution fridge using standard lock-in detection techniques with small ac excitation $< 10\,\mu V$ at low frequency signal $\sim 13\,Hz$ combined with out-of-equilibrium measurements in applied out-of-plane and in-plane magnetic fields.

Outline of this thesis

The thesis involves three experimental main parts, that is first establishing a tailoring supercurrent confinement in BLG weak links, then with a refined device structure the realization of a fully operable quantum point contact (QPC), and finally the pioneering towards an superconducting quantum point contact (SQPC) in BLG which

represents the combination of the two previous parts. Each of these three chapters is written in a rather self-contained manner with a separate introduction and literature review about the key aspects of the respective topic, followed by the experimental results and concluded with a short summary.

Therefore, this thesis is organized as follows: In chapter 2 the reader is introduced to the fundamental aspects of this work. This includes at first a discussion why graphene/hBN vdW heterostructures are predestined for the fabrication of high-quality devices. Thereafter, a theoretical description of the electronic energy spectrum in BLG is given with attention to the relevant parameters that tune the band structure. The chapter is completed with an introduction to the fundamental concepts and physics of Josephson junctions and the peculiarities of graphene weak links are pointed out.
Chapter 3 provides the details of sample fabrication, starting from the exfoliation of 2D materials, followed by the assembly routine of vdW heterostructures, the making of electrical contact, and the final patterning of the devices together with the design of top gate (TG) structures. In the second part of this chapter, the low-temperature experimental setup and the measurement scheme are described.
Chapter 4 presents experiments on gate-defined nanostructures in BLG weak link Josephson junctions. The confinement of the supercurrent is investigated by superconducting magneto-interferometry measurements. Therefore, all the background information about this technique are discussed first. The experimental part itself consists of the study on two different confinement geometries, *i.e.* a QPC-like confinement and a long channel confinement.
In chapter 5, we take the findings of the preceding chapter to the next level by adding an additional overall TG to the device. Thanks to this additional tuning knob, we can study the formation of one-dimensional (1D) subbands in a BLG QPC with a unique set of controllable quantum degrees of freedom. A brief introduction to QPCs in general and a short review on attempts in graphene-based devices is provided beforehand.
With the last experiment presented in chapter 6, the priorly established QPC is studied in the superconducting regime. The theory of SQPCs and previous experiments are outlined in the respective literature review.
Finally, the results of this thesis are summarized in chapter 7 and an outlook for further investigations and future experiments is given.

2 Fundamental aspects and literature overview

In this chapter, the fundamental prerequisites for this thesis are introduced.[1] At first, an overview on the rapidly emerging field of graphene/hBN vdW heterostructures is given (2.1), followed by a brief description of the basic electronic properties of bilayer graphene (2.2). In the last part of this chapter, the elementary physics of Josephson junctions as well as peculiarities of graphene weak links are outlined (2.3).

2.1 Graphene/hexagonal boron nitride van der Waals heterostructures

2.1.1 Extrinsic limits on SiO_2

Whilst 2D materials owe their remarkable properties to their atomically thin crystal structure [Nov+05b], this also brings along a great challenge at the same time: With exposed surfaces on both top and bottom sides of the crystal but no bulk in-between, the experimentally observed characteristics are therefore strongly governed by the interaction with the environment which obscures studies on the intrinsic material properties themselves [YXL14]. In this regard, initial measurements on graphene devices were strongly hampered due to the influence of the employed underlying SiO_2 substrate [Tan+07; CF08; Che+08a; Mor+08].[2] Surface roughness [Ish+07; Cul+10], scattering from interfacial phonons [Che+08b] and charged impurities inherent in the oxide [HAD07; Mar+08a; Des+09; Zha+09a] have been identified as major drawbacks setting an extrinsic limit for the device performance (*i. e.* rather low mobilities and high amount of charge disorder).

[1] Note that other more specific theoretical backgrounds and respective literature overviews are discussed within each of the three experimental chapters 4, 5 and 6, respectively.
[2] An review on early electronic transport experiments can be found in [Das+11].

One possible solution to overcome these limitations is to suspend the graphene layer above a trench by etching away the supporting substrate [Mey+07]. While following this approach significant improvements in the sample quality could be achieved [Bol+08; Du+08], the fragility of this device architecture renders the fabrication challenging and restricts the functionality as the structure might collapse under the application of larger gate bias voltages which strongly limits the reachable charge carrier densities or displacement fields [YXL14]. Thus, it would be highly desirable to design devices in a substrate-supported geometry, yet without the limitations brought along by the amorphous SiO_2.

2.1.2 Hexagonal boron nitride – the ideal substrate

In search of new substrate materials, hBN eventually has been recognized as the ideal candidate in 2010 [Dea+10].[3] Being the insulating isomorph of graphite (with boron and nitrogen atoms in place of the carbon atoms sitting on A and B sublattices, respectively), atomically flat layers free of dangling bonds and surface charge traps can be obtained with the ease of mechanical cleavage from the bulk crystals much like in the case of graphene. Moreover, the lattice mismatch of hBN is only $\sim 1.8\,\%$ with respect to graphene, and it provides a large electronic band gap of $\sim 6\,\mathrm{eV}$ [WTK04]. Finally, with the energies of surface optical phonon modes being two times larger than for comparable modes in SiO_2, graphene/hBN heterostructure devices promise improved performance for the operation at high electric field (or high temperature) [Dea+10].

Initial transport measurements on first of its kind graphene/hBN heterostructure devices [Dea+10; Tay+11; May+11; Zom+11] already revealed the benefit of using hBN as the substrate of choice for graphene, showing enhanced charge carrier mobilities by roughly one order of magnitude in comparison to the best devices on SiO_2. The advances have also been directly visualized on the atomic scale by scanning probe microscopy measurements [Xue+11; Dec+11; Bur+13]. Figure 2.1 shows the topography comparison of graphene on hBN and SiO_2 reported in [Xue+11] using scanning tunneling microscopy. Since graphene behaves like a membrane owing to its atomically thin nature and thus tends to conform to the underlying surface topography [Cul+10], the surface roughness of graphene on hBN is greatly reduced compared to the SiO_2 substrate (*i. e.* typically less than 50 pm on hBN, but $\sim 0.5\,\mathrm{nm}$ on SiO_2), thanks to the atomically flat crystalline hBN surface in contrast to the amorphous structure of the thermally grown SiO_2. Further studies presented in [Xue+11] regarding the charge

[3] Note that hBN has been already proposed earlier to be used as a substrate but for reasons of inducing a gap opening in graphene [Gio+07].

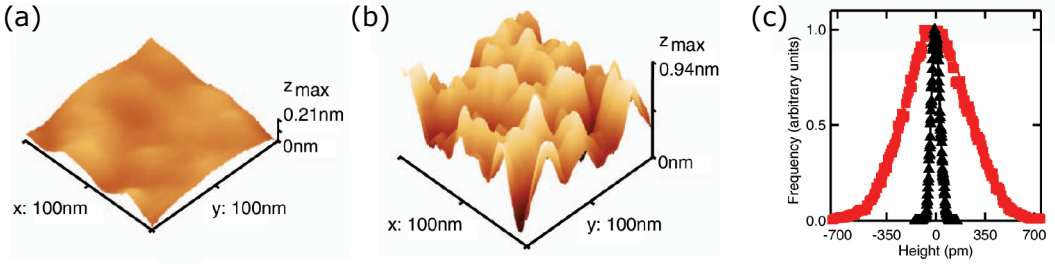

Figure 2.1: Topography comparison of graphene on hBN and SiO_2. STM topography of graphene on (a) hBN and (b) SiO_2. (c) Respective roughness histogram of graphene on hBN (black) or SiO_2 (red). Taken from [YXL14]; original source: [Xue+11].

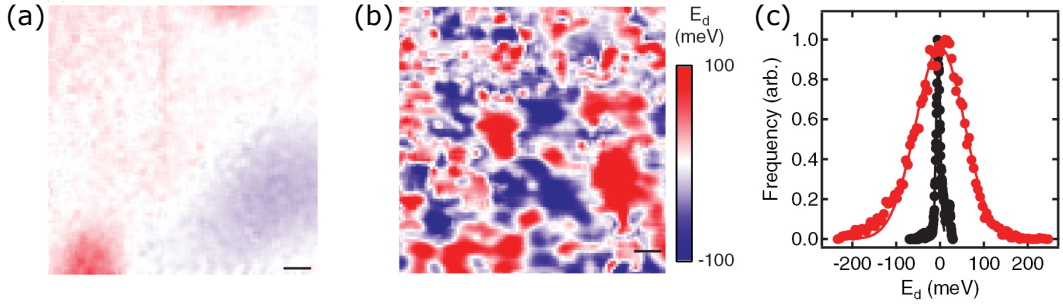

Figure 2.2: Comparison of the spatial charge inhomogeneity in graphene on hBN and SiO_2. Scanning tunneling spectroscopy measurements imaging the spatial charge fluctuations in graphene on (a) hBN and (b) SiO_2.The maps spatially resolve the energy of the Dirac point, corresponding to the tip voltage at the minimum differential conductance. The scale bar is 10 nm in both panels. (c) Respective histograms of the Dirac point energies for graphene on hBN (black) and SiO_2 (red). Taken from [YXL14]; original source: [Xue+11].

inhomogeneity in graphene either on hBN or SiO_2 obtained by scanning tunneling spectroscopy measurements are shown in Fig. 2.2. The results demonstrate the strong reduction of charge fluctuations induced from the underlying substrate. While in standard graphene devices on SiO_2 the charge disorder is typically in the range of $10^{11}\,\mathrm{cm}^{-2}$ to $10^{12}\,\mathrm{cm}^{-2}$, it can be lowered in graphene/hBN heterostructure devices by at least two to three orders of magnitude due to the hBN isolation layer increasing the distance between graphene and charged impurities in the oxide surface. These premises enable to experimentally study the intrinsic properties of graphene down to lowest energies close to the Dirac point singularity. [YXL14]

2.1.3 Sample fabrication improvements

Yet, regardless of all these attributes making hBN the most superior substrate dielectric material for graphene, the required stacking of the different crystallites introduces new sources of disorder by itself. For instance, residual impurities from

the polymer used in initial transfer procedures can hardly be removed completely from the sample. In avoidance of these obstacles, further fabrication improvements have been introduced in 2013 [Wan+13]. Here, the layer assembly is based on a dry and contamination-free transfer method in which the graphene is fully encapsulated between two hBN flakes while electrical contact is made to the 1D graphene edge exposed via selective ion etching, which (apart from minor adaptations) has set the standard in nowadays sample fabrication. Since the devices for this thesis are as well produced following this routine, the details of the procedure are presented later in the methodology chapter 3. At this point, it is only noted that encapsulation with hBN yields extremely clean devices with ultra-low disorder in which ballistic transport has been demonstrated over tens of micrometers [May+11; Wan+13; Tay+13], while edge contacts provide high contact transparency [Wan+13].

2.1.4 Emerging field of 2D materials and vdW heterostructures

Apart from the advances in sample fabrication of graphene/hBN heterostructure devices, it is worth mentioning that the sequential stacking of various 2D materials forming so-called vdW heterostructures has developed into a strongly emerging new research field by its own [GG13]. For instance, engineering artificial material compounds with customized properties has become possible by readily mixing and matching different 2D materials into a heterostructure via the controlled stacking and deterministic placement of the layers without facing the usual constraints of conventional bottom-up approaches [Nov+16; Fri+18]. The selection of the ever-growing family of 2D materials at this stage offers already a broad range of electronic properties including semimetals (graphene), insulators (e. g. hBN), semiconductors (e. g. MoS_2), superconductors (e. g. $NbSe_2$), quantum spin Hall insulators (e. g. WTe_2) or ferromagnets (e. g. CrI_3) [Yan+19].

In addition to the mentioned prospects of combining selectively chosen properties of different 2D materials into a heterostructure, the interplay of the layers becomes concomitantly important. In particular, interlayer interactions in vdW heterostructures have revealed exciting new properties fundamentally distinct from the host layers. As one of the first examples, graphene/hBN heterostructures featured the appearance of secondary Dirac points in the electronic band structure of graphene due to the presence of a moiré superlattice structure [Yan+12]. Indeed, while the hBN crystal acts as featureless but ideal dielectric substrate for graphene at large relative twist angle, it turns out that the arising large-scale lattice interference pattern in case of small rotational misalignment between the layers features rich physics with new emerging physical phenomena, such as the observation of the Hofstadter's butterfly [Dea+13;

Pon+13; Hun+13]. Beyond that, dynamic band structure engineering has been demonstrated by actively tuning the moiré wavelength (*i. e.* the superlattice periodicity) via the controlled twisting of the layers [Rib+18] or by changing the interlayer interactions due to deliberately applied pressure [Yan+18].

In fact, designing artificial structures based on the fabrication of superlattices due to precisely angle-controlled stacking at will is not restricted to graphene/hBN vdW heterostructures. The probably most prominent example has been published only recently, where in a "magic-angle" twisted bilayer graphene unconventional superconductivity could be observed [Cao+18b] (appearing intriguingly next to a Mott-like insulating behavior at slightly different charge carrier density [Cao+18a]). Since then, the excitement in the field is unabated and countless publications followed within the short period of a year, where several groups could reproduce these astonishing results and bring the phenomenon forward to other vdW heterostructures with the observation of further striking effects.

Further readings about the development and future possibilities opening up in the rising field of 2D materials and vdW heterostructures can be found in the reviews [Nov+16; Fri+18; Yan+19] (although not covering the most recent developments in magic-angle twist heterostructures).

2.1.5 Conclusion

In this section, the developments and improvements in fabricating graphene electronic devices have been reviewed. The encapsulation of the graphene sheet between a top and bottom hBN together with electrical contacts designed on the edge of the mesa has set the standard in today's sample fabrication for realizing high-quality mesoscopic devices. Although sometimes cumbersome and at the moment hard to scale up, this provides us the perfect platform for the design of BLG nanostructures. We follow with minor adaptations the vdW assembly routine introduced in [Wan+13], which is presented in chapter 3.

2.2 Why bilayer graphene?

Irrespective of the outstanding and remarkable properties of monolayer graphene, the lack of a band gap [Cas+09], together with the absence of back scattering and the phenomenon of Klein tunneling [KNG06; Kat12] represent a major roadblock when it comes to electronic applications that require the confinement of charge carriers. In

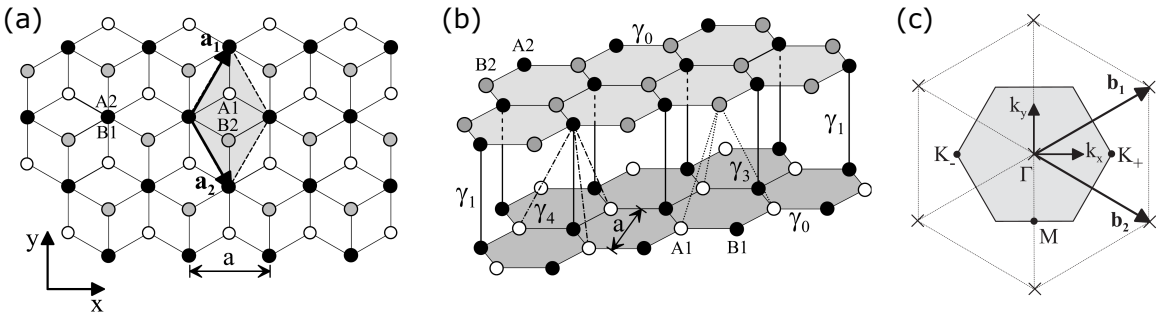

Figure 2.3: Crystal structure of bilayer graphene. (a, b) Plan and side view of the crystal structure of BLG with four different atomic sites A_1 (white), B_1 (black) on the lower layer and A_2 (black) and B_2 (gray) on the upper layer, respectively. The conventional unit cell is shown as a grayish rhombus in (a), with primitive lattice vectors $\boldsymbol{a_1} = \left(\frac{a}{2}, \frac{\sqrt{3}a}{2}\right)^{\mathrm{T}}$ and $\boldsymbol{a_2} = \left(\frac{a}{2}, -\frac{\sqrt{3}a}{2}\right)^{\mathrm{T}}$, where $a = |\boldsymbol{a_1}| = |\boldsymbol{a_2}| = \sqrt{3}a_{\mathrm{CC}} = 2.46\,\text{Å}$ is the lattice constant and $a_{\mathrm{CC}} = 1.42\,\text{Å}$ is the carbon-carbon bond length between neighboring atoms within one layer. Coupling between different atomic orbitals is described by tight-binding parameters γ_0, γ_1, γ_3 and γ_4 as shown in (b). (c) Reciprocal lattice (crosses denote lattice points), with primitive reciprocal lattice vectors $\boldsymbol{b_1} = \left(\frac{2\pi}{a}, \frac{2\pi}{\sqrt{3}a}\right)^{\mathrm{T}}$ and $\boldsymbol{b_2} = \left(\frac{2\pi}{a}, -\frac{2\pi}{\sqrt{3}a}\right)^{\mathrm{T}}$. The first Brillouin zone is a hexagon with center point Γ, featuring two non-equivalent corners K^+ and K^-. Taken from [MK13].

view of these limitations, its bilayer version turns out to just meet with all those challenges. With bilayer graphene, built-up from two coupled single-layers of graphene, it is possible to not only tune the Fermi level but the electronic band structure itself [McC06; MF06; Cas+07]. The opportunity to open an electronic band gap by means of electrostatic gating while drawing on the benefits of high-quality graphene/hBN vdW heterostructures makes BLG an appealing candidate material for the design of electronic devices. In the following, the band structure of BLG is introduced and the parameters that matter in the opening of the gap are discussed. For a detailed description see [MK13].

2.2.1 Band structure

Throughout this thesis we consider Bernal-stacked (*i. e.* AB-stacked) BLG as obtained by cleavage from natural bulk graphite. A schematic of the crystal structure is shown in Fig. 2.3a, b. The lattice structure itself is the same as in monolayer graphene, but the unit cell consists of four atoms A_1, B_1 and A_2, B_2, with two atoms each on lower and upper layer, respectively (unlike monolayer graphene with only A and B atoms on two sublattice sites). The atomic arrangement is such that half of the atoms, *i. e.* B_1 and A_2, is positioned directly on top of each other, while atoms A_1 and B_2 do not have a counterpart as they sit in the center of the hexagon of the respective other layer.

The low-energy band structure can be described in terms of tight-binding theory, involving hopping parameters $\gamma_0 = 3.16\,\text{eV}$, $\gamma_1 = 0.38\,\text{eV}$, $\gamma_3 = 0.38\,\text{eV}$ and $\gamma_4 = 0.14\,\text{eV}$ following the notation of the Slonczewski-Weiss-McClure model for bulk graphite [McC57; SW58].[4] Here, γ_0 denotes the intralayer coupling between electronic orbitals of neighboring atomic sites A_j and B_j ($j = 1, 2$) within one layer, whereas parameters γ_1, γ_3 and γ_4 represent interlayer couplings (see Fig. 2.3b). Note that γ_1 corresponds to a strictly vertical coupling, whereas γ_3 and γ_4 describe skewed couplings with an in-plane hopping component. The resulting band structure consists of four bands with a split pair of each conduction and valence bands. Analogous to monolayer graphene, the six corners of the hexagonal first Brillouin zone denote special points, where the lowest-energy valence and conduction bands touch in the case of intrinsic BLG. In particular, there are two non-equivalent corners K^ξ at $\boldsymbol{k} = \boldsymbol{K}^\xi$ with $\xi = \pm$ (see Fig. 2.3c). Close to these points (*i. e.* at relative momentum $\boldsymbol{p} = \hbar\boldsymbol{k} - \hbar\boldsymbol{K}^\xi$ for $pa \ll \hbar$, where $p = |\boldsymbol{p}| = (p_x^2 + p_y^2)^{1/2}$ with p_x and p_y the x- and y-component of the momentum, respectively), one can write an effective four-band Hamiltonian

$$H_{\text{BLG}}^\xi = \begin{pmatrix} \epsilon_{A_1} & v\pi^\dagger & -v_4\pi^\dagger & v_3\pi \\ v\pi & \epsilon_{B_1} & \gamma_1 & -v_4\pi^\dagger \\ -v_4\pi & \gamma_1 & \epsilon_{A_2} & v\pi^\dagger \\ v_3\pi^\dagger & -v_4\pi & v\pi & \epsilon_{B_2} \end{pmatrix} , \tag{2.1}$$

where $\pi = \xi p_x + i p_y$.[5] The diagonal elements ϵ_{A_1}, ϵ_{B_1}, ϵ_{A_2} and ϵ_{B_2} denote on-site energies on the four atomic sites, respectively, $v = \sqrt{3}a\gamma_0/2\hbar$ is the band velocity and $v_i = \sqrt{3}a\gamma_i/2\hbar$ ($i = 3, 4$) are effective velocities. Neglecting the weakest energy coupling γ_4 and considering an interlayer asymmetry U between the on-site energies of the two layers (*i. e.* $\epsilon_{A_1} = \epsilon_{B_1} = -U/2$ and $\epsilon_{A_2} = \epsilon_{B_2} = +U/2$), one finds four valley degenerate electronic bands given by the energies $\pm E_{\alpha=1,2}$ with

$$\begin{aligned} E_\alpha^2 = {} & \frac{\gamma_1^2}{2} + \frac{U^2}{4} + \left(v^2 + \frac{v_3^2}{2}\right) p^2 + \\ & + (-1)^\alpha \left[\frac{1}{4}(\gamma_1^2 - v_3^2 p^2)^2 + v^2 p^2 (\gamma_1^2 + U^2 + v_3^2 p^2) + 2\xi\gamma_1 v_3 v^2 p^3 \cos 3\varphi\right]^{1/2} , \end{aligned} \tag{2.2}$$

with polar angle of the momentum $\varphi = \arctan(p_y/p_x)$ (a plot of the four bands $\pm E_{\alpha=1,2}$ with $U = 0$ is shown in Fig. 2.4, left panel). [MF06; MK13]

[4] The given hopping parameter values γ_i ($i = 0, 1, 3, 4$) are taken from infrared spectroscopy measurements reported in [Kuz+09].

[5] Note that in the experimental analysis of this thesis we replace the here specified notation for the relative momentum $\boldsymbol{p}$ by the expression $\hbar\boldsymbol{k}$, *i. e.* the wave vector $k = |\boldsymbol{k}|$ and in particular the Fermi wave vector k_F is measured relative to the first Brillouin zone corner points K^+ and K^-.

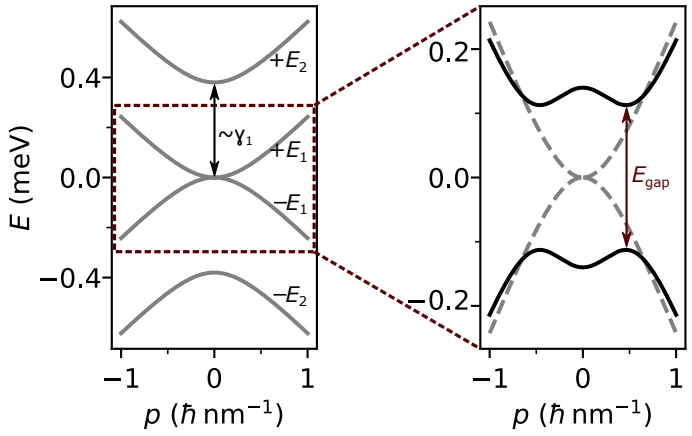

Figure 2.4: Asymmetry band gap – the "Mexican hat". Left: Plot of the four low-energy bands $\pm E_{\alpha=1,2}$ with $U = 0$ (Eq. 2.2). Bands $\pm E_2$ are split away from zero energy in order of γ_1. Right: Plot of the two lowest-energy bands $\pm E_1$ (Eq. 2.4). The presence of a finite layer asymmetry (here $U = 280\,\mathrm{meV}$) opens a band gap (black curves), whereas in the pristine case ($U = 0$) the bands touch at zero energy (gray dashed curves). Note that the asymmetry parameter was chosen large for reasons of clarity. In our experiments $U \lesssim 100\,\mathrm{meV}$, yielding a smaller gap with less pronounced "Mexican hat" shape but more flat bands at the bottom and top of conduction and valence band.

Band structure of the lower-energy bands

In the following, we focus on the lower-energy bands $\pm E_1$, since the higher energy bands $\pm E_2$ are split away from zero energy with a splitting in the order of γ_1, *i. e.* outside the range of typical transport experiments and are of no relevance for the presented results in this thesis.[6]

In order to understand the effects of the involved parameters in Eq. 2.2 on the band structure, it is instructive to first discuss the energy bands $\pm E_1$ in the absence of interlayer asymmetry (*i. e.* $U = 0$) and disregarding terms proportional to γ_3 (*i. e.* $v_3 = 0$). One then obtains a gapless band structure with simplified relation

$$E_1 \approx \frac{1}{2}\gamma_1 \left[\sqrt{1 + \left(\frac{2vp}{\gamma_1} \right)^2} - 1 \right] . \tag{2.3}$$

In this approximation, the dispersion of E_1 interpolates from small to large momentum between a quadratic $\approx p^2/2m$ (with effective mass $m = \gamma_1/2v^2$) and linear $\approx vp$ energy spectrum, with the crossover occurring at $p \approx \gamma_1/2v$ corresponding to a charge carrier density $\sim 10^{12}\,\mathrm{cm}^{-2}$. [MF06; MK13]

[6] Note that the lowest-energy bands can then be described via an effective two-band Hamiltonian [MF06], as explicitly discussed in [MK13]; but here we will not go further into detail and stay with the four-band Hamiltonian in Eq. 2.1 and the lowest-energy bands $\pm E_1$ given in Eq. 2.2 with $\alpha = 1$.

2.2.2 Asymmetry band gap

We now include a finite interlayer asymmetry U, *i.e.* a difference in on-site energies of lower and upper layer. In this scenario the band structure is given by Eq. 2.2 with $v_3 = 0$:

$$E_1^2 = \frac{\gamma_1^2}{2} + \frac{U^2}{2} + v^2p^2 - \sqrt{\frac{\gamma_1^4}{4} + v^2p^2(\gamma_1^2 + U^2)} \quad , \tag{2.4}$$

yielding an electronic band gap between conduction and valence band

$$E_{\text{gap}} = \frac{|U|\gamma_1}{\sqrt{\gamma_1^2 + U^2}} \quad . \tag{2.5}$$

The resulting gapped band structure is shown in Fig. 2.4 (right panel) together with the gapless pristine BLG case. Notably, the gapped spectrum features the shape of a "Mexican hat" with E_{gap} (*i.e.* the closest energy gap between conduction and valence band) occurring at finite momentum $p_{\text{gap}} = |U|\sqrt{(2\gamma_1^2 + U^2)/(\gamma_1^2 + U^2)}/2v$ measured from the center of the K^ξ points, which is a particular characteristic of the BLG band structure with induced asymmetry band gap. Following from Eq. 2.5, the size of the gap is approximately equal to the interlayer asymmetry $E_{\text{gap}} \approx |U|$ in the limit of small $|U| \ll \gamma_1$, but saturates asymptotically $E_{\text{gap}} \to \gamma_1$ in the opposite limit $|U| \gg \gamma_1$. The accessible range in transport experiments is typically $|U| \lesssim 100\,\text{meV} < \gamma_1$. [MK13]

Most importantly, the band gap arising from the broken layer symmetry can be realized experimentally by inducing a perpendicular electric displacement field using the combination of a back gate and top gate [McC06; Cas+07; Oos+08; Zha+09b].[7] The electrostatics of such a dual-gated device can be captured in the picture of a series of parallel-plate capacitors, where the plates are represented by the back gate, the two individual layers of BLG and the top gate, respectively. In a Hartree model of screening [McC06], the interlayer asymmetry U parameterizing the on-site energy difference between the two BLG layers may be written as the sum of externally induced asymmetry plus a screening term

$$U = U_{\text{ext}} + \Lambda\gamma_1\frac{n_2 - n_1}{n_\perp} \quad . \tag{2.6}$$

The externally induced interlayer asymmetry is determined by

$$U_{\text{ext}} = \frac{ec_0}{2\epsilon_0\epsilon_r}(D_{\text{b}} + D_{\text{t}}) \quad , \tag{2.7}$$

[7] Alternatively, but less tunable, the asymmetry of on-site energies between the layers may be induced by chemical doping [Oht+06].

where $c_0 = 3.35\,\text{Å}$ is the interlayer distance between the BLG capacitor plates, $\epsilon_r \approx 1$ is the dielectric constant of the interlayer space and $\bar{D} = (D_\text{b} + D_\text{t})/2$ is the average electric displacement field, generated by back gate $D_\text{b} = +\epsilon_0\epsilon_\text{b}(V_\text{BG} - V_\text{BG}^\text{cnp})$ and top gate $D_\text{t} = -\epsilon_0\epsilon_\text{t}(V_\text{TG} - V_\text{TG}^\text{cnp})$, respectively. Here, ϵ_b, ϵ_t and d_b, d_t are the dielectric constants and thicknesses of the bottom or top dielectric layers, respectively, and the effective offset voltages V_BG^cnp and V_TG^cnp account for the presence of environment-induced charge carrier doping in the absence of applied gate voltages. [MK13]

The second term in Eq. 2.6 takes into account the charge redistribution in the presence of an external field. The rearrangement of charge carriers leads to an imbalance between the layers which causes an internal electric field screening the external one [McC06; Cas+07]. The introduced dimensionless screening parameter Λ is defined as $\Lambda = c_0 e^2 n_\perp / 2\gamma_1\epsilon_0\epsilon_r$ with characteristic density scale $n_\perp = \gamma_1^2/\pi\hbar^2 v^2$. Note that the asymmetry parameter U is related to the layer densities n_1 and n_2 on lower and upper layer (cf. Eq. 2.6), respectively, which in turn include a dependency on U owing to the tuning of the band structure in the case of broken layer symmetry. Thus, the asymmetry parameter U needs to be calculated self-consistently

$$U(n) = U_\text{ext}\left[1 - \frac{\Lambda}{2}\ln\left(\frac{|n|}{2n_\perp} + \frac{1}{2}\sqrt{\left(\frac{n}{n_\perp}\right)^2 + \left(\frac{U}{2\gamma_1}\right)^2}\right)\right]^{-1}, \tag{2.8}$$

where n is the total charge carrier density related to the applied gate voltages in the parallel-plate capacitor model by

$$n = \frac{C_\text{BG}}{e}\left(V_\text{BG} - V_\text{BG}^\text{cnp}\right) + \frac{C_\text{TG}}{e}\left(V_\text{TG} - V_\text{TG}^\text{cnp}\right) \quad . \tag{2.9}$$

Here, $C_\text{BG} = \epsilon_0\epsilon_\text{b}/d_\text{b}$ and $C_\text{TG} = \epsilon_0\epsilon_\text{t}/d_\text{t}$ are the specific gate capacitance per unit area of back gate and top gate, respectively. [MK13]

The tuning of the band gap in a dual-gated device is shown in Fig. 2.5a, b, displaying the typically observed behavior of the resistance as a function of V_BG and V_TG in a three-dimensional (3D) plot and respective 2D color map [Tay+11]. Two different lines of larger resistance are observed, *i. e.* one only tuned by V_BG corresponding to charge neutrality outside the top-gated region, whereas the other line (indicated by a black line in Fig. 2.5b) is tuned by both gates corresponding to charge neutrality within the dual-gated region of the device ($\delta D = D_\text{b} - D_\text{t} = 0$). Clearly, the resistance strongly increases along this diagonal line with increasing displacement fields $\bar{D} = D_\text{b} + D_\text{t})/2$, indicating the opening of a band gap. Cuts along iso-displacement field lines (*i. e.* $\bar{D} = \text{const.}$; indicated by colored lines in Fig. 2.5b) are shown in Fig. 2.5c. For each curve the resistance gets maximal when $\delta D = 0$.

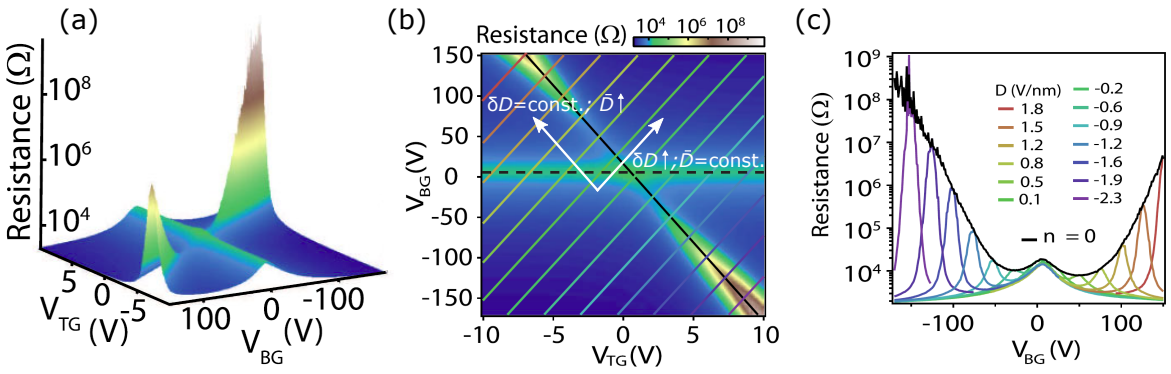

Figure 2.5: Dual-gate map of BLG. (a, b) 3D plot and respective 2D color map of the resistance as a function of V_{TG} and V_{BG}. The opening of a band gap is observed by the increasing resistance along the charge neutrality line $\delta D = D_{\mathrm{b}} - D_{\mathrm{t}} = 0$ (black line) with increasing displacement field $\bar{D}$. (c) Resistance along iso-displacement-field line cuts ($\bar{D} = \text{const.}$). Taken from [Tay+11] (with added white axes of δD and $\bar{D}$ in panel (b)).

2.2.3 Interlayer coupling γ_3 – effects of trigonal warping

Despite the band structure of BLG being mostly governed by the hopping parameters γ_0 and γ_1, the skew interlayer coupling γ_3 becomes important at small energy scales, providing a source of trigonal warping at the bottom or top of the conduction and valence band, respectively [MF06]. In this work, this may be of particular relevance when the system is depleted down to pinch-off in order to successfully design nanostructures by means of band gap engineering in BLG. In this regard, we illuminate the effect of γ_3 in the joint presence of interlayer asymmetry U, where E_1 is determined according to Eq. 2.2. Figure 2.6 shows a respective contour energy plot for the lowest conduction band E_1. Intriguingly, the continuous iso-energetic lines at higher energy break into three isolated pockets (or mini-valleys) at low energy with size of order 1 meV featuring a Lifshitz transition [Lif60] (the exact energy splitting of these pockets depends on the magnitude of interlayer asymmetry parameter U).[8] The presence of these mini-valleys should give rise to a new effective degeneracy in the system at this energy scale, as e. g. observed in the Landau level spectrum of gapped BLG [Var+14b]. However, it is important to note that in a locally gate-defined nanostructure there is a spatially modulated potential acting on the on-site energies, which makes the description less trivial [KF18].

[8] Note that the effect of trigonal warping and the resulting formation of pockets is different in the absence of interlayer asymmetry (*i. e.* $U = 0$); see [MK13].

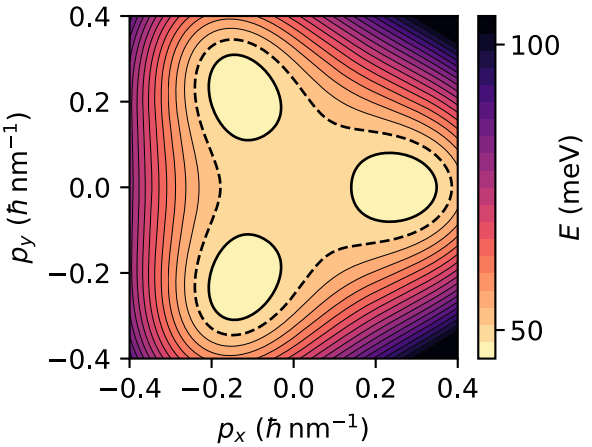

Figure 2.6: Trigonal warping of the bands. Contour plot of the conduction band in valley K^+ following from Eq. 2.2 with interlayer asymmetry $U = 100\,\text{meV}$. The highlighted lines denote the Lifshitz transition from a single continuous iso-energetic line (dashed black line) into three isolated pockets (thicker black line) at the bottom of the band.

2.2.4 Conclusion

In this section, BLG has been introduced as an interesting candidate material for the design of gate-defined nanostructures due to the possibility to open an electronic band gap by applied electrical displacement fields. The relevant parameters in the tight-binding description of the band structure have been discussed, including the layer asymmetry U responsible for the gap opening, as well as trigonal warping effects due to the "skewed" interlayer parameter γ_3 affecting a fine tuning at the bottom or top of conduction and valence bands, respectively. While the gate-tunable band gap is the key throughout all presented experiments, the fine structure tuning of the bands might affect the degeneracy of the system and thus plays in particular a role in the formation of subbands in a BLG QPC (chapter 5).

2.3 Josephson junctions

It is now only a few years back, that the anniversary years of two of the most striking and spectacular phenomenons in condensed matter physics were commemorated [Wil12; War11], that is superconductivity and the Josephson effect. In 1911, H. Kamerlingh Onnes made the groundbreaking discovery that the resistance in a mercury wire abruptly vanished after cooling to 4.2 K in liquid helium, which is together with the Meissner effect (*i. e.* the expulsion of magnetic fields) the manifestation of superconductivity [Tin04]. The absence of resistivity is understood within the Bardeen-Cooper-Schrieffer (BCS) theory [BCS57] by the condensation of electrons

into Cooper pairs, which form a coherent macroscopic quantum state described by a single wave function $\Psi(r) = |\Psi(r)|e^{i\theta(r)}$ with a single phase $\theta(r)$. The fact that an electric current persists indefinitely in a superconducting loop without driving source sparked people to envision a superconducting future.

In the second half of this "century of superconductivity" (1962), Brian Josephson [Jos62] came up with an answer to the question what should happen when two superconductors (with phases θ_1 and θ_2, respectively) are weakly coupled together in a sense that they can feel each other but not so strong that a new coupled superconductor is formed with phase θ_3 [War11]. In the framework of a SIS junction, he postulated interference effects between the two superconducting wavefunctions depending on the phase difference $\varphi = \theta_1 - \theta_2$ and the so-called Josephson effect is ever since one of the most striking and spectacular macroscopic quantum phenomenons in condensed matter physics. Interestingly, although superconductivity is a macroscopic phenomenon, here the junction dynamics rather strongly depend on microscopic properties. In the following, different aspects of Josephson junctions are discussed.

2.3.1 Josephson equations

In his seminal description of two weakly coupled superconductors, Brian Josephson predicted a supercurrent to flow across the junction based on the phase difference of the two superconducting reservoirs $\varphi = \theta_1 - \theta_2$ [Jos62]. This microscopic phase difference, determining the dynamics of the junction, is related to the macroscopic currents and voltages of the junction according to the first and second Josephson equations:

$$I_s = I_c \sin \varphi \tag{2.10}$$

and

$$V = \frac{\hbar}{2e} \frac{\partial \varphi}{\partial t} . \tag{2.11}$$

The first equation denotes a Josephson current I_s through the weak link proportional to $\sin \varphi$ with a maximum Josephson current (or critical current) I_c, whereas the second equation relates the voltage V across the weak link to the evolution of the phase difference in time $\partial\varphi/\partial t$. For a current smaller than I_c, the junction is in the supercurrent state with zero voltage drop and thus, there is no change of the phase difference (dc Josephson effect). On the other hand, in the case of a current exceeding I_c, the junction is no longer in the zero- but in a finite voltage state where the phase difference evolves in time. In the consequence, the current $I_s = I_c \sin(2eVt/\hbar + \varphi_0)$ oscillates with amplitude I_c and a frequency $f_J = 2eV/h$, where $2e/h \approx 483.6\,\mathrm{GHz\,mV^{-1}}$ is a fundamental constant (ac Josephson effect). [Tin04]

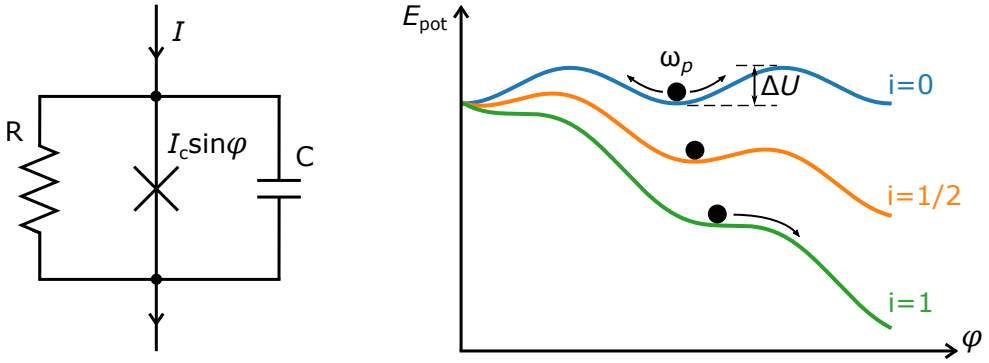

Figure 2.7: RSCJ model. Left: Equivalent circuit of a Josephson junction in the RSCJ model. Right: Dynamics of a fictitious phase particle in the tilted washboard potential E_{pot} for different biasing current $i \equiv I/I_c$.

2.3.2 Resistively and capacitively shunted junction model

In the finite voltage state, the total current is carried in parts by additional current channels other than the Josephson current, which can be described within the RCSJ model as outlined in the following (based on [Tin04; GM05]). An equivalent circuit is shown in Fig.2.7a, consisting of the ideal Josephson junction with current $I_s = I_c \sin(\varphi)$ shunted by parallel resistive and capacitive channels, respectively. The former is due to the contribution of unpaired quasiparticles in the presence of a voltage across the junction with resistive normal current $I_{res} = V/R$, while the latter arises under a time varying voltage due to the geometrically induced capacitive coupling of the two superconductors with displacement current $I_{cap} = C\frac{dV}{dt}$. Note that the resistance R is assumed to be constant within the RCSJ model. The total current through the junction is given according to Kirchhoff's law by the sum $I = I_s + I_{res} + I_{cap}$. In combination with the second Josephson equation (Eq. 2.11), and by introducing a dimensionless normalized time variable $\tau = t/\tau_J$ with $\tau_J = 2eI_cR/\hbar$, one can write

$$\beta_C \frac{d^2\varphi}{d\tau^2} + \frac{d\varphi}{d\tau} + \sin\varphi - \frac{I}{I_c} = 0 \quad , \tag{2.12}$$

where $\beta_C = 2eI_cR^2C/\hbar$ is the so-called Stewart-McCumber parameter. The obtained relation is formally equivalent to the equation of motion of a fictitious phase particle with mass $m = (\hbar/2e)^2 C$ and damping $\eta = (\hbar/2e)^2/R$ moving in an effective "tilted washboard potential" $E_{pot}(\varphi) = E_{J0}(-\cos\varphi - \varphi I/I_c)$, and with its coordinate given by φ.

Figure 2.7b visualizes the situation of a phase particle in $E_{pot}(\varphi)$. At zero temperature and $I < I_c$, the phase particle is trapped in a local minimum (zero-voltage state) and oscillates with the plasma frequency $\omega_p = \sqrt{2eI_c/\hbar C}$. Upon a biasing current the washboard potential is tilted. At the point when $I \geq I_c$, the phase particle is no longer trapped and can move down the potential (finite voltage state). In this picture,

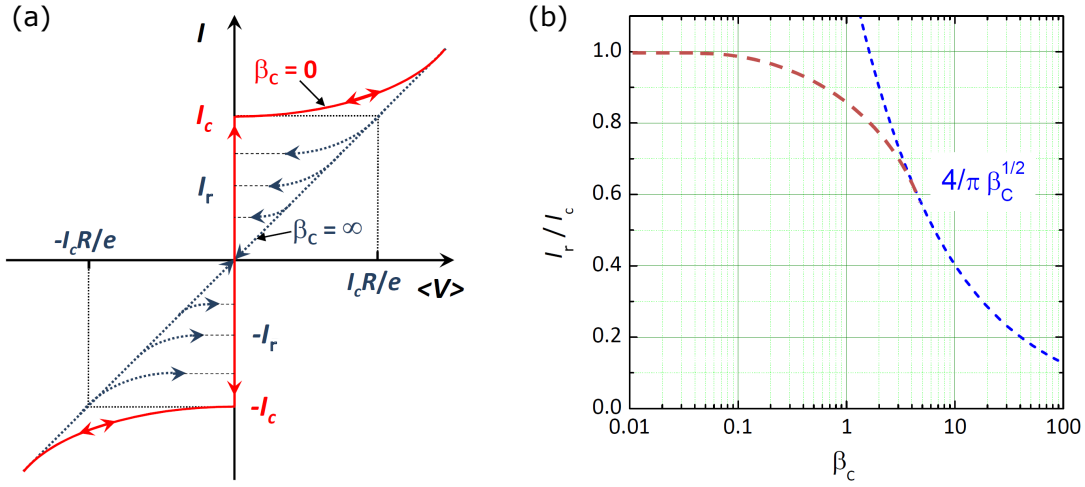

Figure 2.8: Hysteresis effects in underdamped and overdamped Josephson junctions. (a) Current-voltage curves for different values of the Stewart-McCumber parameter β_C. The red curve ($\beta_C = 0$) is the overdamped limit, while for finite β_C hysteresis is observed with retrapping current I_r smaller than I_c. (b) Ratio of I_r/I_c as a function of β_C. Taken from [GM05], with modified axes labeling.

the "speed" of the particle's motion (*i. e.* the phase evolving with time $d\varphi/dt$) is proportional to the voltage drop across the junction according to the second Josephson equation (Eq. 2.11). Experimentally though, *i. e.* at finite temperature and/or in the presence of thermal fluctuations due to noise the phase particle can already escape from the local potential minimum at a switching current $I_{sw} < I_c$.

The retrapping of a running phase particle in the tilted washboard potential depending on its inertia and the damping describes the hysteretic behavior of a junction. In an underdamped JJ ($\beta_C \gg 1$) the mass of the phase particle ($\propto C$) is large and/or the damping ($\propto 1/R$) is small, such that the particle gets only stuck in a potential minimum at a retrapping current $I_r < I_c$, causing a hysteresis in the current-voltage characteristics. On the other hand, in overdamped JJs ($\beta_C \ll 1$) the energy of the phase particle is quickly dissipated due to its small mass and/or large damping. In this case, the phase particle is successively retrapped in the local potential minimum when the current is lowered below I_c and the current-voltage curve displays no hysteresis. The hysteretic characteristics of underdamped and overdamped JJs are exemplified in Fig. 2.8.

Ambegaokar-Halperin theory for overdamped junctions

As mentioned above, the junction dynamics is also influenced by thermal fluctuations, where thermally activated escapes of the phase particle from a potential minimum cause a premature switching. Here we only discuss the consequences for an overdamped junction which will be of relevance for the presented analysis (for respective

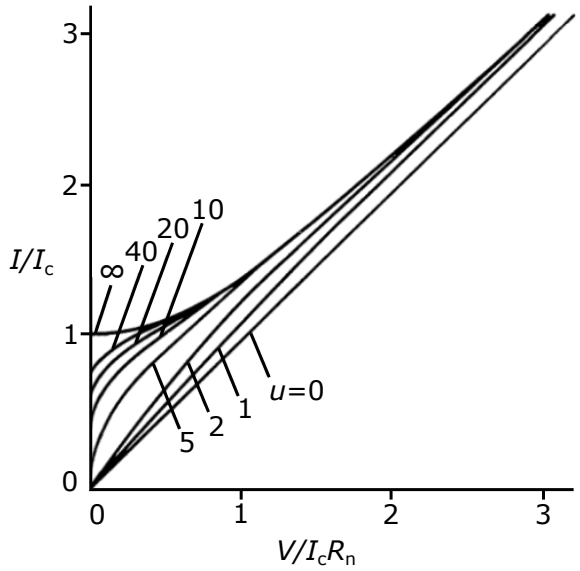

Figure 2.9: Rounded switching in the Ambegaokar-Halperin model. Current-voltage curves with normalized voltage V/I_cR_n and current I/I_c for different values of the normalized activation energy u. Taken from [Tin04], with mirrored axes and new labeling.

details on the thermally activated dynamics of underdamped junctions the reader is referred to [Tin04]). Ambegaokar and Halperin found that the IV curve of an overdamped junction is strongly modified in the presence of an additional thermal noise current in a sense that a finite resistance is always measured [AH69]. Their result is shown in Fig. 2.9. One can see that even below I_c the current remains dissipative depending on the normalized activation energy $u = \hbar I_c/ek_BT$. The finite resistance is due to phase-slip processes in which the phase particle rather diffuses over the barriers. For $I \to I_c$, this activated resistance shows a nonlinear behavior, but trends for $I \to 0$ into a nonzero resistance limit

$$R_0 = R_n \left[I_0(u/2)\right]^{-2} \propto R_n\, ue^{-u}\,. \tag{2.13}$$

Here, R_n is the normal state resistance of the junction and I_0 is the modified Bessel function. The given exponential relation is valid in the limit $u \gg 1$. [Tin04]

2.3.3 Josephson junctions based on conductive weak links

It should be noted that the Josephson effect was originally derived for and experimentally observed in a SIS Josephson junction based on an insulating tunnel barrier between the superconducting contacts [Jos62; AR63]. In more general though, a Josephson junction can be formed by any type of weak link instead of the tunnel barrier [Lik79]. Using a conductive system as the weak link, the Josephson coupling can be mediated over a much larger distance rather than only the few nanometers

in a SIS tunnel junction. The strength of the coupling mostly depends on the contact transparency, disorder in the weak link and temperature [Lik79]. Also it should be noted that the current-phase relation in a conductive weak link Josephson junction, e. g. superconductor–normal metal–superconductor (SNS), may differ from the sinusoidal relation in the case of the tunnel junction (cf. Eq. 2.10).

SNS junctions can be classified in terms of different characteristic length scales by comparison of the junction length L, the superconducting coherence length ξ_0 and the mean free path l_{mfp}, distinguishing between diffusive ($L > l_{\mathrm{mfp}}$) or ballistic ($L < l_{\mathrm{mfp}}$) and short ($L < \xi_0$) or long ($L > \xi_0$) junctions, respectively. The superconducting coherence length is either given by $\xi_0 = \hbar v_{\mathrm{F}}/\Delta_0$ in the ballistic limit or $\xi_0 = \sqrt{\hbar D/\Delta_0}$ in the diffusive limit, where Δ_0 is the superconducting energy gap and $D = v_{\mathrm{F}} l_{\mathrm{mfp}}/2$ is the diffusion constant. Equivalently, the junction can be classified as well in terms of the smallest energy scale by comparing Δ_0 with the relevant Thouless energy $E_{\mathrm{Th}} = \hbar v_{\mathrm{F}}/L$ (ballistic) or $E_{\mathrm{Th}} = \hbar D/L^2$ (diffusive), denoting short ($\Delta_0 < E_{\mathrm{Th}}$) and long ($\Delta_0 > E_{\mathrm{Th}}$) junctions. [Tin04]

2.3.4 Andreev reflection and Andreev bound states

In a Josephson junction formed by a conductive weak link, let's say SNS, the mediated supercurrent across the normal part of the junction can be viewed in terms of the transport of quasiparticles rather than by the tunneling of Cooper pairs through the tunnel barrier of a SIS Josephson junction. Within this quasiclassical picture the Josephson coupling is due to the Andreev reflection [And64; Kla04] taking place at the normal metal–superconductor (NS) interface, which describes the conversion of an electron into a hole excitation due to the pair potential of the superconducting contact (*i. e.* charge carriers with excitation smaller than the superconducting energy gap Δ_0 can only enter pairwise into the superconducting contact). A schematic of this process is shown in Fig. 2.10. When an electron in the normal metal at energy $E_{\mathrm{F}} + \epsilon$ with excitation energy $\epsilon < \Delta_0$ is incident on the interface to the superconductor, it is back reflected in an elastic process as a hole excitation at energy $E_{\mathrm{F}} - \epsilon$, while a charge of $2e$ is absorbed as a Cooper pair by the superconductor. The hole excitation carrying opposite velocity and spin is thereby retro-reflected and retraces the path of the incoming electron. Since this process is time-reversal symmetric, the hole excitation can be transformed back into its original electron state by another Andreev reflection at the opposite NS interface accompanied with the annihilation of a Cooper pair. In a ballistic junction, the back and forth reflection of the electron and hole quasiparticles forms a phase-sensitive Andreev bound level carrying the supercurrent.

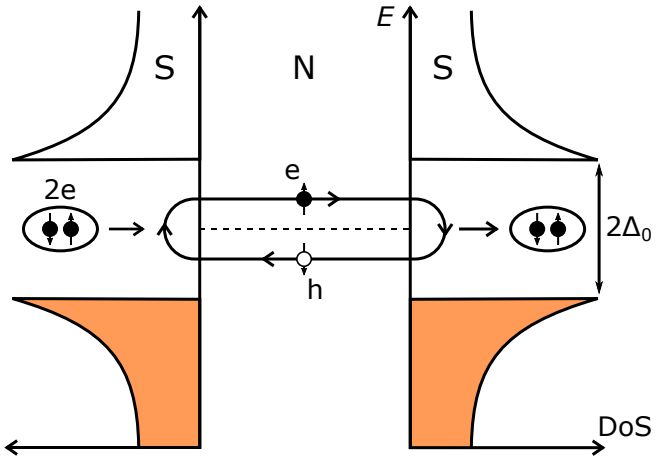

Figure 2.10: Andreev bound state in a SNS Josephson junction. Illustrated principle of a formed Andreev bound state based on the conversion of an electron (at energy $E_F + \epsilon$) into a hole excitation (at energy $E_F - \epsilon$) and vice versa due to Andreev reflections at the two NS interfaces. The superconducting contacts are characterized by the energy gap Δ_0 where no electronic states in the density of states (DoS) exist and charge carriers from the normal region can only enter as a Cooper pair into the superconductor.

Specular Andreev reflection in graphene

Unlike in other materials, there is a special possibility of specular Andreev reflection in graphene [Bee06; Lud07; Efe+16]. Although, this aspect is not studied in this work, we here provide a short description for completeness. For a Fermi energy $E_F > \Delta_0$, quasiparticles are retro-reflected via an intraband Andreev reflection, *i. e.* both electron and hole quasiparticles are from the conduction band but in opposite valleys K^+ and K^-. Note that the valley is switched in order to have the Cooper pair having zero total momentum. However, approaching the charge neutrality point where conduction and valence band touch, the Fermi energy in graphene is eventually $E_F \lesssim \Delta_0$. In that case, and for excitation energy $\epsilon > E_F$ of the incident electron (but still smaller than Δ_0), the Andreev reflection is an interband process with a reflected hole quasiparticle in the valence band. Since a hole in the valence band has its velocity in the same direction as the wave vector, this reflection is specular. It should be noted that to observe specular Andreev reflection ultra-clean devices are required, where the Fermi energy broadening due to disorder is well below the superconducting gap. For a colloquium-style description of Andreev reflection (an its analogy to Klein tunneling) in graphene see [Bee08].

2.3.5 Multiple Andreev reflection

As discussed above, supercurrent is mediated in the zero voltage state of the junction by Andreev reflected quasiparticles. At finite voltage, a quasiparticle traversing

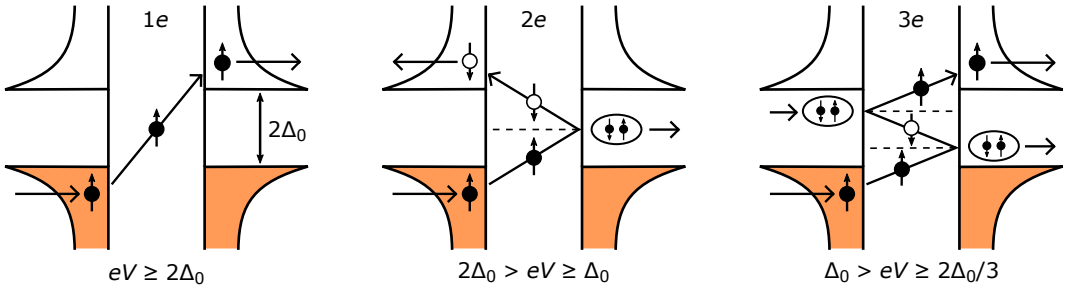

Figure 2.11: Multiple Andreev reflections in a SNS Josephson junction. Illustrated principle of subgap transport at finite voltage V across the weak link. An injected quasiparticle can escape the weak link cavity when its accumulated energy $eV \geq 2\Delta_0$ due to multiple Andreev reflections.

the weak link gains the energy eV. Since electron and hole quasiparticles carry opposite charge, the energy is accumulated in the subgap regime $V < 2\Delta_0/e$ during continuous Andreev reflection processes and the quasiparticle can eventually escape into the quasiparticle continuum of the superconducting contacts when its energy is larger than the superconducting energy gap. This multiparticle transport mechanism, termed multiple Andreev reflection (MAR) [KBT82; Oct+83], is illustrated in Fig. 2.11. Note that at a voltage $V \geq 2\Delta_0/e$, quasiparticles can be directly transmitted into the superconducting reservoirs. The transferred charge q in this process is determined by the number N of involved Andreev reflections $q = (N+1)e$. Therefore, MARs give rise to a subharmonic gap structure featuring non-linear current-voltage characteristics where steps in the current appear at $V = 2\Delta_0/je$ (with j an integer number). Such resonances are clearly resolved as peaks in the differential conductance $\mathrm{d}I/\mathrm{d}V$ (or dip in the differential resistance $\mathrm{d}V/\mathrm{d}I$, respectively) at the respective voltage. Since with each reflection there is a finite probability of being normal reflected resulting in phase-insensitive electronic levels, the signal of higher order processes is typically observed weaker. The subharmonic gap structure in graphene was discussed in [CY06].

2.3.6 Proximity-coupling in graphene weak links

Early on, graphene was proposed as a new class of weak link material to be used in a Josephson junction [TB06], combining the unique relativistic physics in graphene with the Josephson effect. For ballistic graphene weak links, an analytical expression for the current-phase relation at zero temperature can be found in the wide and short junction limit ($L \ll W, \xi_0$) and close to the Dirac point as [TB06]

$$I(\varphi) = \frac{e\Delta_0}{\hbar}\frac{2W}{\pi L}\cos(\varphi/2)\tanh^{-1}[\sin(\varphi/2)] \tag{2.14}$$

with maximum Josephson current

$$I_\mathrm{c} \equiv \max\{I(\varphi)\} = 1.33\frac{e\Delta_0}{\hbar}\frac{W}{\pi L}, \qquad I_\mathrm{c}R_\mathrm{n} = 2.08\Delta_0/e\,. \tag{2.15}$$

Interestingly, although calculated for a graphene Josephson junction in the ballistic regime, the obtained $1/L$ dependence is instead formally identical to the behavior of Josephson junctions made from disordered normal metal weak links. Such a pseudo-diffusive behavior at the Dirac point is manifestation of the relativistic nature of ballistic Dirac fermions in graphene. Note that the given current-phase relation in Eq. 2.14 features an anharmonic forward-skewing with respect to the sinusoidal current-phase relation in tunnel junctions.

For the same junction limit but away from the Dirac point, *i. e.* in the case of large Fermi level, there is no such simple analytic expression for $I(\varphi)$. Yet, the critical current and the $I_c R_n$ product are found as

$$I_c = 1.22 \frac{e\Delta_0}{\hbar} \frac{E_F W}{\pi \hbar v}, \qquad I_c R_n = 2.44 \Delta_0 / e, \tag{2.16}$$

where the critical current is independent of L, and scales linearly with the Fermi level. It should be noted that these values are reduced compared to the ideal ballistic value in ordinary SNS Josephson junctions [KO77] $I_c = 2Ne\Delta_0/\hbar$ (with $N = E_F W/\pi\hbar v$ the number of degenerate modes, *i. e.* per spin and valley) and $I_c R_n = \pi\Delta_0/e$, which is attributed to the Fermi wavelength mismatch at the graphene–superconductor interfaces [TB06].

Further theoretical works included different junction width and/or length limits, as well as finite temperatures [BD08; BL10; HYK10; MCP12; RKC16]. In long ballistic graphene weak links ($L \gg \xi_0$), the Josephson coupling strength $I_c R_n$ scales with $1/L$ which is presumed to hold as well at finite temperature for $L \sim \xi_0$ [RKC16]. Concerning BLG Josephson junctions on the other hand, there exists less theoretical work. Yet, with regard to the strength of the Josephson coupling, the maximum supercurrent in BLG is expected to be equivalent to single layer graphene junctions at large charge carrier density [MCP12], but being modified in gapped devices.

First experimental results were reported in graphene on Si/SiO_2 devices [Hee+07] demonstrating a gate-tunable ambipolar supercurrent, although being restricted to the diffusive regime. In subsequent experiments based on suspended graphene devices, supercurrent in samples approaching or reaching the ballistic transport regime were reported [Du+08; MND13]. Thanks to sample fabrication improvements [Wan+13], where the graphene sheet is encapsulated between hBN and connected from the edge of the mesa (see discussion in section 2.1 and sample fabrication in chapter 3), ballistic superconducting transport is now readily achieved in substrate supported devices with attainable large supercurrent amplitudes over micron distance scales [Cal+15; Ben+16; Bor+16; RKC16; Zhu+18]. A review including different theories and experiments on Josephson coupling in graphene-based weak links can be found in [LL18].

Based on the high-quality and tunability of the encapsulated devices, graphene weak links have been employed to study the supercurrent in the quantum Hall regime [Ame+16] or have been successfully integrated into superconducting microwave circuits [Kro+18; Sch+18] as the basis for new graphene-based transmon qubits. However, despite edge-connected encapsulated graphene has been established as a promising and gate-tunable weak link material, a controllable spatial shaping of the supercurrent has not been demonstrated. Only e. g. a self-induced confinement of the supercurrent at the edges of graphene-based junctions has been reported at low charge carrier density because of edge states [All+16], but which does not allow to define at will the supercurrent distribution.

2.3.7 Conclusion

In this section, the necessary basics of Josephson junctions in general have been introduced. Other relevant but more specific aspects, such as the monitoring of the supercurrent via superconducting magneto-interferometry measurements or the embedding of a QPC into the weak link, are directly addressed in chapters 4 and 6, respectively. At the end of this section, a brief overview on the Josephson coupling in graphene weak links has been discussed. The opportunity to measure the ballistic supercurrent in micron-sized graphene weak links gives enough area to design gate-defined nanostructures. In this work, we take advantage of these promising prerequisites by coupling our electrostatically engineered confinement structures in BLG to superconducting contacts. Therefore, we can probe the confinement via superconducting interferometric measurements (chapter 4) and study Josephson coupling through 1D subbands in a SQPC via individual Andreev bound levels (chapter 6). Further investigations of the subgap conductance in the finite voltage state (*i. e.* looking at the phase-sensitive MAR spectrum) give additional information on the transport properties of the SQPC upon the (de-)population of subbands.

3 Methods

Here, the experimental methods used within this work are presented. The chapter is thereby organized in two parts: In the first part, the procedure of sample fabrication is introduced (3.1), whereas a description of the experimental setup and the measurement techniques follows in the second part (3.2).

3.1 Sample fabrication

As pointed out in chapter 2, high-quality electronic devices can be realized on the basis of edge-connected vdW heterostructures. In respect thereof, we prepare our samples following state-of-the-art dry and contamination-free assembly techniques originally developed in [Wan+13] with minor adoptions.[1] The fabrication procedure (*i. e.* exfoliation, vdW assembly, electrical contact, final device patterning, and adding TG structures) is outlined step by step in the following.

3.1.1 Exfoliation of 2D crystals

As starting point, flakes of graphene and hBN are prepared by micromechanical cleavage from natural bulk graphite (NGS Naturgraphit GmbH) and commercial hBN powder[2] (Momentive, grade PT110), respectively, which has become popular as the so-called "Scotch tape" technique since the early stages of isolating 2D materials [Nov+05b; GN07] but remains up to the present day the method of choice for obtaining highest quality 2D crystallites. In this exfoliation process, 2D layers are cleaved out of the bulk material with a piece of adhesive tape (Nitto Denko, ELP BT-150E-CM; or Scotch Magic tape), taking advantage of the weak interlayer vdW forces.

[1] Note that various amendments of the initially introduced assembly routine have been meanwhile reported in literature, e. g. in [Zom+14] or [Piz+16]. A review about transfer methods of 2D materials in general (including wet transfer techniques etc.) can be found in [Fri+18].

[2] We note, that the usage of commercially available hBN powder instead of the commonly in the literature employed hBN single-crystals provided by T. Taniguchi and K. Watanabe [TW07] showed no apparent negative effect on the sample quality.

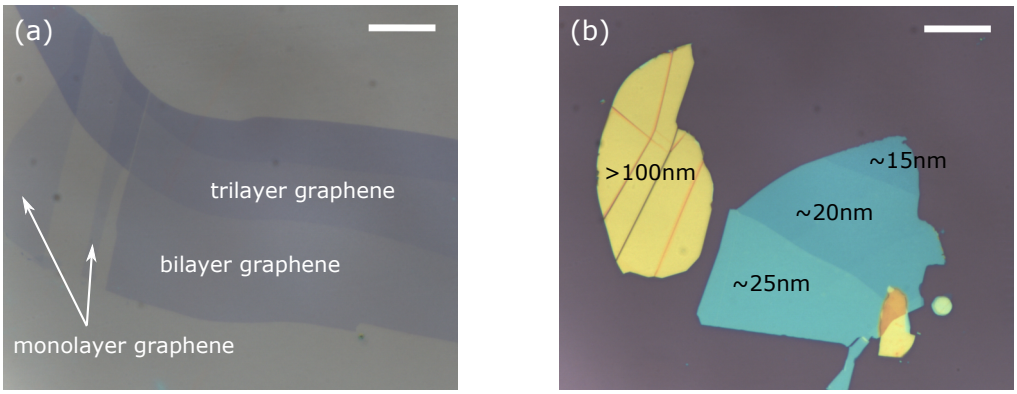

Figure 3.1: Exfoliated 2D crystallites of graphite and hBN. (a, b) Flakes of graphene and hBN. The inset labels denote the number of layers or flake thickness, respectively. Scale bar in both images is 20 µm.

The thickness of the leftover crystallites on the tape is further thinned down due to repetitive exfoliation with other pieces of tape. After several cycles, the remaining graphite flakes start to become more and more transparent (in case of hBN additional thinning steps might not be as important for obtaining a good yield of flakes with tenth of nanometers thickness). In a final exfoliation step, the tape with the thinned crystallites is then pressed down onto the surface of a priorly cleaned Si/SiO_2 chip and after peeling off the tape, 2D layers are partially cleaved and eventually transferred on the substrate. The obtained exfoliated flakes are randomly spread over the surface of the substrate, and vary in size, thickness and shape [Nov+05b].

At this point, suitable flakes have to be found amongst all the other crystallites. This is done by carefully scanning the surface of the substrate under an optical microscope (here done by eye; more ideally this is even possible in a fully automatized scanning process). Indeed, most simple optical inspection allows to find nearly transparent monoatomic layers of graphite (*i. e.* $\approx$ 98 % transparency in the visible light spectrum [Nai+08]) owing to a feeble but visible contrast with respect to an empty wafer due to interference effects (strongly depending on the underlying substrate) [Bla+07; Rod+07]. In this way, flakes with different number of layers can be readily distinguished, making it possible to optically determine and select single-layers, bilayers or multi-layers of graphene (see the exemplary optical images shown in Fig. 3.1a). The number of layers of a potential candidate flake can be finally validated using Raman spectroscopy [Fer+06; FB13], where the obtained Raman spectrum might as well serve as indicator for the flake's quality and cleanliness [Fer07] (although not necessarily meaningful, as even graphene flakes with contaminants and/or local defects may yield large enough clean areas that can be used for designing devices later on). In the case of hBN, appropriately thick flakes with seemingly clean and flat surfaces are selected based on their color which provides a fairly good initial estimate

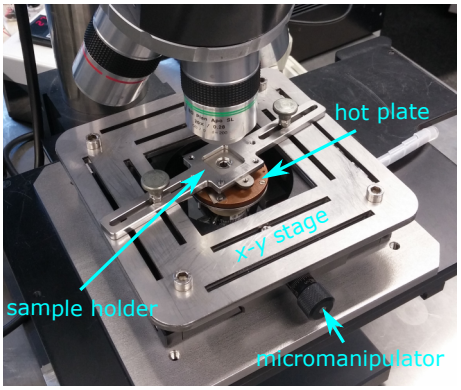

Figure 3.2: Transfer setup. Photograph of the long distance working microscope (the description is given in the main text).

for the thickness [Gol+13], as shown in Fig. 3.1b. For a conclusive final selection, the thickness and surface morphology of the preselected specimens can be inspected via atomic force microscopy (AFM).

3.1.2 Van der Waals assembly

With all flakes prepared, the graphene is then encapsulated between a top and a bottom hBN flake in the fashion of a dry vdW assembly technique [Wan+13] using our home-made transfer setup (see Fig. 3.2 for a photograph), consisting of an optical microscope with long distance working objectives, a transfer stage movable in x- and y-direction (*i. e.* in the horizontal plane) by micromanipulators and a rotatable hot plate that can be adjusted nanometer-wise in the z-direction (*i. e.* up and down). By taking advantage of the strong vdW adhesion forces between the surfaces of 2D crystallites, the individual layers can be piled up into a combined heterostructure without contaminating the active interfaces at any transfer step (*i. e.* only the outer surface of the top hBN flake gets into contact with polymers). The single steps of the employed stacking routine are illustrated in Fig. 3.3 and presented in the following:

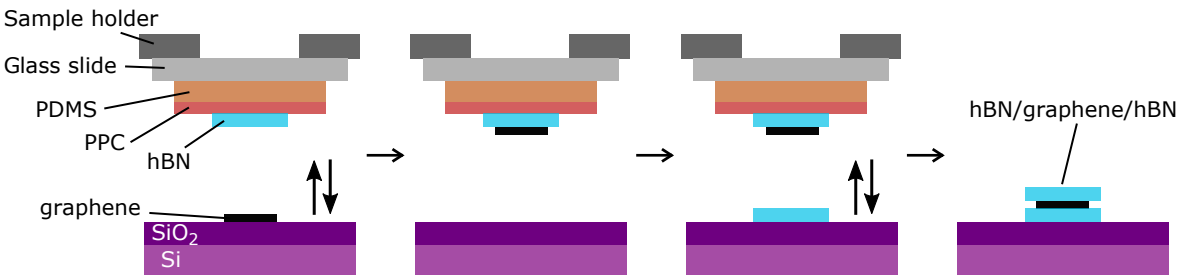

Figure 3.3: Dry, contamination-free van der Waals assembly technique. A series of schematics showing from left to right the stacking routine for the assembly of vdW heterostructures as described in the main text. The 2D crystals are sequentially picked up until the final stack is completed, while non of the active interfaces of the heterostructure get into contact with polymers.

Step 1 In a first step, the hBN flake that is chosen as top dielectric layer has to be picked up. For that, a thin film of poly-propylene carbonate (PPC; 7 wt% dissolved in ethyl acetate), *i. e.* a transparent polymer, is spin-coated onto the wafer with the exfoliated flake. Subsequent baking is done in an oven for 15 min at 80 °C (or alternatively on a hot plate) for evaporating the solvent. After gently lifting the edges of the baked PPC layer (e. g. with the help of a razor blade or scalpel), the film can be picked up with a polydimethylsiloxane (PDMS) stamp which itself sits on a standard microscope glass slide glued to a sample holder. Together with the PPC sticking to the PDMS stamp, most of the flakes are detached as well from the substrate owing to the stronger adhesion forces to the PPC polymer film rather than to the "rough" surface of the Si/SiO_2 wafer.[3]

Step 2 With the hBN flake now sitting on the stamp, the graphene can be picked up in a next step free of contamination by the polymer. To do so, the wafer with the target graphene flake is fixed on the hot plate (either by fastening with a small clamp or by gluing using polymethyl methacrylate (PMMA)) while the sample holder with the stamp is mounted to a metal frame and screwed upside down to the transfer stage. After aligning the hBN flake with respect to the graphene, the hot plate is slowly raised towards the stamp. During the elevation process the scenery is continuously monitored through the microscope and the flakes are re-aligned if necessary. Once brought into contact, the hot plate is heated to 45 °C–60 °C[4] and kept at this temperature for a few minutes for enhancing the interlayer attraction before being cooled down again.

Step 3 At this stage, there are two options to proceed. Either the hot plate is lowered at elevated temperatures while the PPC film is softened allowing to detach the PDMS stamp from the sample or is only retracted after the PPC has again cured to a hardened film at temperatures below 30 °C. In the former scenario, the stacked flakes are left behind on the substrate covered with the PPC film (which is either dissolved in Acetone or could be directly re-used for further transfer steps starting with step one), whereas in the latter case the graphene ideally remains attached to the hBN flake due to the strong adhesion force between the two atomically flat interfacial surfaces and gets thereby picked up from the rougher substrate surface as the hot plate is lowered.

[3] Alternatively, top hBN flakes may be readily exfoliated directly onto a PPC film [Wan+13].

[4] Higher temperatures above 100 °C might help to further improve the final interlayer cleanliness, as proposed in [Piz+16].

Step 4 Then, the target substrate is replaced by the one with the designated bottom hBN flake and the pick-up procedure is repeated. In fact, further iteration steps allow to sequentially pile up quasi unlimited numbers of different 2D crystallites into a vdW heterostructure as long as the stacked structure remains stable and not minding cumulative "bubble" formation with each added interface due to trapped interfacial adsorbates between consecutive layers. The issue of contaminants will be addressed at a later point.

Figure 3.4 presents optical images of the stacking procedure, starting from the first hBN until the encapsulated graphene stack. In this work, a final transfer step is done in which the completed heterostructure is placed onto a pre-patterned gate structure (Cr/Au 5 nm/50 nm) on a sapphire wafer and covered by a dielectric layer of 20 nm Al_2O_3 deposited by ALD (see Appendix A.1). The stack is eventually released on its target position by retracting the hot plate while the PPC is kept softened at elevated temperature (60 °C). At last, the residual PPC film is dissolved in acetone.

We make use of the pre-patterned gate structure mainly for three reasons: First, the Al_2O_3 layer deposited by ALD is expected to provide a better quality dielectric with less charge traps compared to the thermally grown amorphous oxide on Si.[5] Second, the sapphire substrate prevents any leakage which might appear in Si/SiO_2 wafers employed as the BG itself (for instance due to weak spots, *i. e.* cracks in the oxide, possibly appearing due to the wedge bonding of the contact metal pads or other reasons). Third, using an insulating substrate is advisable and beneficial when it comes to measurements with high-frequency signals in order to avoid losses that would otherwise arise due to a parasitic capacitance between the conductive substrate (e. g. Si/SiO_2) and the metallic contacts [Ben14]. Here, the requirement for transmitting high-frequency signals is associated with potential follow up experiments designed on the basis of the results of this thesis, *i. e.* measuring the suppression of shot noise in a quantized conductor [Rez+95]. Finally, sapphire is a good thermal conductor as another positive aspect for thermalization of the sample in the low-temperature measurements.

[5] In the past few years also graphite gates have been established as superior gating structure in comparison to the common Si/SiO_2 back gate. Although infrequently reported as employed gate material throughout the literature priorly, the use of graphite gates just recently has become popular in the field for realizing high-quality devices [Zib+17]. The exfoliated graphitic layer not only provides naturally an atomically flat gate surface but it also ultimately screens any charge inhomogeneities from the substrate surface and thereby, extremely low charge carrier disorder in the order of $\sim 1 \times 10^9\,\mathrm{cm}^{-2}$ could be achieved [Yan+19]. Finally we note, that graphite gates have been successfully employed in most recent complementary experiments on gate-defined BLG nanostructures performed in other groups [Ove+18a; Eic+18a; Ban+18].

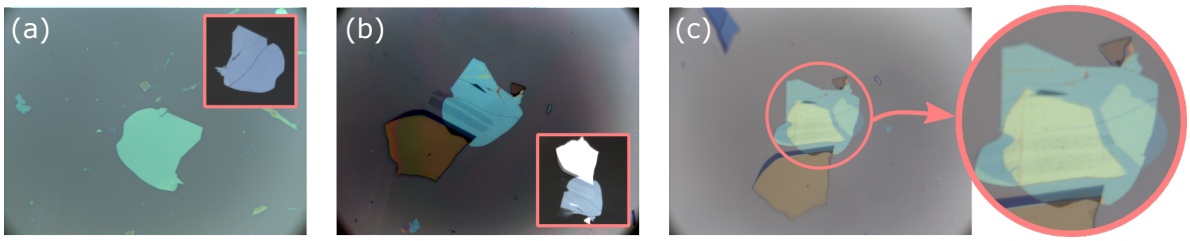

Figure 3.4: Graphene/hexagonal boron nitride van der Waals heterostructure. Optical images of the assembly routine: (a) Picking up the top hBN from the substrate. Inset: hBN on the stamp. (b) The top hBN is placed onto the target graphene flake (here two stripes next to a thicker graphite flake). Inset: hBN/graphene stack on the stamp. (c) hBN/graphene stack transferred onto the bottom hBN flake. A zoom-in on the completed hBN/graphene/hBN heterostructure is shown in the magnifier.

Revised assembly routine with newly designed PDMS stamps

Initially, this transfer and pick-up procedure is done with a rather thick PDMS stamp (*i. e.* $\sim 2\,\mathrm{mm}$ home grown layer cut out of a Petri dish) placed down on a microscope glass slide. To avoid the PDMS stamp to detach during the stamping, a sufficiently large interface to the glass slide is helpful. Though, due to the larger stamp area significant shear forces might be introduced at smallest tilt angles when the stamp is pressed on the target substrate, which will cause a drifting of the aligned flakes after contact is made. Furthermore, the thicker the PDMS (or any other layer, *i. e.* PPC and glass slide, inserted between the microscope objective and the monitored flakes) the worse the contrast and thus the precision of the alignment.

A revised assembly routine is introduced using newly designed PDMS stamps which are shape casted in a predefined mask (albeit all presented results in this thesis are still based on devices fabricated prior to the renewed routine), representing likely an improvement to before as the assembly could now be mastered faster by fresh students. It consists of a much thinner PDMS layer with a small nub in its center but with large interface area to the extra thin (but at the same time more fragile) glass slide. Therefore, a significantly enhanced visibility is gained and the stamping itself can now be done with better accuracy, while one does not need to worry about lateral shifting during transfer or a detaching of the stamp from the glass slide. Finally, it is suggested that the stamping process for a deterministic pick-up and placement of 2D crystallites [Fri+18] may eventually be further improved using a semi-spherical nub, eliminating last downsides of the new PDMS stamp design (*i. e.* slightly roughened edges of the cylindrically shaped nub).

Bubble formation and "self-cleansing" mechanism

With the graphene sheet being eventually "sandwiched" between the top and bottom hBN multilayers, it is thereby protected against outside influences such as e. g. con-

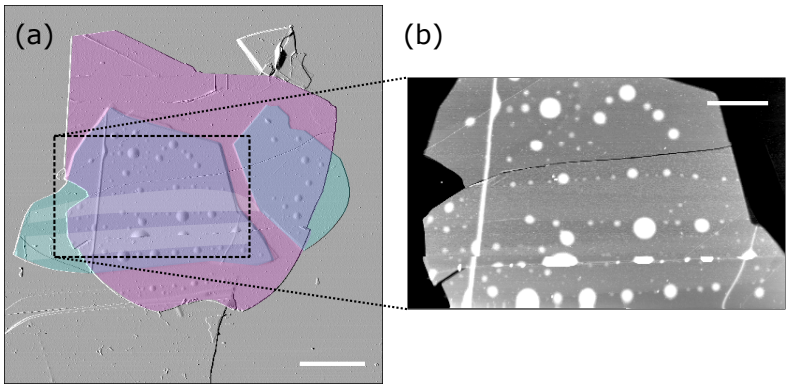

Figure 3.5: Bubble formation and self-cleansing mechanism. (a) AFM images of the stack presented in Fig. 3.4 after heating at 300 °C. The flakes are shown in false-colors: mint (bottom hBN), orchid (top hBN) and whitish (graphene), respectively. (b) Zoom-in on the black dashed box. The bubbles (white) are accumulated along the edges of the graphene strip, but the interfaces themselves appear perfectly clean. In one of the strips bubbles are squeezed into the crack of the top hBN. Since these pockets do not evaporate, they must be from the lower interface between bottom hBN and graphene.

tamination due to adsorbate molecules from the environment or polymer residues caused by lithography steps for device patterning. Yet, since the complete sample fabrication itself (*i. e.* exfoliation of the crystallites and the stacking process) is performed under ambient conditions, it is unavoidable that contaminants (mainly hydrocarbons, water etc.) immediately accumulate on the surfaces of the exfoliated flakes and get eventually trapped at each interface of two 2D crystals during the stacking process. Nonetheless, sufficiently large clean areas ($\sim$ 10 µm in size) are obtained in a compiled heterostructure owing to a so-called "self-cleansing" mechanism [Kre+14], in which trapped contaminants are squeezed into "bubbles" and thereby leaving behind atomically sharp interfaces free of contamination [Hai+12] (a study on the physics of bubble formation in vdW heterostructures has been reported in [Khe+16]).

The diffusion of adsorbate molecules segregating into the larger pockets can be enhanced due to an annealing step (here done in an oven at 300 °C for 3 h). It shows that the self-cleansing mechanism is most effective in rather narrow graphene strips ($\sim$ 5 µm in width) where the contaminants can fully diffuse outside the flake area and coalesce only at the edges of the graphene/hBN interface (an example is shown in Fig. 3.5). But even defects in the heterostructure or cracks in the top hBN layer introduced during the stacking could be helpful for collecting efficiently the contaminants into droplets of larger size or actually completely releasing adsorbate molecules through the fissure, respectively. Furthermore, a slowly made contact between the flakes during the pick-up process is proposed to yield an improved self-cleansing effect [Piz+16].

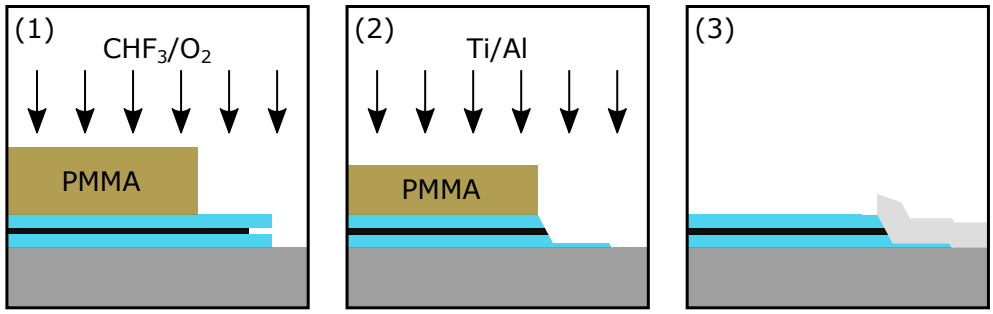

Figure 3.6: Edge connection of encapsulated devices. Series of schematics illustrating the fabrication of edge contacts. (1) Reactive-ion etching using CHF_3/O_2 and with a patterned PMMA etch mask defined by electron-beam lithography. (2) Metal deposition (Ti/Al) making contact along the exposed graphene edge using the same patterned and etched PMMA mask. (3) Metal lift-off with remaining contact leads connected to the encapsulated graphene layer from the edge of the mesa.

Finally, devices can be designed and patterned within the clean and flat regions of the assembled graphene/hBN heterostructure which are identified via an AFM scan (note that the layout and design of devices is thereby sample specific and unique, thus requiring in each case its own planning of the patterning). These last steps of sample fabrication are discussed in the following.

3.1.3 Edge contacts

Making good electrical contact to a material is another important aspect for designing high-quality electronic devices, especially in the case of proximity-coupling in a weak link Josephson junction. Though, one might wonder how to connect the active transport layer once fully encapsulated in the final heterostructure. In fact, what might seem like an impediment at first glance, turns out to be one of the biggest advantages. By etching trenches into the stack using reactive ion etching (see Appendix A.2) the graphene edge is exposed, along which a metal contact can be made. Indeed, the edge contact geometry has proven to yield highly transparent contacts with significantly lowered contact resistance compared to common surface contacts [Wan+13].

In the original procedure for the fabrication of edge contacts [Wan+13], a two-layer resist with a hard etch mask (*i. e.* hydrogen-silsesquioxane; HSQ) is employed for initial patterning of the devices, making an additional subsequent lithography step necessary for the later metalization of the contacts. However, the already exposed graphene edge might get contaminated by resist residues due to the second lithography step. Moreover, the sequentially defined contacts must slightly overlap the edged mesa to make sure that the graphene is connected properly, uncontrollably affecting the electrostatics in the sample. In avoidance of these downsides, we fabricate the

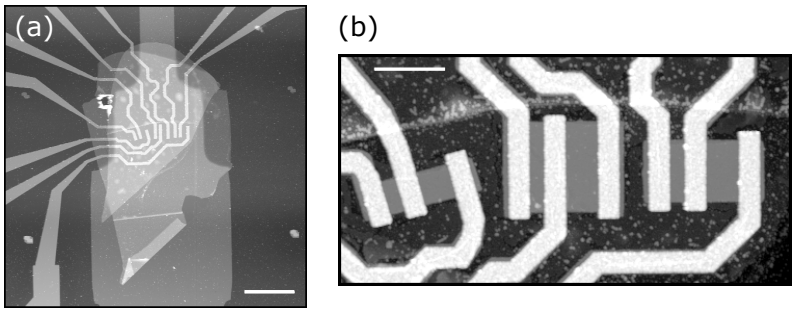

Figure 3.7: Edge contacts and device patterning. (a) AFM image after depositing metal contacts making electrical contact to a graphene/hBN heterostructure placed on a pre-patterned BG structure. (b) Zoom-in on the central part of (a) after the final patterning was done by reactive-ion etching. In total six devices can be seen, connected from the edge of the mesa and shaped into defined junction geometries.

edge contacts in a revised fashion, where a single PMMA resist layer for both etching and subsequent metalization of the contacts is employed. The duration of the etch process is carefully chosen to be long enough in order to etch completely through the top hBN for exposing the graphene layer, but not too deep as the remaining thickness of the bottom hBN limits the maximum applicable voltage on the BG. In the next step, the same already patterned PMMA resist layer is then directly used as lift-off mask for the metal deposition, ensuring clean and self-aligned contacts. The procedure is illustrated in Fig. 3.6.

3.1.4 Final patterning and top gate deposition

The sample fabrication process is finalized by patterning the heterostructure into the desired device geometry and designing local gate structures on top of the sample according to requirements. The final shaping of the devices is done via another cycle of lithography and subsequent etching (note that this step might not be necessary when using a narrow graphene strip where the natural edges of the flake can serve as the device boundaries). An exemplary AFM image of patterned devices is shown in Fig. 3.7. After this etching step, the edges of the graphene layer are again exposed to the environment. Thus, prior to TG deposition an intermediate step is required, *i. e.* adding an insulating layer to prevent the metal gate being electrically connected to the graphene (or if the TG needs to be overlapped with the source and drain contacts; see e. g. the device architecture in chapter 4.3).[6] In this regard, the sample is

[6] Note that if the order is reversed, *i. e.* first TG deposition followed by final shaping of the devices, no insulating layer may be needed but there will be graphene sleeves remaining underneath the TG lead protected from etching.

covered by an Al_2O_3 layer deposited by ALD (as done with the pre-patterned BG). TG structures are then deposited thereafter, which includes another step of lithography followed by metalization. More complex device geometries might consist of several TG electrodes with one superimposed on the other. In this case, the different levels of TGs are again isolated from each other due to an extra layer of Al_2O_3 deposited priorly to the upper TG structure (see e. g. the device architecture in chapter 5.2).

3.2 Measurement setup

Cryostat

The low-temperature electrical measurements are performed in a BlueFors LD250 cryogen-free dilution refrigerator, *i. e.* a "dry" cryostat. The pre-cooling is done with a two-stage pulse tube cooler reaching a temperature below $\lesssim 4\,\mathrm{K}$ (while the warmer stage being at about 50 K). By decoupling mixing chamber stage and still plate from the environment via closed gas-gap heat switches and running the circulation of the ^{3}He/^{4}He mixture (initial condensing during the cooldown process is supported by a compressor), the system is further cooled down. The cooling power is provided by the endothermic dilution of ^{3}He from a concentrated phase ($\sim$ 100 % ^{3}He) into the dilute phase (about 6.4 %/93.6 % ^{3}He/^{4}He for $T \to 0$) in the mixing chamber, while pumping on the still line generates a continuous cycle of ^{3}He. A schematic of the dilution unit operating principle and a photograph of the cryostat are shown in Fig. 3.8a, b. The base temperature reached at the mixing chamber level in the empty cryostat is below 7 mK. When the mixing chamber is equipped with electric lines (and/or high-frequency transmission lines) for the measurement, the temperature is higher (typically about 10 mK–20 mK[7]) due to the installed connections to the room-temperature environment outside the cryostat which act as additional heating loads. It needs thus to be taken great care of thorough thermal anchoring of the cabling at each temperature stage.

Filtering and shielding against outside influences

Another important aspect to be minded for the experiment at low temperature is noise coming from connected instruments at room-temperature (*i. e.* amplifiers etc.), which act as heat sources for the electronic temperature in the sample itself. Therefore, we integrate a combination of low-pass filters into each of the electric lines at the mixing chamber level: three-stage RC filters (consisting of three resistors $R_1 = 330\,\Omega$,

[7] Specific base temperatures of measurements from different cooldowns are given within the particular experimental chapters.

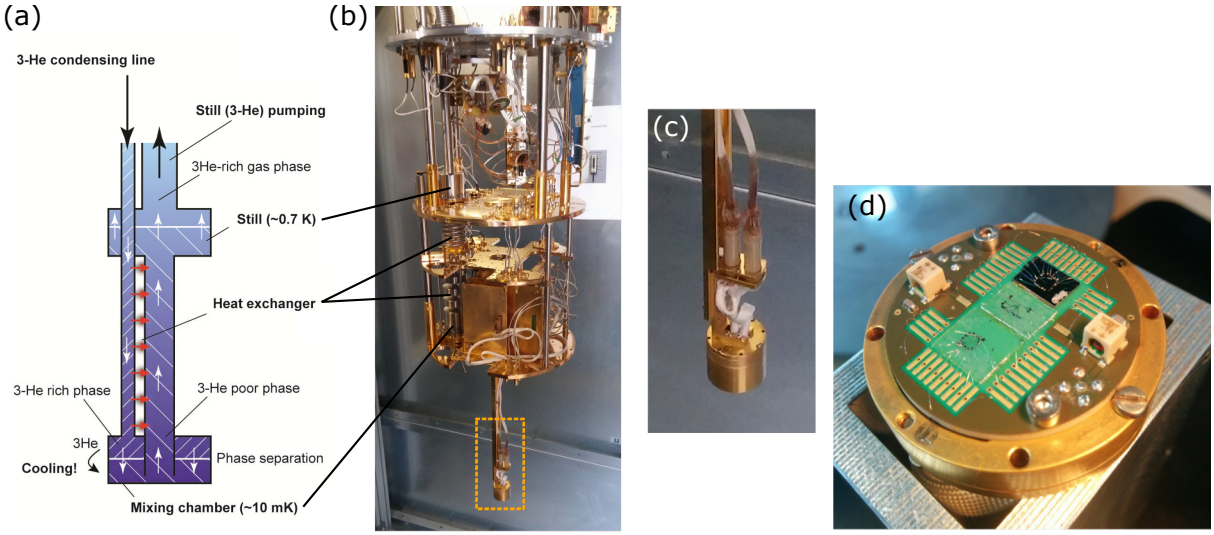

Figure 3.8: Cryogen-free ^{3}He/^{4}He dilution refrigerator with sample holder. (a) Schematic of the principal parts in the dilution refrigerator system (taken from the User manual for BF-LD250, 2011, Version 1.3.1). (b) Photograph of the opened cryostat. (c) Zoom-in on the sample holder mounted at the end of the cold finger (orange dashed box in panel (b)), which will be in the center of the magnet when closed. (d) Photograph of the printed circuit board inside the sample holder, showing three bonded chips.

$R_2 = 220\,\Omega$ and $R_3 = 100\,\Omega$ in turns with a total of four capacitors $C = 100\,\text{nF}$ coupled to ground) with a cut-off frequency of 1 kHz and copper powder filters (2 m conducting track per line on a printed circuit board) with a cut-off frequency of 1 GHz, effectively attenuating noise over a large frequency range.[8,9] In some of the measurements, an additional thermal anchoring is used (*i. e.* cryogenic woven copper loom wiring with a length of $\approx 1\,\text{m}$ immersed into Galinstan).

Further precautions are taken with respect to environmental influences. The complete experimental setup, *i. e.* cryostat together with all electronic equipment, is installed inside a Faraday cage shielding against external radio frequency interferences. Furthermore, twisted pair cabling is utilized for incoming and outgoing lines to the sample, which helps to reduce electromagnetic interference from external sources (as well as crosstalk between neighboring pairs). Finally, the measurement system is fully electrically isolated from the environment and only connected via an optical fiber cable to the measurement control computer.

[8] Details on the performance of the RC filters are discussed in the PhD theses [Bor14; Moh16].

[9] New metal powder filters are designed and fabricated, though not yet used for the measurements in this thesis. The electric line length for the filtering is increased to 5 m using cryogenic woven copper loom encapsulated into a closed oxygen-free and gold-plated copper box with two chambers of stainless steel powder and copper powder, respectively.

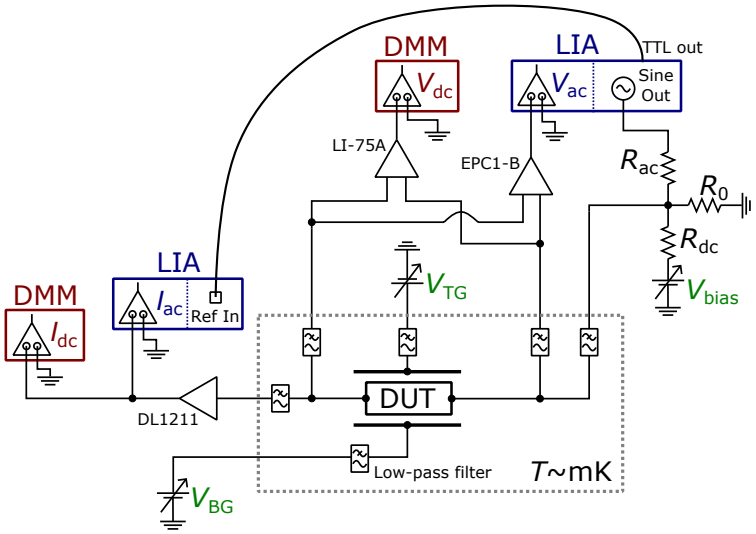

Figure 3.9: Measurement circuitry. The device under test (DUT) at low temperature is connected to the measurement equipment outside the cryostat, *i. e.* dc power sources for source-drain bias and gate voltages (V_{bias}, V_{BG} and V_{TG}), lock-in amplifiers (LIAs) and digital multimeters (DMMs) as described in the main text.

Measurement scheme and instrumentation

For loading the sample into the cryostat, the chip is initially glued onto the printed circuit board of our designed sample holder using thermally conductive varnish (GE 7031) and connected to the metal pads of the printed circuit board (which themselves are soldered to an electrical connector) via ultrasonic wedge bonding (AlSi 1 % bond wires). The sample holder is then mounted to the cold finger of the cryostat which is going to be inside the cylindrical inner bore of the installed magnet. Pictures of the connected sample holder and the bonded chips are shown in Fig. 3.8c, d, respectively. In the measurements, an integrated cryogen-free compensated solenoid superconducting magnet-system is applied (American Magnetics, Inc.; AMI 12 T) generating homogeneous fields in its vertical direction.

The devices are probed in a two terminal single-ended measurement configuration with two lines each at source and drain contacts for measuring voltage and current. Thereby only the contact resistance of the two metal leads to the graphene but no other series resistance (*i. e.* cabling and filters) is included. We use standard low-frequency (10 Hz–15 Hz) lock-in techniques with low ac excitation ($< 10\,\mu$V) for measuring the differential resistance/conductance, with two synchronized lock-in amplifiers (Stanford, SR830) for the detection of both current and voltage (the signal is generated by the internal oscillator of one of the lock-in amplifiers; here the lock-in amplifier for voltage detection). Out-of-equilibrium measurements are performed with applied bias using an ultra-low noise dc-power source (iTest Bilt System, BE2101). The dc voltage is added to the ac signal at a voltage divider (with two input terminal resis-

tors $R_{ac} = 476\,k\Omega$ and $R_{dc} = 1\,k\Omega$, a resistor $R = 10\,\Omega$ to ground and one output terminal). The signal behind the sample is amplified with low noise preamplifiers for current (DL instruments, DL1211) and voltage (dc: LI-75A; ac: Celians EPC1-B), respectively, and the dc component is recorded via digital multimeters (Agilent, 34410A). Finally, the gating is done with applied electrostatic potentials on BG and TGs using further channels of the dc-power source. A schematic of the measurement scheme is shown in Fig. 3.9.

4 Tailoring supercurrent confinement

In this chapter we study the induced supercurrent in gate-defined one-dimensional nanoscale constrictions in BLG weak links by monitoring the confinement via magneto-interferometry measurements. The chapter is organized as follows: At first, a literature review (4.1) is presented including an introduction to superconducting magneto-interferometry, as well as a short discussion about the employed Dynes-Fulton techniques for determining the spatial supercurrent density profiles. The following experimental results are subdivided into two parts based on different devices with distinct gate geometries, *i. e.* QPC-like confinement (4.2) and long channel confinement (4.3). Finally, a short conclusion is given (4.4).

4.1 Literature review

Graphene-based Josephson junctions represent a new class of weak links, combining superconductivity with relativistic effects as introduced in chapter 2 [TB06]. The provided gate-tunability of the Josephson effect together with high contact transparency and ballistic transport makes edge-connected graphene vdW heterostructure weak links an appealing platform for designing versatile superconducting quantum devices [LL18]. However, in spite of these excellent prerequisites for mediating superconductivity, a full control of the supercurrent both in its amplitude and spatial distribution remains challenging. One of the reasons behind this is the difficulty to confine charge carriers in graphene due to the lack of an electronic band gap [Cas+09], the absence of back scattering and the phenomenon of Klein tunneling [KNG06; Kat12]. On the other hand, the use of BLG could circumvent these problems thanks to the possibility to engineer an electronic band gap by breaking the lattice inversion symmetry of the AB-stacked bilayer [McC06; Cas+07; Oos+08; Zha+09b; TJ10; MK13]. For this reason, BLG is employed as weak link material in the here presented studies, providing a way to shape the supercurrent distribution by means of local gating. In the scope of this thesis two different gate geometries are presented, *i. e.* a QPC-like confinement (subsection 4.2) and a long channel confinement (subsection 4.3). [Kra+18b]

It should be remarked that prior to this work, several groups have noted the presence of conductive channels despite the opening of the band gap [Ju+15; All+16; Zhu+17], which impedes the intended spatial control of the supercurrent via local band gap engineering. The reported shunting behavior in the assumed insulating state is explained by induced currents through topological channels which can appear primarily for two reasons: AB stacking faults [ZMM13; Vae+13] or edge states [Cas+08; Li+11].[1] The saturating resistivity in the presence of topological current paths along domain walls or the sample edges could be monitored by near-field infrared nanometer-scale microscopy [Ju+15] or superconducting magneto-interferometry measurements [All+16; Zhu+17], respectively.

Here, we investigate in a similar fashion the spatial distribution of the supercurrent by measuring the interference pattern arising from the response of the Josephson current to the applied perpendicular magnetic field, which contains information on the supercurrent density distribution. The underlying physics of the superconducting magneto-interferometry will be introduced at this point (based on [BP82; Tin04; GM05]).

Superconducting magneto-interferometry

We consider a finite-size Josephson junction (here the BLG weak link) of length and width L, W, respectively, with the junction area oriented in the xy-plane, as sketched in Fig. 4.1a. In an external perpendicular magnetic field $\boldsymbol{B} = (0, 0, B_z)$ different supercurrent paths connecting the two superconducting electrodes pick up a gauge-invariant phase difference with respect to each other. Demanding the phase to be quantized between any two paths for the macroscopic wave function to be single valued, *i. e.* the total phase change along a closed contour is $2\pi n$ (see the white dashed box in Fig. 4.1a), the position dependent phase difference can be written as

$$\varphi(x) = \varphi_0 + \frac{2\pi\Phi}{\Phi_0}\frac{x}{W} \quad , \tag{4.1}$$

where $\varphi_0 = \varphi(x = 0)$ is the phase difference at $x = 0$, $\Phi_0 = h/2e$ is the flux quantum and $\Phi = B_z\tilde{A}$ is the magnetic flux threading the junction area $\tilde{A} = \tilde{L}W$ with $\tilde{L} = L + 2\lambda_L$ the effective length including the London penetration depth of the applied magnetic field into the superconducting electrodes. Inserting $\varphi(x)$ into the current-phase relation (Eq. 2.10) the supercurrent density is obtained to

$$J_s(x) = J_c(x)\sin(\beta x + \varphi_0) \quad , \tag{4.2}$$

[1] Note, that in early experiments with diffusive non-encapsulated BLG junctions on Si/SiO_2 substrates [Oos+08; TJ10] other more trivial reasons would cause the limitation of achievable maximum resistance, such as charge inhomogeneities and disorder in the device causing mid-gap states and the eventual quenching of the transport gap [Miy+10; Jin+10].

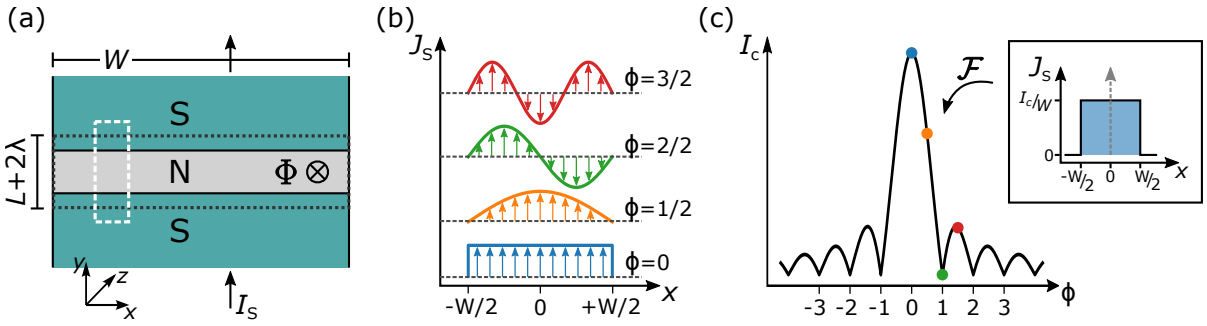

Figure 4.1: Introduction to superconducting magneto-interferometry. (a) Sketch of the SNS junction. (b) Spatial variation of the supercurrent density for different values of the normalized magnetic flux $\phi = \Phi/\Phi_0$. (c) Interference pattern of the maximum supercurrent as a function of the normalized magnetic flux, showing a Fraunhofer interference of a single-slit (*i. e.* short and wide) Josephson junction. Inset: Corresponding supercurrent density profile that can be translated into the interference pattern by solving the Fourier integral in Eq. 4.5b.

where $\beta = \frac{2\pi\Phi}{\Phi_0}\frac{1}{W}$, which describes a sinusoidally oscillating supercurrent density along the x-direction with periodicity depending on the flux (see Fig. 4.1b). The total supercurrent through the junction is then calculated by integrating the supercurrent density over the junction width W:

$$I_s(\beta, \varphi_0) = \int_{-W/2}^{+W/2} J_c(x) \sin(\beta x + \varphi_0)\, dx \quad , \tag{4.3}$$

which can be rewritten into the equivalent expression

$$I_s(\beta, \varphi_0) = \mathrm{Im}\left\{ e^{i\varphi_0} \int_{-W/2}^{+W/2} J_c(x) e^{i\beta x}\, dx \right\} \quad . \tag{4.4}$$

The critical current, *i. e.* the maximum supercurrent, is finally obtained by maximizing Eq. 4.4 with respect to φ_0, which yields simply the magnitude of the integral

$$I_c(\beta) = \max_{\varphi_0}\{I_s(\beta, \varphi_0)\} = |\mathcal{I}(\beta)| \quad , \tag{4.5a}$$

$$\mathcal{I}(\beta) \equiv \int_{-\infty}^{+\infty} J_c(x) e^{i\beta x}\, dx \quad , \tag{4.5b}$$

where $\mathcal{I}(\beta)$ can be identified as the complex Fourier transform of the real space critical current density $J_c(x)$.[2]

[2] Note that here the integration limits have been replaced by $\pm\infty$, which does not change the result of the integral since $J_c(x)$ (and hence the integrand itself) is only finite within the physical junction boundaries $-W/2 \leq x \leq +W/2$, but zero outside.

In the case of a single Josephson junction with homogeneous maximum supercurrent density profile across its width, *i. e.* constant $J_c(x) = J_c$, the resulting critical current as a function of magnetic flux takes the form

$$\frac{I_c(\Phi)}{I_c(0)} = \left| \frac{\sin\left(\frac{\beta W}{2}\right)}{\frac{\beta W}{2}} \right| = \left| \frac{\sin\left(\frac{\pi\Phi}{\Phi_0}\right)}{\frac{\pi\Phi}{\Phi_0}} \right| \quad , \tag{4.6}$$

which is analogous to the Fraunhofer diffraction pattern of a single-slit in optics [Tin04] (see Fig. 4.1c). Here, it is the spatially varying phase difference causing a spatial interference effect of the macroscopic superconducting wave function in the Josephson junction which can be observed as the interference pattern of the maximum supercurrent as a function of the externally applied magnetic field.

The Fraunhofer-like interference pattern has been extensively studied already in earliest experiments based on diffusive SNS junctions in the wide junction limit [Row63; Cla69; NYF82; YF84]. Since then, the response of the critical current subject to magnetic field has been investigated in a large variety of different superconducting junctions, revealing anomalous and non-Fraunhofer interference patterns. For instance, increased oscillation periodicities have been reported in ballistic SNS junctions of comparable length and width [Hei+98]. Theoretically, this has been qualitatively described in terms of quasi-classical trajectories, where reflections from the edges needs to be taken into account for decreasing width-to-length ratios which modifies the $I_c(\Phi)$ behavior in a way of gradually increased oscillation period from Φ_0 to $2\Phi_0$ (or $\Phi_0 \rightarrow 3\Phi_0$ in the diffusive regime) [BZ99; LFB99; MFG16], as well as lifted nodes (non-zero minima) [MFG16].

Further experiments, performed in the narrow junction limit, revealed an unusual monotonic decay of the critical current as a function of perpendicular magnetic field [Ang+08; Chi+12; Ama+13]. The absence of the magnetic interference pattern is understood due to the presence of magnetic vortex structures appearing in the normal region of the junction, eventually effectuating a cross over from the Fraunhofer-like pattern in wide and short junctions to a monotonic decay in long junctions narrower than the magnetic length l_B [CB07; BC08; CI13].

Importantly, the observation of a distinct variety of interference patterns in different junction geometries [BP82] reflects the fact that the response of the critical current to the applied perpendicular magnetic field is correlated to the supercurrent density distribution (cf. Eq. 4.5). Superconducting magneto-interferometry thus provides a powerful tool to probe the supercurrent flow in a device, as it was recently demonstrated experimentally in a 2D HgTe/HgCdTe quantum well topological insulator [Har+14], where the real space supercurrent density profile could be extracted from the measured interference pattern by performing the inverse complex Fourier transform of

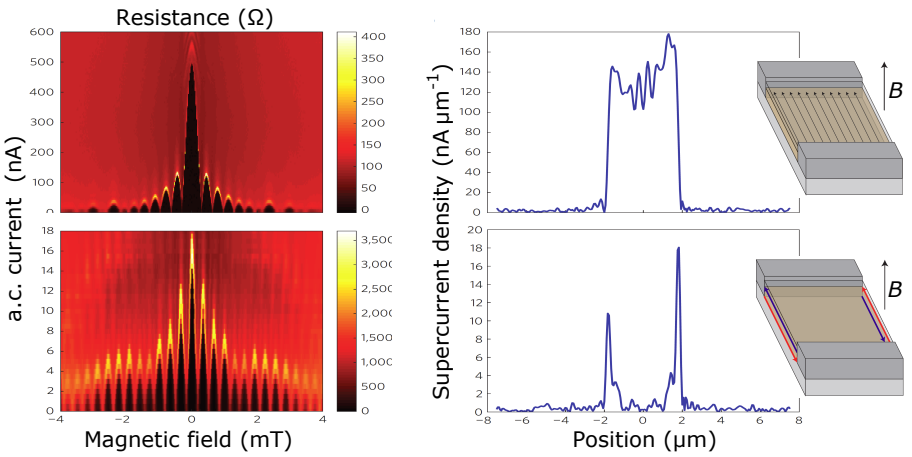

Figure 4.2: Superconducting magneto-interferometry measurements in a topological HgTe/HgCdTe quantum well. Left: Superconducting magnetic interference patterns. Right: Corresponding reconstructed supercurrent density profiles by performing the inverse Fourier transform following the Dynes-Fulton approach. The obtained density profiles represent a uniform supercurrent distribution (top) and induced superconductivity in the helical edge states with suppressed bulk current (bottom), corresponding to the two scenarios as depicted by the schematics in the insets. Taken from [Har+14] (labels have been replaced for better visibility).

Eq. 4.5b following the Dynes-Fulton approach [DF71] (see Fig. 4.2). By now, this method has become a widely used standard protocol for monitoring the supercurrent density distribution [Pri+15; All+16; Zhu+17; Ind+18]. In the following paragraph, the Dynes-Fulton approach is briefly discussed.

The Dynes-Fulton approach

The proposed procedure due to Dynes and Fulton [DF71] allows in principle to reconstruct the maximum supercurrent density profile $J_c(x)$ from the observed superconducting magnetic interference pattern of the critical current as a function of the magnetic flux $I_c(\Phi)$ by performing the inverse complex Fourier transform of the given expression in Eq. 4.5b over the measured sampling range b of β:

$$J_c(x) = \left| \frac{1}{2\pi} \int_{-b/2}^{+b/2} \mathcal{I}(\beta) e^{-i\beta x} \, \mathrm{d}\beta \right| \quad . \tag{4.7}$$

However, due to the fact that only the maximum supercurrent, *i. e.* the critical current $I_c(\beta) = |\mathcal{I}(\beta)|$, is measured in the experiment, all the necessary phase information of the complex $\mathcal{I}(\beta)$ is lost in the obtained interference pattern. In the Dynes-Fulton approach, this lack of knowledge is overcome by writing the total maximum supercurrent density distribution as the sum of an even and odd part $J_c(x) = J_e(x) + J_o(x)$, which yields

$$\mathcal{I}(\beta) = \int_{-\infty}^{+\infty} J_e(x) \cos(\beta x) \, \mathrm{d}x + i \int_{-\infty}^{+\infty} J_o(x) \sin(\beta x) \, \mathrm{d}x \quad , \tag{4.8}$$

decomposed into its real and imaginary parts $\mathcal{I}(\beta) = \mathcal{I}^{\mathrm{real}}(\beta) + i\mathcal{I}^{\mathrm{imag}}(\beta)$ with $\mathcal{I}^{\mathrm{real}}(\beta) \equiv \int_{-\infty}^{+\infty} J_{\mathrm{e}}(x)\cos(\beta x)\,\mathrm{d}x$ and $\mathcal{I}^{\mathrm{imag}}(\beta) \equiv \int_{-\infty}^{+\infty} J_{\mathrm{e}}(x)\sin(\beta x)\,\mathrm{d}x$. Then, by assuming an almost symmetric density profile, *i. e.* $J_{\mathrm{e}}(x) \gg J_{\mathrm{o}}(x)$, the phase information can be recovered by flipping the sign of alternating lobes of the measured pattern $I_{\mathrm{c}}(\beta) = |\mathcal{I}(\beta)|$, since $\mathcal{I}(\beta) \simeq \mathcal{I}^{\mathrm{real}}(\beta)$ becomes purely real.

On the other hand, the odd component $J_{\mathrm{o}}(x)$ of the supercurrent density profile is reflected in the appearance of a non-zero critical current at minima of the pattern, where the real part $\mathcal{I}^{\mathrm{real}}(\beta)$ vanishes and the pattern is instead dominated by the imaginary part $\mathcal{I}^{\mathrm{imag}}(\beta)$, *i. e.* $\mathcal{I}(\beta) \simeq \mathcal{I}^{\mathrm{imag}}(\beta)$. In that sense, $\mathcal{I}^{\mathrm{imag}}(\beta)$ can be estimated semi-quantitatively by interpolation through the minima and flipping sign between lobes. Finally, having recovered the phase information for the complex $\mathcal{I}(\beta)$ from the measured pattern of the absolute $I_{\mathrm{c}}(\beta) = |\mathcal{I}(\beta)|$, it is possible to reconstruct the maximum supercurrent density profile $J_{\mathrm{c}}(x)$ as to Eq. 4.7.

Yet, it is important to note that this approximate analysis due to Dynes and Fulton incorporates strongly simplifying assumptions causing intrinsic limitations of this technique [Hui+14]. First of all, the analysis is strictly based on the constraint of considering a sinusoidal current-phase relation, which itself further demands a short and wide junction with small transmission parameter $D \ll 1$ of the superconducting contacts.[3] Secondly, the sample geometry, *i. e.* width and length of the junction, is treated as a known and especially constant input to the calculations, while in experiment the effective junction area might depend on different experimental parameters, such as gate voltage or externally applied magnetic field (and others).

Moreover, the Fourier integral as given in Eq. 4.5b requests a uniform supercurrent density distribution along the other dimension of the 2D junction plane, *i. e.* in the direction of the current flow normal to the superconducting contacts (say y-direction). Though, in the case of a non-uniform supercurrent density profile in y-direction (e. g. due to the presence of disorder or charge carrier inhomogeneities) the equation would need to be solved for two spatial variables, *i. e.* $J_{\mathrm{c}}(x, y)$ instead of $J_{\mathrm{c}}(x)$, making the problem unsolvable in this simplistic approach. Last but not least, extracting $J_{\mathrm{c}}(x)$ based on the Dynes-Fulton technique provides not a unique solution, similar to an

[3] In ballistic graphene Josephson junctions, the current-phase relation has been calculated in several theoretical works [TB06; BD08; BL10; MCP12; RKC16] predicting anharmonic forward-skewing with respect to the sinusoidal current-phase relation. The non-sinusoidal behavior has been observed experimentally in the diffusive [Eng+16] and ballistic [Nan+17] regime, revealing increasing skewness as a function of the critical current but decreasing upon an increase in temperature. On the other hand, a sinusoidal current-phase relation has been reported in the case of reduced contact transparency due to the formation of *pn*-junctions at the contact interfaces upon hole doping, while forward skewness is present when the sample is electron doped resulting in high transparency and large critical current [Sch+18].

inverse scattering problem with lost phase information about the original unknown function. Here, only the amplitude of the complex Fourier integral is experimentally accessible, making it first necessary to recover the phase information, which itself manipulates the result due to the symmetry constraint of the made assumptions. For instance, it has been shown that different choices of $J_c(x) \neq J_e(x)$ can yield the same interference pattern [Zap75].

Due to its many assumptions, the Dynes-Fulton approach also inherits a lack of internal consistency, as it does not provide a self-consistent solution in further reiteration steps of the Fourier transform, *i. e.* the resultant calculated interference pattern from the initially extracted $J_c(x)$ might not be the same as the original experimental pattern but showing a quantitative disagreement [Hui+14]. The possible inconsistencies could arise due to impracticable prerequisites of the technique. For example, the appearance of non-zero minima is only and exclusively attributed to an asymmetry in the supercurrent density profile, whereas other possible node-lifting mechanisms, such as finite contact transparencies [Hui+14], long junction effects [MFG16] or parity switching at low temperatures in a topological superconducting junction [Lee+14], are not considered.

The problematics of the procedure become also apparent in the appearance of an unwanted byproduct, that is the calculated currents are spilling in parts outside the sample dimensions. This unphysical answer to the problem seems to be an unavoidable artifact of the Dynes-Fulton technique as it can be observed in any of the presented results [Har+14; Pri+15; All+16; Zhu+17; Ind+18]. Finally, it should be noted that the resolution of the extracted supercurrent density is limited and determined by the measured range of β (*i. e.* inversely proportional), being typically in the order of $\sim 100\,\mathrm{nm}$ for applied magnetic fields of order $\sim 10\,\mathrm{mT}$ and an effective junction length $\sim 1\,\mu\mathrm{m}$.[4]

Nevertheless, despite all listed constraints and limitations that need to be considered, the Dynes-Fulton approach can often provide a useful simplistic method to gain a qualitatively adequate understanding of the supercurrent flow in the device, which will be demonstrated in the second experimental part B in the "long channel confinement" (section 4.3), but being not applicable in the first experimental part A with "QPC-like confinement" (section 4.2) which is presented next.

[4] The spatial resolution is given by $\Delta x = 2\pi/b$ (with b the sampling range of β), which can be written in terms of magnetic field as $\Delta x = \Phi_0/(B_r \tilde{L})$, where $B_r = B_{max} - B_{min}$ is the measured range of magnetic field values.

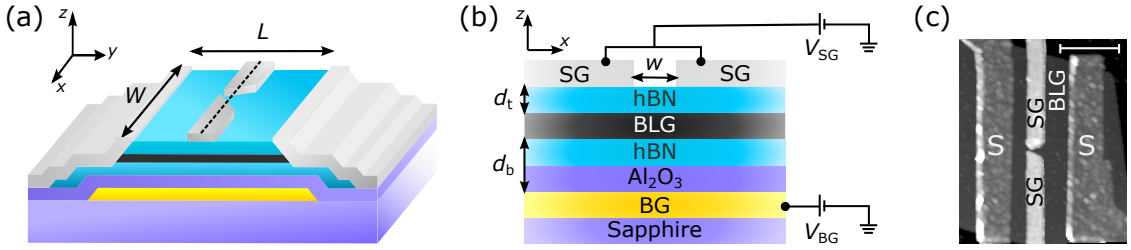

Figure 4.3: Device design. (a) 3D schematic of the device and (b) cross-sectional view as a cut through the dual-gated region. The device consists of a hBN-BLG-hBN heterostructure (with a bottom and top hBN multilayer of $\approx 35\,\text{nm}$ and $\approx 38\,\text{nm}$ thick, respectively) on a pre-patterned back gate (BG) covered with a 20 nm thick Al_2O_3 and a split gate (SG) on top of the heterostructure. The Ti/Al superconducting contacts are edge-connected to the mesa in a self-aligned manner. The junction width and length are $W = 3.2\,\mu\text{m}$ and $L = 0.95\,\mu\text{m}$, respectively, while the closest distance between the two SG electrodes is $w \approx 65\,\text{nm}$ and thicknesses of the dielectric (hetero-) layers are $d_t \approx 38\,\text{nm}$ and $d_b \approx 55\,\text{nm}$, *i. e.* distance between gates and BLG layer. (c) AFM image of the device (the scale bar is 1 µm). We note that the junction geometry is not perfectly rectangular, but rather slightly rhomboid.

4.2 Experimental results – Part A: quantum point contact-like confinement

Here we study a device designed in a QPC-like structure.[5] A schematic as well as the AFM image of the sample is shown in Fig. 4.3. Details on the device geometry are given in the figure caption. The confinement is realized by controlled band gap engineering via the applied displacement fields between the overall pre-patterned BG and the locally defined split gate (SG). The experiments were performed in several thermal cycles, and the obtained results could be reproduced in the different cooldowns (only minor changes in the position of the charge neutrality point are observed).

The here presented results are based on two cooldowns, which will be labeled throughout this section as CD#1 and CD#2 (corresponding to recorded cooldowns #23 and #25 of the cryostat logbook, respectively). Base temperatures of these two cooldowns were about $\lesssim 25\,\text{mK}$ and $\lesssim 55\,\text{mK}$ (unless stated otherwise). In the initial device characterization the shown data is mainly based on CD#2, whereas the rest is primarily based on CD#1 (which will be specified in each figure caption). The normal state measurements were conducted by applying a perpendicular magnetic field $B = 20\,\text{mT}$.

For the supercurrent analysis and magneto-interferometry measurements the critical current I_c is extracted using a threshold voltage method with the threshold value set to 1 µV. The two adjacent data points of recorded IV curves right before and after the

[5] The presented results are partly based on [Kra+18b].

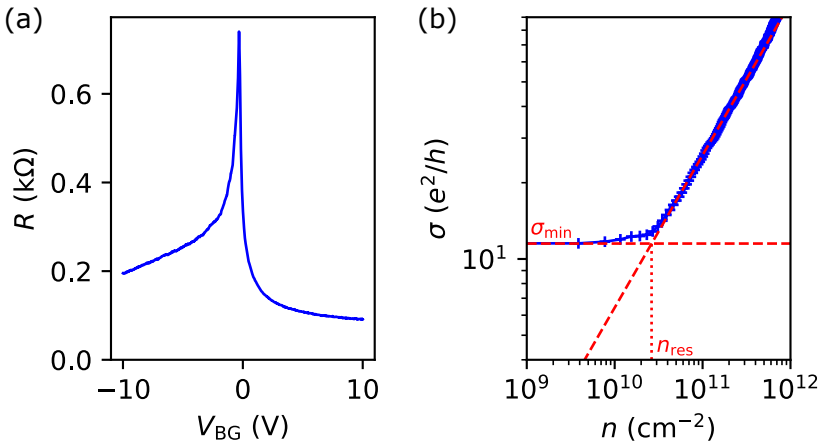

Figure 4.4: The electric field effect – normal state characteristics. (a) Resistance curve as a function of V_{BG} for the approximate uniformly doped 2D system (*i. e.* $V_{SG} = V_{SG}^{cnp} = 0.2\,V$). (b) log-log-plot of the conductivity σ as a function of charge carrier density n, where a contact resistance of $2R_C = 72\,\Omega$ was subtracted. Data is based on CD#2.

threshold are evaluated, and I_c is determined by linear extrapolation in the current between these two points depending on the ratio of the voltage drops with respect to the threshold value. The extracted critical current is finally corrected by subtracting the artificial offset that is produced by this method.

4.2.1 Initial device characterization

Normal state characteristics

Here, the basic characteristics of the sample are presented for which it is instructive to start with a measurement of the electric field effect of the device. Figure 4.4a shows the respective resistance as a function of V_{BG} when the device is measured as 2D junction, *i. e.* with approximately uniform overall doping. At the charge neutrality point, a sharp resistance peak is observed, which is positioned at slightly negative $V_{BG} = V_{BG}^{cnp} = -0.32\,V$ (CD#2) indicating a small intrinsic n-type doping of the BLG. Upon finite induced charge carrier density, the resistance drops and an apparent asymmetry is noticed between the saturating resistance of electron and hole side [Hua+08]. The asymmetric device properties are due to the charge transfer from the Ti/Al contact leads having a smaller work function with respect to graphene, which induces a slight n-type doping to the BLG in their vicinity [Gio+08]. Then, as the graphene sheet itself is tuned to a p-type doping, additional pn-junctions form at the interfaces to the metal contacts.

Next, an upper bound of the contact resistance per contact is estimated as $R_C = (R - R_Q)/2$, where the quantum resistance R_Q is subtracted from the measured

resistance R. The quantum resistance $R_Q = (M \times ge^2/h)^{-1}$ is defined as the resistance set by the ballistic limit of all contributing conductance modes $M = W/(\lambda_F/2)$ with $\lambda_F = 2\pi/k_F = 2\pi/\sqrt{\pi n}$ the Fermi wavelength at charge carrier density n and $g = 4$ accounts for the fourfold degeneracy, *i. e.* spin and valley. At high charge carrier density on the electron side $n \approx 4 \times 10^{12}\,\mathrm{cm}^{-2}$ (corresponding to $M = 361$ and $R_Q = 18\,\Omega$) a resistance of $R = 90\,\Omega$ is measured, yielding $R_C = 36\,\Omega$ and contact resistivity $\rho_C = R_C W = 115\,\Omega\,\mu\mathrm{m}$, comparable to the values given by Wang et al. [Wan+13].

The residual charge carrier density in the device n_{res} on the electron side is estimated as to [Du+08], where Fig. 4.4b shows the log-log-plot of the conductivity (with subtracted contact resistance) as a function of charge carrier density n.[6] The crossing point of the saturation conductivity with the extrapolated linear fit to the data at elevated charge carrier density yields a low residual charge carrier inhomogeneity n_{res} of the order of $\sim 1 \times 10^{10}\,\mathrm{cm}^{-2}$, below which transport is governed by the residual disorder rather than the tuning by the gate voltage. We note that transport above n_{res} is in the ballistic regime, as evident from the apparent presence of Fabry-Pérot interferences in different cavities formed by the SG or by the unintentional doping from the metal leads [SRL08; YK09; Ric+13; Var+14b; Du+18] (see Appendix B.2).

Proximity-induced superconductivity

Next, the junction is characterized in the superconducting state, *i. e.* at zero magnetic field. Figure 4.5a shows again a measurement of the electric field effect of the sample tuned by the overall BG. Although this time, the resistance drops to zero away from charge neutrality indicating the finite supercurrent flowing through the BLG weak link due to the superconducting proximity effect. At the charge neutrality point itself supercurrent is suppressed and the junction remains resistive. The amplitude of the supercurrent in the BLG Josephson junction is studied by measuring a continuous set of IV curves for different values of the BG (*i. e.* different charge carrier densities, respectively). The corresponding differential resistance $\mathrm{d}V/\mathrm{d}I$ is plotted as a function of V_{BG} and current I in Fig. 4.5b, where dissipationless current is observed as black regions. Once again, a clear asymmetry is noticed between electron and hole side. The significantly smaller supercurrent magnitude measured in the case of p-type doping (by about an order of magnitude) is due to the formation of pn-junctions as discussed for the normal state resistance beforehand.

[6] The charge carrier density is calculated as to a parallel-plate capacitor picture $n = (C/e)V$, where C is the specific gate capacitance per unit area extracted from the Landau level fan diagram (see Appendix B.1).

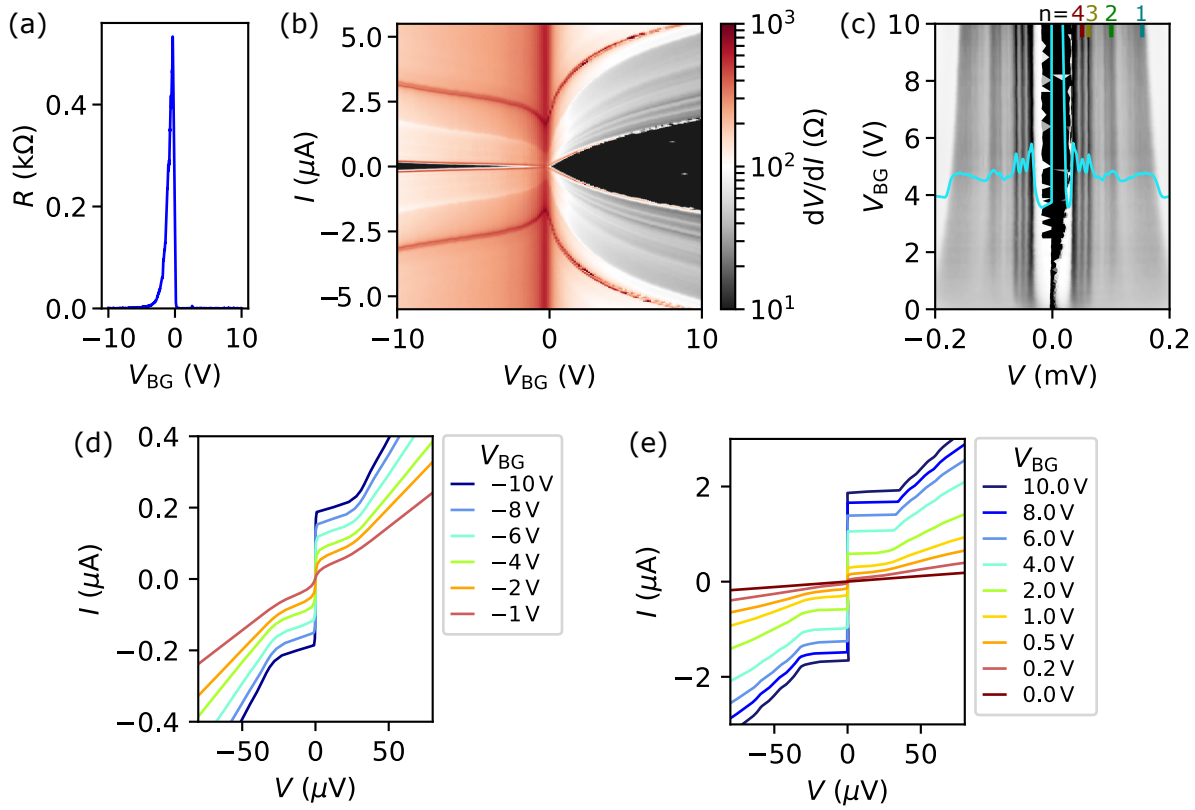

Figure 4.5: Proximity-induced superconductivity – supercurrent in the 2D junction. (a) Resistance curve as a function of V_{BG} at $V_{SG} = 0$ in the superconducting regime. (b) Corresponding bias map, showing the differential resistance as a function of V_{BG} and current I. (c) Respective gray-scale map of the normalized differential conductance (arbitrary units) as a function of bias voltage V and V_{BG}. The additionally shown colored curve denotes the trace at $V_{BG} = 4\,\mathrm{V}$, highlighting the visible subgap resonances (*i. e.* MAR) positioned at $eV = 2\Delta_0/n$ with $n = 1, 2, 3, 4$. (a-c) Data from CD#2. (d, e) Exemplary IV curves at $V_{SG} = 0$ for different V_{BG} as given in the respective legend. Data from CD#1.

Above the critical current the junction is no longer superconducting but switches to the resistive regime, where several resonances are visible. These subharmonic features for energies below the superconducting energy gap are due to MAR [KBT82; Oct+83; CY06], as depicted in Fig. 4.5c showing a gray-scale map of the respective (normalized) differential conductance as a function of bias V and V_{BG} together with an exemplary curve ($V_{BG} = 4\,\mathrm{V}$). Here, the subgap resonances are observed as lines at position $V = 2\Delta_0/(ne)$ (with $n = 1, 2, 3, 4$ an integer number) from which we extract the superconducting energy gap $\Delta_0 = 107\,\mu\mathrm{eV}$. We note that the resonance peak $n = 1$ is not well-positioned at the expected position and reveals a dispersing behavior as a function of V_{BG}, which we attribute to the smearing of the gap at higher bias excitation due to the heating caused by the current being larger at increased BG voltage. The superconducting energy gap Δ_0 is smaller than the Thouless energy $E_{Th} = \hbar v_F/L \approx 600\,\mu\mathrm{eV}$ (in a ballistic junction). The superconducting coherence

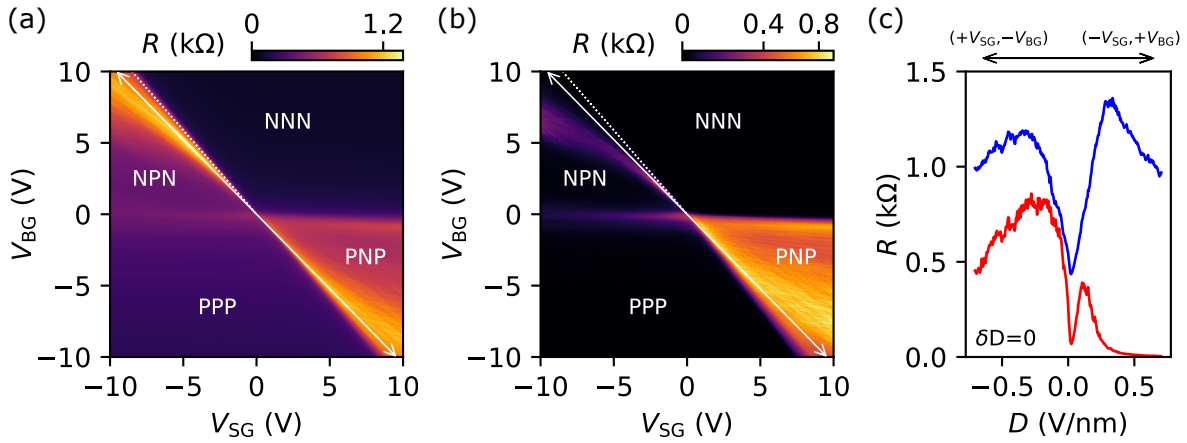

Figure 4.6: Formation of the constriction – gate-gate-map analysis. (a, b) Resistance maps as a function of V_{SG} and V_{BG} in the normal state (a) and superconducting state (b), respectively. Note that in (b) the color scale is non-linear for better visibility of features with low resistance (particularly in the upper left corner). The given labels NNN, PPP and NPN, PNP denote the different quadrants of unipolar and bipolar doping in the device. The displacement field line along which the charge carrier density in the dual-gated region is set to zero ($\delta D = 0$) is indicated by the double-headed arrow. The dotted line marks the transition when E_F is tuned from the conduction band into the induced band gap. (c) Resistance curves (blue: normal state; red: superconducting state) versus displacement field D measured along the displacement field line. Data from CD#1.

length being $\xi_0 = \hbar v_F/\Delta_0 \approx 5.5\,\mu m$ which is larger but in the same order as the junction length ($L \lesssim \xi_0$).

Finally, the critical current I_c and I_cR_n product (being a measure for the strength of the proximity coupling) are extracted from the IV curves shown in Fig. 4.5d, e (note that the IV curves are taken from CD#1 unlike the rest of the figure for better comparison with later discussed supercurrent amplitudes primarily based on the same cooldown). At large charge carrier density $n \sim \pm 4 \times 10^{12}\,cm^2$ the critical current $I_c = 1.86\,\mu A$ ($V_{BG} = 10\,V$) and $I_c = 0.19\,\mu A$ ($V_{BG} = -10\,V$), corresponding to $I_cR_n = 1.64\Delta_0/e$ and $0.35\Delta_0/e$, respectively.

4.2.2 How to read the dual-gate map of a split-gated device

Employing the combination of overall BG and local SG is presupposed to electrostatically confine the charge carriers. In order to figure out suitable gate conditions to probe the confinement, we first analyze resistance maps as a function of V_{SG} and V_{BG} for both normal and superconducting state, respectively, shown in Fig. 4.6a, b. The maps are subdivided into unipolar (NNN, PPP) and bipolar (NPN, PNP) quadrants due to unique doping combinations in the different regions of the device, *i. e.* dual-gated regions controlled by both SG and BG or the outer regions only tuned by the BG.

Though, in both cases (normal and superconducting state) distinct deviations compared to the observed behavior of BLG devices in *pnp*-junction geometry [Oos+08; TJ10; Var+14b] are clearly visible (cf. Fig. 2.5).

Typically, in BLG dual-gated devices a monotonically increase of the resistance would be expected with increasing displacement fields due to the induced insulating state with strongly suppressed conductivity as the band gap develops. Here, we observe a non-monotonic change of the resistance which first increases and then declines after reaching a maximum while following the displacement field line indicated by the gray double-headed arrow in the maps (corresponding to charge neutrality $\delta D = D_\mathrm{b} - D_\mathrm{t} = 0$ [Zha+09b], *i.e.* at equal displacement fields D_b and D_t generated by BG and SG, respectively). The respective resistance curves are plotted in Fig. 4.6c. While the described trend is already noticeable in the normal state (blue curve), it becomes strikingly evident in the superconducting state (red curve) as the resistance fully drops to zero. In the map of Fig. 4.6b, this is seen by the region of zero resistance extending from the unipolar NNN into the part of the map where the displacement field is maximal and the Fermi level is presumed to be positioned within the induced band gap. On the other hand, the observed maximum resistance in both maps does not follow the displacement field line, but instead diverges into the bipolar regions NPN and PNP, respectively.

The non-trivial evolution of the resistance can be understood considering the antagonistic interplay from BG and SG. Since the application of large displacement fields in order to suppress the current underneath the SG electrodes requires large opposite gate voltages, the two gates act in a competitive fashion on the channel. Then, at elevated displacement field the charge carrier density in the channel is mainly driven by the BG but becomes less and less affected by the stray fields developed by the SG, which cannot compensate the influence of the BG on the channel region. In the consequence, this gives rise to the non-monotonic progression of the resistance along the displacement field line as the device remains highly conductive due to the opened channel in contrast to the pinch-off characteristics of gapped BLG with full-width top gate, which is particularly visible in the superconducting state by the observed zero resistance (*i.e.* dissipationless current due to a finite supercurrent through the constriction). The measured maximum resistance instead following a bent line is due to the required overcompensation of the SG voltage to diminish the induced charge carriers within the channel region.

However, this imbalance between applied SG and BG voltages shifts the Fermi level eventually out of the gap into the respective other band (*i.e.* valence or conduction band, respectively), which induces charge carriers of opposite sign in the dual-gated cavities resulting in the formation of *pn*-junctions. As a consequence, the bipolar regions are subdivided into different transport regimes depending on the doping within

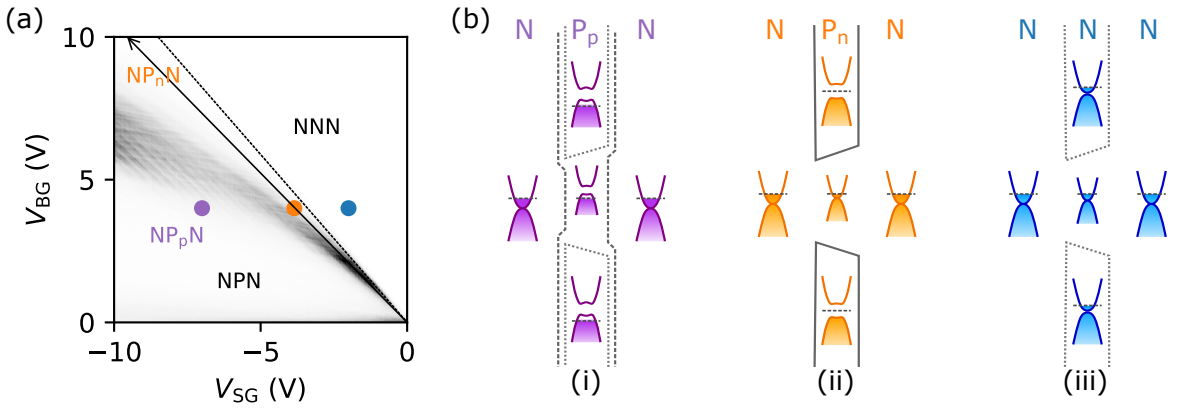

Figure 4.7: Operating regimes of the QPC-like constriction. (a) Zoom-in on the upper left corner of the resistance map in the superconducting state (see Fig. 4.6b), here plotted as gray-scale map. The different transport regimes areas are enlightened by dashed lines and accordingly labeled as introduced in the main text. (b) Schematics of the spatially resolved band structures in the QPC-like geometry observed in a top view for the three different transport regimes (i) NP_pN, (ii) NP_nN and (iii) NNN.

the constriction. Figure 4.7a presents a zoom-in on the upper left corner of the map in the superconducting state, in which the different regions are delineated by colored dashed lines and accordingly labeled with an additional sub-label denoting the channel doping. The QPC-like structure can then be driven in an 'open' NP_nN (the 1D channel doping is of the same type as the 2D reservoirs) or 'closed' NP_pN (the 1D channel doping is of the opposite type as the reservoirs forming a non-uniform potential barrier) regime. The possible scenarios, governing the behavior of such electrostatically induced constriction, are illustrated in Fig. 4.7b showing spatial band structure schematics for (i) the non-uniform NP_pN junction, (ii) the formed 1D constriction NP_nN and (iii) the unipolar regime NNN.

Although the described different transport regimes can be identified for both polarities, it is important to note that the overall resistance on the hole side remains higher compared to the electron side (*i. e.* uniform PPP $\leftrightarrow$ NNN or bipolar PNP $\leftrightarrow$ NPN, respectively). The asymmetry can be attributed to the presence of *pn*-junctions forming at the interfaces to the metal contacts when the graphene itself is hole doped (see subsection 4.2.1). This becomes particularly clear in the superconducting state, where the PNP region remains resistive, while a large part of the NPN section displays a zero resistance state. For this reason, the following analysis is focused on the NPN area and in particular on the NP_nN part, where the supercurrent is expected to flow only via the constriction and thus can be studied in the confined regime.

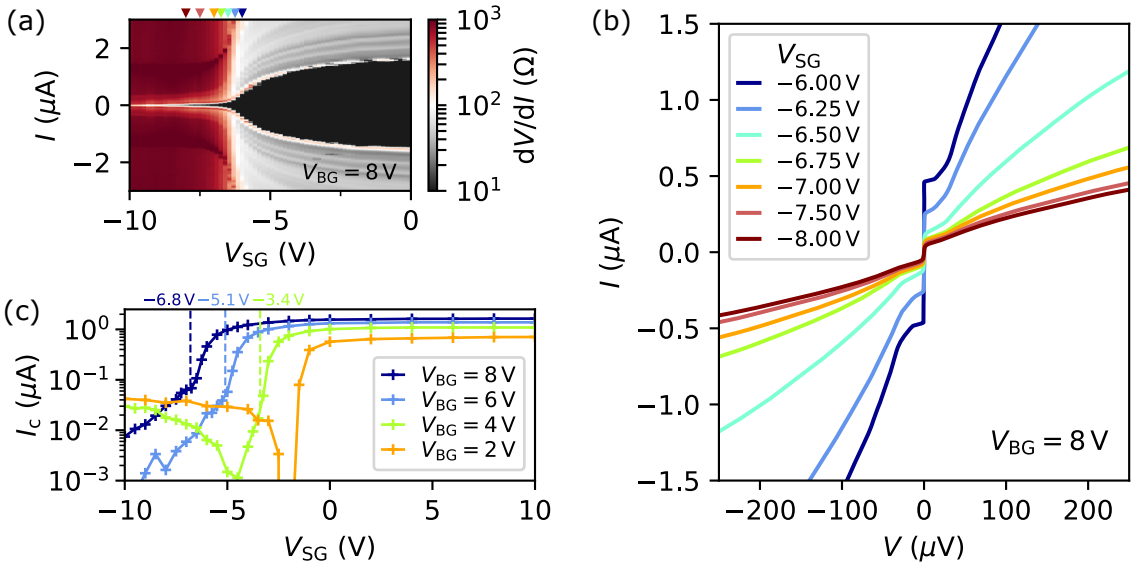

Figure 4.8: Formation of the constriction – supercurrent analysis. (a) Color map of the differential resistance as a function of V_{SG} and current I at constant $V_{BG} = 8\,V$, monitoring the decreasing amplitude of the supercurrent as the constriction forms at larger negative SG values. Data from CD#2. (b) Exemplary IV curves at constant $V_{BG} = 8\,V$ for different V_{SG}. (c) Extracted critical current as a function of V_{SG} for different V_{BG}. Dashed vertical lines denote the position where a change of the slope in the curves of $I_c(V_{SG})$ appears. (b, c) Data from CD#1.

4.2.3 Supercurrent analysis

In the previous subsection (4.2.2) it was demonstrated that the device remains superconducting in a gate range where the constriction is formed, namely the NP_nN regime. Here, the hypothesis of a confined supercurrent is tested by probing the critical current I_c upon a tuning by means of the SG. Figure 4.8a shows a map of the differential resistance as a function of V_{SG} and current I at a constant $V_{BG} = 8\,V$, corresponding to a large charge carrier density in the outer BLG reservoirs. Respective IV curves for different SG voltages are shown in Fig. 4.8b. While at positive V_{SG} the critical current remains fairly constant, a strong tuning of the supercurrent is monitored with increasingly negative V_{SG}. This is due to the supercurrent amplitude through the junction being determined by its weakest link. In case of $V_{SG} > 0$ (*i. e.* $n_{in} > n_{out}$), these are the outer BLG reservoirs, which are kept at constant density. On the other hand, for $V_{SG} < 0$ (*i. e.* $n_{in} < n_{out}$), the charge carrier density is depleted below the SGs and the critical current decreases rapidly until $V_{SG} \approx -6.8\,V$. At this point, the Fermi level underneath the SG is tuned into the band gap and charge carriers can only flow through the 1D channel of the induced confinement. Then, beyond the formation of the constriction, I_c decreases in a much slower fashion as the tuning of the supercurrent amplitude is only due to the stray fields from the SG acting on the channel. We further note that the junction is tuned from underdamped

to overdamped within the picture of the resistively and capacitively shunted junction (RCSJ) model, as the system is depleted with the SG and the confinement develops (shown in Appendix B.3).

The extracted critical current I_c as a function of V_{SG} is plotted in Fig. 4.8c for different charge carrier densities, *i. e.* different V_{BG}. At small density ($V_{BG} = 2\,V$, orange curve), the supercurrent is fully cut off as the Fermi level is positioned within the gap, indicating that the stray fields under this gating conditions are strong enough to close the channel (also see the resistance map in the superconducting state, shown in Fig. 4.6b). With larger negative V_{SG} a small but finite supercurrent reappears despite the presence of a weak *pn*-junction as the Fermi level is tuned already into the valence band (corresponding to the depicted scenario NP_pN in Fig. 4.7b).

In contrast, the BG starts to electrostatically dominate the constriction region for the other shown cases at higher charge carrier densities. The creation of the 1D channel (corresponding to the scenario NP_nN in Fig. 4.7b) is directly reflected in the sudden change of slope of $I_c(V_{SG})$ curves (blue and dark blue curves, with the position of the slope change marked by dashed lines). The supercurrent through the channel is then only slowly reduced owing to the narrowing of the channel with increasing negative V_{SG} as discussed beforehand. Once the constriction is formed, the supercurrent amplitude is quenched by two orders of magnitude compared to the respective 2D current.

In a naive estimate, assuming the same supercurrent density in the 2D and 1D confined regime, the ratio of $I_c^{2D}(V_{BG} = 8\,V;\, V_{SG} = 0) = 1.66\,\mu A$ ($W = 3.2\,\mu m$) and $I_c^{1D}(V_{BG} = 8\,V;\, V_{SG} = -8\,V) \approx 0.04\,\mu A$ would yield an effective junction width $w \sim 80\,nm$ close to the designed lithographic channel width. Yet, it should be noted that the made assumption represents an apparent oversimplification of the problem, e. g. completely ignoring trajectories that could pass diagonally through the channel from the wider 2D reservoirs as the constriction is only formed in the center of the device (*i. e.* the measured I_c^{1D} is increased compared to that in the hypothetical purely 1D device). Thus, the obtained value rather gives a possible upper bound for the width of the formed constriction.

Finally, at intermediate charge carrier density (green curve), the channel is initially created (NP_nN; see change of slope into a more gradual decrease of $I_c(V_{SG})$ after a rapid drop), then closed with the supercurrent switched off, to eventually form a soft non-uniform *pn*-junction with a small supercurrent detected (NP_pN).

4.2.4 Magneto-interferometry measurements

So far, several indicators for a confined supercurrent have been discussed by the analysis of the gate-gate-maps and the supercurrent amplitude. In this subsection, further evidence is provided by studying the response of the critical current to a perpendicular magnetic flux penetrating the junction. The resulting interference patterns contain information about the supercurrent density distribution across the sample width as described in the literature review (section 4.1). Figure 4.9a-d present such patterns, showing the differential resistance as a function of magnetic field B and current I for different V_{SG} at a constant charge carrier density of the outer BLG reservoirs ($V_{BG} = 8\,V$). The patterns reveal a progressive change of the interference patterns with increasingly negative V_{SG}, *i. e.* as the constriction develops. First, at $V_{SG} = 0$ (Fig. 4.9d), a beating pattern is visible, resembling a Fraunhofer-like interference of a 2D junction [Tin04].[7,8] The observed oscillatory behavior of the critical current keeps up for a large range $V_{SG} \to -6.0\,V$ (Fig. 4.9c), although with changed shaped and continuously decreasing supercurrent magnitude as discussed in the previous subsection 4.2.3. In a next step at $V_{SG} = -6.5\,V$ (Fig. 4.9b), the interference pattern features a lifting of the lobes before it finally turns into a non-beating 'bell-shaped' pattern for $V_{SG} = -7.0\,V$ (Fig. 4.9a). Note that such a non-beating pattern has been observed as well in rectangular superconducting weak links with low aspect ratio, *i. e.* narrow long junctions [Ang+08; Chi+12; Ama+13].

We further note, that the transition from a beating to a non-beating pattern occurs within a rather narrow SG voltage range $-7\,V < V_{SG} < -6\,V$ (at the given $V_{BG} = 8\,V$; additional data at $V_{BG} = 6\,V$ is shown in Appendix B.4, as well as for the hole-side in Appendix B.5). As long as a finite supercurrent flows underneath the SGs, the system remains two-dimensional and a beating pattern is recorded. But with the Fermi level eventually shifted into the induced band gap, the supercurrent flows only through the confined 1D constriction signified by the appearance of the non-beating pattern. In Fig. 4.9e, this evolution is mapped carefully by measuring a series of interference

[7] We note that the pattern does not reflect the ideal sinc-function behavior of a short and wide junction, but reveals missing and deformed lobes as well as lifted nodes, which can be attributed to several reasons (cf. the discussion in the paragraph about the Dynes-Fulton approach in section 4.1). Firstly, the electrostatic profile across the junction is disturbed by the presence of the SG, where at $V_{SG} = 0$ the charge carrier distribution might not be perfectly uniform due to a small but non-zero potential induced by the SG. Secondly, the device has a non-rectangular shape while any geometry distortion from the ideal short and wide junction case causes anomalous interference [BP82]. Last but not least, the device is not a short junction but $L \lesssim \xi$, where additional effects (e. g. reflection from the edges) might need to be considered, resulting in a modified pattern [BZ99; LFB99; MFG16; RKC16].

[8] We further note a rather triangular shaped central lobe, which is signature for a pattern of a ballistic weak link [SZ03; MFG16].

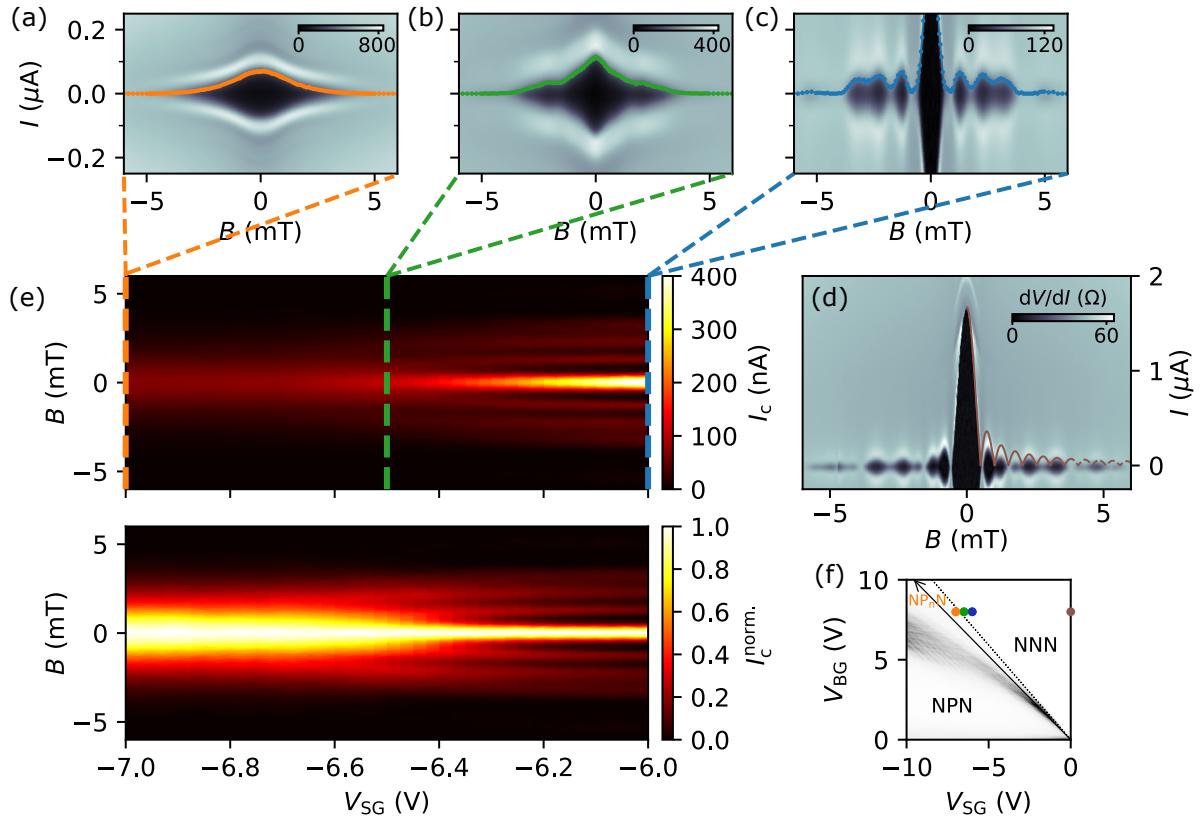

Figure 4.9: Superconducting magneto-interferometry. (a-d) Magnetic interference patterns, showing the differential resistance $\mathrm{d}V/\mathrm{d}I$ (in Ω) as a function of B and current I at $V_{\mathrm{BG}} = 8\,\mathrm{V}$ for different values of V_{SG}: (a) $-7.0\,\mathrm{V}$, (b) $-6.5\,\mathrm{V}$, (c) $-6.0\,\mathrm{V}$ and (d) $0\,\mathrm{V}$. The latter pattern for $V_{\mathrm{SG}} = 0$ is fitted by a sinc-function (brown curve), whereas in the other three cases (a-c) the extracted I_{c} values are plotted on top of the pattern (orange, green and blue data points, respectively). (e) Mapped series of interference patterns, showing the extracted (normalized) critical current amplitude I_{c} (top) and $I_{\mathrm{c}}^{\mathrm{norm.}}$ (bottom) in a color map as a function of V_{SG} and B. Each vertical slice corresponds to the extracted data of a single interference pattern as denoted by colored dashed lines for the three exemplary patterns in panels (a-c). (f) Gray-scale gate-gate-map of the resistance in the superconducting state as shown in Fig. 4.7 with marked gate conditions (colored dots) of the shown interference patterns (a-d). Data from CD#1.

patterns with varying V_{SG}. The extracted critical current I_c (top panel), as well as the critical current $I_c^{norm.}$ normalized with respect to its maximum of each curve (bottom panel), is plotted as a function of magnetic field B and V_{SG}. Each vertical slice of these maps corresponds to the critical current (or normalized critical current, respectively) extracted from a single magnetic interference pattern, as e. g. denoted by the colored dashed lines of the respective patterns shown in Fig. 4.9a-c. The detailed monitoring of the evolving patterns as a function of V_{SG} highlights the transition from 2D (beating pattern) to 1D ('bell-shaped' pattern) supercurrent.

However, despite this clear change in the patterns being evidence of a strongly modified spatial supercurrent density, recovering the real space supercurrent density distribution by employing the techniques due to Dynes and Fulton [DF71] is not possible as this approach is based on the assumption that the current density is strictly homogeneous in the direction normal to the superconducting electrodes (apart from several other presumptions and constraints [Hui+14] as discussed in sections 4.1 and 4.3). Here, the QPC-like geometry clearly does not fulfill this prerequisite. Instead, an analytical model calculating the Josephson current through the sample in the presence of a magnetic field, as well as tight-binding simulations using the Kwant package [Gro+14] are presented in the following.

4.2.5 Modeling the supercurrent confinement

In order to gain deeper understanding how the magnetic interference pattern should evolve with the creation of a QPC-like 1D constriction, an analytical and numerical model are developed.[9]

Analytical model

In this model, the Josephson current through the sample in the presence of a magnetic field is calculated by employing a quasi-classical picture [BZ99; SZ03; MFG16]. Based on this approach, the superconducting current density is expressed in terms of Andreev bound states, which can be viewed as electron-hole 'tubes' of width $\sim \lambda_F$ resulting from the Andreev reflection at the NS interfaces and the magnetic field dependence is included due to the Aharonov-Bohm phase. The magnetic flux dependent Josephson current is then found by summing over all possible paths connecting the

[9] The former model is due to the collaboration with our theory colleagues Nefta Kanilmaz and Igor Gornyi (KIT) who derived the analytical expressions, while numerical tight-binding simulations are performed by Muhammad Irfan under supervision of Anton Akhmerov (Delft University of Technology). For detailed descriptions on the modeling see the electronic supplementary material to [Kra+18b].

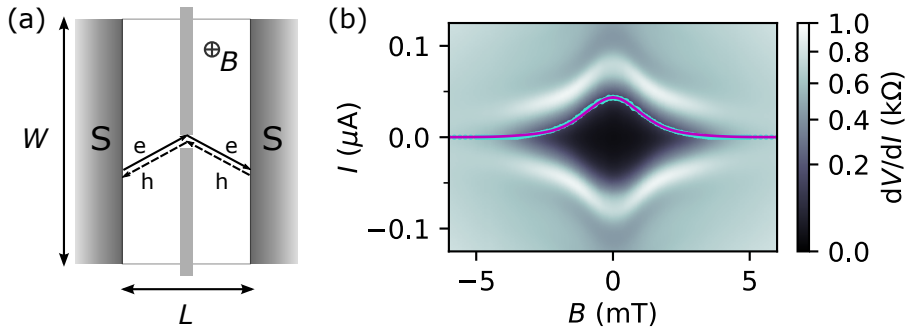

Figure 4.10: Analytical modeling of the magneto-interferometry measurements. (a) Schematic of the device setup for the analytical calculations. (b) Experimental magnetic interference pattern, showing the differential resistance as a function of B and current I at constant $V_{BG} = 8\,V$ and $V_{SG} = -8\,V$ when the 1D constriction is formed. The extracted critical current I_c (turquoise data points) is fitted by our analytical expression (magenta curve). Data from CD#1.

two superconducting electrodes. Here, an additional input is given by the presence of a QPC-like structure in the middle of the device as depicted in Fig. 4.10a, showing a schematic of the considered junction setup. In this geometry, points on the two opposite superconducting electrodes can only be connected by trajectories passing through the constriction itself. Since the width of the constriction is of the order of (or smaller than) the Fermi wavelength λ_F the transmission probability is considered to be isotropic. One can then find simplified analytical expressions for the asymptotic behavior in the two limits $\phi \to 0$ and $\phi \to \infty$, where $\phi = \Phi/\Phi_0$ is the dimensionless flux through the sample in units of $\Phi_0 = h/2e$:

$$\frac{I_c(\phi)}{I_c(0)} \simeq 1 - \frac{\pi^2\phi^2}{32} f_0(W/L)\,, \qquad \phi \to 0\,, \tag{4.9}$$

and

$$\frac{I_c(\phi)}{I_c(0)} \simeq f_1(W/L) \left(\frac{\pi\phi}{2W/L}\right)^{3/2} \exp\left(-\frac{\pi\phi}{2W/L}\right), \qquad \phi \to \infty\,, \tag{4.10}$$

with geometry-dependent functions $f_0(W/L)$ and $f_1(W/L)$ (see Appendix B.6 and [Kra+18b]). Following from these two equations, the magnetic interference pattern of a Josephson current for the here presented sample geometry with a constriction in the center of the junction is well described by a parabolic shape at small ϕ (Eq. 4.9), while it trends into an exponentially decaying tail at large ϕ (Eq. 4.10).

For comparison with the experimental data, the obtained functions for calculating the normalized critical current are evaluated over the whole magnetic field range (note that we do not have such simplified analytic expressions for the intermediate regime). The obtained theoretical normalized critical current as a function of magnetic flux is then matched to the experimentally extracted $I_c(B)$ by scaling the curve with a

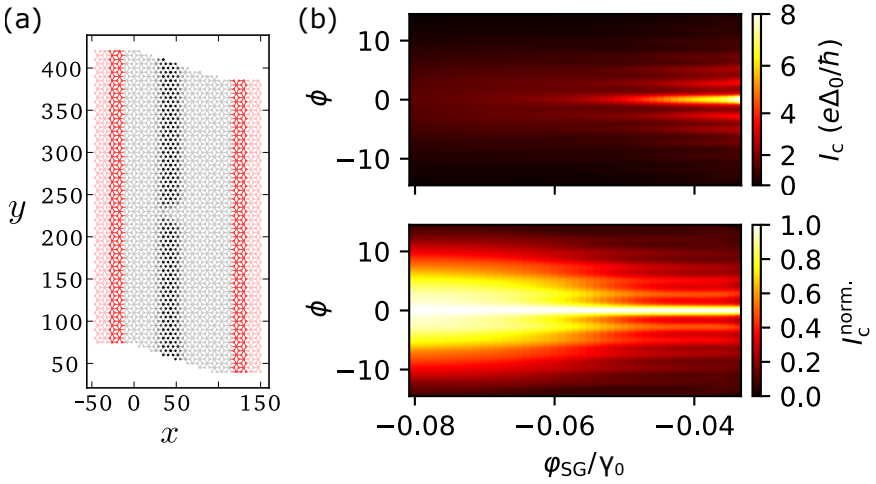

Figure 4.11: Numerical modeling of the magneto-interferometry measurements. (a) Schematic of the device setup for the numerical tight-binding calculations. (b) Calculated evolution of the magnetic interference patterns, plotting the critical current amplitude I_c in units of the superconducting gap $e\Delta_0/\hbar$ (top panel) and normalized $I_c^{norm.}$ (bottom panel) as a function of the SG strength φ_{SG} in units of tight-binding intralayer hopping parameter γ_0 and normalized magnetic flux $\phi = \Phi/\Phi_0$ in units of the flux quantum Φ_0 (for details see [Kra+18b]).

factor of the maximum critical current $I_c(0) = 43.5\,\text{nA}$ and employing a junction area of $\approx 6.1 \times 10^{-12}\,\text{m}^2$ with a total junction length of $\tilde{L} = L + 2\lambda_L \approx 1.9\,\mu\text{m}$, where $\lambda_L \approx 450\,\text{nm}$ is the London penetration depth. Figure 4.10b shows the resulting fit of the analytical model (magenta curve) to the extracted I_c (turquoise crosses) from the experimental interference pattern at $V_{BG} = 8\,\text{V}$ and $V_{SG} = -8\,\text{V}$ where the 1D constriction is formed.

Numerical tight-binding simulations

Additionally, numerical calculations using the Kwant package [Gro+14] are employed to qualitatively capture the evolution of the magnetic interference patterns due to the transition from a 2D-like to 1D confined supercurrent density. The resulting critical current I_c as a function of magnetic field B and φ_{SG} is shown in Fig. 4.11b. Here, φ_{SG} represents the strength of the on-site potentials introduced by the SG on respectively split-gated lattice sites in units of the intralayer hopping constant γ_0. Although a realistic and quantitative comparison with the experimental parameters is not possible, the similar trend of a beating pattern evolving into a monotonically decaying pattern is clearly observed. The good match between experiment and quasi-classical analytical model, as well as the qualitative agreement with the numerical tight-binding simulations are evidence of the confined supercurrent due to the induced QPC-like 1D constriction in our device.

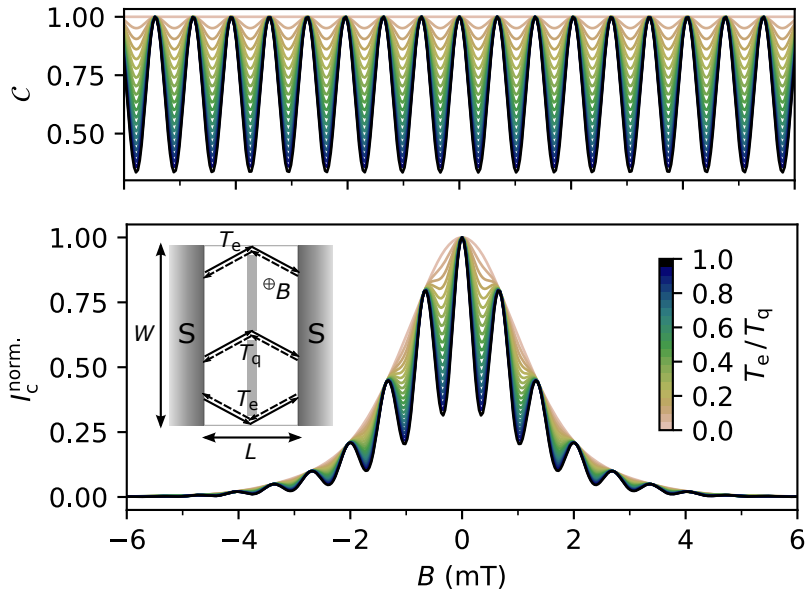

Figure 4.12: Effect of shunting currents on the magnetic interference pattern. Top panel: Correction factor $\mathcal{C}$ as a function of magnetic field for different ratios T_e/T_q (cf. Eq. 4.11). Bottom panel: Resulting interference pattern of the normalized critical current $I_c^{norm.}$ obtained by multiplication of our analytical expressions with $\mathcal{C}$. Inset: Schematic of the considered device setup, involving the QPC and additional edge channels with transmission T_q and T_e, respectively.

4.2.6 Effect of shunting currents

Finally, from the presented magneto-interferometry experiments, no obvious signs of induced currents through topological channels appearing due to AB stacking faults [Ju+15] or edge states [All+16; Zhu+17] are detected. In order to verify this assumption, we estimate what would be the effect of additional shunting currents on the magnetic interference pattern. For that, the analytical model presented in the previous subsection 4.2.5 is extended by allowing extra current paths at the sample edges to contribute to the total current, *i. e.* other than the current flowing through the constriction of the QPC-like confinement. The modified setup is displayed in the inset of Fig. 4.12. In the limits of $\phi \to 0$ and $\phi \to \infty$ one can then find the same expressions as in Eqs. 4.9 and 4.10, respectively, but multiplied with a correction factor $\mathcal{C}$ which reads as follows [Kra+18b]:

$$\mathcal{C} = \frac{|T_q + T_e \cos(\pi\phi)/2|}{T_q + T_e/2} \quad , \tag{4.11}$$

where T_q and T_e correspond to the transmission coefficients of the QPC and edge channels, respectively. Figure 4.12 (top panel) shows the variation of the correction factor $\mathcal{C}$ as a function of B (converted from ϕ as described in subsection 4.2.5) for various values of the ratio T_e/T_q. It can be seen that the correction factor is unity

at $T_e = 0$ (absence of shunting currents) but develops a significant amplitude modulation as $T_e/T_q \to 1$. Thus, the stronger the contribution of shunting currents, the larger the variation in $\mathcal{C}$. We note that with further raised T_e (not shown), the modulation of $\mathcal{C}$ increases with oscillation minima reaching zero for $T_e/T_q = 2$ (nodes of zero critical current in the pattern), and in the limit $T_e \gg T_q$ the correction factor displays a pattern resembling to the one of a superconducting quantum interference device (SQUID) as expected [Tin04].

The consequences of the correction factor $\mathcal{C}$ for the shape of the magnetic interference pattern are shown in Fig. 4.12 (bottom panel). On top of the original pattern determined by the 1D confinement ($T_e = 0$ and $\mathcal{C} = 1$, respectively) a periodic modulation appears due to the shunting currents at the edges of the sample ($T_e/T_q \to 1$). Indeed, the presence of additional currents develops a noticeable beating that can be distinctly monitored for smallest transmission coefficients $T_e \sim T_q/100$. Thus, it is clear that if one would be confronted with the contribution of currents flowing via the edges (or any other additional current path), the experimentally recorded magnetic interference pattern should be directly affected for, at least, current values down to a hundredth of the current through the constriction. Here, we have measured a confined supercurrent down to $\sim 20\,\mathrm{nA}$ and hence, the presence of shunting currents should be detectable down to 200 pA or less. In particular, this upper bound of any edge currents is about 25 times less than reported in [Zhu+17].

We note that at BG and SG values of $V_{BG} = 8\,\mathrm{V}$ and $V_{SG} = -7.6\,\mathrm{V}$ respectively, the induced displacement field of $D \approx 0.56\,\mathrm{V\,nm^{-1}}$ (*i. e.* one order of magnitude larger than in [Zhu+17]) opens a significantly large band gap $E_g \approx 85.4\,\mathrm{meV}$ (see Appendix B.7 for the estimate of the gap size). The absence of contributions from currents flowing via the sample edges could then possibly be explained by the edge-state localization in the case of strongly gapped BLG as reported in [Li+11], where the characteristic value of the localization length was found to be about tens of nanometers, *i. e.* much smaller than the split-gated region, and thus implying a strong suppression of edge currents.

4.3 Experimental results – Part B: Supercurrent guiding

In this second experimental part the confinement of the induced supercurrent is again studied by employing local band gap engineering in the BLG weak link due to applied displacement fields between an overall BG and a SG on top of the device. Though, unlike the sample in the previous section, here the SG electrodes are covering the

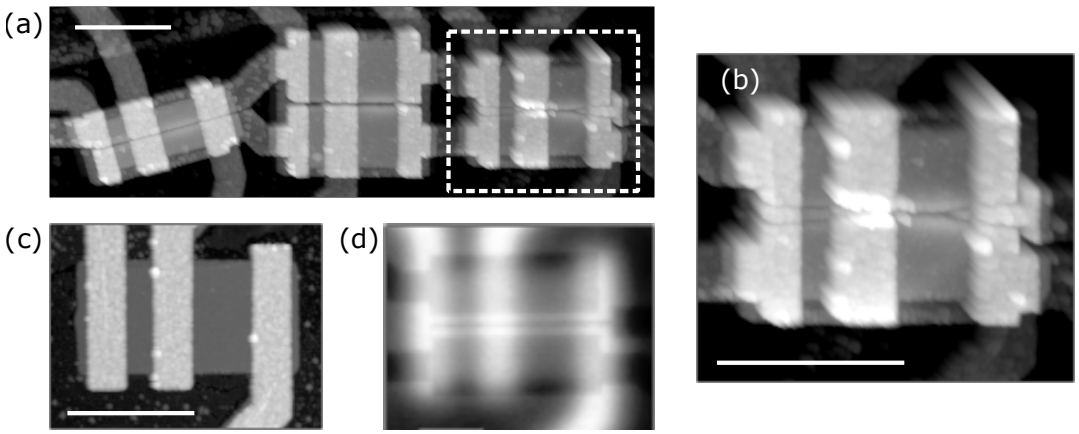

Figure 4.13: Long channel confinement – device design. (a) AFM image of the chip with a total of six devices. The sample is fabricated from an encapsulated BLG/hBN vdW heterostructure with thickness of top and bottom hBN $\approx$ 27 nm and $\approx$ 31 nm, respectively. The whole stack is placed onto a pre-patterned BG covered with 20 nm Al_2O_3 analogous to the previous QPC-like sample (see section 4.2). Additional top SG electrodes overlapping with the metal contacts are isolated by an extra ALD layer of $\approx$ 18 nm. The devices are designed with different junction width and/or length as well as different channel sizes between the top SG electrodes. A zoom-in picture on a pair of devices (white dashed box) is shown in (b). All presented results in this chapter are based on the shorter (left) junction of these two devices. Its width is $W = 1.8\,\mu$m and length $L = 0.5\,\mu$m with a channel of width $w = 300$ nm. Originally in this pair of devices, an additional TG finger gate (100 nm) in-between the two SG electrodes is designed, splitting the channel in two. Unluckily, this gate electrode is broken but remains unconnected (floating), as can be seen in the image. For a better grasp of the device architecture, panels (c) and (d) show the device prior TG deposition and the developed PMMA mask for TG metal lift-off, respectively. The scale bar in all images is 2 µm.

full distance between the superconducting contacts. Importantly, in this geometry the supercurrent through the weak link in the direction normal to the leads is considerable uniform allowing to test the simple Dynes-Fulton approach [DF71] as discussed in section 4.1. The AFM image of the device is depicted in Fig. 4.13, with the geometry details given in the caption.

The experiments are performed at a base temperature $\approx$ 25 mK (cooldown #26 in the cryostat logbook) and measurements in the normal state are due to applying a perpendicular magnetic field of $B = 20$ mT. The critical current is extracted with respect to the position of the maximum resistance peak, marking the transition from supercurrent to dissipative current. More precisely, the value of the current is evaluated at a third of the resistance difference between resistance minimum r_0 (at $I = 0$) and resistance peak r_{max}, multiplied with a correction factor $f = (1 + r_0/100)^{-1}$ to account for resistive, *i. e.* slanted or rounded, steps in the IV curves: $r_{\mathrm{c}} = r_0 + (r_{\mathrm{max}} - r_0)/3 \rightarrow I_{\mathrm{c}} = f \times I(r_{\mathrm{c}})$.

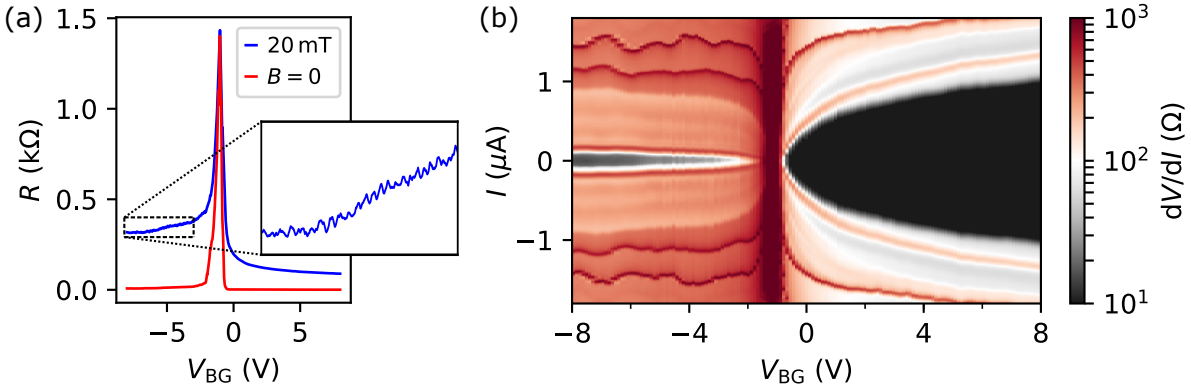

Figure 4.14: Basic characterization of sample B. (a) Resistance curves versus V_{BG} for both normal state (blue) and superconducting state (red) at $V_{SG} = 0$, *i. e.* considerably uniform doping in the sample. The inset shows a zoom-in on the visible conductance oscillations due to Fabry-Pérot interferences on the *p*-side as marked by the black dashed box. (b) Differential resistance as a function of V_{BG} and current I at the same $V_{SG} = 0$.

4.3.1 Initial device characterization

Figure 4.14a shows BG sweeps at approximately uniform overall charge carrier density for both normal state (blue) and superconducting state (red), respectively. Analogous to the other presented device (see section 4.2.1), in the normal state a larger resistance is observed on the *p*-side than on the *n*-side due to the formation of *pn*-junctions at the interfaces to the metal contacts upon induced hole doping. The clearly visible conductance oscillations (see inset) are thus attributed to the Fabry-Pérot interferences arising in the formed cavity between the contacts as a signature of the ballistic transport in the sample [SRL08; YK09; Ric+13; Var+14b; Du+18] (also see Appendix C.1). The presence of these unintentionally induced *pn*-interfaces is also apparent in a small but non-vanishing residual resistance ($< 10\,\Omega$) in the superconducting state, whereas on the electron side the resistance drops to zero. The contact resistivity on the electron side excluding the quantum resistance is estimated[10] as $\rho_C \approx 52\,\Omega\mu m$ and the residual charge carrier density of order $n_{res} \sim 10^{10}\,cm^{-2}$.

The proximity-induced supercurrent of the approximately uniform 2D junction tuned by the BG is observed in Fig. 4.14b, showing a map of the differential resistance as a function of V_{BG} and current I. While at charge neutrality the supercurrent is fully suppressed, the extracted values of the critical current at high charge carrier density ($|n| \approx 3.3 \times 10^{12}\,cm^{-2}$) for both *n*- and *p*-type doping are $I_c = 1.04\,\mu A$ at

[10] At $V_{BG} = 8\,V$ corresponding to $n \approx 4.3 \times 10^{12}\,cm^{-2}$ the quantum resistance $R_Q \approx 31\,\Omega$, and subtracted from the measured resistance $R = 89\,\Omega$ this gives an estimate for the contact resistance $R_C = (R - R_Q)/2 = 29\,\Omega$.

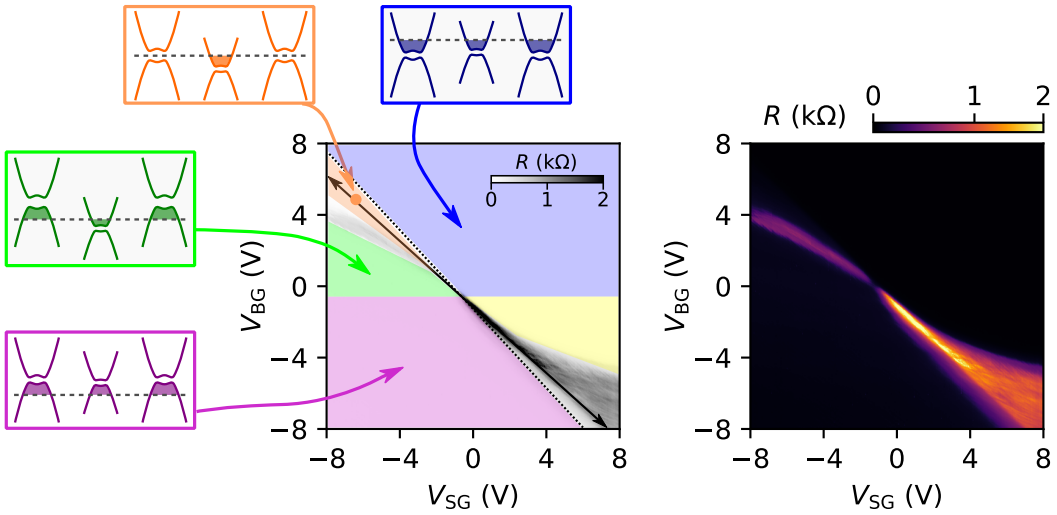

Figure 4.15: Gate-gate-map of the long channel confinement. Right: Color map of the resistance in the superconducting state as a function of V_{SG} and V_{BG}. Left: Same map in gray scale with different regions highlighted due to false coloring. Respective band structure profiles across the junction width are illustrated in the extra panels. The region of interest for studying the confined supercurrent is marked by the additional colored (orange) dot.

$V_{BG} = 6\,\mathrm{V}$ and $0.11\,\mu\mathrm{A}$ at $V_{BG} = -8\,\mathrm{V}$ (*i. e.* I_c being about one order of magnitude smaller on the hole side at comparable charge carrier densities) or the corresponding $I_c R_n = 0.93\Delta_0/e$ and $0.33\Delta_0/e$ (with $R_n = 96\,\Omega$, $317\,\Omega$ and superconducting energy gap $\Delta_0 \approx 107\,\mathrm{eV}$ extracted from the position of $n = 2$ MAR), respectively.

Likewise to the QPC-like confinement, the mediated supercurrent can be spatially tuned by means of local band gap engineering due to the induced displacement fields from BG and SG. Figure 4.15 displays the respective resistance map in the superconducting state as a function of V_{SG} and V_{BG}. Here, the effect of the bent resistance maximum appears even more dramatic, since the induced *npn*- or *pnp*-junctions in the bipolar doping configurations form lengthwise to the transport direction of charge carriers (*i. e.* in particular no barrier). The junction thus remains superconducting nevertheless for almost any gate condition, whereas only along the bent line the device becomes resistive when the channel is closed by the stray fields while the split-gated sides are still pinched off either due to the induced electronic band gap or (non-)transparent *pn*-interfaces (see the depicted spatial band structure schematics). From the resistance map in the superconducting state, we can again identify the gate region of interest, where the supercurrent is expected to be guided within the long channel confinement. We note, that while the bent resistance is observed for both electrons and holes, the *p*-doped channel regime remains resistive similar to the QPC-like confinement. In the following, the spatial shaping of the supercurrent is probed once more by magneto-interferometry measurements.

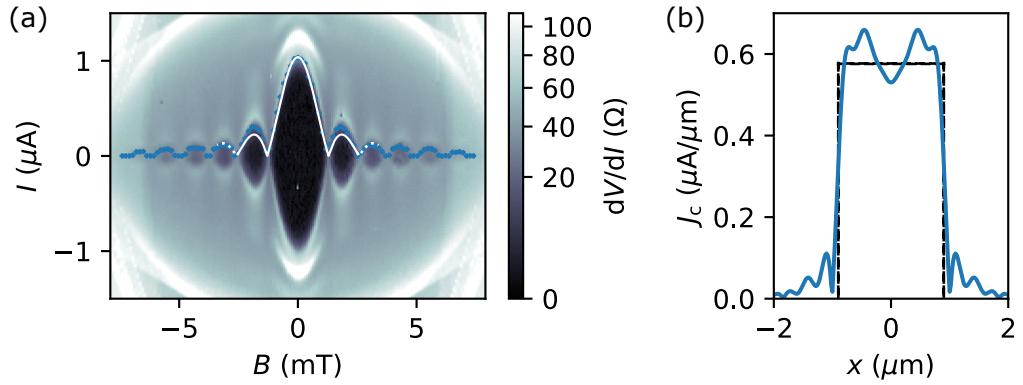

Figure 4.16: The Fraunhofer pattern. (a) Differential resistance as a function of magnetic field B and current I at constant $V_{BG} = 6\,V$ and $V_{SG} = 0$, showing the superconducting magnetic interference pattern of the approximately uniform 2D BLG weak link. The extracted critical current values (every 2nd shown) are marked by the blue crosses. The white line indicates a pattern given by the sinc-function of a single-slit Fraunhofer interference. (b) Reconstructed supercurrent density distribution following the Dynes-Fulton approach. The black dashed lines denote a box-like (*i. e.* uniform) density profile with constant $J_c^{max} = I_c(0)/W$ within the range $-W/2 \leq x \leq +W/2$ of the sample edges.

4.3.2 Dynes-Fulton approach

2D junction

Figure 4.16a presents the superconducting magnetic interference pattern measured at $V_{BG} = 6\,V$ and $V_{SG} = 0$, *i. e.* at high charge carrier density with approximately uniform overall doping. The observed pattern reveals a sinc-function-like behavior, indicated by the white line[11], in close resemblance to the well-known Fraunhofer interference in short wide junctions analogous to the single-slit interference in optics experiments [Tin04]. Though, we note a minor difference, that is the experimental first lobe appears more pronounced compared to the white curve of the sinc-function.

For a further elaboration of the experimental interference pattern, we perform the Dynes-Fulton analysis by employing the inverse Fourier integral over the extracted critical current data points $I_c(B)$ (blue crosses) in order to reconstruct the supercurrent density distribution (see section 4.1). We note that $I_c(B)$ does not feature any lifted lobes but each minimum goes strictly to zero, making it not necessary to recover first the phase information, *i. e.* the real and imaginary contributions of the complex critical current. The resultant supercurrent density profile is plotted in Fig. 4.16b, revealing a center-symmetric distribution due to the purely real interference pattern of the critical current as a function of magnetic field. For comparison, a box-like (*i. e.* uniform)

[11] The sinc-function is plotted by fitting to the maximum critical current $I_c = 1.04\,\mu A$ at $B = 0$ and employing the effective junction area $\tilde{A} = 0.9 \times 1.8\,\mu m^2$ for aligning the position of the first minimum.

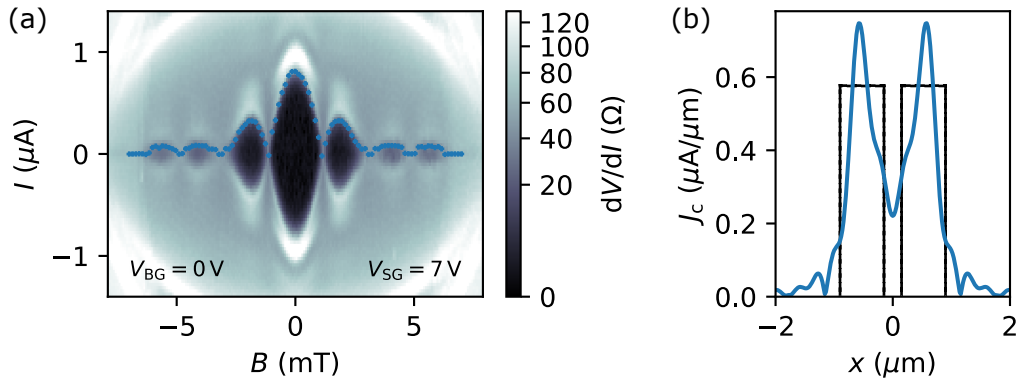

Figure 4.17: Enhanced supercurrent density underneath the split-gates. (a) Superconducting magnetic interference pattern at $V_{BG} = 0$ and $V_{SG} = 7\,V$. Blue crosses denote the extracted critical current values (every 2nd datapoint is plotted). (b) Corresponding supercurrent density distribution obtained due to the Dynes-Fulton technique. The spatial extend of both SGs is visualized by black boxes, split by the $w = 300\,nm$ channel.

supercurrent density profile is additionally plotted, which is given by a constant $J_c^{max} = I_c(0)/W$ within the spatial extend of the sample, but zero outside. Indeed, the major contribution of the obtained density profile appears to be well-positioned within the physical boundaries of the junction width, but showing minor parts of the current spilling outside the sample as a typically observed artifact of the Dynes-Fulton approach [Hui+14]. Moreover, the reconstructed profile, being only roughly constant, features rather enhanced supercurrent densities underneath the split-gated parts of the sample. Thus, it can be concluded that at the applied $V_{SG} = 0$ the sample is not exactly at charge neutrality but slightly doped. Recalling the beforehand described deviation from the ideal sinc-function, the small but finite doping and consequently increased supercurrent density underneath the SGs is directly reflected in the appearance of raised first side-lobes.

Towards SQUID-like pattern of a double-slit junction

In a next step, the applied gating condition is reversed, *i. e.* $V_{BG} = 0$ and $V_{SG} = 7\,V$. In this case, it is expected that the major part of the supercurrent is flowing underneath the SG electrodes, while only a smaller contribution remains in the central channel region.[12] The corresponding superconducting magnetic interference pattern is shown in Fig. 4.17a, exposing increased first side-lobes indicative of a pair of spatially split supercurrent channels with maximal amplitude. Indeed, the obtained supercurrent

[12] The supercurrent density in the channel itself can not be fully suppressed which was originally designed with the additional but unfortunately disconnected/broken TG finger gate between the two SGs (see Fig. 4.13).

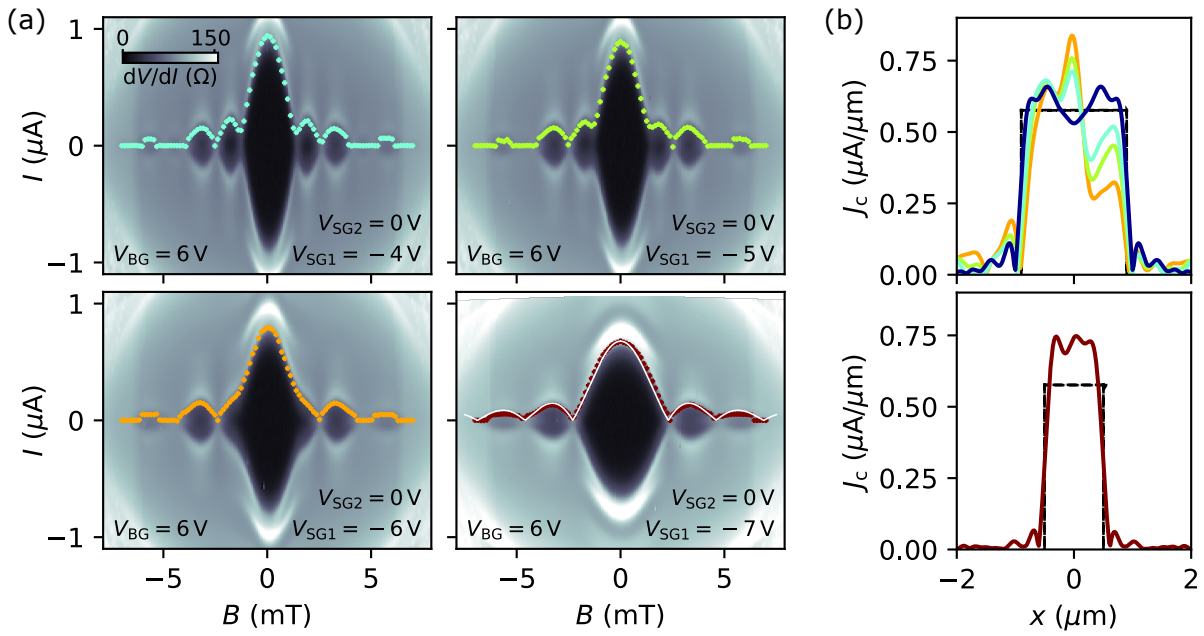

Figure 4.18: Spatial shaping of the supercurrent density with a single split-gate. (a) Four panels of superconducting magnetic interference patterns tuned by only one SG electrode. The respective gate conditions are given within each plot and the color bar is given for all plots together in the top left panel. The extracted values of the critical current for each data set are plotted as colored dots. The additional white curve in the bottom right panel reflects a sinc-function (see main text). (b) Resulting supercurrent density distributions from the Dynes-Fulton method. Top: Profiles for the first three patterns together with the curve at $V_{SG} = 0$ (dark blue) as presented in Fig. 4.16. Bottom: Profile of the last (lower right) panel with given boundaries corresponding to an effectively halved junction width.

density distribution in Fig. 4.17b features two peaks positioned within the SG regions as indicated by the black lines, whereas in the non-split-gated channel a strongly reduced supercurrent density is observed. The smaller but non-vanishing current within the channel itself can be mainly attributed to the induced charge carriers due to the stray-fields developed by the SGs. Note that in the case of a fully suppressed current inside the channel, the junction becomes effectively double-slit-like and $I_c(B)$ would trend into a SQUID-like interference [Tin04].

Half-gate tuning – Spatial shaping of the supercurrent by the use of a single split-gate electrode

The two so far discussed scenarios represent symmetric gating conditions, resulting in problems of purely real critical current interference patterns to be solved. At this point, we test the reliability of the Dynes-Fulton technique under asymmetric conditions, *i. e.* by using only one of the SG electrodes, making it necessary to also consider the imaginary contribution of the complex critical current due to the odd part of the supercurrent density distribution. Figure 4.18a presents superconducting magnetic interference patterns at constant $V_{BG} = 6\,V$ and increasingly negative

$V_{SG1} = -4\,V$, $-5\,V$, $-6\,V$ and $-7\,V$ while the other $V_{SG2} = 0$. We notice a vanished third side-lobe, as well as a continuous lifting of the first minimum. As a consequence thereof, the imaginary supercurrent contributions becomes larger and larger as the first side-lobe is getting "swallowed" by the central main (zeroth) lobe. This evolution is directly reflected in the converted supercurrent density profiles, shown in Fig. 4.18b, where a progressive reduction is observed in one half of the device.

At last, *i. e.* for $V_{SG1} = -7\,V$, the pattern again develops into a sinc-function-like beating of the critical current as a function of magnetic field, although with an observed approximate doubling of the oscillation period (see the white sinc-function curve using an effective junction area $\tilde{A} = 0.9 \times 1.0\,\mu m^2$, *i. e.* approximately half compared to the case at $V_{SG} = 0$). In fact, the reconstructed corresponding supercurrent density profile in Fig. 4.18c fits now into an effective junction that is cut down to (almost) half of its original width, *i. e.* more precisely the width of the unused SG (0.75 µm) plus most of the channel ($\approx 250\,nm$) remain as new effective junction width of about $\approx 1\,\mu m \sim W/2$ (note that only small parts of the channel are suppressed as well due to stray fields of the active SG). We note that the shown distribution is centered with respect to the origin, but not shifted to the actual spatial position within the overall device. This is due to the fact, that the supercurrent is eventually quenched in one part of the device, giving rise to a new junction center as the reference point. The reappearance of the sinc-function-like Fraunhofer pattern accompanied with a nearly doubling of the oscillation period thus demonstrates a full suppression of the supercurrent underneath the employed SG, resulting in a newly formed homogeneous junction on the respective other half of the device.

Supercurrent guiding in the long channel confinement

Now, we turn to the long channel confinement regime induced by the combination of BG and both the SG electrodes, once again probed by means of superconducting magneto-interferometry measurements. The obtained interference patterns are shown in Fig. 4.19a, measured at constant $V_{BG} = 6\,V$ and progressively negative $V_{SG} = -4\,V \rightarrow -7\,V$, with the respective gate conditions marked by colored dots in the gray-scale gate-gate-map in Fig. 4.19b. The monitored evolution reveals separately to the overall reduction of the maximum supercurrent a progressive disappearance of odd-numbered side-lobes concomitant with the growing of even-numbered side-lobes. After the complete vanishing, the interference pattern of the critical current as a function of magnetic field starts to get lifted, *i. e.* minimums not reaching to zero, until finally trending into a monotonically decaying pattern at $V_{SG} = -7\,V$ indicating the imposed supercurrent confinement.

Without much knowledge about the junction geometry, an approach following the Dynes-Fulton method would treat these patterns by considering a large contribution

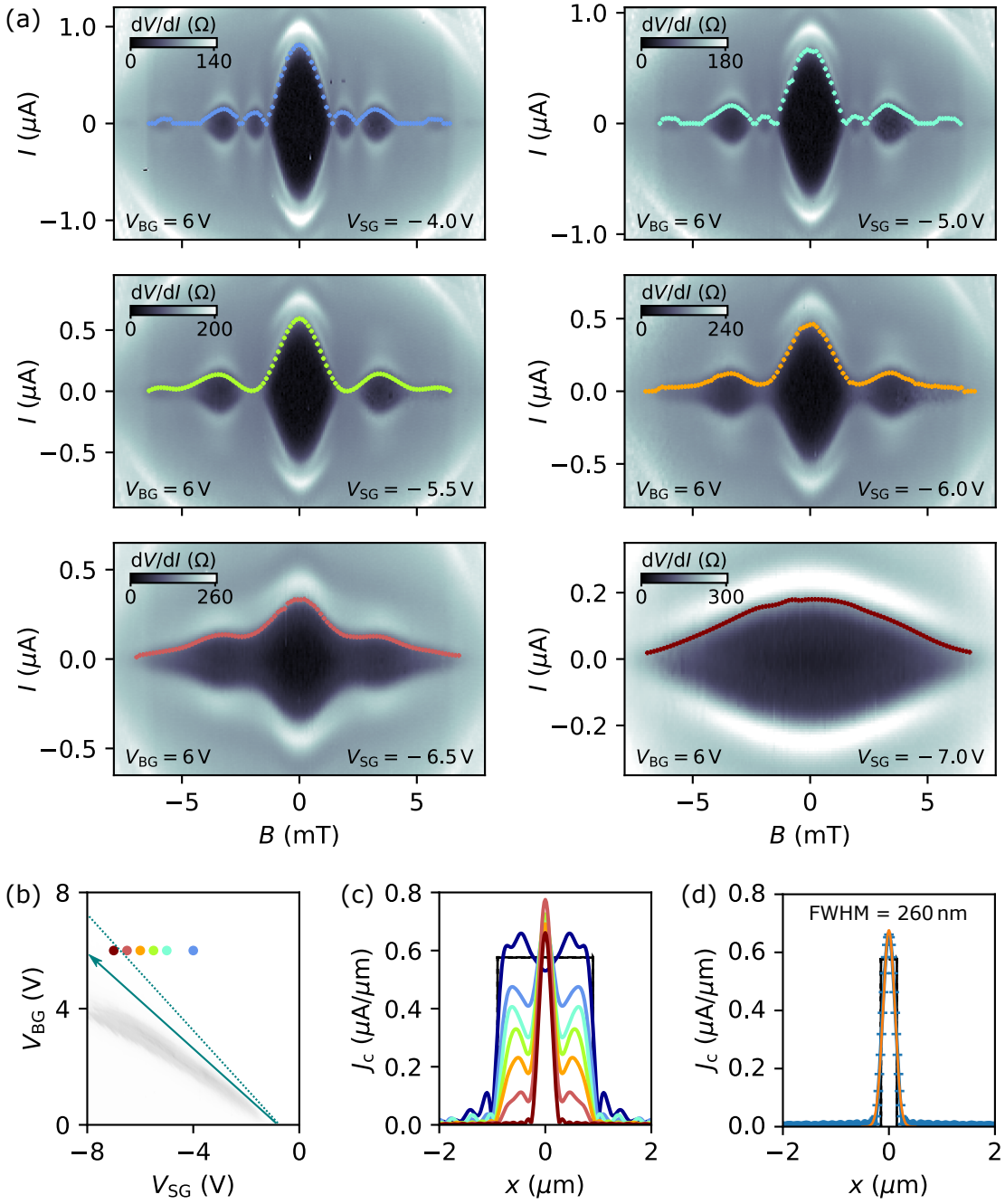

Figure 4.19: Long channel confinement. (a) Different superconducting magnetic interference patterns tuned by the SG (see labeled gate conditions in each panel). (b) Grey-scale gate-gate-map (see Fig. 4.15) with the respective gate conditions of the interference patterns marked by colored dots. (c) Corresponding reconstructed supercurrent density profiles together with the curve of $V_{SG} = 0$ (dark blue; see Fig. 4.16). (d) Gaussian fit (orange) to the supercurrent density distribution in the case of fully developed channel confinement at $V_{SG} = -7\,V$ (here shown as blue crosses, while in the former panel as maroon colored curve). The full width at half maximum (FWHM) of the fit is given in the panel and the depicted channel boundaries (black) correspond to the designed channel width w.

of an odd (*i. e.* asymmetric) supercurrent density component, requesting in turns large imaginary parts contained in the observed patterns with sizable node lifting. However, this seems to be a rather unlikely solution, regarding the fact of the hitherto observed symmetric tuning of the supercurrent by means of the SG. In that sense, we perform the Fourier analysis of the raised interference patterns (*i. e.* $V_{SG} = -6.0\,V$ and $-6.5\,V$) without flipping of alternative lobes but rather treat $I_c(B)$ as a purely real function of the single continuous lobe with modulated amplitude, which admittedly seems somewhat arbitrary. Nevertheless, as it will be seen, this yields the supposedly correct supercurrent density profile, which on the other hand is only possible with knowledge about the expected distribution in the first place.

Figure 4.19c shows the respective calculated supercurrent density profiles following the Dynes-Fulton approach, being more and more suppressed underneath the SGs. At $V_{SG} = -7\,V$, the Fourier transform of the monotonically decaying interference pattern features a single sharp peak at the center of the junction, *i. e.* the channel between the SG electrodes, with a magnitude comparable to the supercurrent density in the approximately uniform junction. In fact, assuming similar supercurrent densities for the two cases, the ratio of the presumably confined critical current $I_c \approx 0.18\,\mu A$ at $V_{SG} = -7\,V$ and the (considerable homogeneous) 2D critical current $I_c \approx 1.04\,\mu A$ at $V_{SG} = 0$ (for the given $V_{BG} = 6\,V$) yields in a naive estimate the effective junction width $0.17 \times W \sim 300\,nm$. For a more profound analysis of the spatial extend of the confined supercurrent, the resultant supercurrent density profile is fitted by a Gauss function, which is shown in Fig. 4.19d. From the fit, we find a full width at half maximum of $\approx 260\,nm$ in good agreement with the lithographically defined channel width $w = 300\,nm$ (depicted by the black frame), providing evidence for the 1D confined supercurrent within the electrostatically induced channel.[13]

We note, that similar results can be obtained by doing the analysis the other way round, *i. e.* starting from an assumed supercurrent density distribution and calculate the corresponding interference pattern of the critical current as a function of magnetic field by performing the Fourier transform as given in Eq. 4.5b. The comparison of calculated with experimentally obtained interference pattern is presented in Fig. 4.20, where we consider box-like supercurrent density profiles across the junction width. Nonetheless, despite this most simplistic approach, the main qualitative features (as e. g. the disappearance of odd-numbered side-lobes and the lifting of the entire interference pattern) are well captured. Yet, it is important to note that in both ways, either predicting the resultant superconducting magnetic interference pattern or

[13] The spatial resolution of the here performed reverse Fourier transform for the applied magnetic field range of $-8\,mT \rightarrow +8\,mT$ and the given effective junction length $0.9\,\mu m$ is $\Delta x \lesssim 150\,nm$ (see section 4.1), being thus sufficient in order to resolve the supercurrent confined to the channel w.

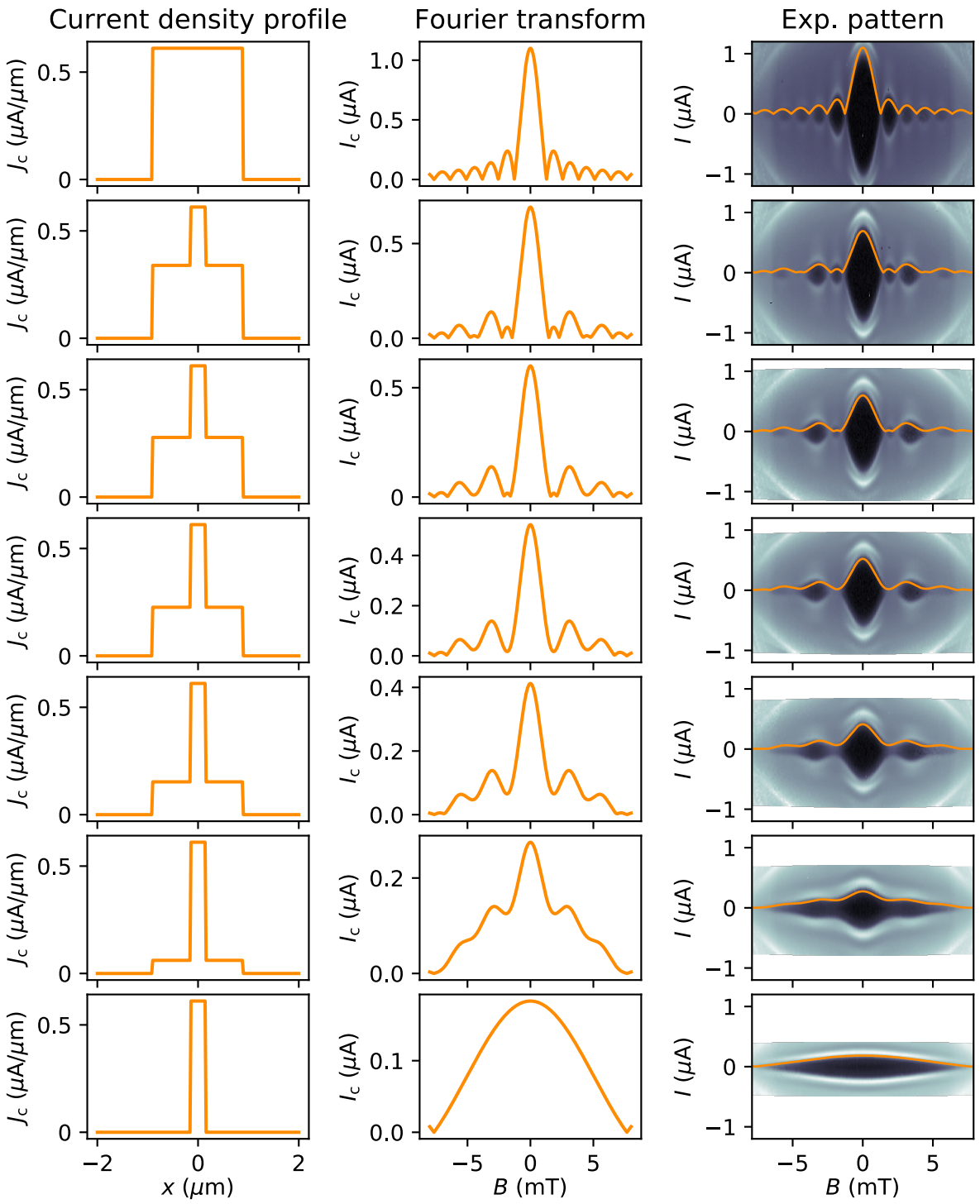

Figure 4.20: Comparison of calculated and experimentally obtained interference patterns. Left column: Considered supercurrent density profiles for different gate conditions in the order $V_{SG} = 0$, $-4.0\,V$, $-5.0\,V$, $-5.5\,V$, $-6.0\,V$, $-6.5\,V$, $-7.0\,V$ at constant $V_{BG} = 6\,V$, employing a simplistic box-function-like distribution. Middle column: Resulting interference patterns of the critical current as a function of magnetic field according to the Fourier transform in Eq. 4.5b. Right column: Plots of the experimentally obtained superconducting magnetic interference patterns (cf. Fig. 4.19) overlaid by the respective interference curves presented in the middle column.

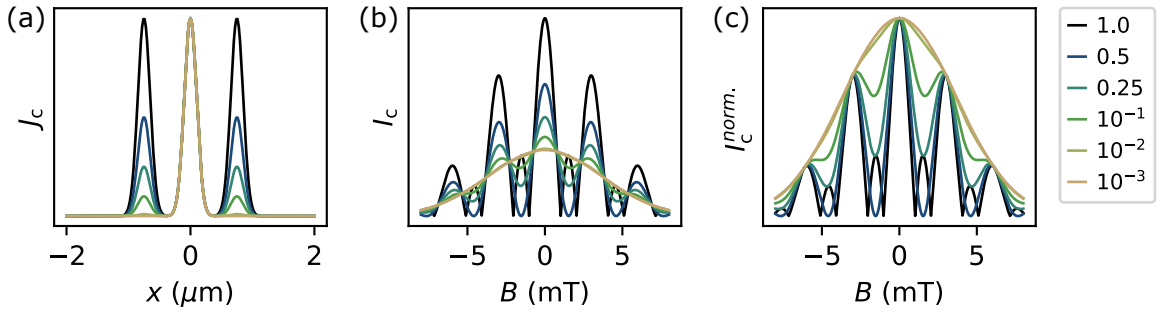

Figure 4.21: Effect of shunting currents. (a) Considered supercurrent density profiles for different strengths of additional current paths at the edges of the sample to the 1D confined supercurrent in the center. The legend to the employed color code is given at the right-hand side of the figure. (b) Interference patterns of the critical current as a function of magnetic field B obtained from Fourier transform (Eq. 4.5b). (c) Corresponding normalized critical current with respect to the maximum at $B = 0$ for each curve.

reconstructing instead the supercurrent density profile, are based on several assumptions (see discussion in section 4.1) which need to be considered when interpreting the results. For a truly quantitative analysis of the supercurrent density distribution from measured superconducting magnetic interference patterns a more complete and sophisticated modeling is required [Hui+14].

Effect of shunting currents

In this final paragraph, we make a validity check for the robustness of the claimed supercurrent guiding in the gate-defined channel. For that, we again estimate the impact of additional supercurrent paths shunting the confinement. Figure 4.21a shows fictional supercurrent density distributions allowing additional current paths at the edges of the sample with a relative amplitude to the 1D confined supercurrent in the junction center as given by the legend at the right-hand side of the figure. The resultant interference patterns of the (normalized) critical current as a function of magnetic field B are plotted in Fig. 4.21b, c. It can be noticed, that the effect of the considered shunting currents is clearly visible down to a factor of $\sim 10^{-2}$, yielding an upper limit of possible shunting currents $\lesssim 1\,\mathrm{nA}$. Although this limit is slightly larger than in the QPC-like case, it is still one order of magnitude smaller than the reported values in [Zhu+17] and thus, substantiating the demonstrated electrostatically induced channel supercurrent confinement based on the spatially full suppression of the supercurrent due to band gap engineering.

4.4 Conclusion

In this chapter, the tailoring confinement of an induced supercurrent in BLG weak links has been explored via superconducting magneto-interferometry measurements in two different local gating structures, *i. e.* a QPC-like confinement and long channel confinement.

QPC-like confinement A full monitoring of the supercurrent, both spatially and in amplitude, has been demonstrated by means of spatial band gap engineering due to the employed combination of overall BG and locally defined SG structure on top of the device. In this dual-gated geometry, an unusual resistance gate-gate-map is observed where the measured maximum resistance does not increase continuously along the displacement field line as typically reported in BLG *pnp*-junction devices. This trend becomes particularly visible in the superconducting state due to the region of zero resistance appearing at maximal displacement field and the Fermi level being presumptively positioned in the induced electronic band gap, which is indication of a finite supercurrent flowing through the formed constriction. Further investigations by out-of-equilibrium measurements revealed the effect of the induced confinement on the supercurrent amplitude. Finally, the spatial tuning of the supercurrent could be monitored by the employed superconducting magneto-interferometry. In these measurements, the observed evolution of the interference patterns directly reflects the transition from a 2D supercurrent to a 1D confined supercurrent, in agreement with the results of the provided analytical and numerical modeling.

Long channel confinement Similar results as in the QPC-like confinement have been obtained. Though, the major difference between these two device geometries is the applicability of the Dynes-Fulton techniques. Due to the approximately uniform supercurrent density profile along the direction normal to the superconducting electrodes in the long channel confinement, a simplistic analysis of the supercurrent flow in the device is possible by solving the Fourier integral relating the supercurrent density distribution to the interference pattern of the critical current as a function of magnetic field. The ease of employing superconducting magneto-interferometry measurements for monitoring spatially the supercurrent density distribution is demonstrated by the consistency of the reconstructed profiles with respect to sample geometry and gate conditions, as well as the good qualitative match between predictively calculated and experimentally measured patterns for a number of supercurrent density profiles (*i. e.* different gate conditions).

In both presented geometries, no signs for the presence of shunting currents have been detected, highlighting the possibility to employ local band gap engineering in BLG to design electrostatically induced nanoscale constrictions.

5 Gate-defined quantum point contact in bilayer graphene

In chapter 4 a 1D QPC-like confinement without edge currents has been demonstrated by investigating the proximity-induced superconductivity in magneto-interferometric measurements. Though, in the hitherto presented sample geometry consisting of a global BG and the local SG electrodes a study of conductance quantization in the normal state due to 1D subband formation was not possible as the confinement is based on the combined use of both gates and thus could not be tuned independently. Here, an overall TG is added providing an additional tuning knob with which it is possible to fully control band structure and confinement, and therefore to observe quantized conductance. The chapter starts with a literature review (5.1) covering a brief introduction to QPCs in general, as well as a summary about different approaches undertaken in order to design constrictions in graphene-based devices. In the results part (5.2) the quantization of conductance is presented containing the tuning of all quantum degrees of freedom in a BLG QPC, *i. e.* spin, valley and mini-valley. Furthermore, signatures of a 0.7 structure are discussed. Finally, the chapter is concluded with a summary (5.3).

5.1 Literature review

A QPC is a ballistic narrow constriction of width W_{QPC} comparable to the Fermi wavelength λ_{F} coupled adiabatically to two wider reservoirs [BH91b; HBW92]. Then, owing to the lateral confinement in the quasi 1D channel, the charge carrier transport is due to discrete transverse modes arising from the size-quantization of the electronic wave function [Büt90]. Importantly, the current $I \propto \int \mathrm{d}E\rho(E)v(E)T(E)$ carried by a 1D subband is mode independent as the energy dependence is canceled in the product of velocity $v(E) \propto \mathrm{d}E/\mathrm{d}k_y$ (k_y is the longitudinal wave vector) times 1D density of states $\rho(E) \propto (\mathrm{d}E/\mathrm{d}k_y)^{-1}$ and transport can be described by the Landauer-Büttiker formalism [Dat95]:

$$G = \frac{ge^2}{h}\sum_n^N T_n \quad , \tag{5.1}$$

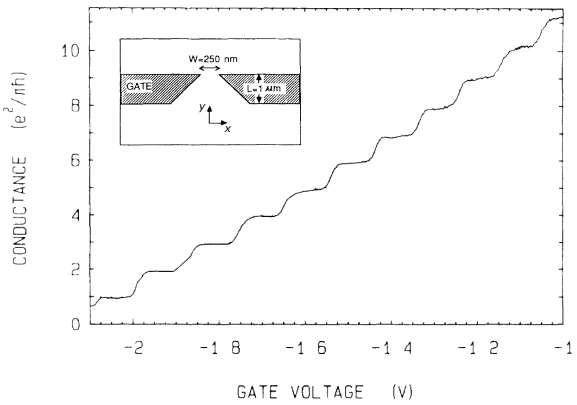

Figure 5.1: Quantized conductance of a QPC defined in the 2DEG of a GaAs/AlGaAs heterojunction. The image shows the original reported results in [Wee+88a], where the conductance data is obtained by subtracting a series resistance from the measured resistance. The inset shows their QPC layout (the coordinate axis labeling has been changed as a matter of consistency).

where the conductance is given by the sum over transmission probabilities T_n of each 1D subband n. For perfect transmission this simplifies to the quantized conductance

$$G = N\frac{ge^2}{h} \quad , \tag{5.2}$$

where all populated 1D subbands contribute equally to the overall conductance by the conductance quantum $G_0 = ge^2/h$ with g-fold degeneracy.

The quantization of conductance in a QPC was first reported in 1988 independently by two groups [Wee+88a; Wha+88], where the constriction is formed in the two-dimensional electron gas (2DEG) of a GaAs/AlGaAs heterostructure via the electrostatically induced confinement potential due to a SG [Tho+86; Zhe+86; Ber+86]. By applying a negative voltage, electrons are depleted underneath the gates allowing transport only through the QPC channel and upon the narrowing of the constriction with increasingly negative voltage the number of transverse modes fitting into the channel is reduced [BP10]. The resulting staircase of quantized conductance of the original experiment by van Wees et al. [Wee+88a] is shown in Fig. 5.1.

Since then, quantized conductance has been explored in a large variety of 1D ballistic systems. While in the vast majority of studied materials conductance quantization appears in units of the twofold-degenerate conductance quantum $2e^2/h$, where the factor of 2 is due to the spin degeneracy, only few involve an additional valley degree of freedom such as Si/SiGe heterostructures [Tob+95; Wie+02; Sca+06; Gos+07; McG+10], AlAs quantum wells [Gun+06] or carbon nanotubes [Bie+05]. Yet, while spin and valley degeneracy should give rise to conductance steps of $4e^2/h$, deviations from this expected quantized value have been typically observed and usually explained by the lifting of the valley degeneracy because of confinement. [Kra+18a]

Graphene represents another material with fourfold degeneracy and realizing quantum confinement in ballistic graphene nanostructures has been a targeted goal early on. The formation of 1D subbands and conductance quantization has been investigated and reported in graphene nanoribbons [Lin+08; Lia+10; Tom+11; Ter+16; Som+17; Car+18], or in (gate-defined) constrictions based on BLG devices [AMY12; Goo+12; Drö+12; Lee+18], but most commonly lifted degeneracies or not well-positioned conductance plateaus have been observed while lacking a clean pinch-off characteristic. One of the reasons explaining the noticeable deficiencies are the unpredictable transport properties due to rough edges in etched graphene nanodevices [Bis+16]. On the other hand, while such uncontrollable device properties may not play a role in the reported quantum confinement induced by electrostatic gating in BLG, limiting aspects are due to leakage currents below the SGs arising from hopping transport in a non-homogeneous electronic band gap for devices on a Si/SiO_2 substrate (probably even if encapsulated between hBN) or due to a too small gap in suspended devices.

Importantly, as demonstrated in the previous chapter, an outright electrostatic confinement is successfully induced in our device based on the BLG/hBN heterostructure on a pre-patterned BG with a deposited Al_2O_3 dielectric via ALD and with a local top SG, although 1D subband formation and quantized conductance was not observed since the channel itself could not be independently depopulated. In respect thereof, here we propose an extended device architecture with additional overall TG as presented in the following section.[1]

5.2 Experimental results

The measurements are based on the device in which the QPC-like supercurrent confinement has been established (see section 4.2 in the previous chapter), but here with an additional subsequently added overall Ti/Cu/Al TG (the Al serves as a capping layer preventing the Cu from oxidation).[2] The TG is isolated from SG and contact

[1] We note that in a double split-gated (top and bottom) BLG device gate-controlled topological conducting channels have been realized with effectively suppressed current underneath the gates [Li+16]. Meanwhile, also the use of a graphite BG has been demonstrated to provide clean electronic band gaps in gate-defined BLG nanostructures [Ove+18a] and employed as a triple-gate structure with two TG layers charge carrier confinement has been realized in a split-gated geometry [Ove+18a] or as QDs [Ban+18; Eic+18a; Eic+18b].

[2] The presented results are partly based on [Kra+18a]; a complementary work of another group with similar device structure but the TG only covering the channel region of the QPC has been published in the same issue of the journal [Ove+18b].

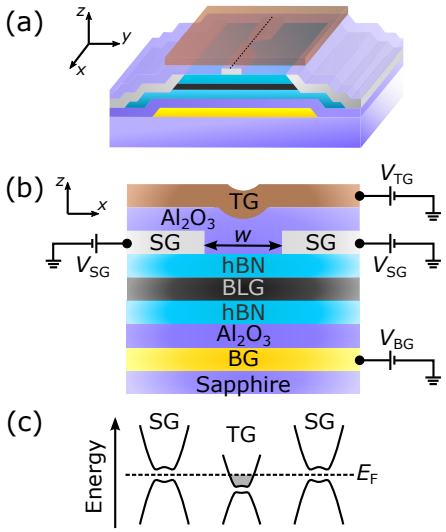

Figure 5.2: Device schematic and working principle of the gate-defined BLG QPC. (a) 3D sketch of the device (see Fig. 4.3 for details, but here with additional TG). (b) Cross-section through the constriction as indicated by the dashed line in panel (a). (c) Corresponding band structure diagram when the device is operated as QPC.

electrodes due to an extra layer of Al_2O_3 (30 nm) deposited by ALD covering the entire sample. A schematic of the device is shown in Fig. 5.2a, b. By employing the combination of all three gates BG, SG and TG the successful operation of an electrostatically induced QPC in BLG is demonstrated. In applied in-plane and out-of-pane magnetic fields the lifting of spin and valley degeneracy is studied.

The experiments are conducted in three cooldown cycles at base temperatures $\lesssim 20$ mK, unless specified otherwise. Data of different cooldowns is referenced in the text as CD#3, CD#4 and CD#5 (corresponding to recorded cooldowns #28, #29 and #30 of the cryostat logbook, respectively). The presented normal state data is due to an applied perpendicular magnetic field $B = 20$ mT. Measurements with in-plane magnetic field orientation are obtained in a separate cooldown (*i. e.* CD#5) than the out-of-plane magnetic field measurements for changing the rotation of the sample holder inside the magnet in order to align the graphene plane to the magnetic field direction. The in-plane angle with respect to the confinement axis is estimated at $\approx 45°$. If not specified, all magnetic fields are applied in an out-of-plane orientation.

5.2.1 Effect of split and top gate

First, the different transport characteristics are analyzed when the device is either tuned by the BG plus SG or TG, respectively, while the other unused gate is grounded. Figure 5.3 shows the resulting resistance maps as a function of V_{BG} and V_{SG} (a) or V_{TG} (b), together with corresponding resistance curves in the panels below. In the

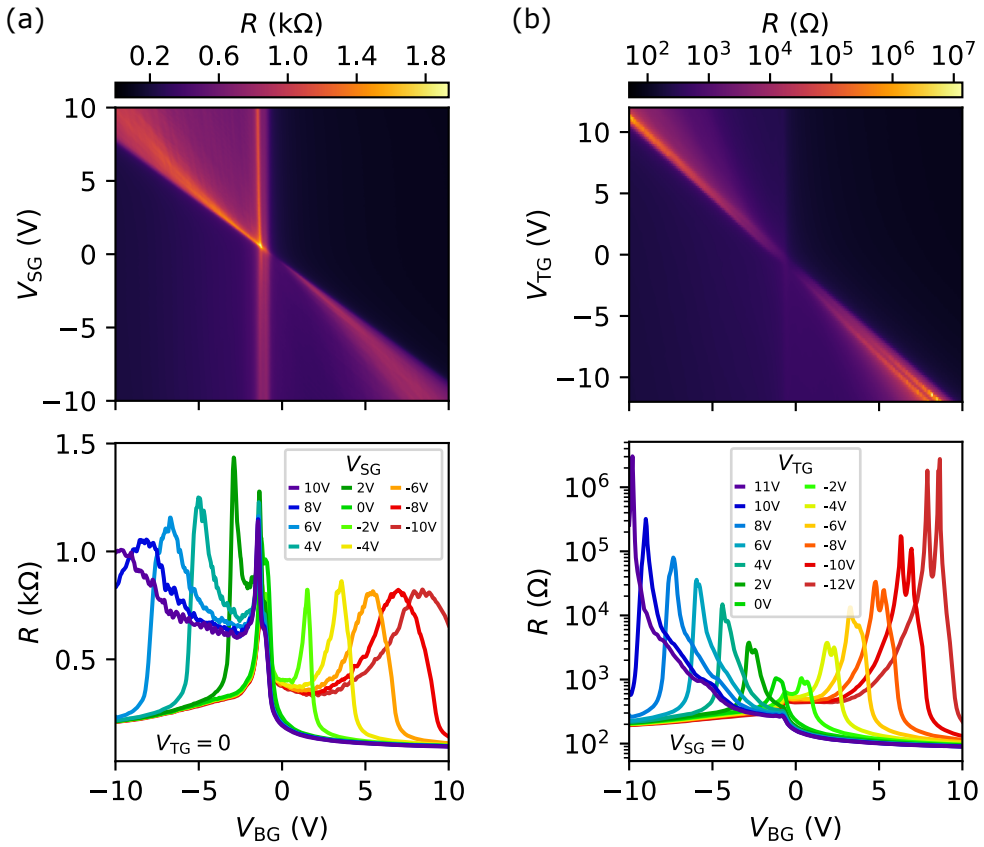

Figure 5.3: Comparison split gate versus top gate. (a, b) Color maps of the resistance as a function of V_{BG} and either V_{SG} (a) or V_{TG} (b). The panels below show corresponding resistance curves as a function of V_{BG} for different V_{SG} or V_{TG}, respectively. The data in (b) is measured at $T = 130\,\text{mK}$. Data from CD#3.

former case, a similar map as without the additional TG is observed (see Fig. 4.6 and the corresponding discussion in subsection 4.2.2). Despite the conductance being fully suppressed underneath the SG, a conductive channel between the SG electrodes remains open and the measured maximum resistance is less than 2 kΩ. In contrast, the TG covers the entirety of the device and hence, the BLG layer is gapped across the full width. Then, as the gap develops with increasing displacement field along the diagonal line, the maximum resistance is progressively rising up to values in the order of 10 MΩ, *i. e.* reaching the limits of our lock-in detection (note that the data is presented in log scale unlike in the SG case). The observed double peak in the resistance might be attributed to regions of slightly different capacitive coupling of the TG (BLG reservoirs and QPC, respectively) due to partial screening from the SG leading to a more complex electrostatic landscape in the device.

Operating all gates together finally enables us to study a BLG QPC. Its working principle is illustrated in Fig. 5.2c, depicting a band structure diagram across the split-gated confinement. While the Fermi level underneath the SG is positioned in the induced

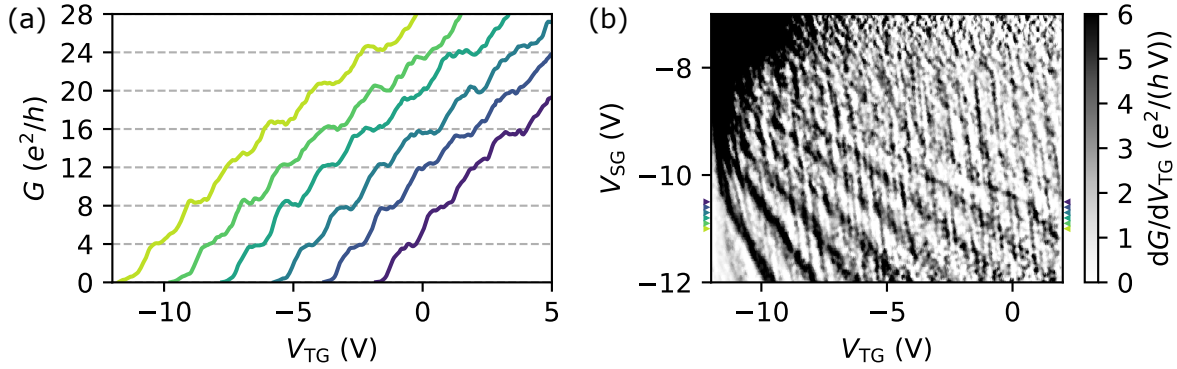

Figure 5.4: Quantization of conductance in a gate-defined BLG QPC. (a) Conductance curves as a function of V_{TG} for different V_{SG} from $-11.0\,V$ (left) to $-10.5\,V$ (right) with increment $0.1\,V$ at a constant $V_{BG} = 9\,V$. The curves are shifted for clarity by $2\,V$ between consecutive traces (the leftmost curve is not shifted). (b) Transconductance as a function of V_{TG} and V_{SG} at $V_{BG} = 9\,V$. Small colored markers denote positions of the line cuts shown in panel (a). Data from CD#3.

band gap, the channel (as well as the reservoirs) can be controllably depopulated down to full pinch-off by means of the TG. It is important to note, that not only the Fermi level is tuned but also the confinement potential as well as the band structure itself, which has non-trivial implications on the 1D subband formation.

5.2.2 Quantization of conductance

Figure 5.4a shows several conductance curves as a function of V_{TG} for different V_{SG} at constant $V_{BG} = 9\,V$. For clarity the curves are shifted as described in the caption. The conductance through the QPC appears robustly quantized down to the lowest subband in steps of $4\,e^2/h$ as it should be expected for a fourfold-degenerate system. In Fig. 5.4b the confinement is studied over a larger gate range, presented as a map of the differentiated conductance, *i. e.* transconductance $\mathrm{d}G/\mathrm{d}V_{TG}$, as a function of both V_{TG} and V_{SG}, with the respective conductance traces of Fig. 5.4a denoted by small colored markers. Here, plateaus in the conductance are visible as large white stripes separated by black lines of large transconductance corresponding to the conductance steps at the crossing of 1D subband edges. The robustness of the electrostatic confinement is demonstrated by the continuous evolution of the plateaus (also see Appendix D.1). Though, it should be noted that the confinement at a given V_{BG} is realized only in a limited range of V_{SG}, *i. e.* the Fermi level underneath the SG needs to be positioned in the induced electronic band gap. At too large negative V_{SG} the Fermi level is tuned into the valence band resulting in rather semi-transparent p–n barriers instead of the fully gapped split-gated constriction, which is discussed in Appendix D.2.

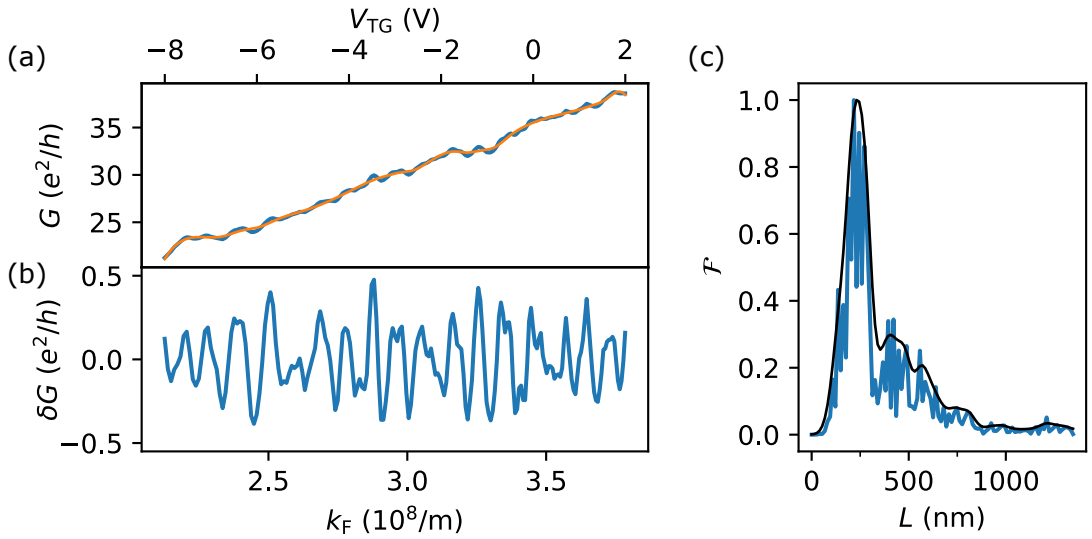

Figure 5.5: Additional conductance oscillations due to Fabry-Pérot interferences. (a) Conductance and (b) net oscillations as functions of V_{TG} (top x-axis) and Fermi wave vector k_F (bottom x-axis) at constant $V_{BG} = 9\,V$ and $V_{SG} = -9.1\,V$. The net oscillations are obtained by subtracting the smooth background (orange) from the raw conductance (blue). (c) Normalized Fourier transform of δG as a function of length L. The black curve corresponds to a smoothed signal. Data from CD#3.

Additionally to the described oblique stripe pattern due to quantized conductance in Fig. 5.4b, faint superimposed vertical lines are observed which correspond to the visible small oscillations on top of the staircase of quantized conductance (see Fig. 5.4a). Being primarily tuned by the TG but only minorly by the SG, these resonances might be due to Fabry-Pérot interferences arising from cavities formed in the non-split-gated regions of the device, *i. e.* the two BLG reservoirs between contacts and the barriers induced by the SG. A trace of the conductance versus V_{TG} or converted Fermi wave vector $k_F = \sqrt{\pi n}$, respectively, at $V_{SG} = -9.1\,V$ is presented in Fig. 5.5a. The net oscillations δG plotted in Fig. 5.5b are obtained by subtracting the smooth background conductance. In order to verify their origin, the associated cavity size is estimated from the frequency of the oscillations by performing a Fourier transformation following from the resonance condition $L = j \cdot \pi / k_F$ with j an integer number. The resulting frequency spectrum, shown in Fig. 5.5c, reveals a pronounced peak at $\approx 230\,nm$ in good agreement with the distance between leads and SG electrodes. Notably, although having different physical origins, both quantized conductance and Fabry-Pérot interferences are phenomena of ballistic charge carrier transport appearing concurrently in the device.

Moreover, we note that the tuning of the QPC by TG and SG is not equivalent. In particular, the widening of the plateaus towards larger negative V_{SG} indicates an unusual increasing subband level spacing at higher subbands as a function of V_{TG}, whereas the level spacing as a function of V_{SG} increases as commonly observed [Tho+95] when

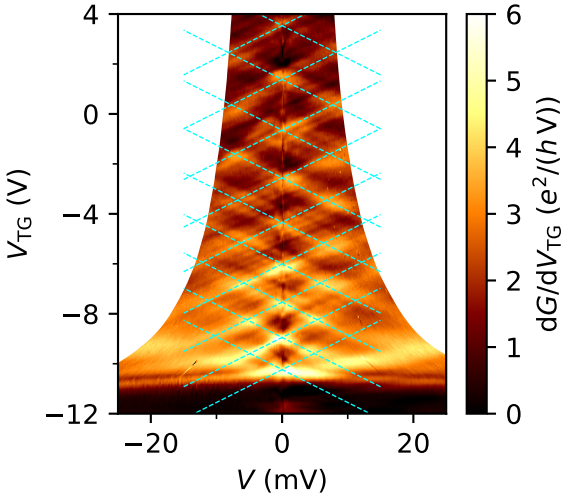

Figure 5.6: Source-drain bias spectroscopy of the size-quantized energy levels. Transconductance as a function of bias voltage V and V_{TG} at constant $V_{BG} = 9\,V$ and $V_{SG} = -10.6\,V$. The additionally plotted overlaying set of cyan dashed lines traces the splitting of energy levels with applied bias. Data from CD#3.

the confinement strengthens. The opposite effects of the two gates might be explained considering their different functionalities. While the SG acts on the confinement especially by squeezing the channel due to stray fields, the TG controls the QPC channel and simultaneously the reservoirs by completely tuning the shape of the confinement potential as well as the band structure.

Out-of-equilibrium measurements

To further probe the confinement and the energy level spacing $\Delta E_{n,n+1}$ of the 1D subbands, source-drain bias spectroscopy measurements are performed [Pat+90; Pat+91; Mar+92]. The corresponding transconductance map as a function of bias voltage V and V_{TG} at a given confinement condition $V_{BG} = 9\,V$ and $V_{SG} = -10.6\,V$ is shown in Fig. 5.6. A diamond-shaped pattern is observed with plateaus appearing in black corresponding to a minimum in the transconductance, while brighter lines represent transitions between plateaus due to the crossing of subband edges. Once more, additional superimposed resonances are visible as parallel lines to the subband edges due to the beforehand mentioned Fabry-Pérot interferences.

At finite applied bias the transitions between plateaus are linearly split as the electrochemical potentials μ_S and μ_D of source and drain contacts are raised or lowered with respect to each other. When the energy difference $eV = |\mu_S - \mu_D|$ is equal to the energy level spacing $\Delta E_{n,n+1}$ the split lines of subsequent 1D subbands are crossing. The extracted energy level spacing is found to be continuously increasing from about $\Delta E_{1,2} \approx 4\,meV$ to $\Delta E_{7,8} \approx 9\,meV$ which highlights the previously mentioned unusual

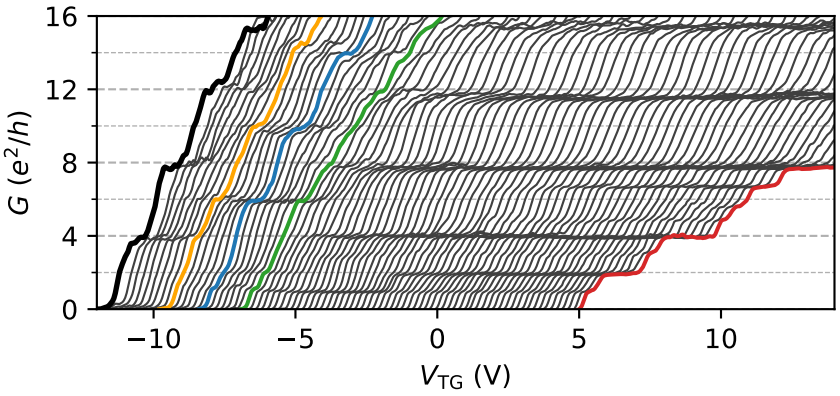

Figure 5.7: Lifted degeneracies in perpendicular magnetic field. Conductance as a function of V_{TG} for different values of B in steps of 100 mT at constant $V_{BG} = 9$ V and $V_{SG} = -10.6$ V. The curves are shifted for clarity by an offset of 2 V/T (200 mV between consecutive curves). The leftmost thicker black curve (not shifted) corresponds to the data acquired at $B = 20$ mT shown in Fig. 5.4. Highlighted colored curves correspond to $B = 0.9$ T (orange), 1.5 T (blue), 2.2 T (green) and 8.0 T (red), respectively. Data from CD#3.

tuning of the confinement via the TG. The observed decreasing energy level spacing towards lower subbands suggests a flattening of the confinement potential at larger negative V_{TG}, though band structure tuning plays as well a crucial role for the lowest subbands which will be discussed in subsection 5.2.5.

Finally, the out-of-equilibrium measurements are employed to estimate the gate coupling parameter α_{TG}, which is given by the slope of the linearly dispersing subband edges: $\alpha_{TG} e(V_{TG} - V_{TG}^0) = E_n^{QPC} \pm eV/2$, where E_n^{QPC} are the energy levels of the 1D subbands counted from respective zero energy reached at $V_{TG} = V_{TG}^0$. Indeed, the transconductance pattern is well described using a single value $\alpha_{TG} = 3.8 \times 10^{-3}$ for all visible subbands (as well as for another confinement condition; see Appendix D.3), which is thus a good estimate for a large range of 1D subband formation in our device. In the analysis below, the extracted coupling parameter from source-drain bias spectroscopy is employed to convert between energy and applied V_{TG}.

5.2.3 Valley subband splitting

Here, the QPC is investigated in an applied out-of-plane magnetic field B, *i.e.* perpendicular to the BLG plane. Figure 5.7 shows a series of conductance curves as a function of V_{TG} for different B in the confined regime at $V_{BG} = 9$ V and $V_{SG} = -10.6$ V. The magnetic field is increasing from 100 mT (left) to 8 T (right) in steps of 100 mT. For clarity the curves are shifted by an offset of 200 mV between consecutive curves. The leftmost thicker black curve (not shifted) corresponds to the staircase of quantized conductance measured at 20 mT as shown in Fig. 5.4a. An apparent change in

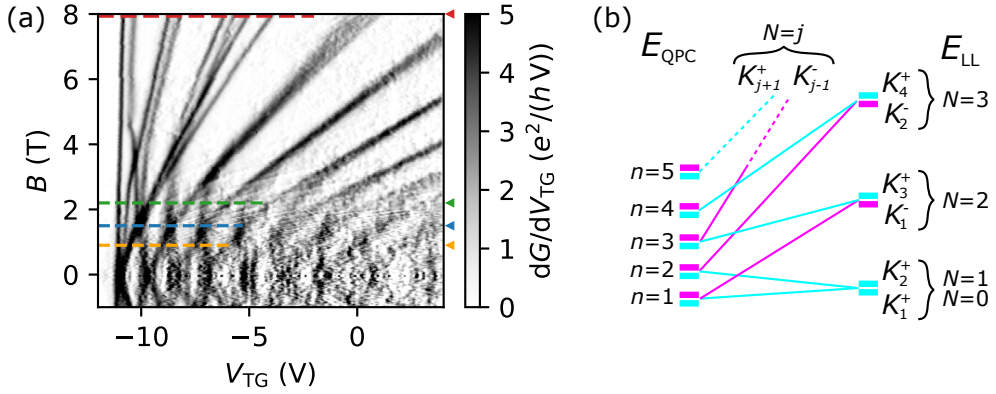

Figure 5.8: Evolution of magnetoelectric subbands. (a) Respective transconductance of the data in Fig. 5.7 as a function of V_{TG} and B, where colored dashed lines denote the correspondingly highlighted conductance curves. (b) Energy level diagram of valley-split magnetoelectric subbands evolving into Landau levels. Data from CD#3.

the sequence of quantized steps is observed with increasing B. Starting from the original sequence with conductance plateaus at every integer of the fourfold-degenerate conductance quantum $G_0 = 4\,e^2/h$ (thick black curve), the steps split until finally the degeneracy of the lowest levels is fully lifted at large B showing steps of $1\,e^2/h$ (see red curve). In the intermediate regime, different sequences appear including steps of $2\,e^2/h$ (see orange and green curves), as well as a restored fourfold-degenerate sequence but with plateaus visible at shifted half-integer values $(n - 1/2) \times 4\,e^2/h$ (see blue curve).

In order to study the continuous evolution of the 1D subbands in a perpendicular magnetic field more carefully, a map of the respective transconductance as a function of V_{TG} and B is shown in Fig. 5.8a, revealing a complex splitting and bunching of individual 1D subbands observed as dark lines (quantized plateaus are visible as bright parts corresponding to a small transconductance).[3] At small applied perpendicular magnetic field ($B < 1\,\mathrm{T}$) all size-quantized 1D subbands start to split. The splitting can be explained by the coupling of the out-of-plane magnetic field to the magnetic-moment carrying states arising due to a finite Berry curvature in gapped BLG, which adds a Zeeman-like contribution $-\boldsymbol{M}(\boldsymbol{k}) \cdot \boldsymbol{B}$, where $\boldsymbol{M}(\boldsymbol{k})$ is the orbital magnetic moment [KF18]. Due to opposite signs of the orbital magnetic moment for valleys K^+ and K^- the valley degeneracy is lifted in a perpendicular magnetic field B leading

[3] We note additional faint blurry lines which are strongly tuned by the magnetic field. Their appearance can be attributed to changes of the filling factor in the two BLG bulk reservoirs [Ove+18a], where Landau levels originate from large negative $V_{TG} \sim V_{TG}^0$ at the given positive $V_{BG} = 10\,\mathrm{V}$, *i. e.* charge neutrality of the reservoirs. Yet, as charge carrier transport is predominantly determined by the magnetoelectric confinement in the QPC, these weak resonances are not further discussed.

to the observed splitting of the subbands into the staircase of quantized conductance with steps of $2\,e^2/h$. The valley levels are shifted linearly within the approximation of a constant magnetic moment for a given 1D subband by $\delta\epsilon_\xi = \xi|M|B$ with $\xi = \pm$ for the two valleys, resulting in a valley Zeeman energy splitting $\Delta E_Z^\nu = 2|M|B$. Note that with increasing magnetic field and shifted energy levels, respectively, the band structure as well as Berry curvature are changing. Thus, the made assumption of linear splitting is only reasonable at small B for split levels close to the original 1D subband energy level. The observed low-magnetic field valley Zeeman-like splitting is estimated at $\approx$ 0.8–1.6 V/T for different subbands translating into $\approx$ 3–6 meV/T (using the relation $\Delta E = e\alpha_{\mathrm{TG}}\Delta V_{\mathrm{TG}}$), *i. e.* 30–50 times stronger than the Zeeman spin splitting for a free electron, similar to what has been reported in a BLG QD [Eic+18a].

At increased magnetic field ($1\,\mathrm{T} \lesssim B \lesssim 2\,\mathrm{T}$) the split lines of neighboring subbands are crossing each other, which leads to the restored but shifted sequence with steps of $4\,e^2/h$ as described beforehand. Yet, the intersection of different subbands occurs not exactly at the same field as the lines start to disperse towards higher energy, *i. e.* more positive V_{TG}, which is due to the formation of so-called magnetoelectric subbands [Wee+88b] based on the combination of both electrostatic confinement from the QPC as well as the additional quantizing harmonic potential for charge carriers in a perpendicular magnetic field [BH91b; HBW92]. With further increasing B the contribution of the magnetic confinement gets stronger and as the cyclotron orbit eventually becomes smaller than the constriction width W_{QPC}, *i. e.* at $B \geq 2\hbar k_{\mathrm{F}}/eW_{\mathrm{QPC}}$, the magnetoelectric subbands evolve into Landau levels. Importantly, the Landau level spectrum of BLG with broken layer symmetry due to a finite displacement field, *i. e.* gapped BLG, consists of two fully valley polarized levels $N = 0$ and $N = 1$ due to the broken valley degeneracy of the originally eightfold-degenerate zero energy Landau level in pristine BLG with the two energy levels of the respective other valley shifted into the valence band [MK13]. On the other hand, higher Landau levels $N \geq 2$ are approximately degenerate in valleys K^+ and K^- as the splitting is only weak and levels are close in their energies, explaining the observed peculiar mixing of two non-adjacent 1D subbands at large B as illustrated by the schematic in Fig. 5.8b.[4]

[4] Without displacement field the series of Landau levels in BLG is degenerate in valleys K^+ and K^- and given by $E_{N,\pm} = \pm\hbar\omega_{\mathrm{c}}\sqrt{N(N-1)}$, where $\pm$ refers to electron and hole states, and with wave functions spread over the two sublattices $\psi_{N\geq 2,\pm} = \frac{1}{\sqrt{2}}\left(\phi_N, \pm\phi_{N-2}\right)^{\mathrm{T}}$ for K^+ or the reversed spinor for K^-. Additionally, two special states $N = 0$ and $N = 1$ exist at zero energy $E_1 = E_0 = 0$ with eightfold degeneracy due to valley, spin and orbital degeneracy of $\psi_0 = (\phi_0, 0)^{\mathrm{T}}$ and $\psi_1 = (\phi_1, 0)^{\mathrm{T}}$ or with reversed roles of the sublattices for K^-, respectively. Most important, these wave functions have a non-zero amplitude only on one of the layers and with induced layer asymmetry the two valleys are split into energy levels $E_0 = -\frac{1}{2}\xi U$ and $E_1 = -\frac{1}{2}\xi U + \xi U\hbar\omega_{\mathrm{c}}/\gamma_1$, whereas higher levels are only weakly split into levels $E_{N\geq 2,\pm} \approx \pm\hbar\omega_{\mathrm{c}}\sqrt{N(N-1)} + \xi U\hbar\omega_{\mathrm{c}}/2\gamma_1$ remaining approximately degenerate in valleys K^+ and K^-. For details see [MK13].

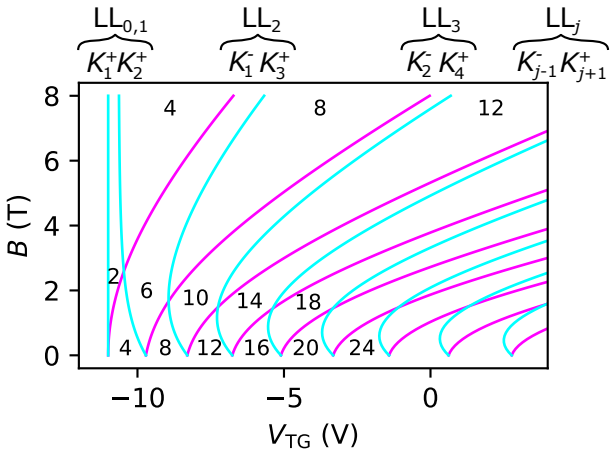

Figure 5.9: Modeled valley splitting and mixing in a perpendicular magnetic field. (a) Valley subband dispersion as a function of B calculated with the semi-phenomenological model. K^+ and K^- subbands are shown as cyan or magenta lines, respectively. The displayed numbers denote the values of quantized conductance plateaus in units of e^2/h.

Note that the roles of valleys K^+ and K^- are interchanged for the emerging pattern of valley splitting and bunching of 1D subbands in a reversed magnetic field $-B$. We further note that apart from the splitting of valley subbands a full lifting of the degeneracy, *i. e.* spin and valley, is visible for the lowest levels with increasing B, resulting in the described conductance steps of $1\,e^2/h$. The additional spin splitting can be attributed to an enhanced Coulomb interaction being strongest at the small charge carrier densities of the lowest subbands in contrast to the higher subbands where no further splitting is monitored within the range of applied B. Finally, we mention that spin and valley splitting under applied out-of-plane magnetic field has been observed as well in 1D ballistic fourfold-degenerate Si/SiGe heterostructures [Tob+95; Gos+07; McG+10], albeit without the described non-trivial valley subband mixing arising from the unique Landau level structure in (gapped) BLG.

Modeling of the valley subband splitting and mixing

In the following a semi-phenomenological model is presented, capturing on a qualitative level the main features of the described intricate bunching of valley-split subbands from two non-adjacent size-quantized energy levels in a perpendicular magnetic field.[5] The model is based on the 2×2 effective Hamiltonian of BLG [McC06;

[5] The model was designed by Igor Krainov, Alexander Dmitriev (both A. F. Ioffe Physico-Technical Institute, St. Petersburg, Russia), Vanessa Gall and Igor Gornyi (both KIT). For a detailed description of the model see the Supplemental Material to [Kra+18a].

MK13],[6] disregarding for simplicity effects related to the fine structure of the gapped BLG spectrum near the bottom of the conduction band or top of the valence band, *i. e.* trigonal warping and the "Mexican hat" band modulation (the effect of these features on the QPC conductance is discussed in [KF18; LKF19] and will be analyzed in subsection 5.2.5). Moreover, Zeeman spin splitting as well as the approximately linear-in-B Zeeman-like valley splitting at small B are neglected. Within this simplified model, the evolution of eigenenergies and eigenstates for the valleys K^+ and K^- with increasing magnetic field can be written as follows:

$$K^+: \qquad E_n = \sqrt{(\Delta/2)^2 + (E_n^0)^2} \quad \xrightarrow[B\to\infty]{} \quad \sqrt{(\Delta/2)^2 + (\hbar\omega_c)^2(n-2)(n-1)} \quad , \tag{5.3a}$$

$$\psi_n = \begin{pmatrix} \varphi_n \\ \frac{\hat{p}_+^2}{2m^*(E+\Delta/2)}\varphi_n \end{pmatrix} \xrightarrow[B\to\infty]{} \begin{pmatrix} \tilde{\varphi}_n \\ \tilde{\varphi}_{n-2} \end{pmatrix} \quad , \tag{5.3b}$$

$$K^-: \qquad E_n = \sqrt{(\Delta/2)^2 + (E_n^0)^2} \quad \xrightarrow[B\to\infty]{} \quad \sqrt{(\Delta/2)^2 + (\hbar\omega_c)^2\, n(n+1)} \quad , \tag{5.4a}$$

$$\psi_n = \begin{pmatrix} \varphi_n \\ \frac{\hat{p}_-^2}{2m^*(E+\Delta/2)}\varphi_n \end{pmatrix} \xrightarrow[B\to\infty]{} \begin{pmatrix} \tilde{\varphi}_n \\ \tilde{\varphi}_{n+2} \end{pmatrix} \quad , \tag{5.4b}$$

where Δ is the band gap induced by the displacement field and E_n^0 denotes the 1D subband energy levels in the QPC at $B = 0$. The magnetic field, appearing in the equations due to cyclotron frequency $\omega_c = eB/m^*$, is included via the shift in the momentum operators $\hat{p}_\pm = \hat{p}_x - eA_x/c \mp i(\hat{p}_y - eA_y)$ by the corresponding vector potential.

The equations describe at $B = 0$ size-quantized energy levels that are degenerate in the two valleys K^+ and K^- with the components of the eigenstate spinors given by the wave functions φ_n ($n = 1, 2, 3, ...$) of an electron confined to a 1D quantum well, which trend with increasing B into a harmonic oscillator wave function with the same number $\varphi_n \to_{(B\to\infty)} \tilde{\varphi}_n$. As can be seen from the expressions for the energy levels at

[6] The 2×2 Hamiltonian is used for a more simplified description of the two lowest-energy bands and can be obtained by reducing the four-band Hamiltonian which was presented in chapter 2.2. For details see [MK13].

large magnetic field, this results in degenerate Landau levels by merging of subbands from valleys K^+ and K^- with indices differing by 2 as previously discussed.

In order to describe the experimental data for the complete magnetic field range, *i. e.* energy levels at intermediate magnetic fields, the two extrema $B = 0$ and $B \to \infty$ are interpolated by simplest formulas instead of solving exactly for the energy levels. The gap $\Delta = 70\,\mathrm{meV}$ is used as a free fitting parameter, whereas $E_n^0 = E_n^{\mathrm{QPC}}$ is extracted from source-drain bias spectroscopy and converted to TG voltage V_{TG} employing the coupling parameter α_{TG} as described in subsection 5.2.2. This is why the model is considered as semi-phenomenological rather than describing the energy levels in a fully analytical manner by considering the electrostatic properties of the setup. The resulting pattern is plotted in Fig. 5.9, showing the evolution of valley subbands with magnetic field following from Eqs. 5.3 and 5.4. Compared to the experimental data, shown in Fig. 5.8, the simplified model well captures the main qualitative features, *i. e.* valley splitting and mixing of valleys K^+ and K^- with non-consecutive indices.

5.2.4 Zeeman spin splitting

For a further analysis of the 1D subbands in the BLG QPC, the Zeeman spin splitting is studied in an in-plane and out-of-plane magnetic field orientation $B_{\parallel}$ and $B_{\perp}$, respectively. Figure 5.10a shows a color map of the transconductance as a function of V_{TG} and $B_{\parallel}$ for the lowest four subbands. The transitions across subband edges appear as black lines (high transconductance), whereas conductance plateaus are visible as white regions. With increasing $B_{\parallel}$ a splitting of the 1D subbands is observed, corresponding to the evolution from spin-degenerate to spin-split energy levels. Within the studied range of magnetic field $B_{\parallel} \leq 8\,\mathrm{T}$ the lifting of spin degeneracy occurs only for the lowest three subbands (equivalently for both positive and negative magnetic field), which is illustrated in Fig. 5.10b in a simplified schematic. We note that the energy levels are partially disturbed by Fabry-Pérot resonances which do not vanish with applied in-plane magnetic field even up to $B_{\parallel} = 8\,\mathrm{T}$ (see Appendix D.4). The splitting is likewise reflected in the appearance of additional half-step conductance plateaus at high in-plane magnetic fields, as highlighted in Fig. 5.10c showing two exemplary conductance curves for different $B_{\parallel} = 0.2\,\mathrm{T}$ (black) and $B_{\parallel} = 6.4\,\mathrm{T}$ (magenta), respectively. Note that the valley degeneracy is not affected by the application of an in-plane magnetic field and the Zeeman spin-split subbands remain degenerate in the two valleys K^+ and K^-.

The transition from spin-degenerate to spin-split subbands is further highlighted in Fig. 5.10d, presenting the same data set of the transconductance as in Fig. 5.10a, but

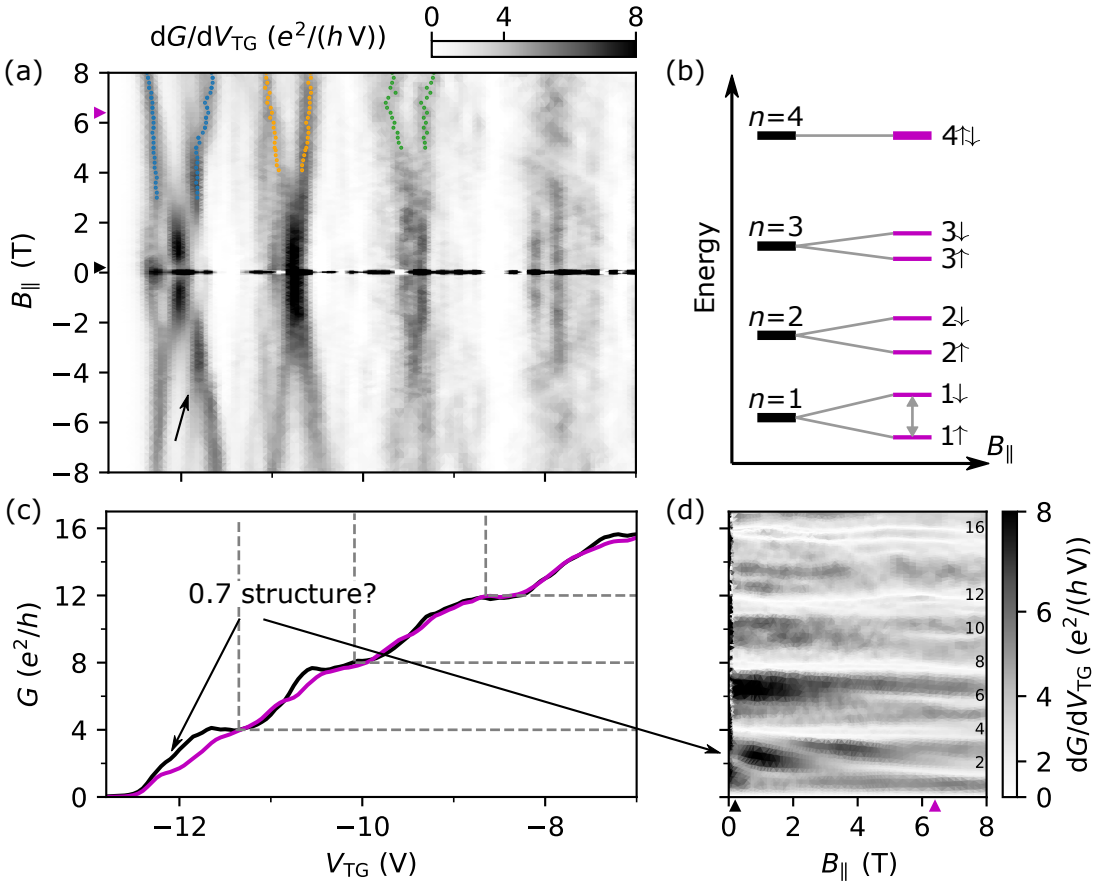

Figure 5.10: Zeeman spin splitting in in-plane magnetic field. (a) Transconductance as a function of V_{TG} and $B_{\parallel}$ at $V_{BG} = 10\,V$ and $V_{SG} = -12\,V$. Small colored dots denote positions of split subband edges (black lines) determined as maxima in the transconductance. The small black arrow marks a crossing of the spin split subband with a Fabry-Pérot resonance. (b) Simplified energy level diagram, depicting the Zeeman spin splitting of 1D subbands. The Zeeman energy splitting ΔE_Z is indicated by a gray double-headed arrow for the lowest subband $n = 1$. (c) Conductance curves versus V_{TG} for two different $B_{\parallel} = 0.2\,T$ (black) and $6.4\,T$ (magenta) corresponding to line cuts as denoted by the colored markers in panel (a) and (d). (d) Same data set as in (a), but plotted as a function of $B_{\parallel}$ and G, allowing to monitor the conductance plateau sequences as white lines. Data from CD#5.

here plotted as a function of $B_{\parallel}$ and the conductance itself. This representation allows a better monitoring of different sequences of the quantized conductance since plateaus are now recognized as rather sharp white lines at the respective conductance values. While at small in-plane magnetic fields the plateaus appear at integer numbers of $4\,e^2/h$, a clear change is observed with increasing $B_{\parallel} \gtrsim 4.5\,\mathrm{T}$ with plateaus visible at every $2\,e^2/h$ for the three lowest subbands. Additionally, the presence of a plateau-like feature in resemblance of a 0.7 structure can be noticed below the first conductance plateau [Tho+96] (as well visible in Fig. 5.10a, c, respectively), which will be discussed at this point.

Signature of the 0.7 structure

The observed conductance feature, which is rather a kink or shoulder than a plateau, is positioned at about $\approx 2.4\,e^2/h$, but starts to drop at finite $B_{\parallel}$. With further increasing in-plane magnetic field, the line finally trends into the plateau of the lowest spin-split subband at $2\,e^2/h$. We note that another dispersing line below the first plateau is visible. While such a splitting one after the other could indicate an interaction-driven spin splitting of the first 1D energy level for only one of the two valleys K^+ and K^-, there is no trivial reason that could explain such a lifting of the valley degeneracy without magnetic field but which gets restored at finite in-plane magnetic fields. Looking closely at the evolution of the Zeeman spin splitting of the first subband in Fig. 5.10a, a crossing with a non-dispersing vertical line is noticed (marked by the small black arrow). This resonance, being not affected by the in-plane magnetic field, is due to the Fabry-Pérot interferences. Then, as the spin-split subband disperses through the resonance, the additional conductance kink trends progressively from the plateau at $4\,e^2/h$ down to $2e^2/h$ as observed in Fig. 5.10d. On the other hand, the lowest conductance shoulder appears distinctly different featuring a non-monotonic evolution of the conductance plateau (Fig. 5.10d) and furthermore its respective position in energy slightly disperses with the applied in-plane magnetic field (Fig. 5.10a) unlike the Fabry-Pérot interferences. Therefore we conclude that this observed conductance kink developing smoothly into the lowest spin-split subband can be attributed to a spin-related anomalous conductance structure.

The appearance of such unexpected conductance structure below the first regular quantized plateau, was first described in [Tho+96] although already visible in earlier published data without taking much of a notice, and has become known as so-called 0.7 anomaly.[7] In the following, the presence of this feature which could not be described in a single-particle framework [Mic11] (unlike the quantized conductance in

[7] Note that the naming is rather misleading, since the anomalous structure has been observed in a larger range 0.25–0.95 of the degenerate conductance quantum [DG17].

the QPC itself [Büt90]) has been widely studied and observed in a variety of experiments based on QPCs or ballistic quantum wires in *n*- or *p*-type GaAs heterostructures [Tho+98; Kri+00; Cro+02; Dan+08], and later as well e. g. in InAs nanowires [Hee+16] or Ge quantum wells [Miz+18]. However, despite being commonly observed in experiments, less consensus exists regarding the understanding of the phenomenon. Amongst the diversity of early on proposed explanations in the existing literature [SZ00; FK00; RRJ00; BCF01; Sus01; Rei+02; SM03; Mat04; Rei05; LSR07; AH09], there exist particularly two popular and mainly invoked mechanisms, that is a semi-phenomenological assumption of spontaneous spin polarization [Tho+96; WB96; LYB11] or Kondo-like effects due to the formation of a many-body state [Cro+02; MHW02; RM06] (a review of initial experiments and theoretical investigations is found in [Mic11]). In fact, the common understanding of more recent works tends more towards the latter explanation of interaction enhancement due to Kondo-like physics [Iqb+13; Bru+14; Hey+15] or rather the presence of a smeared van-Hove singularity in the local density of states appearing at the bottom of the first 1D subband [Bau+13; Sch+14].

Yet, the basic understanding of this phenomenon remains until now debated [Fig16; DG17] and has especially only been vaguely reported but not investigated in a fourfold-degenerate system (*i. e.* in an AlAs quantum well or Si/SiGe heterostructure but with broken valley degeneracies or at unconvincing large out-of-plane magnetic field with fully lifted degeneracy [Gun+06; Sca+06; Gos+07]). Also it should be noted that this anomalous structure is typically energy dependent and extremely sensitive to the confinement itself [Bur+12; Sch+14], which could be the reason why it was not observed in all of our measurements with different gate conditions. For a better understanding of such a conductance anomaly in the here presented fourfold-degenerate system further studies are required including out-of-equilibrium and temperature-dependent measurements under different confinement conditions. Also the effect of the Fabry-Pérot interferences must be ruled out to clearly identify the 0.7 structure.

Effective 1D g-factor

Finally, the Zeeman spin splitting rate of the different 1D subbands is compared which is found to be unequally strong (see the colored dots tracing the spin-split subbands in Fig. 5.10a). The observed renormalization of the spin splitting is generally described by the introduction of a phenomenological effective 1D g-factor $|g^*|$ [Tho+96] different from the bare bulk g-factor (a dimensionless physical quantity relating the magnetic moment of a particle to its total electronic angular momentum, *i. e.* spin and orbit), which allows to effectively incorporate interaction effects within the single-particle description [VSZ12]. We determine the Zeeman energy splitting as $\Delta E_Z = \alpha_{TG} e \Delta V_{TG}$ where the TG voltage difference $\Delta V_{TG} = V_{TG}^{\downarrow} - V_{TG}^{\uparrow}$ of spin-split subbands is con-

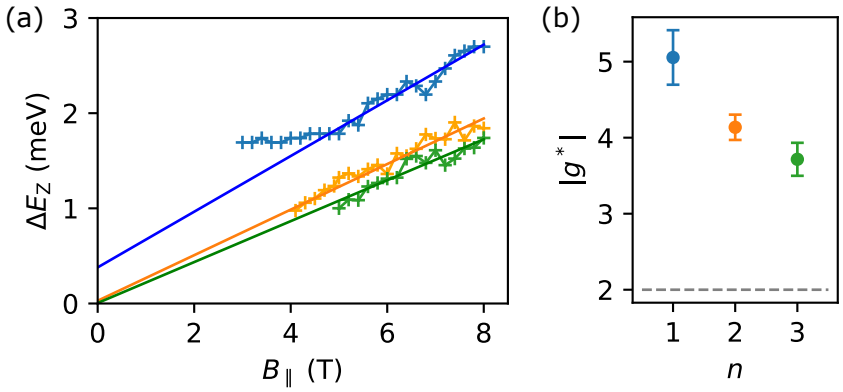

Figure 5.11: Zeeman energy splitting and effective 1D Landé g-factor. (a) Extracted Zeeman energy splittings $\Delta E_Z = e\alpha_{TG}(V_{TG}^{\downarrow} - V_{TG}^{\uparrow})$ from spin-split subbands (see Fig. 5.10a) versus $B_\parallel$ for the lowest three subbands $n = 1$ (blue), 2 (orange) and 3 (green). (b) Effective Landé g-factor $|g^*|$ for the different 1D subbands n. The standard error of the linear fits is shown by errorbars. The bare 2D g-factor in bilayer graphene $g = 2$ is indicated by a gray dashed horizontal line. Data from CD#5.

verted into energy using the coupling parameter α_{TG} extracted from the splitting rate of the energy levels in source-drain bias measurements (see subsection 5.2.2). Figure 5.11a shows the estimated ΔE_Z values as a function of $B_\parallel$ revealing linearly increasing Zeeman energy splittings. Yet, the splitting of the first 1D subband $n = 1$ only trends into a linear behavior for $B_\parallel \gtrsim 5\,\mathrm{T}$, whereas at smaller magnetic fields an almost constant splitting is observed. At this magnetic field range, the dispersing spin-split subband crosses with the Fabry-Pérot resonance as described beforehand, obscuring the exact position of the energy level. Moreover, a finite splitting remains at zero magnetic field due to the observed conductance anomaly. Correspondingly, a non-zero ΔE_Z is found at $B_\parallel = 0$, unlike the cases $n = 2$ and $n = 3$ which can be extrapolated to a zero Zeeman energy splitting.

From the slopes of the linear fit to $\Delta E_Z = |g^*|\mu_B B$ (with μ_B the Bohr magneton) we find magnetic field independent effective Landé g-factors $|g^*|$ for each of the subbands (the data points of $n = 1$ are only fitted for $B_\parallel \geq 5\,\mathrm{T}$), which is plotted in Fig. 5.11b. The obtained $|g^*|$ values are increasingly enhanced for lower subbands in comparison with the bare 2D g-factor in graphene $g \simeq 2$ (*i. e.* close to the free electron value due to the small spin-orbit coupling in carbon materials) as e. g. found via electron spin resonance measurements in graphite [MTS91] as well as in graphene [Rao+11].[8] The maximum enhancement by a factor of about 2–3 at the lowest $n = 1$

[8] We note that in magnetotransport measurements with tilted magnetic fields slightly enhanced values $|g^*| \sim 2.5$ have been reported in graphite [Sch+10] or single- and bilayer graphene [Kur+11] 2D devices, whereas no enhancement of the Zeeman spin splitting in single- and bilayer graphene QDs is observed [Güt+10; Eic+18a]. The observed spin g-factor correction has been attributed to many-body electronic interactions in graphene [Men+17].

subband is similar to what has been reported in QPCs based on (both n- or p-type) GaAs [Pat+91; Tho+96; Tho+98; Dan+97; Dan+06] or InGaAs [Mar+08b; Mar+10] heterostructures.[9] In contrast, no enhancement has been observed in a QPC based on another 2D material, *i. e.* a monolayer MoS_2 device encapsulated in hBN [Mar+17].

Indeed, it should be noted that throughout the literature rather contradictory results in respect thereof are published. For instance, shot noise measurements in a GaAs QPC indicated likewise an enhancement of the g-factor [DiC+06], much like the measurement of spin currents in a GaAs 2DEG with QPC injector and detector [Fro+09], whereas other spin current measurements based on ballistic nanostructure constrictions in GaAs (open QD or QPC) revealed no enhancement [Pot+02; Koo+08]. In this regard, it was argued in [VS16] that the enhanced g-factor strongly depends on the non-equilibrium state in source-drain bias spectroscopy measurements, since the calculated exchange diagrams considering electron-electron interactions in the Hartree-Fock approximation showed rather reduced source-drain bias level splitting but no increase of the magnetic splitting effectively causing a seemingly enhanced Zeeman energy splitting. Otherwise in a previous theoretical work [WB96], an exchange-interaction mechanism is discussed for enhanced Zeeman energy splitting in the case of an infinitely long 1D GaAs quantum wire. However, the calculated enhancement appears to be much stronger than experimentally observed and the applicability to a QPC confinement being much shorter than the spin relaxation length seems questionable.

Now we turn to the scenario of Zeeman spin splitting in an applied out-of-plane magnetic field. As described in the previous subsection 5.2.3, a full lifting of the degeneracy is observed for the lowest subbands in a perpendicular magnetic field $B_\perp$ with 8 entirely spin- and valley-split energy levels. Thus, it is possible to extract the Zeeman energy splitting for the out-of-plane magnetic field orientation as well. Yet, determining the effective 1D g-factor is restricted to small $B_\perp \lesssim 3.5\,\mathrm{T}$ to ensure that not just simply the splitting of 2D Landau levels is probed. That is why only the Zeeman spin splitting of subband K_1^+ is considered. The respective evolution of the subband splitting is monitored in Fig. 5.12a (blue dots tracing the split levels), showing a map of the transconductance as a function of V_{TG} and $B_\perp$ at $V_{\mathrm{BG}} = 10\,\mathrm{V}$ and $V_{\mathrm{SG}} = -12\,\mathrm{V}$, *i. e.* at a different gate voltage condition and measured in another cooldown (CD#4) than Fig. 5.8. The extracted values for ΔE_Z and $|g_\perp^*|$ for the out-of-plane magnetic field orientation are shown in Fig. 5.12b (the non-zero Zeeman energy

[9] Note that the in-plane g-factor in electron based QPCs is observed to be isotropic [Mar+10] (unlike in QPCs based on p-type heterostructures where anisotropy of the in-plane g-factor has been reported [Dan+06]).[Mis+17] Thus, the here applied in-plane magnetic field orientation of $\approx 45°$ with respect to the transport direction through the QPC should not play a role for the presented results.

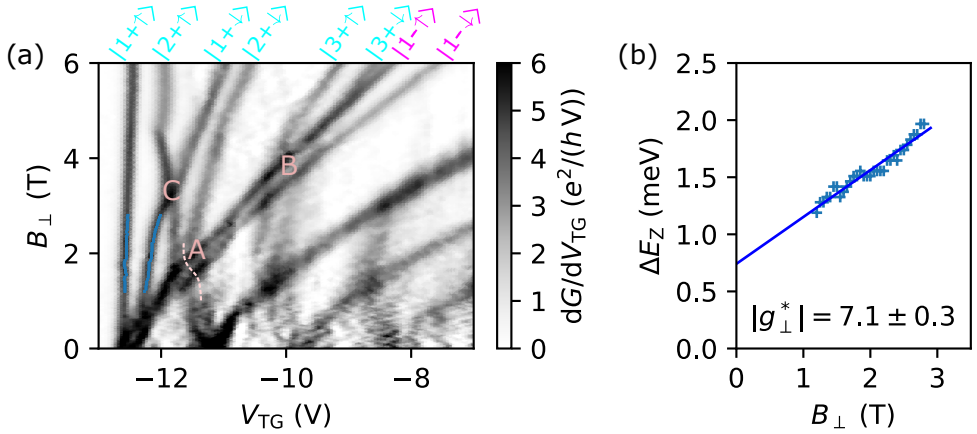

Figure 5.12: Spin splitting in perpendicular magnetic field. (a) Transconductance as a function of V_{TG} and $B_\perp$ at constant $V_{BG} = 10\,V$ and $V_{SG} = -12\,V$. Each subband is labeled according to the notation $|n\,\xi\,\sigma\rangle$ as introduced in the main text. Letters A, B and C denote points referenced in the text. The extracted spin-split subband edges of $|1\,+\rangle$ are indicated by small blue dots. (b) Respective Zeeman energy splitting ΔE_Z. The effective $|g_\perp^*|$ is extracted from the slope of the linear fit. Data from CD#4.

splitting at $B_\perp = 0$ is reminiscent of the beforehand mentioned 0.7 structure). In comparison with the values extracted in the in-plane magnetic field orientation the effective $|g_\perp^*| = 7.1 \pm 0.3$ in out-of-plane magnetic field is stronger enhanced. A similar anisotropic renormalization of the Landé g-factor has been reported in an InGaAs QPC device [Mar+10], which has been attributed to stronger exchange interaction and correlation effects due to the additional orbital confinement [KMS16].[10] Indeed, the effect of electron-electron interactions in graphene under applied perpendicular magnetic field is predicted to induce an enhancement of the g-factor [IZ12; VSZ12]. Importantly, it should be noted that here the Zeeman spin splitting in the out-of-plane magnetic field orientation occurs within an already valley-split subband, while in the in-plane case the splitting is between two spins each up and down due to valley-degenerate subbands, which has not been discussed in literature to the best of our knowledge.

We further note that the spin splitting of other subbands in the out-of-plane magnetic field orientation appears to be more complex due to the additional lifting of the valley degeneracy and the arising interactions at the crossing with other subbands. For a better referencing of individual energy levels the following notation is introduced $|n\,\xi\,\sigma\rangle$ where the three quantum numbers correspond to the orbital wave function of subband with index $n = 1, 2, 3, ...$, valley isospin $\xi = +, -$, and spin $\sigma = \uparrow, \downarrow$ (see Fig. 5.12a). The importance of considering exchange interaction-driven effects for

[10] We note that particularly strong anisotropy between in-plane and out-of-plane magnetic field orientation is observed in systems with prominent spin-orbit coupling, as e. g. reported in InSb QPCs [Qu+16] or long 1D hole channels in Ge quantum wells [Miz+18].

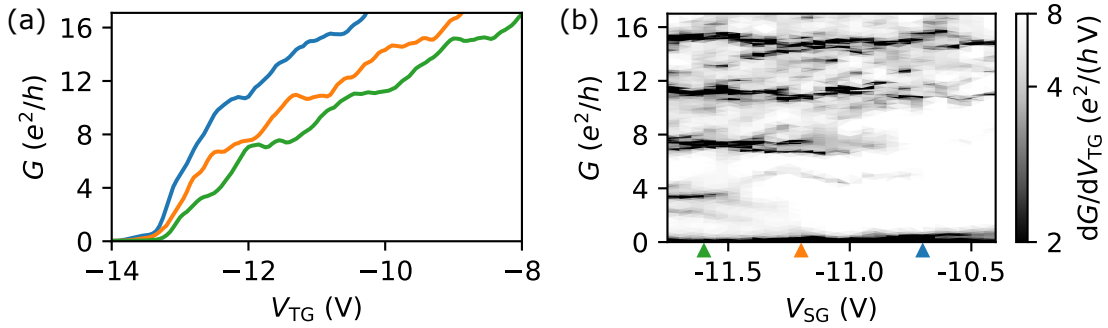

Figure 5.13: Additional degeneracies of the first energy level. (a) Conductance curves as a function of V_{TG} for different $V_{SG} = -10.7\,V$ (blue), $-11.2\,V$ (orange) and $-11.6\,V$ (green) at constant $V_{BG} = 10\,V$. (b) Transconductance as a function of V_{SG} and conductance G obtained from multiple TG sweeps. The respective SG values of the conductance curves in panel (a) are denoted by small colored markers. Data from CD#4.

Zeeman spin splitting of the lowest subbands is e. g. demonstrated by an apparently enhanced splitting of $|1-\rangle$ whenever it intersects with other subband edges, *i. e.* $|2+\rangle$ at the position labeled with A and $|3+\rangle$ at B, respectively, whereas a closing of the splitting is observed in-between. Likewise, energy levels $|2+\rangle$ and $|3+\rangle$ reveal a discernible spin splitting after the mentioned crossings. Moreover, the intersection of $|2+\rangle$ with $|1-\rangle$ at position A features a discontinuous shift as indicated by the dashed line. The appearance of this new conductance structure has been described as the analog of a zero-field 0.7-like anomaly in a GaAs/AlGaAs heterostructure due to enhanced exchange interactions at the crossing of two different 1D subbands [Gra+03]. Finally, a strong enhancement of the spin splitting for magnetoelectric subbands $|1+\rangle$ and $|2+\rangle$ can be noticed after the crossing of $|1+\downarrow\rangle$ and $|2+\uparrow\rangle$ at position C, leading to a spin-sorted sequence ($\uparrow\uparrow\downarrow\downarrow$) of the valley-polarized $N = 0$ and $N = 1$ Landau levels.

5.2.5 Tuning the mini-valley quantum degree of freedom

So far, only the "normal" staircase of quantized conductance with steps of $4\,e^2/h$ down to the lowest subband has been discussed. Yet, unusual conductance quantization in BLG QPCs with the first plateau appearing accidentally at $8\,e^2/h$ have been reported in literature [Ove+18a; Ove+18b], which is attributed to the complex band structure tuning in the BLG channel [KF18]. Here, a controllable tuning of the additional degeneracy of the first transverse mode is demonstrated by varying the confinement potential due to the combination of SG and TG. Figure 5.13a shows conductance curves versus V_{TG} for three values of V_{SG} (see caption). Notably, the first plateau appears at distinct quantized conductance values $4\,e^2/h$ (green), $8\,e^2/h$ (orange) and $12\,e^2/h$ (blue), whereas for higher subbands the regular step height of $4\,e^2/h$

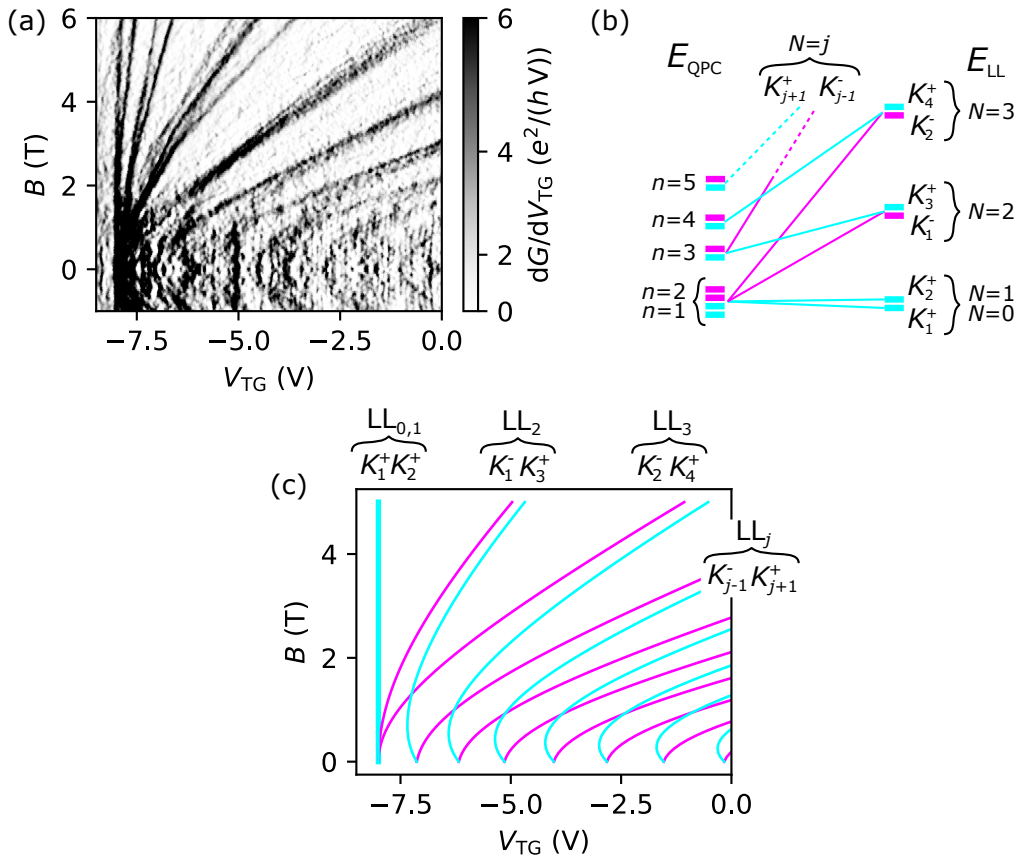

Figure 5.14: Valley subband splitting in the case of eightfold degeneracy of the first 1D energy level. (a) Transconductance as a function of V_{TG} and B at constant $V_{\mathrm{BG}} = 6\,\mathrm{V}$ and $V_{\mathrm{SG}} = -6.7\,\mathrm{V}$. (b) Energy level diagram. (c) Calculated valley subband dispersion in out-of-plane magnetic field, where the size-quantized energy levels are shifted according to $E_n^{\mathrm{QPC}} \rightarrow E_{n-1}^{\mathrm{QPC}}$ for subbands with $n \geq 2$ to account for the additional degeneracy of the first energy level. The double line-width of the leftmost cyan line reflects two K^+ valleys. Data from CD#3.

is observed in all three cases. For a better monitoring of the quantized conductance plateau sequences for a given SG value, the transconductance obtained from multiple TG sweeps is plotted in Fig. 5.13b as a function of V_{SG} and the respective conductance itself, where plateaus are visible as black lines (minima in the transconductance). The corresponding SG values of the presented conductance curves in panel (a) are denoted by small colored markers. A clear change of the quantized conductance plateau sequence is observed as the lowest plateaus at $4\,e^2/h$ and $8\,e^2/h$ subsequently vanish at smaller V_{SG} corresponding to a smoother and wider confinement.

The additional degeneracy is also apparent in the depopulation of the magnetoelectric subbands, here demonstrated for a confinement condition with eightfold degeneracy. Figure 5.14a shows the respective pattern of valley subband splitting in a perpendicular magnetic field. Unlike the data presented previously in Fig. 5.8 the Landau levels $N = 0$ and $N = 1$ fully emerge from the first 1D energy level as illustrated in

Fig. 5.14b. The observed pattern can be captured as well within the presented simplified model (subsection 5.2.3) by shifting the energy levels $E_n^{\mathrm{QPC}} \rightarrow E_{n-1}^{\mathrm{QPC}}$ for $n \geq 2$. The resulting calculated valley subband dispersion is plotted in Fig. 5.14c (Zeeman splitting is again neglected) in good agreement with the experimental data with four emerging valley subbands from the first size-quantized energy level. Note the double line-width of the leftmost cyan line, reflecting two K^+ valley subbands.

The presented additional degeneracies of the lowest 1D subband directly reflect the complex fine structure at the bottom of the conduction band in BLG, where the trigonal warping features the formation of a mini-valley triplet in both K^+ and K^- valleys upon the opening of an interlayer asymmetry band gap [MK13] (as e. g. observed via the evolution of the Landau level spectrum in gapped BLG featuring a Lifshitz transition [Var+14a]). The presence of the mini-valley structure is understood to manipulate the degeneracy of the low-energy subbands depending on the confinement as well as the band alignment between the channel spectra in the QPC and the bulk spectra in the BLG reservoirs [KF18; LKF19]. That's why the additional degeneracy appeared rather accidentally in some experiments [Ove+18a; Ove+18b]. Here, the simultaneous tuning of both QPC channel and BLG reservoirs via the TG allows to couple smoothly into the mini-valley transverse modes with the respective number of modes dependent on V_{SG}, demonstrating that the mini-valleys in the BLG band spectrum provide sufficiently developed energy splittings and separated states in momentum space to be considered as a good quantum number that can be exploited in the transport properties of a BLG QPC.

5.3 Conclusion

In this chapter, we have studied the transport properties of an electrostatically induced QPC in BLG. The QPC is successfully realized by the combination of BG, SG and TG. While the system is confined by means of BG and SG, the additional overall TG allows to controllably depopulate individual 1D subbands down to full pinch-off. The conductance through the QPC is observed to be robustly quantized in steps of $4\,e^2/h$ owing to the fourfold degeneracy in BLG, *i. e.* spin and valley.

The subband degeneracies have been further investigated by the application of magnetic fields. In a perpendicular field, the valley degeneracy is lifted resulting in an intricate pattern of magnetoelectric subbands which undergo a mixing of next-nearest K^+ and K^- subbands at large B. The evolution of the valley-split magnetoelectric subbands could be well described by a simplified semi-phenomenological model, while the Zeeman-like valley splitting at small magnetic field is found to be 30-50 times stronger than the Zeeman spin splitting of a free electron.

On the other hand, the spin degeneracy is lifted in both in-plane and out-of-plane magnetic fields. In the case of in-plane magnetic field orientation, a Zeeman spin splitting of the lowest three energy levels is observed, whereas the valley degeneracy is not affected. The extracted effective 1D g-factors $|g^*|$ are increasingly enhanced for lower subbands by a factor 2–3 at the maximum in comparison with the bare 2D Landé g-factor $g = 2$ in bilayer graphene. When the magnetic field is applied perpendicularly, a more intricate splitting occurs due to the additional lifting of the valley degeneracy. Owing to the renormalization of the Zeeman energy splitting by enhanced exchange interactions the degeneracy of Landau levels $N = 0$, $N = 1$ and $N = 2$ is fully lifted with eight entirely spin- and valley-split subbands. From the Zeeman energy splitting of the first valley-split subband an even stronger enhancement of $|g^*_\perp|$ is reported, revealing an anisotropic renormalization of the Landé g-factor due to enhanced interactions at the small charge carrier densities of the lowest subbands. The importance of considering effects driven by exchange interactions is demonstrated in the appearance of a 0.7-like conductance structure below the first plateau as well as at the crossing of magnetoelectric subbands.

Finally, the consequences of the fine structure in a gapped BLG band spectrum have been discussed, where the presence of mini-valleys due to trigonal warping leads to additional degeneracies of the lowest subband.

6 Towards discretized critical current

As the superconducting analogue of the quantized conductance in a normal conducting ballistic constriction, *i. e.* a QPC, it is predicted that the critical current through a SQPC is accordingly discretized [BH91a; FTT91; FTT92; CLB00; Shc00]. Here, in the final experimental chapter of this thesis, the SQPC in a BLG weak link is demonstrated as a suitable platform to observe the predicted supercurrent discretization. At first, the theoretical framework is briefly introduced and the current state of research reported in other material systems is summarized in a short literature overview (6.1). Next, our experimental results are discussed (6.2), including the analysis of the confined critical current in the SQPC as a function of both SG and TG, as well as a study of the subgap conductance. The chapter ends with a short conclusion (6.3).

6.1 Literature review

6.1.1 Theoretical framework

In a Josephson junction consisting of a normal conducting weak link in the clean limit the ratio of the critical current I_c and normal state conductance G_n becomes a constant value of order $\sim \Delta_0/e$ (with Δ_0 the superconducting energy gap) [Lik79; Tin04], which was first proposed by Kulik and Omel'yanchuk in 1977, who provided a theory of the stationary Josephson effect for the case of a short classical ballistic superconducting point contact [KO77; KO78]. Here, the expressions *short*, *classical* and *ballistic* describe a regime $\lambda_F \ll W$ and $L \ll l, \xi_0$, where W, L are the width and length of the point contact, respectively, λ_F is the Fermi wavelength, l the mean free path and ξ_0 the superconducting coherence length. The critical current at zero temperature is then

calculated according to[1]

$$I_s(\varphi) = G_n \frac{\pi\Delta(T)}{e} \sin(\varphi/2) \tanh\left(\frac{\Delta(T)}{2k_B T}\cos(\varphi/2)\right) \quad , \tag{6.1a}$$

$$I_c(T=0) = \max\{I_s(\varphi)(T=0)\} = G_n \frac{\pi\Delta_0}{e} \quad , \quad |\varphi| = \pi + 2\pi j \quad . \tag{6.1b}$$

Although this semiclassical model based on Boltzmann-type equations cannot be applied to the case of a quantum point contact, one would already expect following from this equation an inherited discretization of the critical current due to a quantized normal state conductance. This idea was put forward by Beenakker and van Houten [BH91a] shortly after the first experimental proof of conductance quantization in a QPC [Wee+88a; Wha+88], using a fully quantum-mechanical approach by solving the Bogoliubov-de Gennes equations for quasiparticle wavefunctions in a short QPC Josephson junction ($L \ll \xi_0$). The resulting critical current at zero temperature is indeed found to be discretized as[2]

$$I_s(\varphi) = Ng \frac{e\Delta(T)}{2\hbar} \sin(\varphi/2) \tanh\left(\frac{\Delta(T)}{2k_B T}\cos(\varphi/2)\right) \quad , \tag{6.2a}$$

$$I_c(T=0) = \max\{I_s(\varphi)(T=0)\} = Ng \frac{e\Delta_0}{2\hbar} \quad , \quad |\varphi| = \pi + 2\pi j \quad , \tag{6.2b}$$

where N is the number of transport modes and g accounts for the degeneracy. Considering a quantized normal state conductance $G_n = NG_0 = Nge^2/h$, the equation becomes the natural quantum-mechanical extension of the classical expression in Eq. 6.1. Importantly, this result describes a maximum supercurrent carried by individual transport modes that are formed via single Andreev bound levels, where each channel contributes an equal amount to the total critical current $I_c = NI_{c0}$ with the discretized unit given by

$$I_{c0} = g \frac{e\Delta_0}{2\hbar} \quad . \tag{6.3}$$

Moreover, I_c in the short SQPC is independent of the junction geometry, but the step height I_{c0} still depends on the non-universal superconducting energy gap Δ_0. This is why I_c is rather discretized than quantized in units of I_{c0}. [BH92]

[1] It should be noted that the underlying zero-temperature relationship of supercurrent I_s and phase difference φ between the two superconducting reservoirs at opposite sides of the constriction is non-sinusoidal with discontinuous jumps, *i. e.* markedly different from that of a tunnel junction. For a detailed discussion the reader is referred to [Lik79].

[2] Equivalently to the remark in footnote 1 referring to Eq. 6.1, the respective zero-temperature current-phase relation $I_s(\varphi)$ is again a discontinuous function. At finite temperature the discontinuities become smoothed out and close to the critical temperature $T \approx T_c$ a sinusoidal current-phase relation is recovered with a reduced $I_c = Ng(e\Delta_0^2/8\hbar k_B T_c)$ reached at $\varphi = \pi/2$. [BH92]

In a concurrent theoretical work, Furusaki, Takayanagi, and Tsukada [FTT91; FTT92] calculated numerically a more general expression following from a geometry-dependent analysis. In the short junction limit ($L \ll \xi_0$) their result is in accordance with Eq. 6.2, whereas in the long junction limit ($L \gtrsim \xi_0$) the current is carried by many bound states proportional to L/ξ_0 instead of a single state. The critical current in a SQPC is then no longer independent of the junction geometry but scales with the ratio v_F/L (v_F is the Fermi velocity) and depends strongly on the shape of the constriction itself [FTT91]. Furthermore, in additional calculations the effects of non-adiabatic transport as well as normal reflections at the NS interfaces were included [FTT92] which has been reviewed and analytically discussed in more detail by Chtchelkatchev, Lesovik, and Blatter [CLB00] or Shchelkachev [Shc00].

According to [CLB00; Shc00] the critical current in a long junction with perfect transmission is discretized in units

$$\delta I_c = g\frac{e}{2\tau} \quad , \tag{6.4}$$

where τ can be understood in a quasiclassical picture as the time it takes from the decay of a Cooper pair into a pair of electron and hole quasiparticles at one superconducting contact till the transformation back into a Cooper pair at the opposite superconducting contact, and is given by

$$\tau = \tau_0 + \tau_\Delta \quad . \tag{6.5}$$

Here, τ_0 is the travel time for a quasiparticle traversing the normal region and $\tau_\Delta = \hbar/\Delta_0$ is the time in which an electron wave packet is transformed into a hole wave packet due to Andreev reflection. With $\tau_0 = L/v_F$ for a fully opened transport mode the step height saturates at

$$\delta I_c = g\frac{ev_F}{2(L + \pi\xi_0)} \quad , \tag{6.6}$$

where steps in the critical current are limited by the Fermi velocity v_F and junction length L.[3]

The step height is further quenched if the supercurrent carrying Andreev bound states are transformed into phase-insensitive electronic levels [FTT92; CLB00; Shc00]. This transformation occurs due to scattering at the constriction with non-perfect transmission amplitudes [CLB00] or due to normal reflection instead of Andreev reflection at the NS boundaries with a finite barrier potential [Shc00]. Taking the scattering from

[3] Note, that in the limit $L \ll \xi_0$ (or respectively $\tau_0 \ll \tau_\Delta$) the geometry-independent result of Eq. 6.3 is recovered.

the potential step at imperfect contacts into account, the critical current exhibits a non-monotonic dependence with additional peaks and dips appearing due to the presence of (Fabry-Pérot-type) resonances. On-resonance (peak), I_c is then obtained by summing over all open transport modes with steps given by Eq. 6.4, but with the travel time being replaced by $\tau_0 \to \tau_0[(2/D_Z) - 1]$ [Shc00] including the transmission probability $D_Z = 1/(1 + Z^2)$, where the factor Z describes the barrier strength [BTK82]. In the off-resonance case (dip), the critical current is equal to the sum over a reduced step height $g(e/2\tau)(D_Z/4\pi)$ if $\tau_0 \ll \tau_\Delta$, or $g(e/2\tau_\Delta)(D_Z^2/8)$ if $\tau_0 \gg \tau_\Delta$ [Shc00].

Considering instead reflections from the confinement potential but perfect transmission at the NS interfaces, a simple expression can be found as well for a short junction ($L \ll \xi_0$) with step heights as given in Eq. 6.3 being reduced according to $I_{c0}(1 - \sqrt{R})$ with R the reflection probability [CLB00]. Particularly, the step height of the discretized critical current is much stronger affected by non-perfect transmission of the transport modes in contrast to the quantized normal state conductance $G_n = G_0(1 - R)$. Finally, it is important to note that all presented cases above, which include a finite reflection at either the NS boundaries or the confinement potential itself, yield discrete steps with a subband-dependent transparency, such that the step height could differ from one transport mode to another.

Superconducting quantum point contact based on graphene nanoribbons

The properties of a SQPC in a graphene-based weak link have been discussed in [MZ07] on the basis of narrow nanoribbons. It is found that the critical current sensitively depends on the edge configuration where smooth, armchair and zigzag edges were considered. In the former two cases, *i. e.* smooth and armchair edges, no quantization of the critical current is observed in contrast to common SQPCs. The overall trend of the critical current is predicted to depend linearly on $E_F W/\hbar v_F$ with additional peaks at the onset of a new propagating mode when the junction width changes by the Fermi wavelength. The overall linear trend of I_c is yet suppressed compared to the ideally expected value $I_c = 2Ne\Delta_0/\hbar$ (cf. Eq. 6.2 with $g = 4$). In the limit of a narrow strip at small charge carrier density, the critical current in both cases takes constant minimum values 0 (smooth) and $e\Delta_0/\hbar$ (armchair), respectively. The corresponding current-phase relation in the smooth case is sinusoidal analogous to a tunnel junction $I_s(\varphi) = I_c \sin(\varphi)$, whereas in a narrow armchair ribbon it is given by $I_s(\varphi) = I_c \sin(\varphi/2)\cos(\varphi/2)/|\cos(\varphi/2)|$ with discontinuous jumps similar to the current-phase relation in a SQPC.

Unlike the other two scenarios, narrow graphene nanoribbons with zigzag edges are predicted to show discrete steps in the critical current, although remarkably different to that in an ordinary SQPC. The calculated sequence of steps appears to be half-integer quantized $(n + 1/2)4\,e\Delta_0/\hbar$ (in resemblance of the half-integer quantum Hall

effect in single-layer graphene) and with steps 2 times larger than would be expected from the ideal value $I_{c0} = 2e\Delta_0/\hbar$ (considering fourfold degeneracy). The corresponding current-phase relation is the same as for the armchair nanoribbon.

However, it should be mentioned that with respect to the here presented experiments based on a BLG weak link with smooth electrostatically induced confinement, the applicability of these predicted results for the case of single-layer graphene nanoribbons seems questionable.

6.1.2 State of research

Several experiments in various material systems have been performed to study the predicted discretization of the critical current in a SQPC. Initially, this concept could be demonstrated in a superconducting mechanically controllable break junction made of Nb, where a discretized critical current with steps of order $\sim e\Delta_0/\hbar$ was observed by mechanically changing the constriction diameter [MRJ92]. Later, measurements on atomic contacts between superconducting electrodes were expanded upon further materials [Sch+98]. However, tunability of these systems appears challenging, *i. e.* controlling transparency and the number of conduction channels which are directly linked to the valence orbital structure and thus sensitively depend on the contact configuration at the atomic-scale. A review on the quantum properties of atomic-sized conductors can be found in [AYR03].

Another, most commonly pursued approach is based on a gate-tunable platform, *i. e.* semiconductor–superconductor hybrid junctions, which offers a suitable route towards the implementation of a SQPC within the weak link by exploiting existing confinement techniques in conventional 2DEG devices but coupled to superconducting electrodes. For instance, measurements reporting on the discretization of I_c have been performed in heterostructures based on InAs [TAN95; TAN96; Bau+05; Iri+14] and Ge/SiGe [Hen+19] as well as in nanowires made of InAs [Aba+13] or Si/Ge [Xia+06]. However, the observed step heights were typically orders of magnitude smaller than the theoretically expected ideal value I_{c0}, with the exception of the result reported in a short Si/Ge nanowire [Xia+06] missing only a factor $\sim$ 3–4. The suppressed critical current is mainly attributed to geometry-dependent quantum size effects in long junctions [FTT91], or explained by non-perfect transmission either in the weak link channel [CLB00] or at the NS interfaces [Shc00].

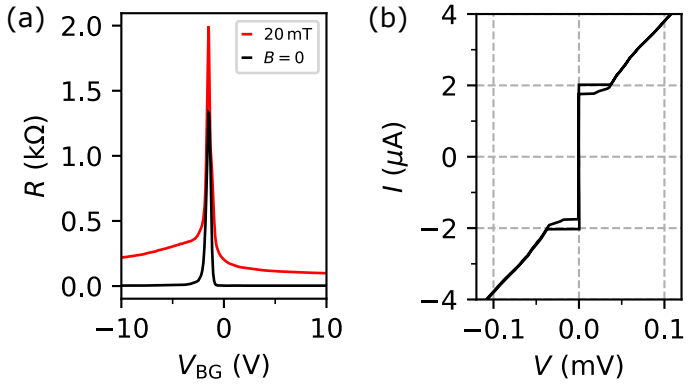

Figure 6.1: Planar 2D BLG weak link. (a) Resistance curves of normal state (red) and superconducting state (black) as a function of V_{BG} at approximately uniform overall doping in the device, *i. e.* $V_{TG} = 0$ and $V_{SG} = V_{SG}^{cnp}$. The normal state data was recorded in a separate cooldown and for better comparison shifted by $-0.2\,V$ in order to align both curves at the same charge neutrality point V_{BG}^{cnp}. (b) Up- and down sweep IV curve at $V_{BG} = 10\,V$.

6.2 Experimental results

Here, based on the foundations of the previous two chapters, *i. e.* confinement of a supercurrent in the BLG weak link [Kra+18b] and conductance quantization in the normal state due to the formation of 1D subbands in the electrostatically induced BLG QPC [Kra+18a], we report a study on a gate-defined SQPC in a BLG weak link junction. The presented measurements are based on the same device as in chapter 5, but probed in the superconducting regime. The experiments are performed at a base temperature of about $\approx 15\,mK$ and for measurements in the normal state an out-of-plane magnetic field $B = 20\,mT$ is applied.

6.2.1 Initial device characterization

To start with, the basic (superconducting) properties of the BLG weak link junction are discussed. We note that the basis for observing a discretized critical current, that is confining the supercurrent together with the formation of quantized 1D subbands, has been already discussed in detail in chapters 4 and 5. In this regard, the here presented initial device characterization is kept only to a necessary minimum. Figure 6.1a shows the BG dependence of the resistance for both normal state (red) and superconducting state (black) at $V_{TG} = 0$ and $V_{SG} = V_{SG}^{cnp}$, corresponding to assumable homogeneous charge carrier density in the overall device, *i. e.* without induced confinement.[4] At

[4] The data for the two curves were recorded in separate cooldowns. Out of convenience, both curves are aligned to the same neutrality point as described in the caption of Fig. 6.1.

the Dirac point a sharp resistance peak is observed in both cases . The presence of *pn*-junctions at the metal contact interfaces is once again reflected in the observed asymmetry of the saturating normal state resistance on electron and hole side at high charge carrier densities (cf. chapter 4 and 5). In contrast to the normal state, the resistance in the superconducting state rapidly decreases to zero away from the charge neutrality point due to a finite supercurrent through the BLG weak link.

An IV curve (up- and down-sweep) at $V_{BG} = 10\,V$, *i. e.* large electron doping $\approx 5 \times 10^{12}\,cm^{-2}$, is shown in Fig. 6.1b. The extracted critical current $I_c = 2.05\,\mu A$ and normalized to the normal state conductance $I_c R_n \gtrsim 200\,\mu V$, corresponding to $\approx 2\Delta_0/e$ (with $\Delta_0 = 101\,\mu eV$ estimated from the position of the $m = 2$ MAR peak $V = \Delta_0/e$). We note that this value is somewhat larger than obtained in the same device prior deposition of the additional overall TG (cf. chapter 4), indicating a stronger proximity-coupling affected by the presence of the overlapping gate to the superconducting electrodes. Importantly, the obtained $I_c R_n$ is close to the theoretically predicted maximum $\sim 2.44\Delta_0/e$ at $T = 0$ for ideal wide and short ballistic graphene weak links [TB06], even despite the fact that the device can be considered in the intermediate regime $L \lesssim \xi_0$ between the two limits of short ($L \ll \xi_0$) and long ($L \gg \xi_0$) junction. In the case of a long ballistic weak link $I_c R_n$ scales with $1/L$, while at finite temperature this dependence is presumed to hold as well for $L \sim \xi_0$ [RKC16] in agreement with experimental observations [Ben+16]. We note that here the weak link is made from a bilayer instead of a monolayer graphene. However, at high doping different models for the BLG case agree on a similar or almost identical supercurrent magnitude compared to a single layer graphene junction [MCP12; TI11; TI12]. We further note that $I_c R_n \approx 2\Delta_0/e$ matches with recently reported largest $I_c R_n$ products in a short ballistic weak link [Par+18].

Confinement of the supercurrent is realized using the combination of BG and SG. Correspondingly, the resistance map in the superconducting state as a function of V_{BG} and V_{SG} is presented in Fig. 6.2a. The details of such a map for a split-gated BLG weak link have been discussed explicitly in chapter 4. Here, only one important point is recapitulated, which is the observation of a dissipationless current, *i. e.* zero resistance, where the Fermi level underneath the SG is positioned in the induced band gap at maximal displacement field. In this configuration the supercurrent is expected to only flow via the 1D channel of the induced SQPC.

The confinement is checked and monitored via superconducting magneto-interferometry measurements, shown in Fig. 6.2b for two different gate conditions $V_{SG} = -8.5\,V$ (orange) and $-12\,V$ (blue) at $V_{BG} = 10\,V$ (the respective conditions are marked in the map of Fig. 6.2a by colored dots). Clear indication of the constriction formation is observed as the interference patterns undergo a change from a beating pattern (top panel; orange) into a monotonically decaying pattern (bottom panel;

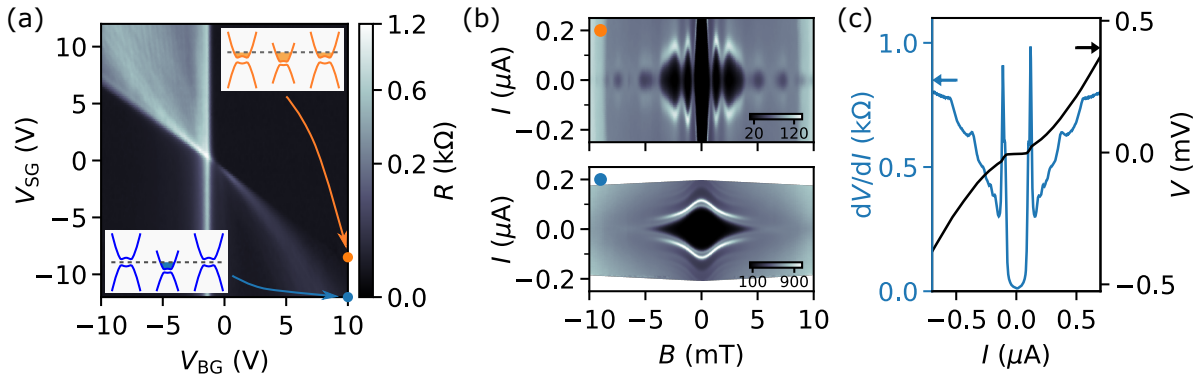

Figure 6.2: Confining the supercurrent. (a) Resistance map in the superconducting state as a function of V_{BG} and V_{SG} at $V_{TG} = 0$. Insets: Illustrated spatial band structure diagrams across the split-gated constriction for two different gate conditions $V_{BG} = 10\,\mathrm{V}$ and $V_{SG} = -8.5\,\mathrm{V}$ (orange; top right corner) or $V_{SG} = -12\,\mathrm{V}$ (blue; bottom left corner), respectively. (b) Respective superconducting magnetic interference patterns for the two scenarios (upper panel: orange; lower panel: blue), showing the differential resistance (in Ω) as a function of magnetic field B and current I. (c) Corresponding curve of the differential resistance $\mathrm{d}V/\mathrm{d}I$ (blue, left y-axis) as a function of current I at $B = 0$ for the lower panel in (b), together with the respective IV curve (black, voltage plotted versus right y-axis).

blue). Sketches of the corresponding spatial band structure across the split-gated confinement for the two scenarios are depicted as insets in Fig. 6.2a.

Figure 6.2c shows the respective curve of the differential resistance $\mathrm{d}V/\mathrm{d}I$ (blue, left y-axis) as a function of current I for the gate condition of the confined supercurrent (*i. e.* corresponding to $B = 0$ of the lower interference panel in Fig. 6.2b; blue marker dot), together with its IV curve (black; voltage plotted versus right y-axis). Importantly, despite the supercurrent being strongly reduced compared to the 2D case, a finite critical current can be measured. In the following analysis, I_c is extracted from the position of the resistance peak maximum marking the switching from superconducting dissipationless to resistive current.[5]

Here, for the fully confined supercurrent at $V_{TG} = 0$, the extracted critical current $I_c = 115\,\mathrm{nA}$ and $I_c R_n = 100\,\mu\mathrm{V}$ corresponding to $\approx \Delta_0/e$, respectively. Although the contact interfaces and reservoirs are not tuned (*i. e.* same $V_{BG} = 10\,\mathrm{V}$ and $V_{TG} = 0$), the coupling strength expressed in the $I_c R_n$ product appears weakened in the 1D confined regime ($V_{SG} = -12\,\mathrm{V}$) compared to the 2D weak link ($V_{SG} = 0$). However, we note that the value $\approx \Delta_0/e$ is amongst the largest (or greater than) reported in 1D superconductor–semi-conductor hybrid junctions [TAN95; TAN96; Bau+05; Doh+05; JvK06; Xia+06; Nil+11; Aba+13; Iri+14; Hen+19].

[5] We note that a slight kink in the resistance peak is visible. This constituted double peak structure (also more pronounced visible under different gate conditions) is primarily observed in the confined regime and may indicate a non-homogeneous switching in different regions of the junction.

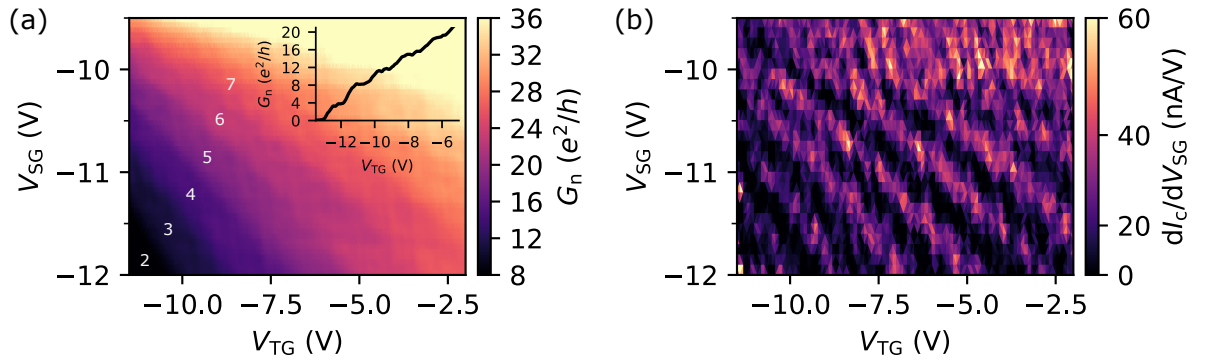

Figure 6.3: Mapping the discretization of the critical current. (a) Color map of the normal state conductance G_n as a function of V_{TG} and V_{SG} at constant $V_{BG} = 10\,V$. Plateaus are labeled with the corresponding 1D subband index n. Inset: Trace of G_n at $V_{SG} = -12\,V$. (b) Differentiated critical current dI_c/dV_{SG} mapped under the same gate voltage conditions as in (a). Dark colors and bright colors reflect plateaus and steps in the critical current I_c, respectively.

Thus, the presented preconditions of a tailoring supercurrent confinement in the BLG weak link (for a detailed description see the discussion in chapter 4) provide a convenient basis for studying a discretization of the critical current. Therefore, we now explore the maximum supercurrent, *i. e.* critical current I_c, in a varying confinement tuned by SG and TG.

6.2.2 Discretization of the critical current

As already demonstrated in chapter 5, the confinement and thereby the number of populated transverse modes through the constriction can be controlled by tuning SG and TG while keeping the BG fixed. In the same fashion, we here start by mapping the critical current, *i. e.* by measuring a series of current-voltage curves, as a function of V_{TG} and V_{SG} at a constant $V_{BG} = 10\,V$. The resulting map of the differentiated dI_c/dV_{SG} is shown in Fig. 6.3b in comparison with the corresponding normal state conductance G_n in Fig. 6.3a. In the latter case, a stripe pattern of conductance plateaus is observed as already presented and discussed in chapter 5. Likewise, the critical current I_c exhibits a step-like variation, where plateaus and steps are visible as black regions and bright lines, respectively. Importantly, the map of quantized normal state conductance G_n is directly reflected in the changes of the critical current dI_c/dV_{SG}. Also, it should be noted that again faint and blurry vertical lines can be seen, where I_c is additionally modulated by the conductance oscillations observed in the normal state due to Fabry-Pérot interferences within the BLG reservoirs as discussed earlier in this thesis (chapters 4 and 5). The ballistic conductance resonances being directly reflected in an oscillating critical current is considered as a signature of ballistic supercurrent [Cal+15; Ben+16].

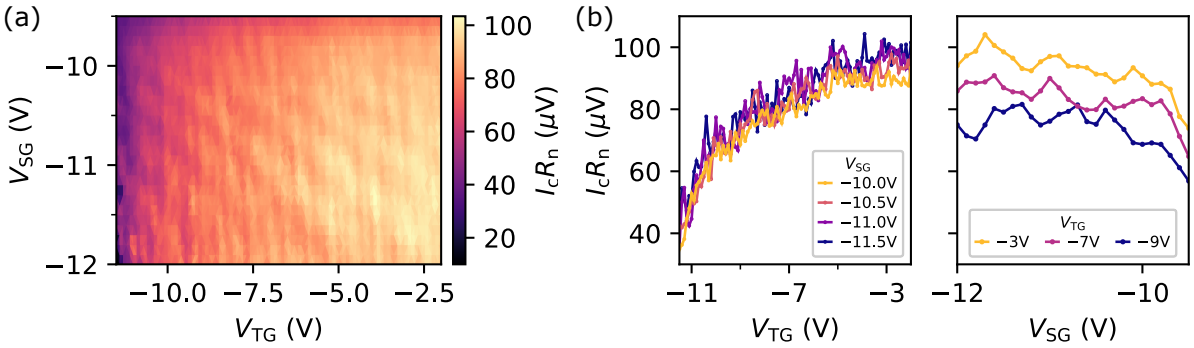

Figure 6.4: Mapped critical current normalized with respect to its normal state conductance. (a) Color map of the I_cR_n product as a function of V_{TG} and V_{SG}. (b) Traces of I_cR_n as either a function of V_{TG} (left panel) or V_{SG} (right panel), respectively.

Figure 6.4a shows the critical current normalized with respect to its normal state conductance (*i. e.* the corresponding I_cR_n product of the data in Fig. 6.3) for which ideally a constant value would be expected [BH91a]. However, the map clearly does not show a single value. Instead, individual features such as Fabry-Pérot resonances are distinctly resolved, indicating that the relative oscillation amplitude is different in the normal state conductance and critical current. Also, blurry stripes at the step positions remain visible due to unequally sharp transitions between the plateaus.

The TG and SG dependence of I_cR_n is further elaborated in Fig. 6.4b, showing curves as either a function of V_{TG} (left panel) or V_{SG} (right panel) for different voltages of the respective other gate. In the former case, I_cR_n saturates for $V_{TG} \to 0$ at about 100 µV corresponding to $\approx \Delta/e$, but is progressively suppressed upon increasingly negative V_{TG}. Notably, the described trend is consistently observed for any SG voltage such that all the curves sit nearly on top of each other independently of the applied V_{SG}. This implies that I_cR_n should be constant as a function of V_{SG} which is indeed observed in Fig. 6.4b (right panel). Here, curves of I_cR_n reveal within the range of noticed 1D subband formation ($V_{SG} \lesssim -10\,\mathrm{V}$) a fairly constant value with only small variations, but the magnitude of I_cR_n depends on V_{TG}.

Briefly summarized, the mapped critical current I_c through the SQPC reveals a limiting effect of the TG, especially apparent in the gate dependence of the I_cR_n product. Here it should be noted, that the TG not only controls the confinement and channel of the SQPC itself, but tunes simultaneously the band structure in the entire BLG weak link as well as the transmission at the contacts. Therefore, by depleting the 1D subbands via the TG the supercurrent amplitude in the complete weak link is quenched. On the other hand, the SG can be used to squeeze the channel independently of the BLG bulk reservoirs. However, the range of applicable V_{SG} appears limited before the confinement collapses as the Fermi level underneath the SG is no longer positioned in the gap but already tuned into the valence band, forming *pnp*-junctions rather than a

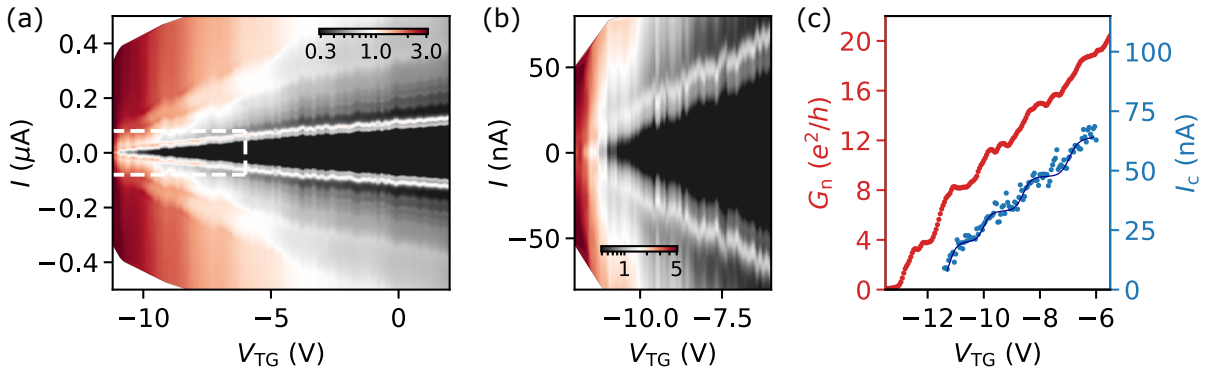

Figure 6.5: Top gate dependence of the critical current in the SQPC. (a) Color map of the differential resistance $\mathrm{d}V/\mathrm{d}I$ (in kΩ) as a function of V_{TG} and I at constant $V_{\mathrm{BG}} = 10\,\mathrm{V}$ and $V_{\mathrm{SG}} = -12\,\mathrm{V}$. (b) Zoom-in measurement of (a) as denoted by the white dashed box. (c) Extracted critical current I_{c} (blue, right y-axis) and the respective normal state conductance G_{n} (red, left y-axis) as a function of V_{TG}. A smoothed curve is added (thin darker blue line) as guide to the eye, emphasizing the rather step-like evolution of I_{c}.

constriction (see Appendix D.2 and discussions in chapter 4 and 5). In what follows, the gate dependence of I_{c} is analyzed in more detail, first as a function of V_{TG} (6.2.3) and finally as a function of V_{SG} (6.2.4).

6.2.3 Top gate dependence of the discretized critical current

Figure 6.5a shows the differential resistance $\mathrm{d}V/\mathrm{d}I$ as a function of current I tuned by V_{TG} at constant $V_{\mathrm{BG}} = 10\,\mathrm{V}$ and $V_{\mathrm{SG}} = -12\,\mathrm{V}$. At this configuration of BG and SG the SQPC is operated in the confined regime as e. g. demonstrated by the superconducting magnetic interference pattern in Fig. 6.2b. It can be seen that the maximum supercurrent in the SQPC gets reduced when the system is depleted with increasingly negative V_{TG}, but at this scale no discretized steps are discernible. However, it is important to note that outside the superconducting region additional resonant lines are recognized, which are due to MAR [Oct+83; CY06], revealing a step-like behavior in the current. Clearly, the subgap conductance is governed by the number of transport modes through the SQPC, but will be discussed later (see subsection 6.2.5).[6]

In Fig. 6.5b a zoom-in measurement with higher resolution is presented for the range $-12\,\mathrm{V} < V_{\mathrm{TG}} < -6\,\mathrm{V}$. Now, a rather step-like behavior is vaguely observed, partially obscured by oscillations which can be attributed to the presence of Fabry-Pérot interferences in the normal state as pointed out beforehand. The extracted critical current

[6] It is more instructive to study these subharmonic gap structures as a function of bias voltage V rather than current I.

I_c is shown in Fig. 6.5c (blue; right y-axis) together with the corresponding normal state conductance G_n (red; left y-axis), which displays a well-developed sequence of quantized conductance plateaus down to the lowest subband (cf. chapter 5). Unlike G_n, steps in I_c are less recognizable. Especially I_c being highly sensitive to any influence on the weak link, the additional oscillations due to Fabry-Pérot resonances tuned by the TG appear strongly pronounced in the critical current, *i. e.* their amplitude is of comparable size to the step height. In the consequence, only a faint but rather obscured step-like variation of I_c as a function of V_{TG} is visible. Moreover, the step height is seemingly decreasing and below the second conductance plateau a more and more rounded switching occurs in the current-voltage curves, such that extracting I_c becomes unreasonable. Thus, the critical current finally trends towards zero, but reappearing signatures of a Josephson coupling are observed at the position of the first plateau, *i. e.* a finite excess current I_{exc} and increased subgap conductance.

6.2.4 Split gate dependence of the discretized critical current

At this point, the SG dependence of the discretized critical current is studied. Unlike the overall TG the locally defined SG does not act on the entire BLG weak link but only controls the confinement of the SQPC itself. Figure 6.6a shows a color map of the differential resistance $\mathrm{d}V/\mathrm{d}I$ as a function of I continuously measured for different V_{SG} at constant $V_{BG} = 10\,\mathrm{V}$ and $V_{TG} = -10\,\mathrm{V}$. Unambiguously, the switching of the supercurrent exhibits a staircase-like variation, demonstrating the discretization of I_c. The extracted critical current I_c is plotted in Fig. 6.6b (blue; right y-axis) in direct comparison with the normal state conductance G_n (red; left y-axis) under the same gate condition. At this combination of BG and TG, a sequence of conductance plateaus is observed down to the third lowest 1D subband within the range of maximal applied V_{SG}. In accordance with the quantized normal state conductance a step-like increase of the critical current occurs with each additionally contributing transport mode. The correlation between G_n and I_c is also reflected in a considerably constant $I_c R_n$ product, shown in Fig. 6.6c. Within the range of observed 1D subband formation, $I_c R_n$ varies by less than 10% around the mean value of 74 µV, where fluctuations can be mainly attributed to the unequally sharp steps.

Below, a quantitative analysis of the discretized critical current is presented. For that, I_c is fitted according to the following equation adopted from the Landauer formalism:

$$I_c = \delta I_c \sum_n T_n \quad , \tag{6.7}$$

where the critical current is calculated by the sum over the transmission probabilities T_n of each 1D transport mode n multiplied by the discretized unit δI_c. Out of

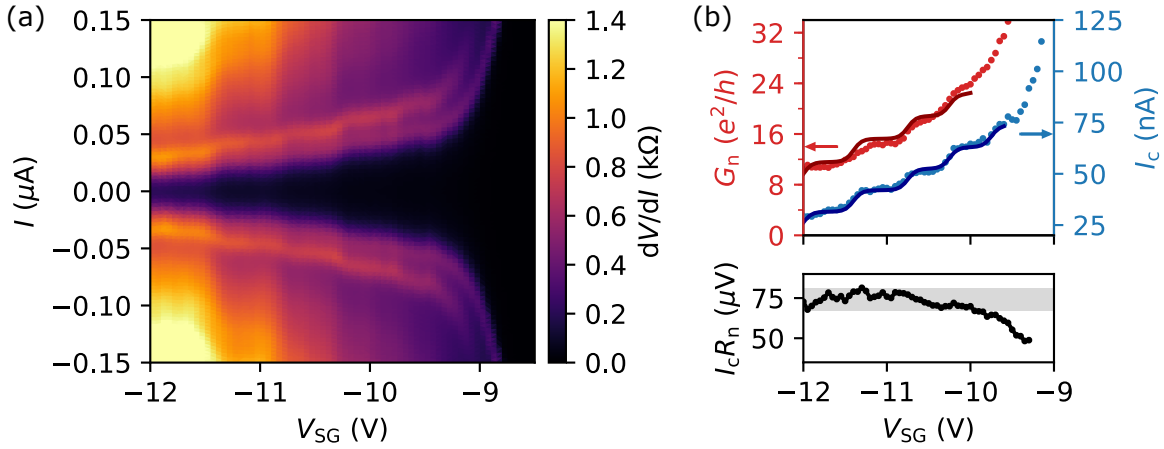

Figure 6.6: Split gate dependence of the critical current in the SQPC. (a) Color map of the differential resistance $\mathrm{d}V/\mathrm{d}I$ as a function of V_{SG} and I at constant $V_{\mathrm{BG}} = 10\,\mathrm{V}$ and $V_{\mathrm{TG}} = -10\,\mathrm{V}$. (b) Extracted critical current I_{c} (blue; right y-axis) as a function of V_{SG} in comparison to the normal state conductance G_{n} (red; left y-axis). Solid lines are fits to the data using Eqs. 6.7 and 6.9, respectively. (c) Corresponding $I_{\mathrm{c}}R_{\mathrm{n}}$ product. The gray shaded region denotes a range of the mean value plus and minus twice the standard deviation ($\approx 74 \pm 7\,\mu\mathrm{V}$).

simplicity, we have used a saddle-point confinement potential, neglecting geometry-dependent factors [Gla+88] as well as the complex band structure tuning within the BLG channel [KF18]. The transmission probability is then given by [Büt90]

$$T_n = \frac{1}{1 + \mathrm{e}^{-\pi\epsilon_n}} \quad , \tag{6.8}$$

with $\epsilon_n = 2(E_{\mathrm{F}} - E_n)/\hbar\omega_x$, where E_{F} is the Fermi energy and E_n is the nth 1D subband energy level. Based on the form of T_n, the transmission probability of subbands above E_{F} is exponentially suppressed, whereas all open transport modes contribute equally by the same discretized value δI_{c} to the total critical current I_{c}. The sharpness of the steps is determined by the curvature of the confinement potential $\hbar\omega_x$. For fitting this energy dependent equation to the data as a function of gate voltage, we assume a linear relationship $E = \alpha_{\mathrm{SG}} e V_{\mathrm{SG}}$ [Kra+18b].

The resulting fit to I_{c} with the respective set of parameters $\delta I_{\mathrm{c}} = 10.5\,\mathrm{nA}$ and $\hbar\omega_x = 0.32\,\mathrm{V}$, yielding a curve with uniform steps of equal height, is plotted in Fig. 6.6b (dark blue solid line). Additionally, a curve for the normal state conductance G_{n} is provided (dark red solid line), using the exact same parameters but replacing the step height δI_{c} with the fourfold degenerate conductance quantum $G_0 = 4e^2/h$ and including a contact resistance of $2R_{\mathrm{C}} = 80\,\Omega$:

$$G_{\mathrm{n}}^{-1} = \left[G_0 \sum_{n=1} T_n \right]^{-1} + 2R_{\mathrm{C}} \quad . \tag{6.9}$$

The fact that the extracted I_c can be fitted by employing a universal step height δI_c for all visible plateaus $n = 3, 4, 5, 6, (7)$ (at this given $V_{BG} = 10\,V$ and $V_{TG} = -10\,V$) with steps occurring at the same positions as in the quantized normal state conductance G_n demonstrates that the supercurrent is carried by individual Andreev bound states via size-quantized transport modes through the SQPC without mixing of the channels at the plateaus [BH91a].

The described fitting is done for another confinement condition at different TG voltage (*i. e.* $V_{TG} = -8\,V$; shown in Appendix E.1). Consistently, the data can be described with a constant step height, although with a TG dependent different value $\delta I_c^{(2)} = 12\,nA$. However, in comparison with the theoretically expected ideal value $I_{c0} = 2e\Delta_0/\hbar = 49.2\,nA$, our reported step heights δI_c turn out to be suppressed but are in the same order of magnitude (comparable to the reported suppression in [Xia+06] getting the most close to the expected ideal value throughout literature to the best of our knowledge). Possible reasons and arguments that could explain the observed reduction and TG dependence of δI_c are discussed in the following.

Discussion of suppressed step heights in the critical current

First, taking the finite weak link channel length $L \lesssim \xi_0$ into account, the theoretical step height for perfect transmission is reduced to $\delta I_{c0} = 2e/(\tau_0 + \hbar/\Delta_0)$, involving the travel time $\tau_0 = L/v_F$ of a quasiparticle traversing the weak link channel (see Eq. 6.6 in subsection 6.1.1) [CLB00; Shc00]. Although the Fermi velocity is unknown due to the complex band structure tuning in the BLG weak link, an upper bound $\delta I_{c0} = 42.9\,nA$ for steps in the discretized critical current is estimated with assumed maximum Fermi velocity $v_F = \sqrt{3}a\gamma_0/2\hbar \approx 1 \times 10^6\,m\,s^{-1}$ from the rather linear band structure at higher energies [MK13]. Still, our reported values of δI_c lack by a factor 3–4 compared to the theoretical expectation δI_{c0} in the junction with finite length. We note that with a possibly smaller v_F due to the band structure tuning at the bottom of the bands the calculated step height δI_{c0} could be significantly further reduced.

Second, as aforementioned, the overall TG acts on the entirety of the weak link, *i. e.* depleting both SQPC channel and BLG reservoirs, while tuning the contact interfaces to the superconducting metal leads at the same time. In the consequence, the proximity-coupling is quenched upon the increasing opening of a gap in the BLG reservoirs as observed in the SG- and TG-dependence of the I_cR_n product (see subsection 6.2.2), resulting in the reduction of the extracted δI_c at larger negative V_{TG} (for positive V_{BG}). This limiting effect on the supercurrent injection into the BLG weak link can be understood to a certain extend due to an effectively reduced superconducting energy gap $\Delta_0^*(V_{TG})$ as a function of TG voltage which is shown later in subsection 6.2.5 with a discussion on the subgap conductance. Considering the quenched gap size

$\Delta_0^*/\Delta_0 < 1$ in turn yields an effectively reduced ideal step height $I_{c0}^* = 2e\Delta_0^*/\hbar$ or $\delta I_{c0}^* = 2ev_F/(L + \pi\xi_0^*)$ with $\xi_0^* = v_F\hbar/\pi\Delta_0^*$, respectively.

A comparison of all extracted δI_c with the theoretical values I_{c0}^* and δI_{c0}^* is summarized in Tab. 6.1. The displayed numbers in parenthesis correspond to the ratio of experimental to theoretical values $\delta I_c/I_{c0}^*$ or $\delta I_c/\delta I_{c0}^*$, respectively. We note that taking into account the reduction of the critical current due to the two reasons discussed above, *i. e.* a finite channel length as well as a smaller effective superconducting energy gap, can not fully explain the observed reduction of the step height. The remaining difference could be probably explained by a non-perfect transmission of the transport modes carried by Andreev bound states, which could be due to normal reflections from the NS boundaries [CLB00; Shc00].[7] However, while the presence of Fabry-Pérot resonances might be indication of a barrier potential at the contact interfaces leading to a reduced probability of Andreev reflection, we recall that without tuning directly the contact interfaces (*i. e.* constant $V_{BG} = 10\,V$ and $V_{TG} = 0$) the strength of the 1D supercurrent expressed in $I_cR_n \approx \Delta_0/e$ measured at $V_{SG} = -12\,V$ appears already suppressed compared to the value $\approx 2\Delta_0/e$ in case of the uniform configuration at $V_{SG} = 0$ (see subsection 6.2.1). On the other hand, the SG acts on the channel in the confined regime due to stray-fields, implying that band structure tuning might be an important aspect.

V_{TG}/V	Δ_0^*/Δ_0	δI_c/nA	I_{c0}^*/nA	δI_{c0}^*/nA
−8	0.95	12.0	46.7 (0.26)	41.0 (0.29)
−10	0.86	10.5	42.3 (0.25)	37.6 (0.28)

Table 6.1: Summarized step height values of the critical current in the SQPC. Extracted step height δI_c for two different V_{TG} in comparison with theoretical step heights I_{c0}^* of an ideal SQPC or δI_{c0}^* for a SQPC embedded in a weak link of finite length L and considering perfect transmission. The experimental values are extracted from the fit to the data according to Eq. 6.7, and calculated values are obtained from Eqs. 6.3 and 6.6 assuming $v_F = 1 \times 10^6\,m\,s^{-1}$ and taking the effectively reduced superconducting energy gap $\Delta_0^*(V_{TG})$ into account (numbers in parenthesis give the ratio of measured to calculated step height). For gap size $\Delta_0 = 101\,\mu eV$ found in our 2D BLG weak link junction the ideal step height $I_{c0} = 49.2\,nA$.

Finally, it should be noted that the maximum supercurrent in ballistic graphene weak link junctions is already predicted to be cut-off to only about half of the ideal value $2Ne\Delta_0/\hbar$ (with N the number of degenerate transport modes) due to a mismatching

[7] Scattering from the confinement potential [CLB00] seems less likely regarding the fact that in the normal state conductance robustly quantized steps in units of $4e^2/h$ are observed without subtracting a small (TG-dependent) contact resistance, which implies a transmission probability of 1D channels through the QPC close to unity.

Fermi wavelength at the NS interfaces [TB06] (cf. subsection 2.3.6). Taking such limited I_c for graphene Josephson junctions into account, our reported steps δI_c almost match with the theoretical discretized values δI_{c0}^* with perfect transmission. However it should be remarked that this reduced critical current is discussed in the case of wide graphene junctions. In contrast, another theoretical work [MZ07] deals with narrow graphene nanoribbon weak links in the context of SQPCs, where it is found that the critical current sensitively depends on the edge configuration (cf. subsection 6.1.1). While for smooth and armchair edges the absence of discrete steps is predicted, zigzag nanoribbons should show a half-integer sequence with enhanced steps. Considering the smooth electrostatic potential in our SQPC, the smooth edge configuration seems to have the best correspondence but would not show the discretization of the critical current. Yet, all the different calculations for graphene weak links show that this system is indeed special due to the interplay of relativity and superconductivity and can diverge from the norm of ordinary weak links (or SQPCs). After all, it remains an open question what should be expected for an SQPC in a BLG weak link, especially with regard to the complex band structure tuning within the weak link channel itself (even fundamentally different from the single-layer case).

6.2.5 Subgap conductance

As a last point, we study the subgap transport in order to further analyze the SQPC properties. Figure 6.7a shows a gray-scale map of the numerical derivative of the differential conductance $\mathrm{d}^2I/\mathrm{d}V^2$ as a function of bias voltage V and V_{TG} at $V_{BG} = 10\,\mathrm{V}$ and $V_{SG} = -12\,\mathrm{V}$ (note that this is the same data set as in Fig. 6.5). The bright line at $V = 0$ is due to the finite supercurrent through the weak link. Besides, as aforementioned, additional resonant features are observed within the subgap bias voltage range $V < 2\Delta_0/e$. These conductance resonances occur at $V = 2\Delta_0/(me)$ with $m = 1, 2, 3, 4$ and are attributed to MAR [Oct+83; CY06]. Note, that the $m = 1$ subharmonic structure is positioned at decreased bias V, which might be due to an effectively reduced superconducting energy gap caused by self-heating effects for the higher applied bias voltages [Xia+06]. Another point to be noted is that the MAR peaks trend towards smaller bias voltage with increasingly negative V_{TG}, as visualized by the dashed orange line tracing the $m = 2$ resonance. Since the bias voltage of the subharmonic gap structure directly depends on the superconducting energy gap, we find an effectively reduced gap size Δ_0^* as a function of V_{TG} (as mentioned previously), which is shown as inset in Fig. 6.7a. Notably, the TG dependence of Δ_0^* is similar to the one of the I_cR_n product (see Fig. 6.4b), which partly explains the supercurrent suppression when 1D subbands are depopulated by means of the TG.

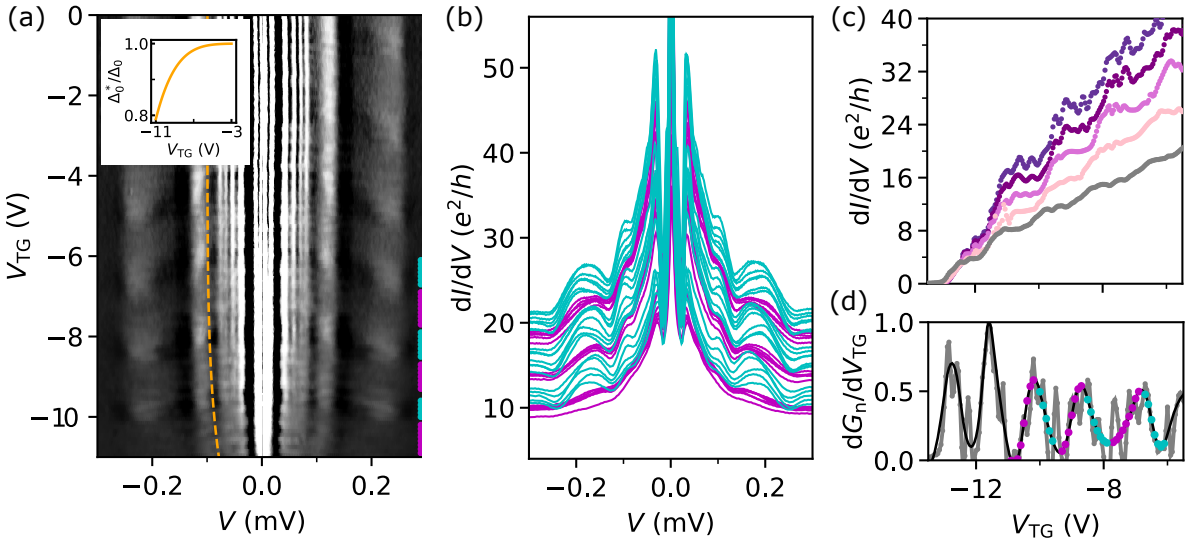

Figure 6.7: Subgap conductance in the SQPC. (a) Numerical derivative of the differential conductance $\mathrm{d}^2I/\mathrm{d}V^2$ as a function of V and V_{TG} at constant $V_{\mathrm{BG}} = 10\,\mathrm{V}$ and $V_{\mathrm{SG}} = -12\,\mathrm{V}$ (data is differentiated from large bias towards zero for both positive and negative polarities, respectively). Inset: Effective superconducting energy gap $\Delta_0^*(V_{\mathrm{TG}})/\Delta_0$, extracted from the MAR peak $m = 2$ at bias $V = \Delta_0^*/e$ (shown by the dashed orange line in the main panel). Colored dots at the right edge of the panel mark V_{TG} values of the curves shown in (b). (b) Differential conductance $\mathrm{d}I/\mathrm{d}V$ versus V for different V_{TG} (note that curves are not shifted). The color code denotes strong (cyan) or weak (magenta) MARs. (c) Subgap differential conductance $\mathrm{d}I/\mathrm{d}V$ as a function of V_{TG} for different $V = 2\Delta_0/(em)$ with $m = 1$ (pink), 2 (orchid), 3 (purple) and 4 (dark purple) in comparison with the normal state conductance G_{n} (gray). (d) Differentiated normal state conductance $\mathrm{d}G_{\mathrm{n}}/\mathrm{d}V_{\mathrm{TG}}$ normalized to its maximum (gray curve) and smoothed (black curve) in order to remove additional oscillations due to the Fabry-Pérot interferences. The position of strong/weak MARs is marked by cyan/magenta dots, respectively.

Finally, it can be noticed that the amplitude of the subharmonic structures is not constant but modulated as a function of V_{TG}, which is observed as an alternation of stronger and weaker resonances (particularly visible for $m = 1$ and $m = 2$). Respective curves of the differential conductance $\mathrm{d}I/\mathrm{d}V$ versus bias voltage V for different V_{TG} in the range $-10.9\,\mathrm{V} \rightarrow -6.2\,\mathrm{V}$ are plotted in Fig. 6.7b (from bottom to top; note that curves are not shifted but only modulated by the applied V_{TG}). We observe a notable suppression of MARs in turns with increased resonances represented by magenta and cyan colored curves, respectively. The corresponding gate conditions of the color coded curves are also marked in Fig. 6.7a.

In Fig. 6.7d the alternating sequence of the subharmonic gap structure is compared with the transconductance $\mathrm{d}G_{\mathrm{n}}/\mathrm{d}V_{\mathrm{TG}}$ in the normal state (here the minimums, *i. e.* ideally zero, correspond to the conductance plateaus, whereas transconductance maximums reflect the steps in-between occurring at the crossing of a 1D subband). Remarkably, the positions of observed enhancement or suppression of the subgap resonances (cyan and magenta dots) are distinctly arranged within the transconductance

curve. Concomitant with a level crossing (peak) appears an on-resonant state with pronounced MARs (cyan) [Ing+01]. In contrast, the MARs are suppressed (magenta) when the next-higher subband starts to contribute (increasing transconductance after traversing a conductance plateau, *i. e.* the minimum in transconductance). Then, as the next subband edge is reached, the MARs are again enhanced (cyan).

The observed interchanging from on- and off-resonances is indication of a channel mixing of two Andreev bound levels when the Fermi level is positioned in between 1D subbands which is not captured within the theory provided in [BH91a] (the theoretical predictions for the discrete supercurrent amplitude being only valid on the plateaus but not at the transition between subbands). We note that a suppression of the transport based on Andreev reflections has been observed as a dip structure in the subgap conductance at the transition to the next energy level (but absent in the normal state conductance) [Kja+16; Zha+17; Hen+19], which is explained due to the presence of a van-Hove singularity at the onset of a new channel resulting in the strong mixing of subbands.

The transport of quasiparticles through the SQPC is as well demonstrated in Fig. 6.7c, showing the differential subgap conductance $\mathrm{d}I/\mathrm{d}V$ for $V = 2\Delta_0/(em)$ with $m = 1, 2, 3, 4$ in comparison with the normal state conductance G_n (gray) as a function of V_TG. While G_n displays the expected staircase conductance with quantized steps in units of $4\,e^2/h$, the subgap conductance varies likewise in a step-like fashion, but with step heights notably increased compared to that of the normal state conductance. The enhanced subgap conductance is a direct consequence of the transport mechanism based on Andreev reflection processes [And64; BTK82], where a multiple of the electronic charge can be transmitted through the SQPC due to the MARs. Noteworthy, the step height of the subgap conductance further increases with higher order MARs, although the higher order subharmonic gap structures diminish as the confinement strengthens. In a QPC facing only one superconductor interface, *i. e.* in a NS junction, a doubling of the conductance due to a single Andreev reflection has been theoretically predicted [HB91; Bee92] as well as experimentally observed [Kja+16]. Here, we find the subgap conductance exceeding twice the (fourfold-degenerate) conductance quantum $G_0 = 4\,e^2/h$ in the normal state due to MARs, similar to what has been reported in a SNS junction based on an InGaAs channel [Iri+14], which is evidence of the phase-sensitive transport down to the lowest subband in our SQPC.

6.3 Conclusion

In this chapter, the discretization of the supercurrent in a BLG SQPC has been investigated based on the foundation of the preceding results in chapters 4 and 5, *i. e.* tunable

formation of 1D subbands in a gate-defined QPC induced within a BLG weak link. While in the uniform 2D junction the measured critical current normalized to the normal state conductance $I_c R_n \approx 2\Delta_0/e$ is close to the theoretically predicted limit for ideal short and wide ballistic graphene Josephson weak links, the supercurrent is successfully confined to 1D with the combination of SG and BG as monitored by superconducting magneto-interferometry. In this confined regime, a large (*i. e.* in comparison to other reported values in literature) $I_c R_n \approx \Delta_0/e$ is recorded at $V_{TG} = 0$.

By tuning the confinement with SG and TG, the number of modes through the 1D channel is controllably varied and the critical current exhibits a step-like variation in accordance with the quantized steps in the normal state conductance. However, it is found that the $I_c R_n$ product as a function of V_{TG} is not a constant value as it would be expected for a discrete critical current, but gets progressively suppressed as the weak link is tuned towards pinch-off using the TG. In the consequence, the critical current features decreasing step heights δI_c weakly resolved as a function of V_{TG}. On the other hand, clearly discretized critical current has been demonstrated as a function of V_{SG} appearing in direct correlation with the respective quantized staircase in the normal state conductance. The observed steps in the critical current are well described by a single step height as fitting parameter for all subbands at a given V_{TG}.

Yet, despite the provided evidence for coupling of the supercurrent via discrete energy levels in the SQPC carried by individual Andreev bound states, the extracted step heights δI_c appear quenched compared to the theoretically expected ideal value. The main limiting factor is due to the required depletion at larger negative V_{TG} in order to reach the lowest subbands with the SG, which at the same time suppresses the supercurrent injection into the weak link as the BLG reservoirs are gapped. Other discussed aspects consider the finite junction length of the weak link $L \lesssim \xi_0$, as well as the observation of an effectively reduced superconducting energy gap size $\Delta_0^*/\Delta_0 < 1$ tuned by the overall TG. Further optimization of the device geometry, such as employing shorter distances between the superconducting leads as well as independent control over the 1D channel and BLG/superconductor boundaries, might help to improve the described shortages in the step height of the critical current.

Finally, the subgap transport properties of the SQPC have been studied. Observed steps in the staircase of the subgap conductance are significantly enhanced, exceeding at the maximum twice the step height in the normal state, which demonstrates a phase-sensitive quasiparticle transport mechanism due to MARs. The amplitude of these subharmonic energy gap structures is found to be modulated by tuning the subband population. While after the transition across a 1D energy level the MAR resonances are enhanced, a suppression is noticed in-between energy levels at the onset of the next-higher subband indicating a strong channel mixing at the transition itself.

7 Summary and outlook

In this thesis, gate-defined nanostructures in BLG weak link Josephson junctions were studied. The samples were fabricated following a dry and contamination-free vdW assembly for encapsulation of the graphene into hBN/BLG/hBN heterostructures where electrical contact is made from the edge of the mesa with superconducting Ti/Al electrodes, providing high-quality state-of-the-art hybrid superconductor–graphene devices in the ballistic regime. The electrical characterization was done at mK temperature using standard lock-in detection techniques and performing out-of-equilibrium transport measurements in out-of-plane as well as in-plane magnetic field orientations.

At first, a tunable shaping of the supercurrent through the BLG weak link was demonstrated both spatially and in its amplitude based on electrostatic confinement in two different geometries, *i. e.* QPC-like and long channel confinement. The constrictions were realized by local band gap engineering via the employed combination of a global BG and locally defined top SG structures, owing to the possibility of opening an electronic band gap in BLG by breaking the layer symmetry due to applied perpendicular displacement fields. In both structures, unusual gate-gate-maps of a dual-gated BLG junction were discussed due to the effect of a split gate. The induced 1D supercurrent confinement was studied and monitored by means of superconducting magneto-interferometry measurements. In case of the long-channel confinement it was possible to reconstruct the spatial supercurrent density profile using the Dynes-Fulton approach, while in the QPC-like confinement the results are supported by analytical and numerical modeling. No presence of shunting currents (e. g. due to edge states) was detected.

However, in spite of the demonstrated 1D supercurrent confinement, a controllable depopulation of the channel was not possible in this sample configuration because of a lacking independent control on the channel density as the combination of BG and SG is necessary for inducing the constriction itself. In respect thereof, an additional overall TG was added. Thanks to this extra tuning knob, 1D subband formation was observed with robustly quantized conductance in steps of $4\,e^2/h$ as expected for the fourfold degeneracy in this system (*i. e.* spin and valley) down to the lowest subband until finally complete pinch-off is reached. A lifting of spin and valley degeneracy of

the 1D subbands was investigated with applied in-plane and out-of-plane magnetic fields. In the perpendicular magnetic field orientation a complex valley splitting and mixing of 1D subbands with indices differing by 2 was observed which could be explained in a semi-phenomenological model and was understood due to the peculiar Landau level spectrum of gapped BLG. Additionally, from the observed enhancement of the Zeeman energy spin splitting (for both in-plane and out-of-plane magnetic field) an effective 1D g-factor $|g^*|$ was determined with strongest renormalization at the lowest subband and noticed anisotropy between in-plane and out-of-plane magnetic field orientation. Indeed, interaction effects were noticed to come into play at the lowest subbands in this confined system, as visible by the appearance of a 0.7-like conductance structure below the first plateau as well as at the crossing of split subbands at finite magnetic field accompanied with intriguing non-monotonic enhancement of the spin splitting. Finally in this BLG QPC, an additional mini-valley quantum degree of freedom was identified, appearing as a feature of the fine structure at the bottom of the conductance band due to trigonal warping of the bands. The consequence is an unusual degeneracy of the lowest subband with the first conductance plateau appearing either at $4\,e^2/h$, $8\,e^2/h$ or $12\,e^2/h$. It was demonstrated that the coupling from the bulk reservoirs into the "accidentally" degenerate channel modes can be selectively controlled by tuning the reservoirs and induced confinement via SG and TG.

In a last experiment, the successfully implemented QPC within the BLG weak link was studied in the superconducting regime. In this SQPC, the critical current was observed to change in discretized steps in correlation with the quantized conductance in the normal state as the number of modes is varied, demonstrating a supercurrent coupling via discrete energy levels carried by individual Andreev bound states. However, the extracted step heights were smaller than the expected ideal value of quantized supercurrent, mainly attributed to the tuning of the entire weak link by the overall TG. The phase-sensitive transport of quasiparticles through the SQPC was further revealed by subgap measurements (*i. e.* at finite voltage below the superconducting energy gap), where the finding of enhanced steps in the subgap conductance larger than in the normal state indicated a charge transport mechanism due to MARs. Strikingly, the MAR resonances appeared with a modulated amplitude depending on the position of the Fermi level with respect to the 1D subbands. The monitored suppression of MARs at the transition to the next energy level revealed a subband mixing at the opening of a new channel.

Outlook

The presented results provide a promising platform for future experiments. In fact, the demonstrated control of the quantum degrees of freedom (*i. e.* valley, spin and mini-valley) in the BLG QPC is a necessity in the development of new quantum elec-

tronic devices in the field of spin- or valleytronics [ŽFD04; Sch+16]. For instance, the design of valley filters and valley valves in graphene has been proposed based on ballistic QPCs [RTB07]. Moreover, the lifting of the valley degeneracy appears to be a crucial requirement in view of the proposal for using graphene QDs as spin qubits [Tra+07].

Another interesting aspect would be measurements of this confined system in the quantum Hall regime. Here, the gate-tunable selective transmission of quantum Hall channels can be utilized as beam splitters in the design of electronic interferometers [Hen+99; Ji+03]. Also, the controllable mixing and partitioning of opposite edge channels brought together in the QPC allows to probe fractional quantum Hall states [Mil+07; Dol+08], where even-denominator phases are predicted to host non-abelian anyons that are investigated for encoding quantum information in topological qubits [Kit03]. The observation of even-denominator fractional quantum Hall states in BLG has been recently reported [Zib+17; Li+17], as well as a study on the selective transmission of integer and fractional quantum Hall channels in a monolayer graphene QPC based on *pn*-junctions in the quantum Hall regime [Zim+17].

In view of the demonstrated electrostatic spatial shaping of the supercurrent in the BLG weak link, more complex hybrid superconductor–semiconductor devices and circuits [De +10] may be realized, such as a superconducting electronic interferometer based on a gate-defined Y-shape BLG weak link junction coupled to a superconducting loop and injector [Lan+02; Ama+14] or an Aharonov-Bohm interferometer connected with superconducting leads which can be used as a sign-switch of the Josephson current [DG07].

Furthermore, it is noteworthy that a single channel Andreev bound state operation in a SQPC is described by a two-level Hamiltonian [IF99] which serves as a building block for designing Andreev level qubits [Zaz+03]. Yet, single channel operation in the here presented work was limited by the quenching of the proximity-coupling upon depletion of the entire weak link with the overall TG, thus requiring further optimization of the junction architecture.

Finally, we mention that a new device design with additional superconducting leads from the sides were tested for enhancing the superconductivity coupling in extremely long junctions. In particular, induced supercurrent in a BLG weak link was measured over 4 µm distance scales, *i. e.* much longer than would be possible without the superconducting side reservoirs, which could be helpful for enlarging the space of designing gate-defined nanostructures within the weak link channel. While such multi-terminal Josephson junctions are also proposed to provide novel realizations of topological matter [Riw+16], the preliminary results on these devices appear to be highly promising.

Bibliography

[Aba+13] S. Abay, D. Persson, H. Nilsson, H. Q. Xu, M. Fogelström, V. Shumeiko, and P. Delsing: *Quantized Conductance and Its Correlation to the Supercurrent in a Nanowire Connected to Superconductors*. Nano Lett. **13**, 3614–3617 (2013). DOI: 10.1021/nl4014265 (cit. on pp. 105, 108).

[AYR03] N. Agraït, A. L. Yeyati, and J. M. van Ruitenbeek: *Quantum properties of atomic-sized conductors*. Phys. Rep. **377**, 81–279 (2003). DOI: 10.1016/s0370-1573(02)00633-6 (cit. on p. 105).

[AMY12] M. T. Allen, J. Martin, and A. Yacoby: *Gate-defined quantum confinement in suspended bilayer graphene*. Nat. Commun. **3**, 934 (2012). DOI: 10.1038/ncomms1945 (cit. on p. 79).

[All+16] M. T. Allen, O. Shtanko, I. C. Fulga, A. R. Akhmerov, K. Watanabe, T. Taniguchi, P. Jarillo-Herrero, L. S. Levitov, and A. Yacoby: *Spatially resolved edge currents and guided-wave electronic states in graphene*. Nat. Phys. **12**, 128–133 (2016). DOI: 10.1038/nphys3534 (cit. on pp. 25, 42, 45, 47, 62).

[Ama+14] M. Amado, A. Fornieri, G. Biasiol, L. Sorba, and F. Giazotto: *A ballistic two-dimensional-electron-gas Andreev interferometer*. Appl. Phys. Lett. **104**, 242604 (2014). DOI: 10.1063/1.4884952 (cit. on p. 123).

[Ama+13] M. Amado, A. Fornieri, F. Carillo, G. Biasiol, L. Sorba, V. Pellegrini, and F. Giazotto: *Electrostatic tailoring of magnetic interference in quantum point contact ballistic Josephson junctions*. Phys. Rev. B **87**, 134506 (2013). DOI: 10.1103/physrevb.87.134506 (cit. on pp. 44, 57).

[AH69] V. Ambegaokar and B. I. Halperin: *Voltage Due to Thermal Noise in the dc Josephson Effect*. Phys. Rev. Lett. **22**, 1364–1366 (1969). DOI: 10.1103/physrevlett.22.1364 (cit. on pp. 20, 161).

[Ame+16] F. Amet, C. T. Ke, I. V. Borzenets, J. Wang, K. Watanabe, T. Taniguchi, R. S. Deacon, M. Yamamoto, Y. Bomze, S. Tarucha, and G. Finkelstein: *Supercurrent in the quantum Hall regime*. Science **352**, 966–969 (2016). DOI: 10.1126/science.aad6203 (cit. on p. 25).

[AR63] P. W. Anderson and J. M. Rowell: *Probable Observation of the Josephson Superconducting Tunneling Effect*. Phys. Rev. Lett. **10**, 230–232 (1963). DOI: 10.1103/physrevlett.10.230 (cit. on pp. 3, 20).

[And64] A. F. Andreev: *The Thermal Conductivity of the Intermediate State in Superconductors*. JETP **19**, 1228 (1964) (cit. on pp. 21, 118).

[Ang+08] L. Angers, F. Chiodi, G. Montambaux, M. Ferrier, S. Guéron, H. Bouchiat, and J. C. Cuevas: *Proximity dc squids in the long-junction limit*. Phys. Rev. B **77**, 165408 (2008). DOI: 10.1103/physrevb.77.165408 (cit. on pp. 44, 57).

[AH09] K. Aryanpour and J. E. Han: *Ferromagnetic Spin Coupling as the Origin of 0.7 Anomaly in Quantum Point Contacts*. Phys. Rev. Lett. **102**, 056805 (2009). DOI: 10.1103/physrevlett.102.056805 (cit. on p. 93).

[Ban+18] L. Banszerus, B. Frohn, A. Epping, D. Neumaier, K. Watanabe, T. Taniguchi, and C. Stampfer: *Gate-Defined Electron–Hole Double Dots in Bilayer Graphene*. Nano Lett. **18**, 4785–4790 (2018). DOI: 10.1021/acs.nanolett.8b01303 (cit. on pp. 31, 79).

[BCS57] J. Bardeen, L. N. Cooper, and J. R. Schrieffer: *Theory of Superconductivity*. Phys. Rev. **108**, 1175–1204 (1957). DOI: 10.1103/physrev.108.1175 (cit. on p. 16).

[BP82] A. Barone and G. Paternò: *Physics and Applications of the Josephson Effect*. Wiley, 1982. DOI: 10.1002/352760278x (cit. on pp. 42, 44, 57).

[BZ99] V. Barzykin and A. M. Zagoskin: *Coherent transport and nonlocality in mesoscopic SNS junctions: anomalous magnetic interference patterns*. Superlattices Microstruct. **25**, 797–807 (1999). DOI: 10.1006/spmi.1999.0731 (cit. on pp. 44, 57, 59).

[Bau+05] T. Bauch, E. Hürfeld, V. M. Krasnov, P. Delsing, H. Takayanagi, and T. Akazaki: *Correlated quantization of supercurrent and conductance in a superconducting quantum point contact*. Phys. Rev. B **71**, 174502 (2005). DOI: 10.1103/physrevb.71.174502 (cit. on pp. 105, 108).

[Bau+13] F. Bauer, J. Heyder, E. Schubert, D. Borowsky, D. Taubert, B. Bruognolo, D. Schuh, W. Wegscheider, J. von Delft, and S. Ludwig: *Microscopic origin of the '0.7-anomaly' in quantum point contacts*. Nature **501**, 73–78 (2013). DOI: 10.1038/nature12421 (cit. on p. 93).

[Bee92] C. W. J. Beenakker: *Quantum transport in semiconductor-superconductor microjunctions*. Phys. Rev. B **46**, 12841–12844 (1992). DOI: 10.1103/physrevb.46.12841 (cit. on p. 118).

[Bee06] C. W. J. Beenakker: *Specular Andreev Reflection in Graphene*. Phys. Rev. Lett. **97**, 067007 (2006). DOI: 10.1103/physrevlett.97.067007 (cit. on p. 22).

[Bee08] C. W. J. Beenakker: *Colloquium: Andreev reflection and Klein tunneling in graphene*. Rev. Mod. Phys. **80**, 1337–1354 (2008). DOI: 10.1103/revmodphys.80.1337 (cit. on p. 22).

[BH91a] C. W. J. Beenakker and H. van Houten: *Josephson current through a superconducting quantum point contact shorter than the coherence length*. Phys. Rev. Lett. **66**, 3056–3059 (1991). DOI: 10.1103/physrevlett.66.3056 (cit. on pp. 101, 102, 110, 114, 118).

[BH91b] C. W. J. Beenakker and H. van Houten: *Quantum Transport in Semiconductor Nanostructures*. Semiconductor Heterostructures and Nanostructures. Elsevier, 1991, pp. 1–228. DOI: 10.1016/s0081-1947(08)60091-0 (cit. on pp. 77, 87).

[BH92] C. W. J. Beenakker and H. van Houten: *THE SUPERCONDUCTING QUANTUM POINT CONTACT*. Nanostructures and Mesoscopic Systems. Elsevier, 1992, pp. 481–497. DOI: 10.1016/b978-0-12-409660-8.50051-1 (cit. on p. 102).

[Ben+16] M. Ben Shalom, M. J. Zhu, V. I. Fal'ko, A. Mishchenko, A. V. Kretinin, K. S. Novoselov, C. R. Woods, K. Watanabe, T. Taniguchi, A. K. Geim, and J. R. Prance: *Quantum oscillations of the critical current and high-field superconducting proximity in ballistic graphene*. Nat. Phys. **12**, 318–322 (2016). DOI: 10.1038/nphys3592 (cit. on pp. 24, 107, 109, 160).

[Ben14] C. Benz: *Graphene field-effect devices at high frequencies*. PhD thesis. Karlsruhe Institute of Technology, 2014 (cit. on p. 31).

[BC08] F. S. Bergeret and J. C. Cuevas: *The Vortex State and Josephson Critical Current of a Diffusive SNS Junction*. JLTP **153**, 304–324 (2008). DOI: 10.1007/s10909-008-9826-2 (cit. on p. 44).

[BP10] K.-F. Berggren and M. Pepper: *Electrons in one dimension*. Philos. Trans. Royal Soc. A **368**, 1141–1162 (2010). DOI: 10.1098/rsta.2009.0226 (cit. on p. 78).

[Ber+86] K.-F. Berggren, T. J. Thornton, D. J. Newson, and M. Pepper: *Magnetic Depopulation of 1D Subbands in a Narrow 2D Electron Gas in a GaAs:AlGaAs Heterojunction*. Phys. Rev. Lett. **57**, 1769–1772 (1986). DOI: 10.1103/physrevlett.57.1769 (cit. on p. 78).

[Bie+05] M. J. Biercuk, N. Mason, J. Martin, A. Yacoby, and C. M. Marcus: *Anomalous Conductance Quantization in Carbon Nanotubes*. Phys. Rev. Lett. **94**, 026801 (2005). DOI: 10.1103/physrevlett.94.026801 (cit. on p. 78).

[Bis+16] D. Bischoff, P. Simonet, A. Varlet, H. C. Overweg, M. Eich, T. Ihn, and K. Ensslin: *The importance of edges in reactive ion etched graphene nanodevices*. phys. status solidi RRL **10**, 68–74 (2016). DOI: 10.1002/pssr.201510163 (cit. on pp. 2, 79).

[BD08] A. M. Black-Schaffer and S. Doniach: *Self-consistent solution for proximity effect and Josephson current in ballistic graphene SNS Josephson junctions*. Phys. Rev. B **78**, 024504 (2008). DOI: 10.1103/physrevb.78.024504 (cit. on pp. 24, 46).

[BL10] A. M. Black-Schaffer and J. Linder: *Strongly anharmonic current-phase relation in ballistic graphene Josephson junctions*. Phys. Rev. B **82**, 184522 (2010). DOI: 10.1103/physrevb.82.184522 (cit. on pp. 24, 46).

[Bla+07] P. Blake, E. W. Hill, A. H. Castro Neto, K. S. Novoselov, D. Jiang, R. Yang, T. J. Booth, and A. K. Geim: *Making graphene visible*. Appl. Phys. Lett. **91**, 063124 (2007). DOI: 10.1063/1.2768624 (cit. on p. 28).

[BTK82] G. E. Blonder, M. Tinkham, and T. M. Klapwijk: *Transition from metallic to tunneling regimes in superconducting microconstrictions: Excess current, charge imbalance, and supercurrent conversion*. Phys. Rev. B **25**, 4515–4532 (1982). DOI: 10.1103/physrevb.25.4515 (cit. on pp. 104, 118).

[Bol+08] K. I. Bolotin, K. J. Sikes, Z. Jiang, M. Klima, G. Fudenberg, J. Hone, P. Kim, and H. L. Stormer: *Ultrahigh electron mobility in suspended graphene*. Solid State Commun. **146**, 351–355 (2008). DOI: 10.1016/j.ssc.2008.02.024 (cit. on p. 6).

[Bor14] J. Bordaz: *Proximity-induced superconductivity in single-layer and bilayer graphene*. PhD thesis. Karlsruhe Institute of Technology, 2014 (cit. on p. 37).

[Bor+16] I. V. Borzenets, F. Amet, C. T. Ke, A. W. Draelos, M. T. Wei, A. Seredinski, K. Watanabe, T. Taniguchi, Y. Bomze, M. Yamamoto, S. Tarucha, and G. Finkelstein: *Ballistic Graphene Josephson Junctions from the Short to the Long Junction Regimes*. Phys. Rev. Lett. **117**, 237002 (2016). DOI: 10.1103/physrevlett.117.237002 (cit. on p. 24).

[Bru+14] B. Brun, F. Martins, S. Faniel, B. Hackens, G. Bachelier, A. Cavanna, C. Ulysse, A. Ouerghi, U. Gennser, D. Mailly, S. Huant, V. Bayot, M. Sanquer, and H. Sellier: *Wigner and Kondo physics in quantum point contacts revealed by scanning gate microscopy*. Nat. Commun. **5**, 4290 (2014). DOI: 10.1038/ncomms5290 (cit. on p. 93).

[BCF01] H. Bruus, V. V. Cheianov, and K. Flensberg: *The anomalous 0.5 and 0.7 conductance plateaus in quantum point contacts*. Phys. E **10**, 97–102 (2001). DOI: 10.1016/s1386-9477(01)00061-3 (cit. on p. 93).

[Bur+12] A. M. Burke, O. Klochan, I. Farrer, D. A. Ritchie, A. R. Hamilton, and A. P. Micolich: *Extreme Sensitivity of the Spin-Splitting and 0.7 Anomaly to Confining Potential in One-Dimensional Nanoelectronic Devices*. Nano Lett. **12**, 4495–4502 (2012). DOI: 10.1021/nl301566d (cit. on p. 93).

[Bur+13] K. M. Burson, W. G. Cullen, S. Adam, C. R. Dean, K. Watanabe, T. Taniguchi, P. Kim, and M. S. Fuhrer: *Direct Imaging of Charged Impurity Density in Common Graphene Substrates*. Nano Lett. **13**, 3576–3580 (2013). DOI: 10.1021/nl4012529 (cit. on p. 6).

[Büt90] M. Büttiker: *Quantized transmission of a saddle-point constriction*. Phys. Rev. B **41**, 7906–7909 (1990). DOI: 10.1103/physrevb.41.7906 (cit. on pp. 77, 93, 113).

[Cal+15] V. E. Calado, S. Goswami, G. Nanda, M. Diez, A. R. Akhmerov, K. Watanabe, T. Taniguchi, T. M. Klapwijk, and L. M. K. Vandersypen: *Ballistic Josephson junctions in edge-contacted graphene*. Nat. Nanotechnol. **10**, 761–764 (2015). DOI: 10.1038/nnano.2015.156 (cit. on pp. 24, 109, 160).

[Cao+18a] Y. Cao, V. Fatemi, A. Demir, S. Fang, S. L. Tomarken, J. Y. Luo, J. D. Sanchez-Yamagishi, K. Watanabe, T. Taniguchi, E. Kaxiras, R. C. Ashoori, and P. Jarillo-Herrero: *Correlated insulator behaviour at half-filling in magic-angle graphene superlattices*. Nature **556**, 80–84 (2018). DOI: 10.1038/nature26154 (cit. on p. 9).

[Cao+18b] Y. Cao, V. Fatemi, S. Fang, K. Watanabe, T. Taniguchi, E. Kaxiras, and P. Jarillo-Herrero: *Unconventional superconductivity in magic-angle graphene superlattices*. Nature **556**, 43–50 (2018). DOI: 10.1038/nature26160 (cit. on p. 9).

[Car+18] J. M. Caridad, S. R. Power, M. R. Lotz, A. A. Shylau, J. D. Thomsen, L. Gammelgaard, T. J. Booth, A.-P. Jauho, and P. Bøggild: *Conductance quantization suppression in the quantum Hall regime*. Nat. Commun. **9**, 659 (2018). DOI: 10.1038/s41467-018-03064-8 (cit. on p. 79).

[Cas+07] E. V. Castro, K. S. Novoselov, S. V. Morozov, N. M. R. Peres, J. M. B. Lopes dos Santos, J. Nilsson, F. Guinea, A. K. Geim, and A. H. Castro Neto: *Biased Bilayer Graphene: Semiconductor with a Gap Tunable by the Electric Field Effect*. Phys. Rev. Lett. **99**, 216802 (2007). DOI: 10.1103/physrevlett.99.216802 (cit. on pp. 10, 13, 14, 41).

[Cas+08] E. V. Castro, N. M. R. Peres, T. Stauber, and N. A. P. Silva: *Low-Density Ferromagnetism in Biased Bilayer Graphene*. Phys. Rev. Lett. **100**, 186803 (2008). DOI: 10.1103/physrevlett.100.186803 (cit. on p. 42).

[Cas+09] A. H. Castro Neto, F. Guinea, N. M. R. Peres, K. S. Novoselov, and A. K. Geim: *The electronic properties of graphene*. Rev. Mod. Phys. **81**, 109–162 (2009). DOI: 10.1103/revmodphys.81.109 (cit. on pp. 1, 9, 41).

[Che+08a] J.-H. Chen, C. Jang, S. Adam, M. S. Fuhrer, E. D. Williams, and M. Ishigami: *Charged-impurity scattering in graphene*. Nat. Phys. **4**, 377–381 (2008). DOI: 10.1038/nphys935 (cit. on p. 5).

[Che+08b] J.-H. Chen, C. Jang, S. Xiao, M. Ishigami, and M. S. Fuhrer: *Intrinsic and extrinsic performance limits of graphene devices on SiO_2*. Nat. Nanotechnol. **3**, 206–209 (2008). DOI: 10.1038/nnano.2008.58 (cit. on p. 5).

[Chi+12] F. Chiodi, M. Ferrier, S. Guéron, J. C. Cuevas, G. Montambaux, F. Fortuna, A. Kasumov, and H. Bouchiat: *Geometry-related magnetic interference patterns in long **SNS** Josephson junctions*. Phys. Rev. B **86**, 064510 (2012). DOI: 10.1103/physrevb.86.064510 (cit. on pp. 44, 57).

[CF08] S. Cho and M. S. Fuhrer: *Charge transport and inhomogeneity near the minimum conductivity point in graphene*. Phys. Rev. B **77**, 081402(R) (2008). DOI: 10.1103/physrevb.77.081402 (cit. on p. 5).

[CLB00] N. M. Chtchelkatchev, G. B. Lesovik, and G. Blatter: *Supercurrent quantization in narrow-channel superconductor–normal-metal–superconductor junctions*. Phys. Rev. B **62**, 3559–3564 (2000). DOI: 10.1103/physrevb.62.3559 (cit. on pp. 101, 103–105, 114, 115).

[Cla69] J. Clarke: *Supercurrents in lead—copper—-lead sandwiches*. Proc. Royal Soc. Lond., Ser. A **308**, 447–471 (1969). DOI: 10.1098/rspa.1969.0020 (cit. on p. 44).

[Cro+02] S. M. Cronenwett, H. J. Lynch, D. Goldhaber-Gordon, L. P. Kouwenhoven, C. M. Marcus, K. Hirose, N. S. Wingreen, and V. Umansky: *Low-Temperature Fate of the 0.7 Structure in a Point Contact: A Kondo-like Correlated State in an Open System*. Phys. Rev. Lett. **88**, 226805 (2002). DOI: 10.1103/physrevlett.88.226805 (cit. on p. 93).

[CI13] B. Crouzy and D. A. Ivanov: *Magnetic interference patterns in long disordered Josephson junctions*. Phys. Rev. B **87**, 024514 (2013). DOI: 10.1103/physrevb.87.024514 (cit. on p. 44).

[CB07] J. C. Cuevas and F. S. Bergeret: *Magnetic Interference Patterns and Vortices in Diffusive SNS Junctions*. Phys. Rev. Lett. **99**, 217002 (2007). DOI: 10.1103/physrevlett.99.217002 (cit. on p. 44).

[CY06] J. C. Cuevas and A. L. Yeyati: *Subharmonic gap structure in short ballistic graphene junctions*. Phys. Rev. B **74**, 180501(R) (2006). DOI: 10.1103/physrevb.74.180501 (cit. on pp. 23, 51, 111, 116).

[Cul+10] W. G. Cullen, M. Yamamoto, K. M. Burson, J. H. Chen, C. Jang, L. Li, M. S. Fuhrer, and E. D. Williams: *High-Fidelity Conformation of Graphene to SiO_2 Topographic Features*. Phys. Rev. Lett. **105**, 215504 (2010). DOI: 10.1103/physrevlett.105.215504 (cit. on pp. 5, 6).

[Dan+97] A. J. Daneshvar, C. J. B. Ford, A. R. Hamilton, M. Y. Simmons, M. Pepper, and D. A. Ritchie: *Enhanced g factors of a one-dimensional hole gas with quantized conductance*. Phys. Rev. B **55**, R13409–R13412 (1997). DOI: 10.1103/physrevb.55.r13409 (cit. on p. 95).

[Dan+08] R. Danneau, O. Klochan, W. R. Clarke, L. H. Ho, A. P. Micolich, M. Y. Simmons, A. R. Hamilton, M. Pepper, and D. A. Ritchie: *0.7 Structure and Zero Bias Anomaly in Ballistic Hole Quantum Wires*. Phys. Rev. Lett. **100**, 016403 (2008). DOI: 10.1103/physrevlett.100.016403 (cit. on p. 93).

[Dan+06] R. Danneau, O. Klochan, W. R. Clarke, L. H. Ho, A. P. Micolich, M. Y. Simmons, A. R. Hamilton, M. Pepper, D. A. Ritchie, and U. Zülicke: *Zeeman Splitting in Ballistic Hole Quantum Wires*. Phys. Rev. Lett. **97**, 026403 (2006). DOI: 10.1103/physrevlett.97.026403 (cit. on p. 95).

[DG17] M. P. Das and F. Green: *Conductance anomalies in quantum point contacts and 1D wires*. ANSN **8**, 023001 (2017). DOI: 10.1088/2043-6254/aa5e17 (cit. on pp. 92, 93).

[Das+11] S. Das Sarma, S. Adam, E. H. Hwang, and E. Rossi: *Electronic transport in two-dimensional graphene*. Rev. Mod. Phys. **83**, 407–470 (2011). DOI: 10.1103/revmodphys.83.407 (cit. on p. 5).

[Dat95] S. Datta: *Electronic Transport in Mesoscopic Systems*. Cambridge University Press, 1995. DOI: 10.1017/cbo9780511805776 (cit. on p. 77).

[De +10] S. De Franceschi, L. Kouwenhoven, C. Schönenberger, and W. Wernsdorfer: *Hybrid superconductor–quantum dot devices*. Nat. Nanotechnol. **5**, 703–711 (2010). DOI: 10.1038/nnano.2010.173 (cit. on p. 123).

[Dea+13] C. R. Dean, L. Wang, P. Maher, C. Forsythe, F. Ghahari, Y. Gao, J. Katoch, M. Ishigami, P. Moon, M. Koshino, T. Taniguchi, K. Watanabe, K. L. Shepard, J. Hone, and P. Kim: *Hofstadter's butterfly and the fractal quantum Hall effect in moiré superlattices*. Nature **497**, 598–602 (2013). DOI: 10.1038/nature12186 (cit. on p. 8).

[Dea+10] C. R. Dean, A. F. Young, I. Meric, C. Lee, L. Wang, S. Sorgenfrei, K. Watanabe, T. Taniguchi, P. Kim, K. L. Shepard, and J. Hone: *Boron nitride substrates for high-quality graphene electronics*. Nat. Nanotechnol. **5**, 722–726 (2010). DOI: 10.1038/nnano.2010.172 (cit. on pp. 2, 6).

[Dec+11] R. Decker, Y. Wang, V. W. Brar, W. Regan, H.-Z. Tsai, Q. Wu, W. Gannett, A. Zettl, and M. F. Crommie: *Local Electronic Properties of Graphene on a BN Substrate via Scanning Tunneling Microscopy*. Nano Lett. **11**, 2291–2295 (2011). DOI: 10.1021/nl2005115 (cit. on p. 6).

[Des+09] A. Deshpande, W. Bao, F. Miao, C. N. Lau, and B. J. LeRoy: *Spatially resolved spectroscopy of monolayer graphene on SiO_2*. Phys. Rev. B **79**, 205411 (2009). DOI: 10.1103/physrevb.79.205411 (cit. on p. 5).

[DiC+06] L. DiCarlo, Y. Zhang, D. T. McClure, D. J. Reilly, C. M. Marcus, L. N. Pfeiffer, and K. W. West: *Shot-Noise Signatures of 0.7 Structure and Spin in a Quantum Point Contact*. Phys. Rev. Lett. **97**, 036810 (2006). DOI: 10.1103/physrevlett.97.036810 (cit. on p. 95).

[Doh+05] Y.-J. Doh, J. A. van Dam, A. L. Roest, E. P. A. M. Bakkers, L. P. Kouwenhoven, and S. De Franceschi: *Tunable Supercurrent Through Semiconductor Nanowires*. Science **309**, 272–275 (2005). DOI: 10.1126/science.1113523 (cit. on p. 108).

[DG07] F. Dolcini and F. Giazotto: *Switching the sign of Josephson current through Aharonov-Bohm interferometry*. Phys. Rev. B **75**, 140511(R) (2007). DOI: 10.1103/physrevb.75.140511 (cit. on p. 123).

[Dol+08] M. Dolev, M. Heiblum, V. Umansky, A. Stern, and D. Mahalu: *Observation of a quarter of an electron charge at the $\nu = 5/2$ quantum Hall state*. Nature **452**, 829–834 (2008). DOI: 10.1038/nature06855 (cit. on p. 123).

[Drö+12] S. Dröscher, C. Barraud, K. Watanabe, T. Taniguchi, T. Ihn, and K. Ensslin: *Electron flow in split-gated bilayer graphene*. New J. Phys. **14**, 103007 (2012). DOI: 10.1088/1367-2630/14/10/103007 (cit. on pp. 3, 79).

[Du+18] R. Du, M.-H. Liu, J. Mohrmann, F. Wu, R. Krupke, H. v. Löhneysen, K. Richter, and R. Danneau: *Tuning Anti-Klein to Klein Tunneling in Bilayer Graphene*. Phys. Rev. Lett. **121**, 127706 (2018). DOI: 10.1103/PhysRevLett.121.127706 (cit. on pp. 50, 65, 159, 165).

[Du+08] X. Du, I. Skachko, A. Barker, and E. Y. Andrei: *Approaching ballistic transport in suspended graphene*. Nat. Nanotechnol. **3**, 491–495 (2008). DOI: 10.1038/nnano.2008.199 (cit. on pp. 6, 24, 50).

[DF71] R. C. Dynes and T. A. Fulton: *Supercurrent Density Distribution in Josephson Junctions*. Phys. Rev. B **3**, 3015–3023 (1971). DOI: 10.1103/physrevb.3.3015 (cit. on pp. 45, 59, 64).

[Efe+16] D. K. Efetov, L. Wang, C. Handschin, K. B. Efetov, J. Shuang, R. Cava, T. Taniguchi, K. Watanabe, J. Hone, C. R. Dean, and P. Kim: *Specular interband Andreev reflections at van der Waals interfaces between graphene and $NbSe_2$*. Nat. Phys. **12**, 328–332 (2016). DOI: 10.1038/nphys3583 (cit. on p. 22).

[Eic+18a] M. Eich, R. Pisoni, H. Overweg, A. Kurzmann, Y. Lee, P. Rickhaus, T. Ihn, K. Ensslin, F. Herman, M. Sigrist, K. Watanabe, and T. Taniguchi: *Spin and Valley States in Gate-Defined Bilayer Graphene Quantum Dots*. Phys. Rev. X **8**, 031023 (2018). DOI: 10.1103/physrevx.8.031023 (cit. on pp. 31, 79, 87, 94).

[Eic+18b] M. Eich, R. Pisoni, A. Pally, H. Overweg, A. Kurzmann, Y. Lee, P. Rickhaus, K. Watanabe, T. Taniguchi, K. Ensslin, and T. Ihn: *Coupled Quantum Dots in Bilayer Graphene*. Nano Lett. **18**, 5042–5048 (2018). DOI: 10.1021/acs.nanolett.8b01859 (cit. on p. 79).

[Eng+16] C. D. English, D. R. Hamilton, C. Chialvo, I. C. Moraru, N. Mason, and D. J. Van Harlingen: *Observation of nonsinusoidal current-phase relation in graphene Josephson junctions*. Phys. Rev. B **94**, 115435 (2016). DOI: 10.1103/physrevb.94.115435 (cit. on p. 46).

[Fer+06] A. C. Ferrari, J. C. Meyer, V. Scardaci, C. Casiraghi, M. Lazzeri, F. Mauri, S. Piscanec, D. Jiang, K. S. Novoselov, S. Roth, and A. K. Geim: *Raman Spectrum of Graphene and Graphene Layers*. Phys. Rev. Lett. **97**, 187401 (2006). DOI: 10.1103/physrevlett.97.187401 (cit. on p. 28).

[Fer07] A. C. Ferrari: *Raman spectroscopy of graphene and graphite: Disorder, electron–phonon coupling, doping and nonadiabatic effects*. Solid State Commun. **143**, 47–57 (2007). DOI: 10.1016/j.ssc.2007.03.052 (cit. on p. 28).

[FB13] A. C. Ferrari and D. M. Basko: *Raman spectroscopy as a versatile tool for studying the properties of graphene*. Nat. Nanotechnol. **8**, 235–246 (2013). DOI: 10.1038/nnano.2013.46 (cit. on p. 28).

[Fig16] T. Figielski: *The 0.7-Anomaly in Quantum Point Contact; Many-Body or Single-Electron Effect?* World J. Condens. Matter Phys. **06**, 217–223 (2016). DOI: 10.4236/wjcmp.2016.63021 (cit. on p. 93).

[FK00] V. V. Flambaum and M. Y. Kuchiev: *Possible mechanism of the fractional-conductance quantization in a one-dimensional constriction*. Phys. Rev. B **61**, R7869–R7872 (2000). DOI: 10.1103/physrevb.61.r7869 (cit. on p. 93).

[Fri+18] R. Frisenda, E. Navarro-Moratalla, P. Gant, D. P. De Lara, P. Jarillo-Herrero, R. V. Gorbachev, and A. Castellanos-Gomez: *Recent progress in the assembly of nanodevices and van der Waals heterostructures by deterministic placement of 2D materials*. Chem. Soc. Rev. **47**, 53–68 (2018). DOI: 10.1039/c7cs00556c (cit. on pp. 8, 9, 27, 32).

[Fro+09] S. M. Frolov, A. Venkatesan, W. Yu, J. A. Folk, and W. Wegscheider: *Electrical Generation of Pure Spin Currents in a Two-Dimensional Electron Gas*. Phys. Rev. Lett. **102**, 116802 (2009). DOI: 10.1103/physrevlett.102.116802 (cit. on p. 95).

[FTT91] A. Furusaki, H. Takayanagi, and M. Tsukada: *Theory of quantum conduction of supercurrent through a constriction*. Phys. Rev. Lett. **67**, 132–135 (1991). DOI: 10.1103/physrevlett.67.132 (cit. on pp. 101, 103, 105).

[FTT92] A. Furusaki, H. Takayanagi, and M. Tsukada: *Josephson effect of the superconducting quantum point contact*. Phys. Rev. B **45**, 10563–10575 (1992). DOI: 10.1103/physrevb.45.10563 (cit. on pp. 101, 103).

[GG13] A. K. Geim and I. V. Grigorieva: *Van der Waals heterostructures*. Nature **499**, 419–425 (2013). DOI: 10.1038/nature12385 (cit. on pp. 2, 8).

[GN07] A. K. Geim and K. S. Novoselov: *The rise of graphene*. Nat. Mater. **6**, 183–191 (2007). DOI: 10.1038/nmat1849 (cit. on pp. 1, 27).

[Gio+08] G. Giovannetti, P. A. Khomyakov, G. Brocks, V. M. Karpan, J. van den Brink, and P. J. Kelly: *Doping Graphene with Metal Contacts*. Phys. Rev. Lett. **101**, 026803 (2008). DOI: 10.1103/physrevlett.101.026803 (cit. on p. 49).

[Gio+07] G. Giovannetti, P. A. Khomyakov, G. Brocks, P. J. Kelly, and J. van den Brink: *Substrate-induced band gap in graphene on hexagonal boron nitride:* Ab initio *density functional calculations*. Phys. Rev. B **76**, 073103 (2007). DOI: 10.1103/physrevb.76.073103 (cit. on p. 6).

[Gla+88] L. I. Glazman, G. B. Lesovik, D. E. Khmel'nitskii, and R. I. Shekhter: *Reflectionless quantum transport and fundamental ballistic-resistance steps in microscopic constrictions*. JETP Lett. **48**, 238–241 (1988) (cit. on p. 113).

[Gol+13] D. Golla, K. Chattrakun, K. Watanabe, T. Taniguchi, B. J. LeRoy, and A. Sandhu: *Optical thickness determination of hexagonal boron nitride flakes*. Appl. Phys. Lett. **102**, 161906 (2013). DOI: 10.1063/1.4803041 (cit. on p. 29).

[Goo+12] A. S. M. Goossens, S. C. M. Driessen, T. A. Baart, K. Watanabe, T. Taniguchi, and L. M. K. Vandersypen: *Gate-Defined Confinement in Bilayer Graphene-Hexagonal Boron Nitride Hybrid Devices*. Nano Lett. **12**, 4656–4660 (2012). DOI: 10.1021/nl301986q (cit. on pp. 3, 79).

[Gos+07] S. Goswami, K. A. Slinker, M. Friesen, L. M. McGuire, J. L. Truitt, C. Tahan, L. J. Klein, J. O. Chu, P. M. Mooney, D. W. van der Weide, R. Joynt, S. N. Coppersmith, and M. A. Eriksson: *Controllable valley splitting in silicon quantum devices*. Nat. Phys. **3**, 41–45 (2007). DOI: 10.1038/nphys475 (cit. on pp. 78, 88, 93).

[Gra+03] A. C. Graham, K. J. Thomas, M. Pepper, N. R. Cooper, M. Y. Simmons, and D. A. Ritchie: *Interaction Effects at Crossings of Spin-Polarized One-Dimensional Subbands*. Phys. Rev. Lett. **91** (2003). DOI: 10.1103/physrevlett.91.136404 (cit. on p. 97).

[GM05] R. Gross and A. Marx: *Applied Superconductivity: Josephson Effect and Superconducting Electronics*. Manuscript to the Lectures. Department of Physics - Technical University of Munich. 2005 (cit. on pp. 18, 19, 42).

[Gro+14] C. W. Groth, M. Wimmer, A. R. Akhmerov, and X. Waintal: *Kwant: a software package for quantum transport*. New J. Phys. **16**, 063065 (2014). DOI: 10.1088/1367-2630/16/6/063065 (cit. on pp. 59, 61).

[Gun+06] O. Gunawan, B. Habib, E. P. D. Poortere, and M. Shayegan: *Quantized conductance in an AlAs two-dimensional electron system quantum point contact*. Phys. Rev. B **74**, 155436 (2006). DOI: 10.1103/physrevb.74.155436 (cit. on pp. 78, 93).

[Güt+10] J. Güttinger, T. Frey, C. Stampfer, T. Ihn, and K. Ensslin: *Spin States in Graphene Quantum Dots*. Phys. Rev. Lett. **105**, 116801 (2010). DOI: 10.1103/physrevlett.105.116801 (cit. on p. 94).

[Hai+12] S. J. Haigh, A. Gholinia, R. Jalil, S. Romani, L. Britnell, D. C. Elias, K. S. Novoselov, L. A. Ponomarenko, A. K. Geim, and R. Gorbachev: *Cross-sectional imaging of individual layers and buried interfaces of graphene-based heterostructures and superlattices*. Nat. Mater. **11**, 764–767 (2012). DOI: 10.1038/nmat3386 (cit. on p. 33).

[Har+14] S. Hart, H. Ren, T. Wagner, P. Leubner, M. Mühlbauer, C. Brüne, H. Buhmann, L. W. Molenkamp, and A. Yacoby: *Induced superconductivity in the quantum spin Hall edge*. Nat. Phys. **10**, 638–643 (2014). DOI: 10.1038/nphys3036 (cit. on pp. 44, 45, 47).

[HYK10] M. Hayashi, H. Yoshioka, and A. Kanda: *Superconducting proximity effect in graphene nanostructures*. J. Phys.: Conf. Ser. **248**, 012002 (2010). DOI: 10.1088/1742-6596/248/1/012002 (cit. on p. 24).

[Hee+16] S. Heedt, W. Prost, J. Schubert, D. Grützmacher, and T. Schäpers: *Ballistic Transport and Exchange Interaction in InAs Nanowire Quantum Point Contacts*. Nano Lett. **16**, 3116–3123 (2016). DOI: 10.1021/acs.nanolett.6b00414 (cit. on p. 93).

[Hee+07] H. B. Heersche, P. Jarillo-Herrero, J. B. Oostinga, L. M. K. Vandersypen, and A. F. Morpurgo: *Bipolar supercurrent in graphene*. Nature **446**, 56–59 (2007). DOI: 10.1038/nature05555 (cit. on p. 24).

[Hei+98] J. P. Heida, B. J. van Wees, T. M. Klapwijk, and G. Borghs: *Nonlocal supercurrent in mesoscopic Josephson junctions*. Phys. Rev. B **57**, R5618–R5621 (1998). DOI: 10.1103/physrevb.57.r5618 (cit. on p. 44).

[Hen+19] N. W. Hendrickx, M. L. V. Tagliaferri, M. Kouwenhoven, R. Li, D. P. Franke, A. Sammak, A. Brinkman, G. Scappucci, and M. Veldhorst: *Ballistic supercurrent discretization and micrometer-long Josephson coupling in germanium*. Phys. Rev. B **99**, 075435 (2019). DOI: 10.1103/physrevb.99.075435 (cit. on pp. 105, 108, 118).

[Hen+99] M. Henny, S. Oberholzer, C. Strunk, T. Heinzel, K. Ensslin, M. Holland, and C. Schönenberger: *The Fermionic Hanbury Brown and Twiss Experiment*. Science **284**, 296–298 (1999). DOI: 10.1126/science.284.5412.296 (cit. on p. 123).

[Hey+15] J. Heyder, F. Bauer, E. Schubert, D. Borowsky, D. Schuh, W. Wegscheider, J. von Delft, and S. Ludwig: *Relation between the 0.7 anomaly and the Kondo effect: Geometric crossover between a quantum point contact and a Kondo quantum dot*. Phys. Rev. B **92**, 195401 (2015). DOI: 10.1103/physrevb.92.195401 (cit. on p. 93).

[HB91] H. van Houten and C. W. J. Beenakker: *Andreev reflection and the Josephson effect in a quantum point contact: An analogy with phase-conjugating resonators*. Phys. B **175**, 187–197 (1991). DOI: 10.1016/0921-4526(91)90712-n (cit. on p. 118).

[HBW92] H. van Houten, C. W. J. Beenakker, and B. J. van Wees: *Chapter 2: Quantum Point Contacts*. Semiconductors and Semimetals. Elsevier, 1992, pp. 9–112. DOI: 10.1016/s0080-8784(08)62392-3 (cit. on pp. 77, 87).

[Hua+08] B. Huard, N. Stander, J. A. Sulpizio, and D. Goldhaber-Gordon: *Evidence of the role of contacts on the observed electron-hole asymmetry in graphene*. Phys. Rev. B **78**, 121402(R) (2008). DOI: 10.1103/physrevb.78.121402 (cit. on p. 49).

[Hui+14] H.-Y. Hui, A. M. Lobos, J. D. Sau, and S. D. Sarma: *Proximity-induced superconductivity and Josephson critical current in quantum spin Hall systems*. Phys. Rev. B **90**, 224517 (2014). DOI: 10.1103/physrevb.90.224517 (cit. on pp. 46, 47, 59, 68, 74).

[Hun+13] B. Hunt, J. D. Sanchez-Yamagishi, A. F. Young, M. Yankowitz, B. J. LeRoy, K. Watanabe, T. Taniguchi, P. Moon, M. Koshino, P. Jarillo-Herrero, and R. C. Ashoori: *Massive Dirac Fermions and Hofstadter Butterfly in a van der Waals Heterostructure*. Science **340**, 1427–1430 (2013). DOI: 10.1126/science.1237240 (cit. on p. 9).

[HAD07] E. H. Hwang, S. Adam, and S. Das Sarma: *Carrier Transport in Two-Dimensional Graphene Layers*. Phys. Rev. Lett. **98**, 186806 (2007). DOI: 10.1103/physrevlett.98.186806 (cit. on pp. 2, 5).

[IZ12] S. Ihnatsenka and I. V. Zozoulenko: *Spin polarization and* **g***-factor enhancement in graphene nanoribbons in a magnetic field*. Phys. Rev. B **86**, 155407 (2012). DOI: 10.1103/physrevb.86.155407 (cit. on p. 96).

[Ind+18] D. I. Indolese, R. Delagrange, P. Makk, J. R. Wallbank, K. Wanatabe, T. Taniguchi, and C. Schönenberger: *Signatures of van Hove Singularities Probed by the Supercurrent in a Graphene-hBN Superlattice*. Phys. Rev. Lett. **121**, 137701 (2018). DOI: 10.1103/physrevlett.121.137701 (cit. on pp. 45, 47).

[Ing+01] Å. Ingerman, G. Johansson, V. S. Shumeiko, and G. Wendin: *Coherent multiple Andreev reflections and current resonances in SNS quantum point contacts*. Phys. Rev. B **64**, 144504 (2001). DOI: 10.1103/physrevb.64.144504 (cit. on p. 118).

[Iqb+13] M. J. Iqbal, R. Levy, E. J. Koop, J. B. Dekker, J. P. de Jong, J. H. M. van der Velde, D. Reuter, A. D. Wieck, R. Aguado, Y. Meir, and C. H. van der Wal: *Odd and even Kondo effects from emergent localization in quantum point contacts*. Nature **501**, 79–83 (2013). DOI: 10.1038/nature12491 (cit. on p. 93).

[Iri+14] H. Irie, Y. Harada, H. Sugiyama, and T. Akazaki: *Josephson coupling through one-dimensional ballistic channel in semiconductor-superconductor hybrid quantum point contacts*. Phys. Rev. B **89**, 165415 (2014). DOI: 10.1103/physrevb.89.165415 (cit. on pp. 105, 108, 118).

[Ish+07] M. Ishigami, J. H. Chen, W. G. Cullen, M. S. Fuhrer, and E. D. Williams: *Atomic Structure of Graphene on SiO_2*. Nano Lett. **7**, 1643–1648 (2007). DOI: 10.1021/nl070613a (cit. on p. 5).

[IF99] D. A. Ivanov and M. V. Feigel'man: *Two-level Hamiltonian of a superconducting quantum point contact*. Phys. Rev. B **59**, 8444–8446 (1999). DOI: 10.1103/physrevb.59.8444 (cit. on p. 123).

[JvK06] P. Jarillo-Herrero, J. A. van Dam, and L. P. Kouwenhoven: *Quantum supercurrent transistors in carbon nanotubes*. Nature **439**, 953–956 (2006). DOI: 10.1038/nature04550 (cit. on p. 108).

[Ji+03] Y. Ji, Y. Chung, D. Sprinzak, M. Heiblum, D. Mahalu, and H. Shtrikman: *An electronic Mach–Zehnder interferometer*. Nature **422**, 415–418 (2003). DOI: 10.1038/nature01503 (cit. on p. 123).

[Jin+10] L. Jing, J. Velasco Jr., P. Kratz, G. Liu, W. Bao, M. Bockrath, and C. N. Lau: *Quantum Transport and Field-Induced Insulating States in Bilayer Graphene pnp Junctions*. Nano Lett. **10**, 4000–4004 (2010). DOI: 10.1021/nl101901g (cit. on p. 42).

[Jos62] B. D. Josephson: *Possible new effects in superconductive tunnelling*. Phys. Lett. **1**, 251–253 (1962). DOI: 10.1016/0031-9163(62)91369-0 (cit. on pp. 3, 17, 20).

[Ju+15] L. Ju, Z. Shi, N. Nair, Y. Lv, C. Jin, J. Velasco Jr, C. Ojeda-Aristizabal, H. A. Bechtel, M. C. Martin, A. Zettl, J. Analytis, and F. Wang: *Topological valley transport at bilayer graphene domain walls*. Nature **520**, 650–655 (2015). DOI: 10.1038/nature14364 (cit. on pp. 42, 62).

[KNG06] M. I. Katsnelson, K. S. Novoselov, and A. K. Geim: *Chiral tunnelling and the Klein paradox in graphene*. Nat. Phys. **2**, 620–625 (2006). DOI: 10.1038/nphys384 (cit. on pp. 1, 9, 41).

[Kat12] M. I. Katsnelson: *Graphene: Carbon in Two Dimensions*. Cambridge University Press, 2012. URL: https://www.ebook.de/de/product/18277709/mikhail_i_katsnelson_graphene.html (cit. on pp. 9, 41).

[Khe+16] E. Khestanova, F. Guinea, L. Fumagalli, A. K. Geim, and I. V. Grigorieva: *Universal shape and pressure inside bubbles appearing in van der Waals heterostructures*. Nat. Commun. **7**, 12587 (2016). DOI: 10.1038/ncomms12587 (cit. on p. 33).

[Kit03] A. Y. Kitaev: *Fault-tolerant quantum computation by anyons*. Ann. Phys. **303**, 2–30 (2003). DOI: 10.1016/s0003-4916(02)00018-0 (cit. on p. 123).

[Kja+16] M. Kjaergaard, F. Nichele, H. J. Suominen, M. P. Nowak, M. Wimmer, A. R. Akhmerov, J. A. Folk, K. Flensberg, J. Shabani, C. J. Palmstrøm, and C. M. Marcus: *Quantized conductance doubling and hard gap in a two-dimensional semiconductor–superconductor heterostructure*. Nat. Commun. **7**, 12841 (2016). DOI: 10.1038/ncomms12841 (cit. on p. 118).

[Kla04] T. M. Klapwijk: *Proximity Effect From an Andreev Perspective*. J. Supercond. **17**, 593–611 (2004). DOI: 10.1007/s10948-004-0773-0 (cit. on p. 21).

[KBT82] T. M. Klapwijk, G. E. Blonder, and M. Tinkham: *Explanation of subharmonic energy gap structure in superconducting contacts*. Phys. B+C **109-110**, 1657–1664 (1982). DOI: 10.1016/0378-4363(82)90189-9 (cit. on pp. 23, 51).

[KF18] A. Knothe and V. Fal'ko: *Influence of minivalleys and Berry curvature on electrostatically induced quantum wires in gapped bilayer graphene*. Phys. Rev. B **98**, 155435 (2018). DOI: 10.1103/physrevb.98.155435 (cit. on pp. 15, 86, 89, 97, 99, 113).

[KMS16] K. Kolasiński, A. Mreńca-Kolasińska, and B. Szafran: *Transconductance and effective Landé factors for quantum point contacts: Spin-orbit coupling and interaction effects*. Phys. Rev. B **93**, 035304 (2016). DOI: 10.1103/physrevb.93.035304 (cit. on p. 96).

[Koo+08] E. J. Koop, B. J. van Wees, D. Reuter, A. D. Wieck, and C. H. van der Wal: *Spin Accumulation and Spin Relaxation in a Large Open Quantum Dot*. Phys. Rev. Lett. **101**, 056602 (2008). DOI: 10.1103/physrevlett.101.056602 (cit. on p. 95).

[Kra+18a] R. Kraft, I. V. Krainov, V. Gall, A. P. Dmitriev, R. Krupke, I. V. Gornyi, and R. Danneau: *Valley Subband Splitting in Bilayer Graphene Quantum Point Contacts*. Phys. Rev. Lett. **121**, 257703 (2018). DOI: 10.1103/physrevlett.121.257703 (cit. on pp. 78, 79, 88, 106, 166).

[Kra+18b] R. Kraft, J. Mohrmann, R. Du, P. B. Selvasundaram, M. Irfan, U. N. Kanilmaz, F. Wu, D. Beckmann, H. von Löhneysen, R. Krupke, A. Akhmerov, I. Gornyi, and R. Danneau: *Tailoring supercurrent confinement in graphene bilayer weak links*. Nat. Commun. **9**, 1722 (2018). DOI: 10.1038/s41467-018-04153-4 (cit. on pp. 41, 48, 59–62, 106, 113, 160, 164).

[Kre+14] A. V. Kretinin, Y. Cao, J. S. Tu, G. L. Yu, R. Jalil, K. S. Novoselov, S. J. Haigh, A. Gholinia, A. Mishchenko, M. Lozada, T. Georgiou, C. R. Woods, F. Withers, P. Blake, G. Eda, A. Wirsig, C. Hucho, K. Watanabe, T. Taniguchi, A. K. Geim, and R. V. Gorbachev: *Electronic Properties of Graphene Encapsulated with Different Two-Dimensional Atomic Crystals*. Nano Lett. **14**, 3270–3276 (2014). DOI: 10.1021/nl5006542 (cit. on p. 33).

[Kri+00] A. Kristensen, H. Bruus, A. E. Hansen, J. B. Jensen, P. E. Lindelof, C. J. Marckmann, J. Nygård, C. B. Sørensen, F. Beuscher, A. Forchel, and M. Michel: *Bias and temperature dependence of the 0.7 conductance anomaly in quantum point contacts*. Phys. Rev. B **62**, 10950–10957 (2000). DOI: 10.1103/physrevb.62.10950 (cit. on p. 93).

[Kro+18] J. G. Kroll, W. Uilhoorn, K. L. van der Enden, D. de Jong, K. Watanabe, T. Taniguchi, S. Goswami, M. C. Cassidy, and L. P. Kouwenhoven: *Magnetic field compatible circuit quantum electrodynamics with graphene Josephson junctions*. Nat. Commun. **9**, 4615 (2018). DOI: 10.1038/s41467-018-07124-x (cit. on p. 25).

[KO77] I. O. Kulik and A. N. Omel'yanchuk: *Properties of superconducting microbridges in the pure limit*. Sov. J. Low Temp. Phys. **3:7** (1977) (cit. on pp. 24, 101).

[KO78] O. I. Kulik and A. N. Omel'yanchuk: *Josephson effect in superconducting bridges - Microscopic theory*. Fiz. Nisk. Temp. **4**, 296–311 (1978) (cit. on p. 101).

[Kur+11] E. V. Kurganova, H. J. van Elferen, A. McCollam, L. A. Ponomarenko, K. S. Novoselov, A. Veligura, B. J. van Wees, J. C. Maan, and U. Zeitler: *Spin splitting in graphene studied by means of tilted magnetic-field experiments*. Phys. Rev. B **84**, 121407(R) (2011). DOI: 10.1103/physrevb.84.121407 (cit. on p. 94).

[Kuz+09] A. B. Kuzmenko, I. Crassee, D. van der Marel, P. Blake, and K. S. Novoselov: *Determination of the gate-tunable band gap and tight-binding parameters in bilayer graphene using infrared spectroscopy*. Phys. Rev. B **80**, 165406 (2009). DOI: 10.1103/physrevb.80.165406 (cit. on p. 11).

[LKF19] T. L. M. Lane, A. Knothe, and V. I. Fal'ko: *Semimetallic features in quantum transport through a gate-defined point contact in bilayer graphene*. Phys. Rev. B **100**, 115427 (2019). DOI: 10.1103/physrevb.100.115427 (cit. on pp. 89, 99).

[Lan+02] J. Lantz, V. S. Shumeiko, E. Bratus, and G. Wendin: *Phase-dependent multiple Andreev reflections in SNS interferometers*. Phys. Rev. B **65**, 134523 (2002). DOI: 10.1103/physrevb.65.134523 (cit. on p. 123).

[LSR07] A. Lassl, P. Schlagheck, and K. Richter: *Effects of short-range interactions on transport through quantum point contacts: A numerical approach*. Phys. Rev. B **75**, 045346 (2007). DOI: 10.1103/physrevb.75.045346 (cit. on p. 93).

[LFB99] U. Ledermann, A. L. Fauchère, and G. Blatter: *Nonlocality in mesoscopic Josephson junctions with strip geometry*. Phys. Rev. B **59**, R9027–R9030 (1999). DOI: 10.1103/physrevb.59.r9027 (cit. on pp. 44, 57).

[LL18] G.-H. Lee and H.-J. Lee: *Proximity coupling in superconductor-graphene heterostructures*. Rep. Prog. Phys. **81**, 056502 (2018). DOI: 10.1088/1361-6633/aaafe1 (cit. on pp. 24, 41).

[Lee+18] H. Lee, G.-H. Park, J. Park, G.-H. Lee, K. Watanabe, T. Taniguchi, and H.-J. Lee: *Edge-Limited Valley-Preserved Transport in Quasi-1D Constriction of Bilayer Graphene*. Nano Lett. **18**, 5961–5966 (2018). DOI: 10.1021/acs.nanolett.8b02750 (cit. on p. 79).

[Lee+14] S.-P. Lee, K. Michaeli, J. Alicea, and A. Yacoby: *Revealing Topological Superconductivity in Extended Quantum Spin Hall Josephson Junctions*. Phys. Rev. Lett. **113**, 197001 (2014). DOI: 10.1103/physrevlett.113.197001 (cit. on p. 47).

[Li+17] J. I. A. Li, C. Tan, S. Chen, Y. Zeng, T. Taniguchi, K. Watanabe, J. Hone, and C. R. Dean: *Even-denominator fractional quantum Hall states in bilayer graphene*. Science **358**, 648–652 (2017). DOI: 10.1126/science.aao2521 (cit. on p. 123).

[Li+11] J. Li, I. Martin, M. Büttiker, and A. F. Morpurgo: *Topological origin of subgap conductance in insulating bilayer graphene*. Nat. Phys. **7**, 38–42 (2011). DOI: 10.1038/nphys1822 (cit. on pp. 42, 63).

[Li+16] J. Li, K. Wang, K. J. McFaul, Z. Zern, Y. Ren, K. Watanabe, T. Taniguchi, Z. Qiao, and J. Zhu: *Gate-controlled topological conducting channels in bilayer graphene*. Nat. Nanotechnol. **11**, 1060–1065 (2016). DOI: 10.1038/nnano.2016.158 (cit. on p. 79).

[Lia+10] C. Lian, K. Tahy, T. Fang, G. Li, H. G. Xing, and D. Jena: *Quantum transport in graphene nanoribbons patterned by metal masks*. Appl. Phys. Lett. **96**, 103109 (2010). DOI: 10.1063/1.3352559 (cit. on p. 79).

[Lif60] I. M. Lifshitz: *Anomalies of Electron Characteristics of a Metal in the High Pressure Region*. JETP **11**, 1130 (1960) (cit. on p. 15).

[Lik79] K. K. Likharev: *Superconducting weak links*. Rev. Mod. Phys. **51**, 101–159 (1979). DOI: 10.1103/revmodphys.51.101 (cit. on pp. 3, 20, 21, 101, 102).

[Lin+08] Y.-M. Lin, V. Perebeinos, Z. Chen, and P. Avouris: *Electrical observation of subband formation in graphene nanoribbons*. Phys. Rev. B **78**, 161409(R) (2008). DOI: 10.1103/physrevb.78.161409 (cit. on p. 79).

[LYB11] H. Lind, I. I. Yakimenko, and K.-F. Berggren: *Electric-field control of magnetization in biased semiconductor quantum wires and point contacts*. Phys. Rev. B **83**, 075308 (2011). DOI: 10.1103/physrevb.83.075308 (cit. on p. 93).

[Lud07] T. Ludwig: *Andreev reflection in bilayer graphene*. Phys. Rev. B **75**, 195322 (2007). DOI: 10.1103/physrevb.75.195322 (cit. on p. 22).

[Mar+17] K. Marinov, A. Avsar, K. Watanabe, T. Taniguchi, and A. Kis: *Resolving the spin splitting in the conduction band of monolayer MoS_2*. Nat. Commun. **8**, 1938 (2017). DOI: 10.1038/s41467-017-02047-5 (cit. on p. 95).

[Mar+08a] J. Martin, N. Akerman, G. Ulbricht, T. Lohmann, J. H. Smet, K. von Klitzing, and A. Yacoby: *Observation of electron–hole puddles in graphene using a scanning single-electron transistor*. Nat. Phys. **4**, 144–148 (2008). DOI: 10.1038/nphys781 (cit. on p. 5).

[Mar+08b] T. P. Martin, A. Szorkovszky, A. P. Micolich, A. R. Hamilton, C. A. Marlow, H. Linke, R. P. Taylor, and L. Samuelson: *Enhanced Zeeman splitting in $Ga_{0.25}In_{0.75}As$ quantum point contacts*. Appl. Phys. Lett. **93**, 012105 (2008). DOI: 10.1063/1.2957033 (cit. on p. 95).

[Mar+10] T. P. Martin, A. Szorkovszky, A. P. Micolich, A. R. Hamilton, C. A. Marlow, R. P. Taylor, H. Linke, and H. Q. Xu: *Field-orientation dependence of the Zeeman spin splitting in (In,Ga)As quantum point contacts*. Phys. Rev. B **81**, 041303(R) (2010). DOI: 10.1103/physrevb.81.041303 (cit. on pp. 95, 96).

[Mar+92] L. Martin-Moreno, J. T. Nicholls, N. K. Patel, and M. Pepper: *Non-linear conductance of a saddle-point constriction*. J. Phys.: Condens. Matter **4**, 1323–1333 (1992). DOI: 10.1088/0953-8984/4/5/012 (cit. on p. 84).

[MTS91] K. Matsubara, T. Tsuzuku, and K. Sugihara: *Electron spin resonance in graphite*. Phys. Rev. B **44**, 11845–11851 (1991). DOI: 10.1103/physrevb.44.11845 (cit. on p. 94).

[Mat04] K. A. Matveev: *Conductance of a quantum wire at low electron density*. Phys. Rev. B **70**, 245319 (2004). DOI: 10.1103/physrevb.70.245319 (cit. on p. 93).

[May+11] A. S. Mayorov, R. V. Gorbachev, S. V. Morozov, L. Britnell, R. Jalil, L. A. Ponomarenko, P. Blake, K. S. Novoselov, K. Watanabe, T. Taniguchi, and A. K. Geim: *Micrometer-Scale Ballistic Transport in Encapsulated Graphene at Room Temperature*. Nano Lett. **11**, 2396–2399 (2011). DOI: 10.1021/nl200758b (cit. on pp. 6, 8).

[McC06] E. McCann: *Asymmetry gap in the electronic band structure of bilayer graphene*. Phys. Rev. B **74**, 161403(R) (2006). DOI: 10.1103/physrevb.74.161403 (cit. on pp. 2, 10, 13, 14, 41, 88).

[MF06] E. McCann and V. I. Fal'ko: *Landau-Level Degeneracy and Quantum Hall Effect in a Graphite Bilayer*. Phys. Rev. Lett. **96**, 086805 (2006). DOI: 10.1103/physrevlett.96.086805 (cit. on pp. 10–12, 15).

[MK13] E. McCann and M. Koshino: *The electronic properties of bilayer graphene*. Rep. Prog. Phys. **76**, 056503 (2013). DOI: 10.1088/0034-4885/76/5/056503 (cit. on pp. 2, 10–15, 41, 87, 89, 99, 114).

[McC57] J. W. McClure: *Band Structure of Graphite and de Haas-van Alphen Effect*. Phys. Rev. **108**, 612–618 (1957). DOI: 10.1103/physrev.108.612 (cit. on p. 11).

[McG+10] L. M. McGuire, M. Friesen, K. A. Slinker, S. N. Coppersmith, and M. A. Eriksson: *Valley splitting in a Si/SiGe quantum point contact*. New J. Phys. **12**, 033039 (2010). DOI: 10.1088/1367-2630/12/3/033039 (cit. on pp. 78, 88).

[MFG16] H. Meier, V. I. Fal'ko, and L. I. Glazman: *Edge effects in the magnetic interference pattern of a ballistic SNS junction*. Phys. Rev. B **93**, 184506 (2016). DOI: 10.1103/physrevb.93.184506 (cit. on pp. 44, 47, 57, 59).

[MHW02] Y. Meir, K. Hirose, and N. S. Wingreen: *Kondo Model for the "0.7 Anomaly" in Transport through a Quantum Point Contact*. Phys. Rev. Lett. **89**, 196802 (2002). DOI: 10.1103/physrevlett.89.196802 (cit. on p. 93).

[Men+17] N. Menezes, V. S. Alves, E. C. Marino, L. Nascimento, L. O. Nascimento, and C. M. Smith: *Spin g -factor due to electronic interactions in graphene*. Phys. Rev. B **95**, 245138 (2017). DOI: 10.1103/physrevb.95.245138 (cit. on p. 94).

[Mey+07] J. C. Meyer, A. K. Geim, M. I. Katsnelson, K. S. Novoselov, T. J. Booth, and S. Roth: *The structure of suspended graphene sheets*. Nature **446**, 60–63 (2007). DOI: 10.1038/nature05545 (cit. on p. 6).

[Mic11] A. P. Micolich: *What lurks below the last plateau: experimental studies of the* $0.7 \times 2e^2/h$ *conductance anomaly in one-dimensional systems*. J. Phys.: Condens. Matter **23**, 443201 (2011). DOI: 10.1088/0953-8984/23/44/443201 (cit. on pp. 92, 93).

[Mil+07] J. B. Miller, I. P. Radu, D. M. Zumbühl, E. M. Levenson-Falk, M. A. Kastner, C. M. Marcus, L. N. Pfeiffer, and K. W. West: *Fractional quantum Hall effect in a quantum point contact at filling fraction 5/2*. Nat. Phys. **3**, 561–565 (2007). DOI: 10.1038/nphys658 (cit. on p. 123).

[Mis+17] D. S. Miserev, A. Srinivasan, O. A. Tkachenko, V. A. Tkachenko, I. Farrer, D. A. Ritchie, A. R. Hamilton, and O. P. Sushkov: *Mechanisms for Strong Anisotropy of In-Plane g-Factors in Hole Based Quantum Point Contacts*. Phys. Rev. Lett. **119**, 116803 (2017). DOI: 10.1103/physrevlett.119.116803 (cit. on p. 95).

[Miy+10] H. Miyazaki, K. Tsukagoshi, A. Kanda, M. Otani, and S. Okada: *Influence of Disorder on Conductance in Bilayer Graphene under Perpendicular Electric Field*. Nano Lett. **10**, 3888–3892 (2010). DOI: 10.1021/nl1015365 (cit. on pp. 2, 42).

[Miz+18] R. Mizokuchi, R. Maurand, F. Vigneau, M. Myronov, and S. De Franceschi: *Ballistic One-Dimensional Holes with Strong g-Factor Anisotropy in Germanium*. Nano Lett. **18**, 4861–4865 (2018). DOI: 10.1021/acs.nanolett.8b01457 (cit. on pp. 93, 96).

[MND13] N. Mizuno, B. Nielsen, and X. Du: *Ballistic-like supercurrent in suspended graphene Josephson weak links*. Nat. Commun. **4**, 2716 (2013). DOI: 10.1038/ncomms3716 (cit. on p. 24).

[MZ07] A. G. Moghaddam and M. Zareyan: *Graphene-based superconducting quantum point contacts*. Appl. Phys. A **89**, 579–585 (2007). DOI: 10.1007/s00339-007-4187-2 (cit. on pp. 104, 116).

[Moh16] J. Mohrmann: *Quantum Transport and Shot Noise in Graphene-Boron Nitride Heterostructures*. PhD thesis. Karlsruhe Institute of Technology, 2016 (cit. on p. 37).

[Mor+08] S. V. Morozov, K. S. Novoselov, M. I. Katsnelson, F. Schedin, D. C. Elias, J. A. Jaszczak, and A. K. Geim: *Giant Intrinsic Carrier Mobilities in Graphene and Its Bilayer*. Phys. Rev. Lett. **100**, 016602 (2008). DOI: 10.1103/physrevlett.100.016602 (cit. on p. 5).

[MRJ92] C. J. Muller, J. M. van Ruitenbeek, and L. J. de Jongh: *Conductance and supercurrent discontinuities in atomic-scale metallic constrictions of variable width*. Phys. Rev. Lett. **69**, 140–143 (1992). DOI: 10.1103/physrevlett.69.140 (cit. on p. 105).

[MCP12] W. A. Muñoz, L. Covaci, and F. M. Peeters: *Tight-binding study of bilayer graphene Josephson junctions*. Phys. Rev. B **86**, 184505 (2012). DOI: 10.1103/physrevb.86.184505 (cit. on pp. 24, 46, 107).

[NYF82] S. Nagata, H. C. Yang, and D. K. Finnemore: *Oscillations in the temperature dependence of Josephson supercurrents in **SNS** junctions*. Phys. Rev. B **25**, 6012–6014 (1982). DOI: 10.1103/physrevb.25.6012 (cit. on p. 44).

[Nai+08] R. R. Nair, P. Blake, A. N. Grigorenko, K. S. Novoselov, T. J. Booth, T. Stauber, N. M. R. Peres, and A. K. Geim: *Fine Structure Constant Defines Visual Transparency of Graphene*. Science **320**, 1308 (2008). DOI: 10.1126/science.1156965 (cit. on p. 28).

[Nan+17] G. Nanda, J. L. Aguilera-Servin, P. Rakyta, A. Kormányos, R. Kleiner, D. Koelle, K. Watanabe, T. Taniguchi, L. M. K. Vandersypen, and S. Goswami: *Current-Phase Relation of Ballistic Graphene Josephson Junctions*. Nano Lett. **17**, 3396–3401 (2017). DOI: 10.1021/acs.nanolett.7b00097 (cit. on p. 46).

[Nil+11] H. A. Nilsson, P. Samuelsson, P. Caroff, and H. Q. Xu: *Supercurrent and Multiple Andreev Reflections in an InSb Nanowire Josephson Junction*. Nano Lett. **12**, 228–233 (2011). DOI: 10.1021/nl203380w (cit. on p. 108).

[Nov+12] K. S. Novoselov, V. I. Fal'ko, L. Colombo, P. R. Gellert, M. G. Schwab, and K. Kim: *A roadmap for graphene*. Nature **490**, 192–200 (2012). DOI: 10.1038/nature11458 (cit. on p. 2).

[Nov+05a] K. S. Novoselov, A. K. Geim, S. V. Morozov, D. Jiang, M. I. Katsnelson, I. V. Grigorieva, S. V. Dubonos, and A. A. Firsov: *Two-dimensional gas of massless Dirac fermions in graphene*. Nature **438**, 197–200 (2005). DOI: 10.1038/nature04233 (cit. on p. 1).

[Nov+04] K. S. Novoselov, A. K. Geim, S. V. Morozov, D. Jiang, Y. Zhang, S. V. Dubonos, I. V. Grigorieva, and A. A. Firsov: *Electric Field Effect in Atomically Thin Carbon Films*. Science **306**, 666–669 (2004). DOI: 10.1126/science.1102896 (cit. on p. 1).

[Nov+05b] K. S. Novoselov, D. Jiang, F. Schedin, T. J. Booth, V. V. Khotkevich, S. V. Morozov, and A. K. Geim: *Two-dimensional atomic crystals*. PNAS **102**, 10451–10453 (2005). DOI: 10.1073/pnas.0502848102 (cit. on pp. 5, 27, 28).

[Nov+16] K. S. Novoselov, A. Mishchenko, A. Carvalho, and A. H. Castro Neto: *2D materials and van der Waals heterostructures*. Science **353**, aac9439 (2016). DOI: 10.1126/science.aac9439 (cit. on pp. 2, 8, 9).

[Oct+83] M. Octavio, M. Tinkham, G. E. Blonder, and T. M. Klapwijk: *Subharmonic energy-gap structure in superconducting constrictions*. Phys. Rev. B **27**, 6739–6746 (1983). DOI: 10.1103/physrevb.27.6739 (cit. on pp. 23, 51, 111, 116).

[Oht+06] T. Ohta, A. Bostwick, T. Seyller, K. Horn, and E. Rotenberg: *Controlling the Electronic Structure of Bilayer Graphene*. Science **313**, 951–954 (2006). DOI: 10.1126/science.1130681 (cit. on p. 13).

[Oos+08] J. B. Oostinga, H. B. Heersche, X. Liu, A. F. Morpurgo, and L. M. K. Vandersypen: *Gate-induced insulating state in bilayer graphene devices*. Nat. Mater. **7**, 151–157 (2008). DOI: 10.1038/nmat2082 (cit. on pp. 2, 13, 41, 42, 53).

[Ove+18a] H. Overweg, H. Eggimann, X. Chen, S. Slizovskiy, M. Eich, R. Pisoni, Y. Lee, P. Rickhaus, K. Watanabe, T. Taniguchi, V. Fal'ko, T. Ihn, and K. Ensslin: *Electrostatically Induced Quantum Point Contacts in Bilayer Graphene*. Nano Lett. **18**, 553–559 (2018). DOI: 10.1021/acs.nanolett.7b04666 (cit. on pp. 31, 79, 86, 97, 99).

[Ove+18b] H. Overweg, A. Knothe, T. Fabian, L. Linhart, P. Rickhaus, L. Wernli, K. Watanabe, T. Taniguchi, D. Sánchez, J. Burgdörfer, F. Libisch, V. I. Fal'ko, K. Ensslin, and T. Ihn: *Topologically Nontrivial Valley States in Bilayer Graphene Quantum Point Contacts*. Phys. Rev. Lett. **121**, 257702 (2018). DOI: 10.1103/physrevlett.121.257702 (cit. on pp. 79, 97, 99).

[Par+18] J. Park, J. H. Lee, G.-H. Lee, Y. Takane, K.-I. Imura, T. Taniguchi, K. Watanabe, and H.-J. Lee: *Short Ballistic Josephson Coupling in Planar Graphene Junctions with Inhomogeneous Carrier Doping*. Phys. Rev. Lett. **120**, 077701 (2018). DOI: 10.1103/physrevlett.120.077701 (cit. on p. 107).

[Pat+90] N. K. Patel, L. Martin-Moreno, M. Pepper, R. Newbury, J. E. F. Frost, D. A. Ritchie, G. A. C. Jones, J. T. M. B. Janssen, J. Singleton, and J. A. A. J. Perenboom: *Ballistic transport in one dimension: additional quantisation produced by an electric field*. J. Phys.: Condens. Matter **2**, 7247–7254 (1990). DOI: 10.1088/0953-8984/2/34/018 (cit. on p. 84).

[Pat+91] N. K. Patel, J. T. Nicholls, L. Martn-Moreno, M. Pepper, J. E. F. Frost, D. A. Ritchie, and G. A. C. Jones: *Evolution of half plateaus as a function of electric field in a ballistic quasi-one-dimensional constriction*. Phys. Rev. B **44**, 13549–13555 (1991). DOI: 10.1103/physrevb.44.13549 (cit. on pp. 84, 95).

[Piz+16] F. Pizzocchero, L. Gammelgaard, B. S. Jessen, J. M. Caridad, L. Wang, J. Hone, P. Bøggild, and T. J. Booth: *The hot pick-up technique for batch assembly of van der Waals heterostructures*. Nat. Commun. **7**, 11894 (2016). DOI: 10.1038/ncomms11894 (cit. on pp. 27, 30, 33).

[Pon+13] L. A. Ponomarenko, R. V. Gorbachev, G. L. Yu, D. C. Elias, R. Jalil, A. A. Patel, A. Mishchenko, A. S. Mayorov, C. R. Woods, J. R. Wallbank, M. Mucha-Kruczynski, B. A. Piot, M. Potemski, I. V. Grigorieva, K. S. Novoselov, F. Guinea, V. I. Fal'ko, and A. K. Geim: *Cloning of Dirac fermions in graphene superlattices*. Nature **497**, 594–597 (2013). DOI: 10.1038/nature12187 (cit. on p. 9).

[Pot+02] R. M. Potok, J. A. Folk, C. M. Marcus, and V. Umansky: *Detecting Spin-Polarized Currents in Ballistic Nanostructures*. Phys. Rev. Lett. **89**, 266602 (2002). DOI: 10.1103/physrevlett.89.266602 (cit. on p. 95).

[Pri+15] V. S. Pribiag, A. J. A. Beukman, F. Qu, M. C. Cassidy, C. Charpentier, W. Wegscheider, and L. P. Kouwenhoven: *Edge-mode superconductivity in a two-dimensional topological insulator*. Nat. Nanotechnol. **10**, 593–597 (2015). DOI: 10.1038/nnano.2015.86 (cit. on pp. 45, 47).

[Qu+16] F. Qu, J. van Veen, F. K. de Vries, A. J. A. Beukman, M. Wimmer, W. Yi, A. A. Kiselev, B.-M. Nguyen, M. Sokolich, M. J. Manfra, F. Nichele, C. M. Marcus, and L. P. Kouwenhoven: *Quantized Conductance and Large g-Factor Anisotropy in InSb Quantum Point Contacts*. Nano Lett. **16**, 7509–7513 (2016). DOI: 10.1021/acs.nanolett.6b03297 (cit. on p. 96).

[RKC16] P. Rakyta, A. Kormányos, and J. Cserti: *Magnetic field oscillations of the critical current in long ballistic graphene Josephson junctions*. Phys. Rev. B **93**, 224510 (2016). DOI: 10.1103/physrevb.93.224510 (cit. on pp. 24, 46, 57, 107).

[Rao+11] S. S. Rao, A. Stesmans, K. Keunen, D. V. Kosynkin, A. Higginbotham, and J. M. Tour: *Unzipped graphene nanoribbons as sensitive O_2 sensors: Electron spin resonance probing and dissociation kinetics*. Appl. Phys. Lett. **98**, 083116 (2011). DOI: 10.1063/1.3559229 (cit. on p. 94).

[Rei05] D. J. Reilly: *Phenomenological model for the 0.7 conductance feature in quantum wires*. Phys. Rev. B **72**, 033309 (2005). DOI: 10.1103/physrevb.72.033309 (cit. on p. 93).

[Rei+02] D. J. Reilly, T. M. Buehler, J. L. O'Brien, A. R. Hamilton, A. S. Dzurak, R. G. Clark, B. E. Kane, L. N. Pfeiffer, and K. W. West: *Density-Dependent Spin Polarization in Ultra-Low-Disorder Quantum Wires*. Phys. Rev. Lett. **89**, 246801 (2002). DOI: 10.1103/physrevlett.89.246801 (cit. on p. 93).

[RRJ00] T. Rejec, A. Ramšak, and J. H. Jefferson: *Spin-dependent resonances in the conduction edge of quantum wires*. Phys. Rev. B **62**, 12985–12989 (2000). DOI: 10.1103/physrevb.62.12985 (cit. on p. 93).

[RM06] T. Rejec and Y. Meir: *Magnetic impurity formation in quantum point contacts*. Nature **442**, 900–903 (2006). DOI: 10.1038/nature05054 (cit. on p. 93).

[Rez+95] M. Reznikov, M. Heiblum, H. Shtrikman, and D. Mahalu: *Temporal Correlation of Electrons: Suppression of Shot Noise in a Ballistic Quantum Point Contact*. Phys. Rev. Lett. **75**, 3340–3343 (1995). DOI: 10.1103/physrevlett.75.3340 (cit. on p. 31).

[Rib+18] R. Ribeiro-Palau, C. Zhang, K. Watanabe, T. Taniguchi, J. Hone, and C. R. Dean: *Twistable electronics with dynamically rotatable heterostructures*. Science **361**, 690–693 (2018). DOI: 10.1126/science.aat6981 (cit. on p. 9).

[Ric+13] P. Rickhaus, R. Maurand, M.-H. Liu, M. Weiss, K. Richter, and C. Schönenberger: *Ballistic interferences in suspended graphene*. Nat. Commun. **4**, 2342 (2013). DOI: 10.1038/ncomms3342 (cit. on pp. 50, 65, 159).

[Riw+16] R.-P. Riwar, M. Houzet, J. S. Meyer, and Y. V. Nazarov: *Multi-terminal Josephson junctions as topological matter*. Nat. Commun. **7**, 11167 (2016). DOI: 10.1038/ncomms11167 (cit. on p. 123).

[Rod+07] S. Roddaro, P. Pingue, V. Piazza, V. Pellegrini, and F. Beltram: *The Optical Visibility of Graphene: Interference Colors of Ultrathin Graphite on SiO_2*. Nano Lett. **7**, 2707–2710 (2007). DOI: 10.1021/nl0711581 (cit. on p. 28).

[Row63] J. M. Rowell: *Magnetic Field Dependence of the Josephson Tunnel Current*. Phys. Rev. Lett. **11**, 200–202 (1963). DOI: 10.1103/physrevlett.11.200 (cit. on p. 44).

[RTB07] A. Rycerz, J. Tworzydło, and C. W. J. Beenakker: *Valley filter and valley valve in graphene*. Nat. Phys. **3**, 172–175 (2007). DOI: 10.1038/nphys547 (cit. on pp. 2, 123).

[Sca+06] G. Scappucci, L. Di Gaspare, E. Giovine, A. Notargiacomo, R. Leoni, and F. Evangelisti: *Conductance quantization in etched* Si/SiGe *quantum point contacts*. Phys. Rev. B **74**, 035321 (2006). DOI: 10.1103/physrevb.74.035321 (cit. on pp. 78, 93).

[Sch+16] J. R. Schaibley, H. Yu, G. Clark, P. Rivera, J. S. Ross, K. L. Seyler, W. Yao, and X. Xu: *Valleytronics in 2D materials*. Nat. Rev. Mater. **1**, 16055 (2016). DOI: 10.1038/natrevmats.2016.55 (cit. on p. 123).

[Sch+98] E. Scheer, N. Agraït, J. C. Cuevas, A. L. Yeyati, B. Ludoph, A. Martín-Rodero, G. R. Bollinger, J. M. van Ruitenbeek, and C. Urbina: *The signature of chemical valence in the electrical conduction through a single-atom contact*. Nature **394**, 154–157 (1998). DOI: 10.1038/28112 (cit. on p. 105).

[Sch+18] F. E. Schmidt, M. D. Jenkins, K. Watanabe, T. Taniguchi, and G. A. Steele: *A ballistic graphene superconducting microwave circuit*. Nat. Commun. **9**, 4069 (2018). DOI: 10.1038/s41467-018-06595-2 (cit. on pp. 25, 46).

[Sch+10] J. M. Schneider, N. A. Goncharuk, P. Vašek, P. Svoboda, Z. Výborný, L. Smrčka, M. Orlita, M. Potemski, and D. K. Maude: *Using magnetotransport to determine the spin splitting in graphite*. Phys. Rev. B **81**, 195204 (2010). DOI: 10.1103/physrevb.81.195204 (cit. on p. 94).

[Sch+14] E. Schubert, J. Heyder, F. Bauer, B. Waschneck, W. Stumpf, W. Wegscheider, J. von Delft, S. Ludwig, and A. Högele: *Toward combined transport and optical studies of the 0.7-anomaly in a quantum point contact*. phys. status solidi B **251**, 1931–1937 (2014). DOI: 10.1002/pssb.201350218 (cit. on p. 93).

[SM03] G. Seelig and K. A. Matveev: *Electron-Phonon Scattering in Quantum Point Contacts*. Phys. Rev. Lett. **90**, 176804 (2003). DOI: 10.1103/physrevlett.90.176804 (cit. on p. 93).

[Shc00] N. M. Shchelkachev: *Critical current in superconducting quantum point contacts*. JETP Lett. **71**, 504–507 (2000). DOI: 10.1134/1.1307476 (cit. on pp. 101, 103–105, 114, 115).

[SZ03] D. E. Sheehy and A. M. Zagoskin: *Theory of anomalous magnetic interference pattern in mesoscopic superconducting/normal/superconducting Josephson junctions*. Phys. Rev. B **68**, 144514 (2003). DOI: 10.1103/physrevb.68.144514 (cit. on pp. 57, 59).

[SRL08] A. V. Shytov, M. S. Rudner, and L. S. Levitov: *Klein Backscattering and Fabry-Pérot Interference in Graphene Heterojunctions*. Phys. Rev. Lett. **101**, 156804 (2008). DOI: 10.1103/physrevlett.101.156804 (cit. on pp. 50, 65, 159, 165).

[SW58] J. C. Slonczewski and P. R. Weiss: *Band Structure of Graphite*. Phys. Rev. **109**, 272–279 (1958). DOI: 10.1103/physrev.109.272 (cit. on p. 11).

[Som+17] S. Somanchi, B. Terrés, J. Peiro, M. Staggenborg, K. Watanabe, T. Taniguchi, B. Beschoten, and C. Stampfer: *From Diffusive to Ballistic Transport in Etched Graphene Constrictions and Nanoribbons*. Ann. Phys. **529**, 1700082 (2017). DOI: 10.1002/andp.201700082 (cit. on p. 79).

[SCL06] Y.-W. Son, M. L. Cohen, and S. G. Louie: *Energy Gaps in Graphene Nanoribbons*. Phys. Rev. Lett. **97**, 216803 (2006). DOI: 10.1103/physrevlett.97.216803 (cit. on p. 2).

[SZ00] B. Spivak and F. Zhou: *Ferromagnetic correlations in quasi-one-dimensional conducting channels*. Phys. Rev. B **61**, 16730–16735 (2000). DOI: 10.1103/physrevb.61.16730 (cit. on p. 93).

[Sus01] O. P. Sushkov: *Conductance anomalies in a one-dimensional quantum contact*. Phys. Rev. B **64**, 155319 (2001). DOI: 10.1103/physrevb.64.155319 (cit. on p. 93).

[TI11] Y. Takane and K.-I. Imura: *Josephson Current through a Planar Junction of Graphene*. J. Phys. Soc. JPN **80**, 043702 (2011). DOI: 10.1143/jpsj.80.043702 (cit. on p. 107).

[TI12] Y. Takane and K.-I. Imura: *Quasiclassical Theory of the Josephson Effect in Ballistic Graphene Junctions*. J. Phys. Soc. JPN **81**, 094707 (2012). DOI: 10.1143/jpsj.81.094707 (cit. on p. 107).

[TAN95] H. Takayanagi, T. Akazaki, and J. Nitta: *Observation of Maximum Supercurrent Quantization in a Superconducting Quantum Point Contact*. Phys. Rev. Lett. **75**, 3533–3536 (1995). DOI: 10.1103/physrevlett.75.3533 (cit. on pp. 105, 108).

[TAN96] H. Takayanagi, T. Akazaki, and J. Nitta: *Observation of the quantized critical current in a superconducting quantum point contact*. Surf. Sci. **361-362**, 298–301 (1996). DOI: 10.1016/0039-6028(96)00407-4 (cit. on pp. 105, 108).

[Tan+07] Y.-W. Tan, Y. Zhang, K. Bolotin, Y. Zhao, S. Adam, E. H. Hwang, S. Das Sarma, H. L. Stormer, and P. Kim: *Measurement of Scattering Rate and Minimum Conductivity in Graphene*. Phys. Rev. Lett. **99**, 246803 (2007). DOI: 10.1103/physrevlett.99.246803 (cit. on p. 5).

[TW07] T. Taniguchi and K. Watanabe: *Synthesis of high-purity boron nitride single crystals under high pressure by using Ba–BN solvent*. J. Cryst. Growth **303**, 525–529 (2007). DOI: 10.1016/j.jcrysgro.2006.12.061 (cit. on p. 27).

[TJ10] T. Taychatanapat and P. Jarillo-Herrero: *Electronic Transport in Dual-Gated Bilayer Graphene at Large Displacement Fields*. Phys. Rev. Lett. **105**, 166601 (2010). DOI: 10.1103/physrevlett.105.166601 (cit. on pp. 41, 42, 53).

[Tay+11] T. Taychatanapat, K. Watanabe, T. Taniguchi, and P. Jarillo-Herrero: *Quantum Hall effect and Landau-level crossing of Dirac fermions in trilayer graphene*. Nat. Phys. **7**, 621–625 (2011). DOI: 10.1038/nphys2008 (cit. on pp. 6, 14, 15).

[Tay+13] T. Taychatanapat, K. Watanabe, T. Taniguchi, and P. Jarillo-Herrero: *Electrically tunable transverse magnetic focusing in graphene*. Nat. Phys. **9**, 225–229 (2013). DOI: 10.1038/nphys2549 (cit. on p. 8).

[Ter+16] B. Terrés, L. A. Chizhova, F. Libisch, J. Peiro, D. Jörger, S. Engels, A. Girschik, K. Watanabe, T. Taniguchi, S. V. Rotkin, J. Burgdörfer, and C. Stampfer: *Size quantization of Dirac fermions in graphene constrictions*. Nat. Commun. **7**, 11528 (2016). DOI: 10.1038/ncomms11528 (cit. on p. 79).

[Tho+98] K. J. Thomas, J. T. Nicholls, N. J. Appleyard, M. Y. Simmons, M. Pepper, D. R. Mace, W. R. Tribe, and D. A. Ritchie: *Interaction effects in a one-dimensional constriction*. Phys. Rev. B **58**, 4846–4852 (1998). DOI: 10.1103/physrevb.58.4846 (cit. on pp. 93, 95).

[Tho+96] K. J. Thomas, J. T. Nicholls, M. Y. Simmons, M. Pepper, D. R. Mace, and D. A. Ritchie: *Possible Spin Polarization in a One-Dimensional Electron Gas*. Phys. Rev. Lett. **77**, 135–138 (1996). DOI: 10.1103/physrevlett.77.135 (cit. on pp. 92, 93, 95).

[Tho+95] K. J. Thomas, M. Y. Simmons, J. T. Nicholls, D. R. Mace, M. Pepper, and D. A. Ritchie: *Ballistic transport in one-dimensional constrictions formed in deep two-dimensional electron gases*. Appl. Phys. Lett. **67**, 109–111 (1995). DOI: 10.1063/1.115498 (cit. on p. 83).

[Tho+86] T. J. Thornton, M. Pepper, H. Ahmed, D. Andrews, and G. J. Davies: *One-Dimensional Conduction in the 2D Electron Gas of a GaAs-AlGaAs Heterojunction*. Phys. Rev. Lett. **56**, 1198–1201 (1986). DOI: 10.1103/physrevlett.56.1198 (cit. on p. 78).

[Tin04] M. Tinkham: *Introduction to Superconductivity*. Dover, New York, 2004. 480 pp. (cit. on pp. 16–18, 20, 21, 42, 44, 57, 63, 67, 69, 101, 160, 161).

[TB06] M. Titov and C. W. J. Beenakker: *Josephson effect in ballistic graphene*. Phys. Rev. B **74**, 041401(R) (2006). DOI: 10.1103/physrevb.74.041401 (cit. on pp. 23, 24, 41, 46, 107, 116).

[Tob+95] D. Tobben, D. A. Wharam, G. Abstreiter, J. P. Kolthaus, and F. Schaffler: *Ballistic electron transport through a quantum point contact defined in a Si/$Si_{0.7}Ge_{0.3}$ heterostructure*. Semicond. Sci. Technol. **10**, 711–714 (1995). DOI: 10.1088/0268-1242/10/5/025 (cit. on pp. 78, 88).

[Tom+11] N. Tombros, A. Veligura, J. Junesch, J. J. van den Berg, P. J. Zomer, M. Wojtaszek, I. J. Vera Marun, H. T. Jonkman, and B. J. van Wees: *Large yield production of high mobility freely suspended graphene electronic devices on a polydimethylglutarimide based organic polymer*. J. Appl. Phys. **109**, 093702 (2011). DOI: 10.1063/1.3579997 (cit. on p. 79).

[Tra+07] B. Trauzettel, D. V. Bulaev, D. Loss, and G. Burkard: *Spin qubits in graphene quantum dots*. Nat. Phys. **3**, 192–196 (2007). DOI: 10.1038/nphys544 (cit. on pp. 2, 123).

[Vae+13] A. Vaezi, Y. Liang, D. H. Ngai, L. Yang, and E.-A. Kim: *Topological Edge States at a Tilt Boundary in Gated Multilayer Graphene*. Phys. Rev. X **3**, 021018 (2013). DOI: 10.1103/physrevx.3.021018 (cit. on p. 42).

[Var+14a] A. Varlet, D. Bischoff, P. Simonet, K. Watanabe, T. Taniguchi, T. Ihn, K. Ensslin, M. Mucha-Kruczyński, and V. I. Fal'ko: *Anomalous Sequence of Quantum Hall Liquids Revealing a Tunable Lifshitz Transition in Bilayer Graphene*. Phys. Rev. Lett. **113**, 116602 (2014). DOI: 10.1103/physrevlett.113.116602 (cit. on p. 99).

[Var+14b] A. Varlet, M.-H. Liu, V. Krueckl, D. Bischoff, P. Simonet, K. Watanabe, T. Taniguchi, K. Richter, K. Ensslin, and T. Ihn: *Fabry-Pérot Interference in Gapped Bilayer Graphene with Broken Anti-Klein Tunneling*. Phys. Rev. Lett. **113**, 116601 (2014). DOI: 10.1103/physrevlett.113.116601 (cit. on pp. 15, 50, 53, 65, 159, 165).

[VS16] G. Vionnet and O. P. Sushkov: *Enhancement Mechanism of the Electron* **g** *Factor in Quantum Point Contacts*. Phys. Rev. Lett. **116**, 126801 (2016). DOI: 10.1103/physrevlett.116.126801 (cit. on p. 95).

[VSZ12] A. V. Volkov, A. A. Shylau, and I. V. Zozoulenko: *Interaction-induced enhancement of* **g** *factor in graphene*. Phys. Rev. B **86**, 155440 (2012). DOI: 10.1103/physrevb.86.155440 (cit. on pp. 93, 96).

[WB96] C.-K. Wang and K.-F. Berggren: *Spin splitting of subbands in quasi-one-dimensional electron quantum channels*. Phys. Rev. B **54**, R14257–R14260 (1996). DOI: 10.1103/physrevb.54.r14257 (cit. on pp. 93, 95).

[Wan+13] L. Wang, I. Meric, P. Y. Huang, Q. Gao, Y. Gao, H. Tran, T. Taniguchi, K. Watanabe, L. M. Campos, D. A. Muller, J. Guo, P. Kim, J. Hone, K. L. Shepard, and C. R. Dean: *One-Dimensional Electrical Contact to a Two-Dimensional Material*. Science **342**, 614–617 (2013). DOI: 10.1126/science.1244358 (cit. on pp. 3, 8, 9, 24, 27, 29, 30, 34, 50).

[War11] P. A. Warburton: *The Josephson effect: 50 years of science and technology*. Phys. Educ. **46**, 669–675 (2011). DOI: 10.1088/0031-9120/46/6/s02 (cit. on pp. 16, 17).

[WTK04] K. Watanabe, T. Taniguchi, and H. Kanda: *Direct-bandgap properties and evidence for ultraviolet lasing of hexagonal boron nitride single crystal*. Nat. Mater. **3**, 404–409 (2004). DOI: 10.1038/nmat1134 (cit. on p. 6).

[Wee+88a] B. J. van Wees, H. van Houten, C. W. J. Beenakker, J. G. Williamson, L. P. Kouwenhoven, D. van der Marel, and C. T. Foxon: *Quantized conductance of point contacts in a two-dimensional electron gas*. Phys. Rev. Lett. **60**, 848–850 (1988). DOI: 10.1103/physrevlett.60.848 (cit. on pp. 78, 102).

[Wee+88b] B. J. van Wees, L. P. Kouwenhoven, H. van Houten, C. W. J. Beenakker, J. E. Mooij, C. T. Foxon, and J. J. Harris: *Quantized conductance of magnetoelectric subbands in ballistic point contacts*. Phys. Rev. B **38**, 3625–3627 (1988). DOI: 10.1103/physrevb.38.3625 (cit. on p. 87).

[Wha+88] D. A. Wharam, T. J. Thornton, R. Newbury, M. Pepper, H. Ahmed, J. E. F. Frost, D. G. Hasko, D. C. Peacock, D. A. Ritchie, and G. A. C. Jones: *One-dimensional transport and the quantisation of the ballistic resistance*. J. Phys. C **21**, L209–L214 (1988). DOI: 10.1088/0022-3719/21/8/002 (cit. on pp. 78, 102).

[Wie+02] U. Wieser, U. Kunze, K. Ismail, and J. O. Chu: *Quantum-ballistic transport in an etch-defined Si/SiGe quantum point contact*. Appl. Phys. Lett. **81**, 1726–1728 (2002). DOI: 10.1063/1.1503157 (cit. on p. 78).

[Wil+09] J. R. Williams, D. A. Abanin, L. DiCarlo, L. S. Levitov, and C. M. Marcus: *Quantum Hall conductance of two-terminal graphene devices*. Phys. Rev. B **80**, 045408 (2009). DOI: 10.1103/physrevb.80.045408 (cit. on p. 158).

[Wil12] M. N. Wilson: *100 Years of Superconductivity and 50 Years of Superconducting Magnets*. IEEE Trans. Appl. Supercond. **22**, 3800212 (2012). DOI: 10.1109/tasc.2011.2174628 (cit. on p. 16).

[Xia+06] J. Xiang, A. Vidan, M. Tinkham, R. M. Westervelt, and C. M. Lieber: *Ge/Si nanowire mesoscopic Josephson junctions*. Nat. Nanotechnol. **1**, 208–213 (2006). DOI: 10.1038/nnano.2006.140 (cit. on pp. 105, 108, 114, 116).

[Xue+11] J. Xue, J. Sanchez-Yamagishi, D. Bulmash, P. Jacquod, A. Deshpande, K. Watanabe, T. Taniguchi, P. Jarillo-Herrero, and B. J. LeRoy: *Scanning tunnelling microscopy and spectroscopy of ultra-flat graphene on hexagonal boron nitride*. Nat. Mater. **10**, 282–285 (2011). DOI: 10.1038/nmat2968 (cit. on pp. 6, 7).

[YF84] H. C. Yang and D. K. Finnemore: *Pair-breaking mechanisms in superconductor—normal-metal—superconductor junctions*. Phys. Rev. B **30**, 1260–1265 (1984). DOI: 10.1103/physrevb.30.1260 (cit. on p. 44).

[Yan+18] M. Yankowitz, J. Jung, E. Laksono, N. Leconte, B. L. Chittari, K. Watanabe, T. Taniguchi, S. Adam, D. Graf, and C. R. Dean: *Dynamic band-structure tuning of graphene moiré superlattices with pressure*. Nature **557**, 404–408 (2018). DOI: 10.1038/s41586-018-0107-1 (cit. on p. 9).

[Yan+19] M. Yankowitz, Q. Ma, P. Jarillo-Herrero, and B. J. LeRoy: *van der Waals heterostructures combining graphene and hexagonal boron nitride*. Nat. Rev. Phys. **1**, 112–125 (2019). DOI: 10.1038/s42254-018-0016-0 (cit. on pp. 2, 8, 9, 31).

[Yan+12] M. Yankowitz, J. Xue, D. Cormode, J. D. Sanchez-Yamagishi, K. Watanabe, T. Taniguchi, P. Jarillo-Herrero, P. Jacquod, and B. J. LeRoy: *Emergence of superlattice Dirac points in graphene on hexagonal boron nitride*. Nat. Phys. **8**, 382–386 (2012). DOI: 10.1038/nphys2272 (cit. on p. 8).

[YXL14] M. Yankowitz, J. Xue, and B. J. LeRoy: *Graphene on hexagonal boron nitride*. J. Phys.: Condens. Matter **26**, 303201 (2014). DOI: 10.1088/0953-8984/26/30/303201 (cit. on pp. 5–7).

[YK09] A. F. Young and P. Kim: *Quantum interference and Klein tunnelling in graphene heterojunctions*. Nat. Phys. **5**, 222–226 (2009). DOI: 10.1038/nphys1198 (cit. on pp. 50, 65, 159, 165).

[Zap75] H. H. Zappe: *Determination of the current density distribution in Josephson tunnel junctions*. Phys. Rev. B **11**, 2535–2538 (1975). DOI: 10.1103/physrevb.11.2535 (cit. on p. 47).

[Zaz+03] A. Zazunov, V. S. Shumeiko, E. N. Bratus', J. Lantz, and G. Wendin: *Andreev Level Qubit*. Phys. Rev. Lett. **90**, 087003 (2003). DOI: 10.1103/physrevlett.90.087003 (cit. on p. 123).

[ZMM13] F. Zhang, A. H. MacDonald, and E. J. Mele: *Valley Chern numbers and boundary modes in gapped bilayer graphene*. PNAS **110**, 10546–10551 (2013). DOI: 10.1073/pnas.1308853110 (cit. on p. 42).

[Zha+17] H. Zhang, Ö. Gül, S. Conesa-Boj, M. P. Nowak, M. Wimmer, K. Zuo, V. Mourik, F. K. de Vries, J. van Veen, M. W. A. de Moor, J. D. S. Bommer, D. J. van Woerkom, D. Car, S. R. Plissard, E. P. A. M. Bakkers, M. Quintero-Pérez, M. C. Cassidy, S. Koelling, S. Goswami, K. Watanabe, T. Taniguchi, and L. P. Kouwenhoven: *Ballistic superconductivity in semiconductor nanowires*. Nat. Commun. **8**, 16025 (2017). DOI: 10.1038/ncomms16025 (cit. on p. 118).

[Zha+09a] Y. Zhang, V. W. Brar, C. Girit, A. Zettl, and M. F. Crommie: *Origin of spatial charge inhomogeneity in graphene*. Nat. Phys. **5**, 722–726 (2009). DOI: 10.1038/nphys1365 (cit. on p. 5).

[Zha+05] Y. Zhang, Y.-W. Tan, H. L. Stormer, and P. Kim: *Experimental observation of the quantum Hall effect and Berry's phase in graphene*. Nature **438**, 201–204 (2005). DOI: 10.1038/nature04235 (cit. on p. 1).

[Zha+09b] Y. Zhang, T.-T. Tang, C. Girit, Z. Hao, M. C. Martin, A. Zettl, M. F. Crommie, Y. R. Shen, and F. Wang: *Direct observation of a widely tunable bandgap in bilayer graphene*. Nature **459**, 820–823 (2009). DOI: 10.1038/nature08105 (cit. on pp. 13, 41, 53).

[Zhe+86] H. Z. Zheng, H. P. Wei, D. C. Tsui, and G. Weimann: *Gate-controlled transport in narrow GaAs/$Al_xGa_{1-x}As$ heterostructures*. Phys. Rev. B **34**, 5635–5638 (1986). DOI: 10.1103/physrevb.34.5635 (cit. on p. 78).

[Zhu+17] M. J. Zhu, A. V. Kretinin, M. D. Thompson, D. A. Bandurin, S. Hu, G. L. Yu, J. Birkbeck, A. Mishchenko, I. J. Vera-Marun, K. Watanabe, T. Taniguchi, M. Polini, J. R. Prance, K. S. Novoselov, A. K. Geim, and M. Ben Shalom: *Edge currents shunt the insulating bulk in gapped graphene*. Nat. Commun. **8**, 14552 (2017). DOI: 10.1038/ncomms14552 (cit. on pp. 42, 45, 47, 62, 63, 74).

[Zhu+18] M. Zhu, M. B. Shalom, A. Mishchsenko, V. Fal'ko, K. Novoselov, and A. Geim: *Supercurrent and multiple Andreev reflections in micrometer-long ballistic graphene Josephson junctions*. Nanoscale **10**, 3020–3025 (2018). DOI: 10.1039/c7nr05904c (cit. on p. 24).

[Zib+17] A. A. Zibrov, C. Kometter, H. Zhou, E. M. Spanton, T. Taniguchi, K. Watanabe, M. P. Zaletel, and A. F. Young: *Tunable interacting composite fermion phases in a half-filled bilayer-graphene Landau level*. Nature **549**, 360–364 (2017). DOI: 10.1038/nature23893 (cit. on pp. 31, 123).

[Zim+17] K. Zimmermann, A. Jordan, F. Gay, K. Watanabe, T. Taniguchi, Z. Han, V. Bouchiat, H. Sellier, and B. Sacépé: *Tunable transmission of quantum Hall edge channels with full degeneracy lifting in split-gated graphene devices*. Nat. Commun. **8**, 14983 (2017). DOI: 10.1038/ncomms14983 (cit. on p. 123).

[Zom+11] P. J. Zomer, S. P. Dash, N. Tombros, and B. J. van Wees: *A transfer technique for high mobility graphene devices on commercially available hexagonal boron nitride*. Appl. Phys. Lett. **99**, 232104 (2011). DOI: 10.1063/1.3665405 (cit. on p. 6).

[Zom+14] P. J. Zomer, M. H. D. Guimarães, J. C. Brant, N. Tombros, and B. J. van Wees: *Fast pick up technique for high quality heterostructures of bilayer graphene and hexagonal boron nitride*. Appl. Phys. Lett. **105**, 013101 (2014). DOI: 10.1063/1.4886096 (cit. on p. 27).

[ŽFD04] I. Žutić, J. Fabian, and S. Das Sarma: *Spintronics: Fundamentals and applications*. Rev. Mod. Phys. **76**, 323–410 (2004). DOI: 10.1103/revmodphys.76.323 (cit. on p. 123).

Appendix

A Sample fabrication recipes

A.1 Atomic layer deposition

The Al_2O_3 layers are fabricated with atomic layer deposition (ALD) using the following parameters: 182 TMA/H_2O (trymethylaluminium/water) cycles at 90 °C for 20 nm oxide.

A.2 Reactive ion etching

The hBN/BLG/hBN vdW heterostructure stacks are etched using reactive ion etching (Oxford Instruments Plasmalab 80 reactor) with a mixture of 40 sccm/4 sccm CHF_3/O_2 at a pressure of 60 mTorr. The etch rate for hBN is first calibrated using a test hBN which was initially determined as $\approx 48\,\mathrm{nm\,min^{-1}}$, and later after several maintaining steps of the machine as $\approx 40\,\mathrm{nm\,min^{-1}}$.

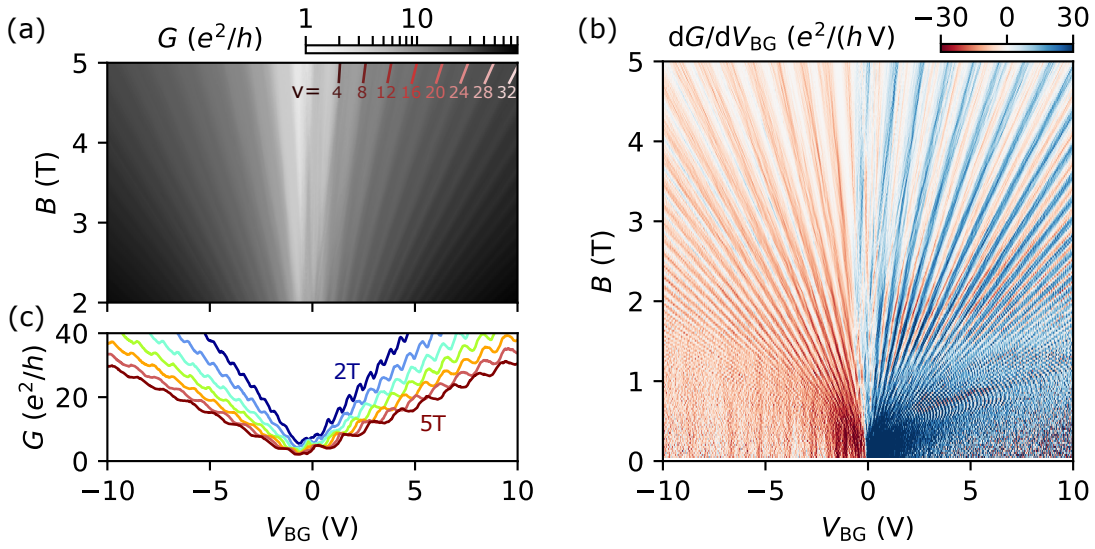

Figure B.1: Landau level fan diagram. (a, b) Conductance and differentiated conductance as a function of V_{BG} and magnetic field B at constant $V_{SG} = 0$. Labels ν denote the filling factor of the Landau levels. The Landau fan is well-developed down to a few hundred mT, highlighting the high quality of the device. (c) Respective conductance traces at constant $B = 2\,\mathrm{T} \rightarrow 5\,\mathrm{T}$ in steps of 0.5 T. The curves reveal a characteristic "N-shape" distortion of the plateaus as expected for two-terminal magnetotransport measurements in samples with high aspect ratio W/L [Wil+09]. The overshoot of the conductance plateaus is caused by the finite contribution of the longitudinal conductivity in the two-terminal setup and appears stronger pronounced on the electron side due to the higher mobility. Data from CD#1.

B Supplementary information: QPC-like confinement

B.1 Specific gate capacitances

Charge carrier densities induced by BG and SG are calculated in the parallel plate capacitor model as $n_{BG} = \frac{C_{BG}}{e}(V_{BG} - V_{BG}^{cnp})$ and $n_{SG} = \frac{C_{SG}}{e}(V_{SG} - V_{SG}^{cnp})$. In the outer regions of the device the charge carrier density is given by $n_{out} = n_{BG}$, while in the dual-gated region the charge carrier density is obtained by the sum $n_{in} = n_{BG} + n_{SG}$. We determine the specific BG capacitance C_{BG} from the Landau level fan diagram at $V_{SG} = 0$, shown in Fig. B.1. By fitting the slopes of the Landau levels $B = nh/e\nu$ for different filling factors ν, we find $C_{BG} = 3.9 \times 10^{11}\,\mathrm{cm}^{-2}\,\mathrm{V}^{-1}$. The specific SG capacitance C_{SG} can then be determined from the slope of the charge neutrality line $\delta D = 0$ in the SG-BG resistance map (see Fig. 4.6a): $C_{SG} = C_{BG}\,|\Delta V_{BG}/\Delta V_{SG}| = 4.15 \times 10^{11}\,\mathrm{cm}^{-2}\,\mathrm{V}^{-1}$.

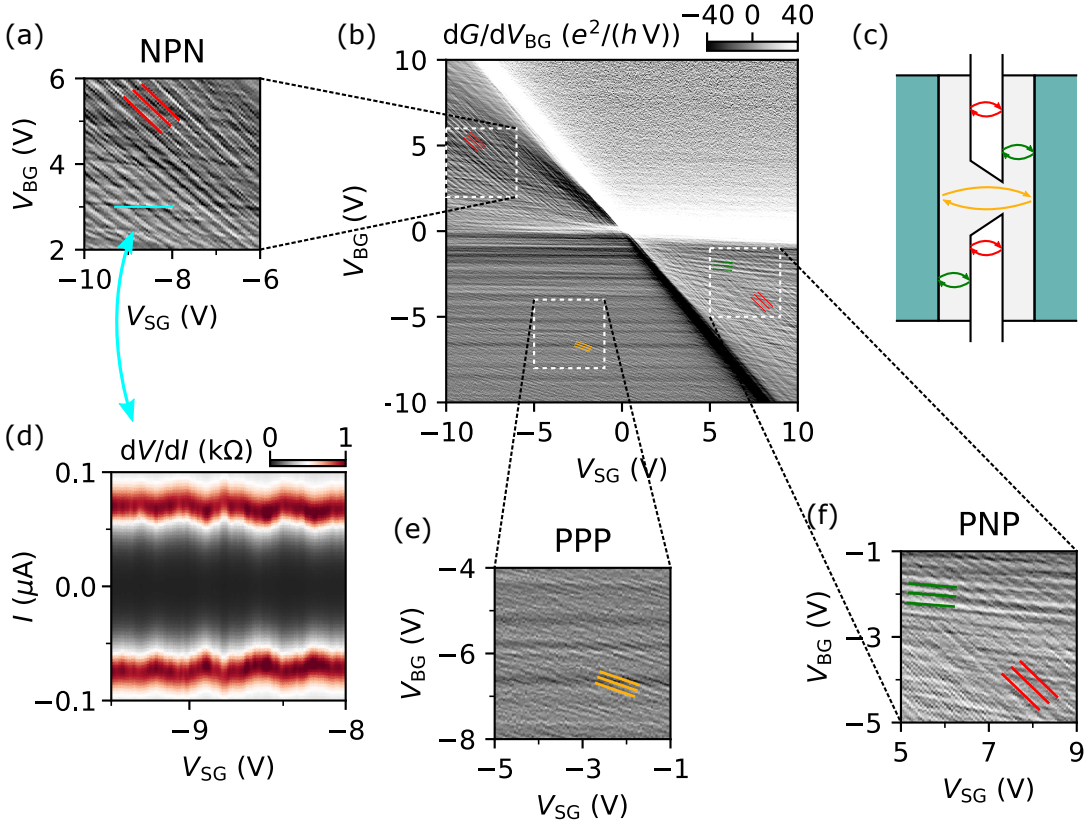

Figure B.2: Fabry-Pérot interferences and ballistic supercurrent. (b) Numerical derivative of the conductance in the normal state ($B = 20\,\mathrm{mT}$) as a function of V_{SG} and V_{BG} (corresponds to the data of the gate-gate-map shown in Fig. 4.6a). (a, e, f) Zoom-in panels on regions NPN, PPP and PNP, respectively. Colored exemplary lines highlight visible resonances. (c) Schematic of the device with indicated cavities that are responsible for the observed sets of Fabry-Pérot interferences. (d) Color map of the differential resistance (at $B = 0$) as a function of V_{SG} and bias current I at constant $V_{BG} = 3\,\mathrm{V}$, showing the tuning of the supercurrent in region NPN as denoted by the cyan line in (a). Data from CD#1.

B.2 Fabry-Pérot interferences and ballistic supercurrent

The gate dependence of the conductance in the normal state reveals multiple oscillation patterns that can be attributed to Fabry-Pérot interferences arising from different cavities in the device [SRL08; YK09; Ric+13; Var+14b; Du+18]. Figure B.2b shows the map of the differentiated conductance as a function of V_{SG} and V_{BG} (corresponding to the data in Fig. 4.6a). The different sets of observed interference patterns can be assigned to their respective cavities by evaluating periodicity, slope and appearance in the map (see Fig. B.2a, c, e, f). The effective cavity length can be determined following from the resonance condition $\Delta k_F \times L = \pi$ (where $\Delta k_F = k_{F,j+1} - k_{F,j}$ is the difference in Fermi wave vector between two resonances). In the unipolar regime PPP, the cavity is formed by the *pn*-junctions at the interfaces of the graphene sheet with the two metallic electrodes. The spacing between resonances is $\Delta k_F \approx 3.2 \times 10^6\,\mathrm{m}^{-1}$,

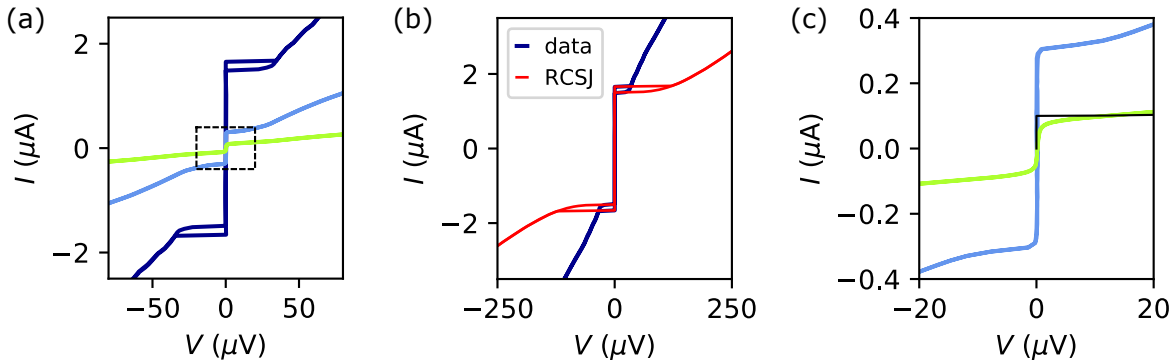

Figure B.3: Hysteretic behavior. (a) Up- and down-sweep IV curves at constant $V_{BG} = 8\,V$ for three different conditions: approximately uniform 2D weak link ($V_{SG} = 0$; dark blue), and right before or after the constriction is fully developed ($V_{SG} = -6.2\,V$; light blue and $V_{SG} = -7.0\,V$; green, respectively). (b) Fitted underdamped IV curve of the uniform 2D weak link ($V_{SG} = 0$) following the RCSJ model in Eq. 2.12 with parameters $R_n = 100\,\Omega$, $C = 27\,fF$ and $I_c = 1.67\,\mu A$. (c) Zoom-in on the other two curves (black dashed box in (a)). The additional black line is plotted based on the simplified expression of the RCSJ model for overdamped junctions (cf. Eq. B.1) using $I_c = 100\,nA$ and $R_n = 816\,\Omega$. Data from CD#1.

yielding an effective cavity size of $L \lesssim 1\,\mu m$ which is consistent with the geometrical size of the device. Thus, the occurrence of Fabry-Pérot interferences in region PPP indicate ballistic transport on a length scale larger than the device dimensions, *i. e.* at least twice the cavity size. [Kra+18b]

The amplitude of the supercurrent is found to be as well modulated in correlation with the Fabry-Pérot interferences. Figure B.2d shows a bias current map of the differential resistance versus V_{SG} recorded at $V_{BG} = 3\,V$, *i. e.* in region NPN. The critical current clearly oscillates following the Fabry-Pérot resonances in the normal state as observed in ballistic graphene weak links [Cal+15; Ben+16]. [Kra+18b]

B.3 Hysteresis of the IV curve under influence of confinement

The impact of the constriction on the hysteretic behavior of the Josephson effect is shown in Fig. B.3a. As we can see on the IV curves (up and down bias sweeps), a slight hysteresis ($I_r/I_c \approx 0.9$) occurs at sufficiently high charge carrier density ($V_{BG} = 8\,V$ and $V_{SG} = 0$; dark blue curve) and disappears once the constriction develops ($V_{SG} = -6.2\,V$ or $V_{SG} = -7.0\,V$; light blue and green curves, respectively). Within the RCSJ model (see subsection 2.3.2) [Tin04], the Josephson junction is tuned from underdamped to overdamped. We note that also for small n-type doping $\lesssim 1.5 \times 10^{12}\,cm^{-2}$, as well as for p-type doping no hysteresis is detected. [Kra+18b]

Figure B.3b shows a fit with the RCSJ model (Eq. 2.12) to the underdamped case of the approximately uniform junction at $V_{SG} = 0$, from which a plasma frequency $\omega_p = 4.34 \times 10^{11}\,\mathrm{Hz}$ ($\beta = 1.37$) is obtained. We note that although the hysteretic behavior can be captured within the RCSJ model, the larger current (enhanced subgap conductance) due to MAR is not. This is because of the assumed constant resistance R_n which does clearly not describe the weak link dynamics properly.

A zoom-in on the other two cases with finite negative SG voltage is shown in Fig. B.3c. As mentioned above, the junction becomes overdamped (*i. e.* no hysteresis is observed) with developing confinement which is the regime of interest for our experiments. For the overdamped junction case ($\beta \ll 1$) the equation of motion in the RCSJ framework (Eq. 2.12) can be simplified by neglecting the capacitance, resulting in a first order differential equation with solution [Tin04]

$$V = I_c R_n \sqrt{\left(\frac{I}{I_c} - 1\right)}\,, \qquad |I| \geq I_c\,. \tag{B.1}$$

The additionally shown thin black curve in Fig. B.3c is plotted according to this equation for comparison with the green curve ($V_{SG} = -7\,\mathrm{V}$). The employed parameters are the normal state resistance $R_n = 816\,\Omega$ and a value for the critical current $I_c = 100\,\mathrm{nA}$ determined from the position of the maximum resistance peak ($\mathrm{d}V/\mathrm{d}I$ as a function of I) at the switching. The experimentally measured curve is clearly different and displays a rather rounded switching and is not perfectly straight at zero current with a small but finite resistance $< 5\,\Omega$. In the Ambegaokar-Halperin model [AH69] (see subsection 2.3.2) this is understood as the phase diffusion due to thermal activation. For the measured critical current in the confined regime $I_c \sim 100\,\mathrm{nA}$ one finds for the normalized activation energy $u \approx 238$ at the base temperature of the experiment $T \approx 20\,\mathrm{mK}$ or $u \approx 48$ considering a somewhat higher electronic temperature of 100 mK. From Fig. 2.9 it can be seen that the IV curve starts to get rounded in shape at values of u in the same order.

With respect to the analysis in chapters 4 and 6 the rounding of the IV curves makes the definition for extracting the critical current I_c difficult. The extracted values are rather switching currents smaller than the critical current $I_{sw} < I_c$. This is of particular importance to notice for comparing our step heights of the discretized critical current δI_c with the theoretical expectation I_{c0} (or δI_{c0}, respectively). Therefore, we have defined in chapter 6 the position of the maximum resistance at the switching as the criteria for extracting I_c, although this maximum appears at finite voltage due to the gradual transition to the voltage state of the junction.

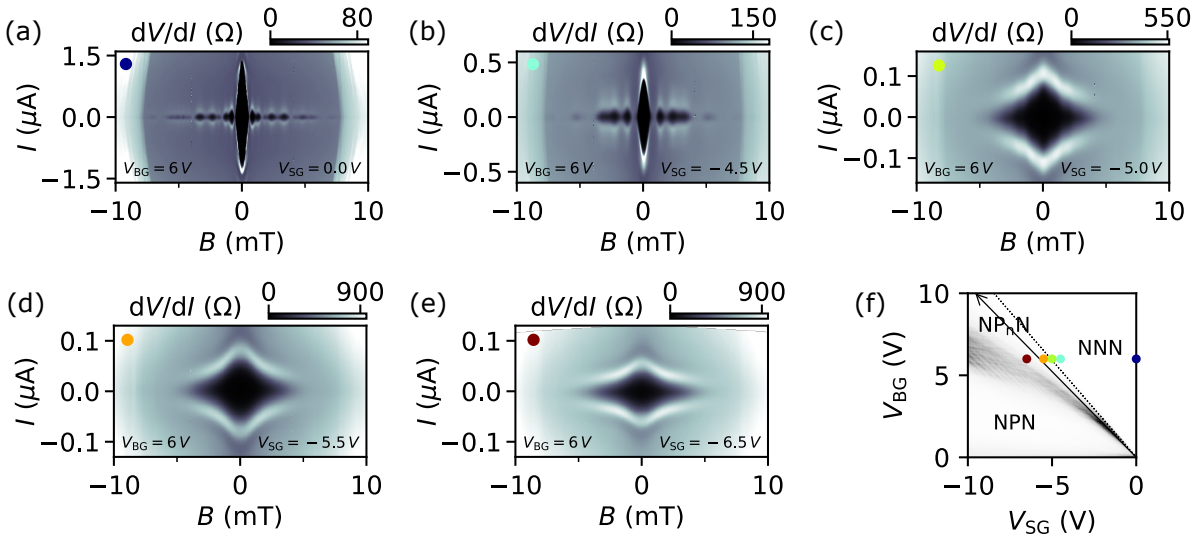

Figure B.4: Additional superconducting magneto-interferometry data. (a-e) Color maps of the differential resistance as a function of magnetic field B and current I at constant $V_{BG} = 6\,V$ for different values of V_{SG} as given in the plots. The respective gate conditions (V_{SG} and V_{BG}) of each panel are displayed by colored dots in the gate-gate-map (superconducting state, $B = 0$) shown in (f). Data from CD#1.

B.4 Additional superconducting magneto-interferometry data

Here, an additional series of superconducting magnetic interference patterns is presented for a different gate condition $V_{BG} = 6\,V$ (Fig. B.4a-e), clearly revealing the transition from a beating to a non-beating pattern corresponding to the creation of the 1D constriction. The crossover occurs consistently with the other data in the main text upon the tuning of the Fermi level into the band gap (see Fig. B.4f), here observed between $-5.0\,V < V_{SG} < -5.5\,V$ (although not precisely mapped out).

B.5 Ambipolar supercurrent confinement

As discussed in the main text, there is a large asymmetry between n- and p-type doping due to the formation of pn-junctions at the metal contacts, resulting in critical current values reduced by about an order of magnitude. Nonetheless, the formation of the constriction can be observed as well on the p-side. Figure B.5 shows a series of superconducting magnetic interference patterns at $V_{BG} = -10\,V$. Even though the monitored patterns are somewhat fainter developed, the trend from beating to non-beating pattern is clearly visible (but it should be noted that the IV curves have a finite slope).

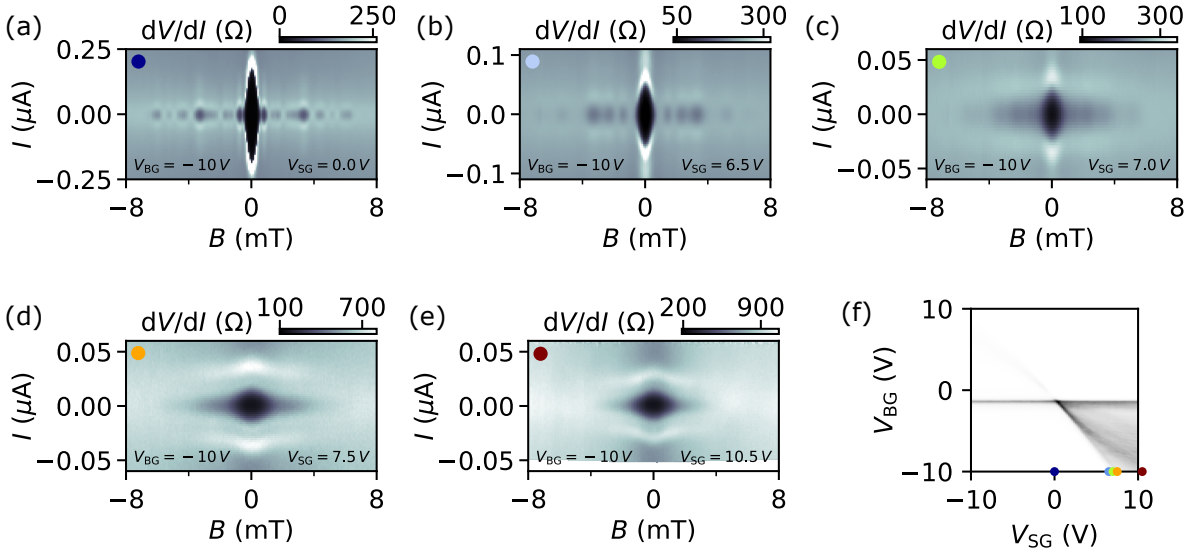

Figure B.5: Supercurrent confinement in the case of hole doping. (a-e) Color maps of the differential resistance as a function of B and I, showing superconducting magnetic interference patterns at constant $V_{\mathrm{BG}} = -10\,\mathrm{V}$ for different values of V_{SG} as given in the plots. The respective gate conditions (V_{SG} and V_{BG}) of each panel are displayed by colored dots in the gate-gate-map (superconducting state, $B = 0$) shown in (f). Note that these data sets were only recorded after added overall TG. Data from CD#4.

B.6 Geometry-dependent functions for the analytical model

The geometry-dependent functions $f_0(W/L)$ and $f_1(W/L)$ appearing in Eqs. 4.9 and 4.10 of the main text, respectively, are defined as follows ($x \equiv W/L$) [Kra+18b]:

$$f_0(x) = \frac{\sqrt{x^2+1}\log\left(\sqrt{x^2+1}+x\right)}{x} - \frac{x}{x+(x^2+1)\arctan(x)} \tag{B.2}$$

and

$$f_1(x) = \frac{\pi^{3/2}\left(1+x^2\right)^{3/2}}{8x^2[x+(1+x^2)\arctan(x)]}\,. \tag{B.3}$$

B.7 Estimate of the band gap

We provide a quantitative estimation of the electronic band gap induced by the displacement field. The gap should be much larger than the potential fluctuations coming from the residual charge carrier inhomogeneity $n_{\mathrm{res}} \approx 2.6 \times 10^{10}\,\mathrm{cm}^{-2}$ (see main text) which corresponds to an energy $E \approx 1\,\mathrm{meV}$. Such a band gap could be obtained following Eqs. 2.5 and 2.8 by applying back gate and top gate values of for example $V_{\mathrm{BG}} = 0.14\,\mathrm{V}$ and $V_{\mathrm{SG}} = -0.13\,\mathrm{V}$, respectively. In our experiments (see section 4.2), we studied the confinement at $V_{\mathrm{BG}} = 8\,\mathrm{V}$. Then at $V_{\mathrm{SG}} = -7.6\,\mathrm{V}$ (*i. e.* a value within the range of observed fully developed confinement, and corresponding to a displacement field of $\bar{D} \approx 0.56\,\mathrm{V\,nm}^{-1}$) we find a theoretical electronic band gap of $E_{\mathrm{gap}} \approx 85\,\mathrm{meV}$, which is in particular much larger than the potential fluctuations. [Kra+18b]

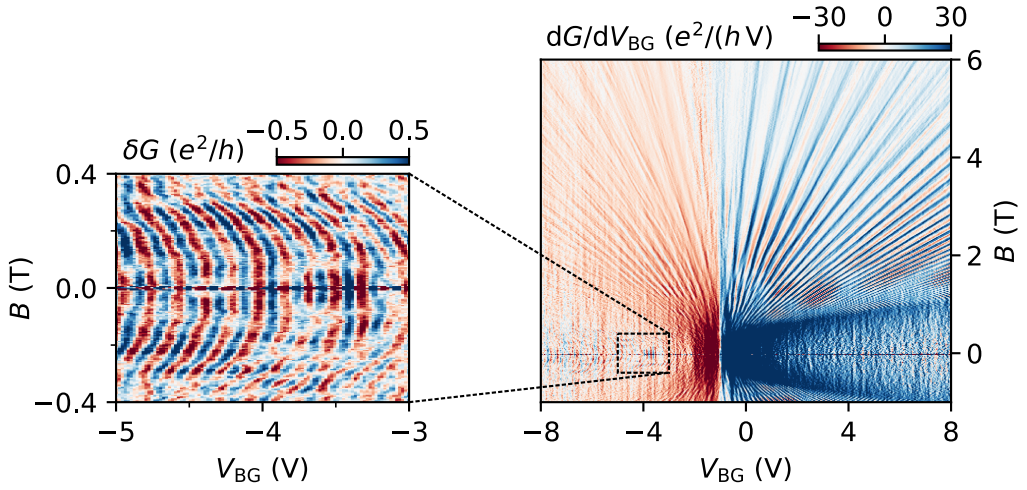

Figure C.1: Landau level fan and Fabry-Pérot interferences. Right: Differentiated conductance as a function of V_{BG} and magnetic field B at $V_{SG} = 0$. Left: Zoom-in measurement on the black dashed box with higher resolution, showing the conductance oscillations $\delta G = G - \bar{G}$ (with subtracted smooth background conductance $\bar{G}$).

C Supplementary information: Long channel confinement

C.1 Landau level fan and Fabry-Pérot interferences

As done for the other device with the QPC gate structure (see Appendix B.1), the specific gate capacitance of the BG is determined from the slope of the Landau levels in the Landau fan diagram at $V_{SG} = 0$, shown in Fig. C.1 (right panel). We find $C_{BG} = 4.75 \times 10^{11}\,\mathrm{cm^{-2}\,V^{-1}}$ for the specific gate capacitance of the BG and $C_{SG} = C_{BG}\,|\Delta V_{BG}/\Delta V_{SG}| = 4.52 \times 10^{11}\,\mathrm{cm^{-2}\,V^{-1}}$ for the SG determined from the slope of the charge neutrality line $\delta D = 0$ in the gate-gate-map (see Fig. 4.15).

The left panel in Fig. C.1 corresponds to a zoom-in on the black dashed box in the lower magnetic field range obtained in another measurement with higher resolution. The plot shows the net conductance oscillations $\delta G = G - \bar{G}$ (with subtracted smooth background conductance $\bar{G}$), which are due to the Fabry-Pérot interferences arising from the cavity between the two metal electrodes. As expected, the fringes show a parabolic-like dispersion with magnetic field. The dispersing behavior is because of the additional contribution of the Aharonov-Bohm phase [SRL08]. Furthermore it can be noted that the fringes disperse in a continuous fashion. The absence of any phase shift is characteristic for the anti-Klein tunneling behavior in BLG (without gap) [Var+14b; Du+18], in contrast to the π-shift signature of Klein tunneling in single-layer graphene [SRL08; YK09].

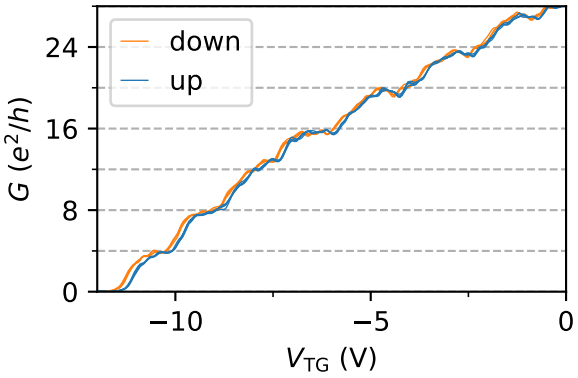

Figure D.1: Stability and robustness of the quantized conductance. Conductance as a function of V_{TG} at $V_{BG} = 9\,V$ and $V_{SG} = -10.6\,V$ with a total of four curves each up ($V_{TG} \to 0$) and down ($V_{TG} \to -12\,V$) for consecutive measurements. Data from CD#3.

D Supplementary information: QPC

D.1 Stability of the quantized conductance plateaus

Here, we report on the stability of the conductance quantization. Multiple TG sweeps (up and down) are recorded under the same gate condition as the presented data in the main text ($V_{BG} = 9\,V$ and $V_{SG} = -10.6\,V$ in CD#3; cf. Fig. 5.4). In total four curves each up ($V_{TG} = -12\,V \to 0$) and down ($V_{TG} = 0 \to -12\,V$) are measured and plotted in Fig. D.1. We note that all four curves perfectly sit on top of each other making them indistinguishable and both features conductance plateaus and Fabry-Pérot interferences are fully reproduced. We further note that a very small hysteresis between up- and down-sweeps is visible. [Kra+18a]

D.2 Confinement window at a given back gate voltage

Unlike in other systems (e. g. 2DEGs), charge carriers cannot be continuously depleted by changing a single gate. For instance, at a given V_{BG} the Fermi level is only positioned for a limited range of the applied V_{SG} in the induced band gap. For a too large opposite voltage though, the Fermi level underneath the SGs is already shifted into the respective other band, forming thereby *pn*-junctions in combination with the not split-gated outer regions of the device. Here, we show the complete transition from an unconfined unipolar junction, to a 1D confinement with the Fermi level tuned into the gap, and finally to the formation of a *npn*-junction in the bipolar regime. Figure D.2 presents data of the QPC device with overall TG at $V_{BG} = 6\,V$, for which the maximum applied $V_{SG} \leq -12\,V$ (*i. e.* without risking the device) is sufficient to cover the full range of the different scenarios, which can be clearly discerned in the observed

gray-scale map of the transconductance (normal state) as a function of V_{TG} and V_{SG}. With increasingly negative V_{SG} first the familiar stripe pattern of quantized conductance plateaus appears with the additional vertical resonances due to Fabry-Pérot interferences of the outer BLG reservoirs (cf. Fig. 5.4). Yet, with further increased negative V_{SG}, the stripe pattern dies down while an extra set of rather horizontal resonances turns up, which can be attributed to Fabry-Pérot interferences arising in the newly formed cavity underneath the SGs when the Fermi level is tuned into the valence band. The described transition is furthermore clearly reflected in the resultant superconducting magnetic interference patterns, shown on the right-hand side of Fig. D.2, where finally the reappearance of a beating pattern is observed when the current is again flowing through the split-gated cavities but being no longer confined.

D.3 Additional source-drain bias spectroscopy

As described in the main text (subsection 5.2.2) source-drain bias measurements were employed to determine the gate coupling factor α_{TG}. Here we extract this parameter for another confinement condition, *i.e.* $V_{BG} = 10\,\mathrm{V}$ and $V_{SG} = -11.6\,\mathrm{V}$ (CD#3). Figure D.3 shows the resulting color map of the transconductance as a function of bias voltage V and V_{TG}. Additionally, an overlaying set of cyan lines is plotted, which trace transitions across subband edges according to the relation as used in the main text $\alpha_{TG} e(V_{TG} - V_{TG}^0) = E_n^{QPC} \pm eV/2$. The observed source-drain bias pattern is well described using a subband and energy independent proportionality factor $\alpha_{TG} = 3.8 \times 10^{-3}$, in particular the same as extracted in the other discussed case with different gate conditions. Therefore, we employ this value in the rest of our analysis for converting between TG voltage and energy.

D.4 Fabry-Pérot interferences in in-plane magnetic field

The Zeeman energy spin splitting of 1D subbands (see subsection 5.2.4) is partially disturbed by the presence of Fabry-Pérot interferences. While the spin split subband edges disperse with changes in the in-plane magnetic field, the resonances do not. Thereby crossings of the different levels can occur. For a better monitoring of the behavior of the Fabry-Pérot interferences under the influence of an in-plane magnetic field, the resonances are studied without confinement and 1D subband formation. Figure D.4 shows the conductance oscillations δG, where the smooth background $\bar{G}$ is subtracted from the measured conductance G, as a function of V_{TG} and $B_{\parallel}$ at $V_{BG} = V_{SG} = 0$. Clearly, the resonances are hardly if at all affected by the in-plane magnetic field and stay at a given value of V_{TG} or Fermi wave vector, respectively (in contrast to an out-of-plane magnetic field with cyclotron motion).

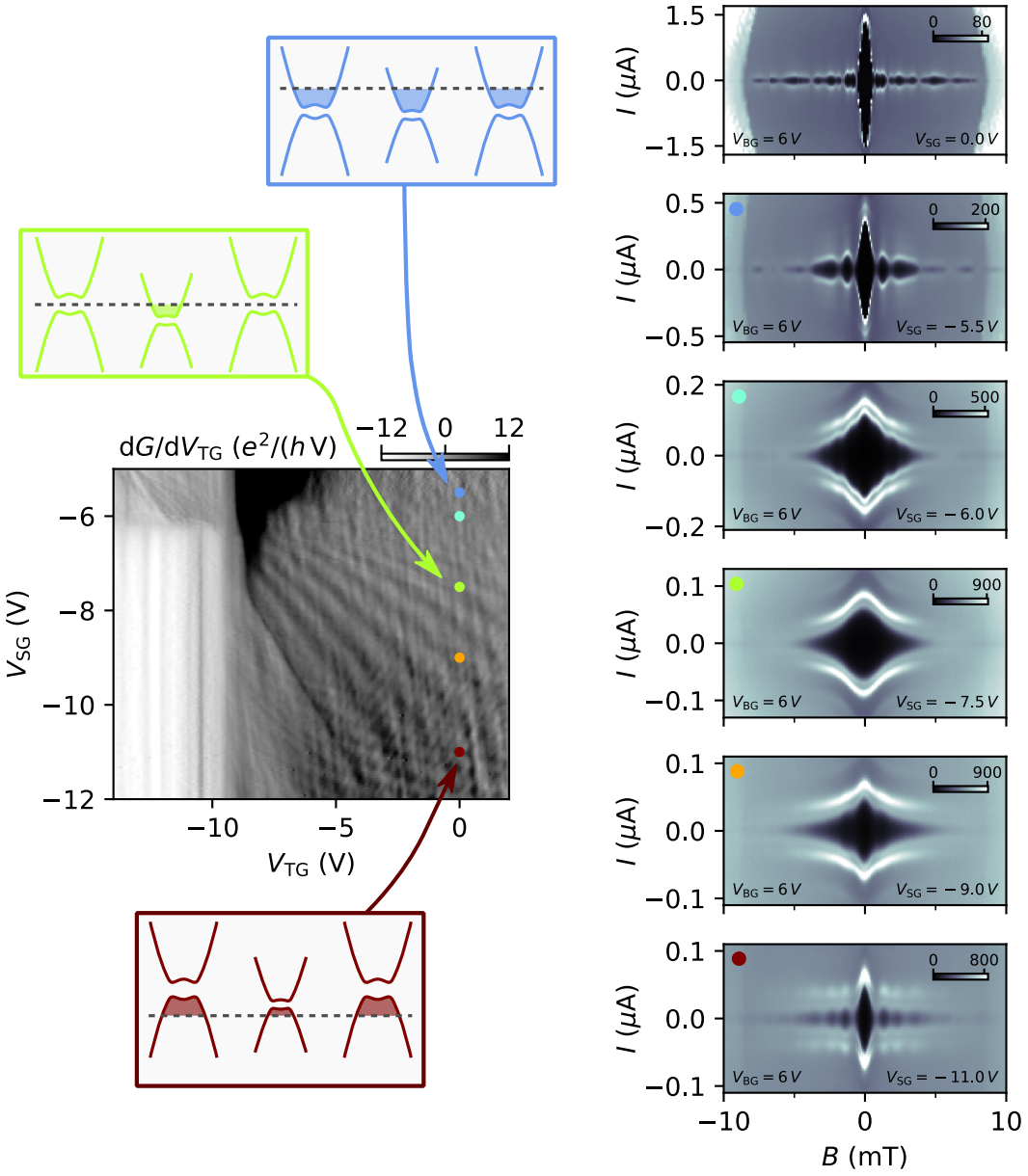

Figure D.2: Applicable SG window for creating a confinement at a given BG voltage. Right column: Color maps of the differential resistance (in Ω) as a function of magnetic field B and current I, showing superconducting magnetic interference patterns at constant $V_{BG} = 6\,V$ and $V_{TG} = 0$ for different values of V_{SG} as given in the plots. Left side: Differentiated conductance in the normal state ($B = 20\,mT$) as a function of V_{TG} and V_{SG} at respectively constant $V_{BG} = 6\,V$. The positions of the corresponding superconducting magnetic interference patterns are marked by colored dots. Additional panels sketch the respective spatial band structure profile across the split-gated region. Data from CD#4.

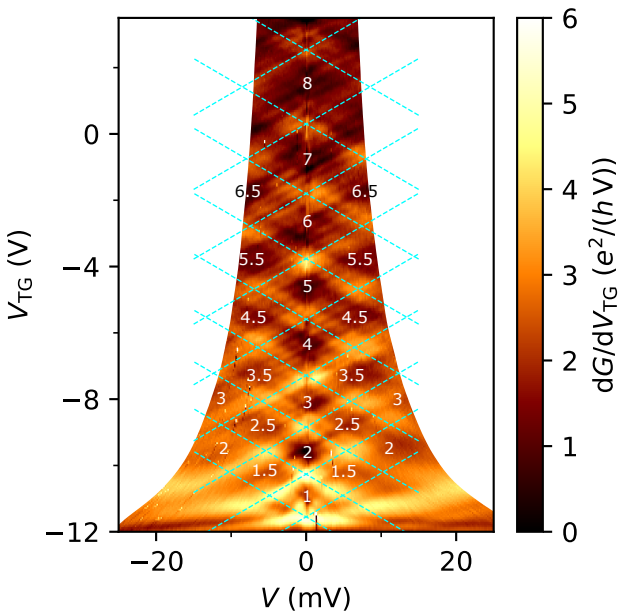

Figure D.3: Source-drain bias spectroscopy. Transconductance as a function of bias voltage V and V_{TG} at $V_{BG} = 10\,\text{V}$ and $V_{SG} = -11.6\,\text{V}$ (*i. e.* another confinement condition than discussed in the main text Fig. 5.6). The set of cyan dashed lines tracing the subband edges is plotted with the same gate coupling parameter $\alpha_{TG} = 3.8 \times 10^{-3}$ as in the main text. White numbers denote the value of the conductance plateaus in units of $4\,e^2/h$. Data from CD#3.

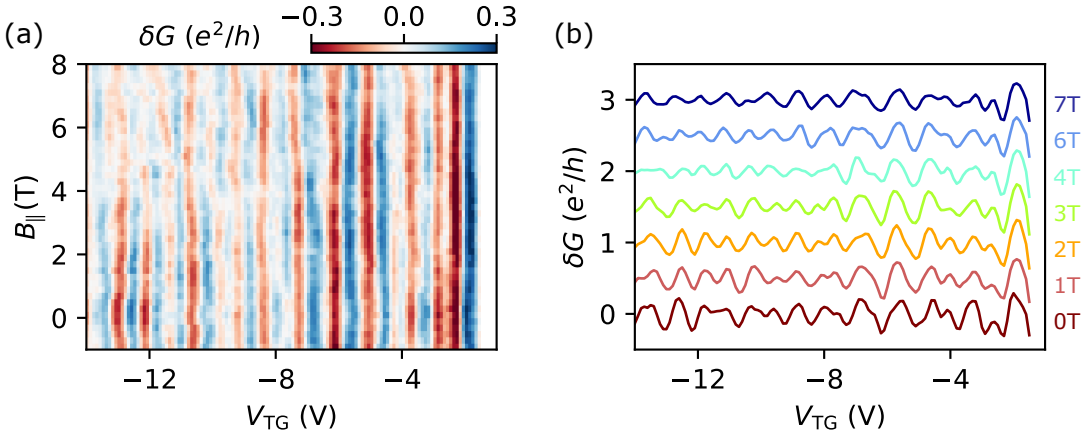

Figure D.4: Fabry-Pérot interferences under applied in-plane magnetic field. (a) Conductance oscillations $\delta G = G - \bar{G}$ (with subtracted smooth background conductance $\bar{G}$) as a function of V_{TG} and in-plane magnetic field $B_{||}$ at $V_{BG} = V_{SG} = 0$. (b) Several traces of δG for different $B_{||}$. Curves are shifted for clarity. Data from CD#5.

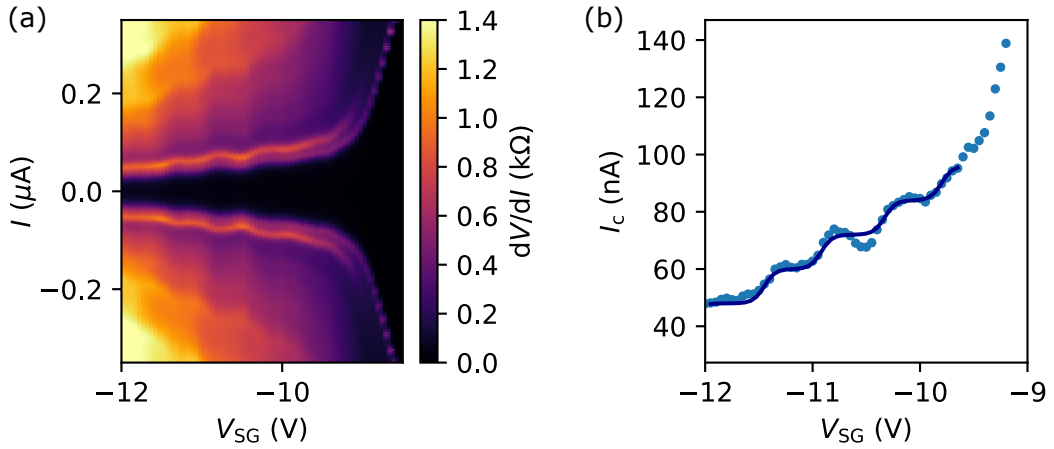

Figure E.1: Discretization of the critical current at another gate voltage condition. (a) Color map of the differential resistance as a function of V_{SG} and current I at $V_{BG} = 10\,V$ and $V_{TG} = -8\,V$. (b) Extracted critical current (dotted) with a fitted curve (solid line) using Eq. 6.7.

E Supplementary information: SQPC

E.1 Additional measurement of the discretized critical current

Here, the SG dependence of the critical current is presented for another gate condition at $V_{BG} = 10\,V$ and $V_{TG} = -8\,V$. Figure E.1a shows the respective color map of the differential resistance as a function of V_{SG} and current I. Similar to the presented data in the main text (cf. Fig. 6.6), the critical current is observed to vary in a step-like fashion. The extracted critical current (dotted) is plotted in Fig. E.1b. From the fit (solid line), a constant step height $\delta I_c^{(2)} = 12\,nA$ is determined for all visible 1D subbands.